Aus der Radiologischen Universitätsklinik Tübingen
Abteilung Präklinische Bildgebung und Radiopharmazie

Towards the Development of a Breast PET/MRI Insert for a Clinical Whole-Body PET/MRI Scanner

Inaugural-Dissertation
zur Erlangung des Doktorgrades
der Humanwissenschaften

der Medizinischen Fakultät
der Eberhard Karls Universität
zu Tübingen

vorgelegt von

Schmidt, Fabian Peter

2022

Dekan:	Professor Dr. B. J. Pichler
1. Berichterstatter:	Professor Dr. B. J. Pichler
2. Berichterstatter:	Professor Dr. J. Jochum

Tag der Disputation: 04.04.2022

Abstract

Amongst the noninvasive imaging technologies that are routinely used for clinical diagnostics, two are of particular interest for oncological imaging: positron emission tomography (PET), which utilizes a radioactive labeled tracer to monitor biological processes with great precision down to the molecular level, and magnetic resonance imaging (MRI), a radiation-free technology that makes use of magnetic fields and their distinct responses to different tissues to gather both anatomical and functional information with high soft tissue contrast. The complementary combination of both modalities further boosts their value for oncological imaging by enhancing the accuracy of the diagnosis, allowing for individual therapy planning, and monitoring the treatment response. Combined PET/MRI is currently used to detect breast cancer, the most commonly diagnosed cancer in women. To this end, a radio frequency (RF) coil dedicated to the breast is used to enhance the quality of the MR image. PET imaging, however, is still performed using clinical whole-body PET systems without taking into account the demand for high resolution in the submillimeter range to detect small lesions inside the breast. To overcome the inherent disadvantages, such as limited spatial resolution and sensitivity, this thesis considers the design and development of a dedicated breast PET/MRI insert.

For this purpose, design concepts were developed, including the initial geometry of the insert, its integration into the RF coil, the constraints on the PET detectors, and the possibility of a simultaneous operation with the whole-body PET/MRI scanner. This thesis also introduces the idea of processing mixed events, or events that are detected in coincidence between both PET systems (the breast PET/MRI insert and the whole-body PET/MRI scanner). This method has the potential to resolve small metastases in the thorax and the axilla region of the breast and would significantly improve diagnostic and therapeutic choices.

PET detectors and system electronics are essential for building the PET/MRI insert. A promising candidate for this purpose is the Hamamatsu PET modules (Hamamatsu Photonics K.K., Hamamatsu, Japan), as they feature high performance, compact integration, and modular technology, thus providing the flexibility required for prototyping. This study performed comprehensive tests of these modules to evaluate their suitability for use as the breast PET/MRI insert.

The results showed that the PET modules could stably operate over time and temperature changes. However, the PET modules were only available with scintillation crystals of such large sizes that the corresponding spatial resolution would be unacceptable for the breast PET/MRI insert. This thesis demonstrated that the Hamamatsu modules could be used with the researcher's own photosensors and scintillation blocks with a small crystal size of 1.5 mm, enabling a high spatial resolution. Therefore, a prototype detector with a light sharing approach and a corresponding data processing algorithm was developed.

In addition to extensively testing the PET hardware, one focus of this work was to evaluate the detector's performance inside the MRI scanner. The integration of a PET system into an MRI scanner naturally comes with several problems for both modalities. On the one hand, the MRI scanner is a highly sensitive device that can be distorted by the smallest electromagnetic interference. On the other hand, the MRI scanner itself is a harsh environment due to the presence of strong magnetic fields and can potentially interact with the communication lines and electronics of the PET modules. The original PET modules were not designed to operate inside an MRI scanner. Therefore, the work conducted for this thesis included several modifications of the PET system setup and iterative tests for MRI compatibility inside the MRI scanner. Special test sequences and corresponding analysis methods were utilized to gain insight into how the digital PET event data was affected by the individual components of the MRI scanner. Finally, the mutual interference between both systems could be limited to an acceptable level through the following actions: locating the back-end electronics outside of the MRI room, constructing a proper RF shield for the detectors, filtering the power lines, and generating a signal transmission via optical fibers.

In summary, this thesis reached essential milestones for developing a breast PET/MRI insert for a clinical whole-body PET/MRI scanner. This work enables a further refined development of the detectors and the entire insert driven by advanced simulations to guide the experimental setup. In addition, the results of this thesis are not specifically limited to the breast insert; instead, they can be applied to other PET systems, such as those used for small animals or brain imaging, as well as to the operation of PET detectors inside MRI scanners in general.

Zusammenfassung

Die Positronen Emissions Tomographie (PET) und die Magnet Resonanz Tomographie (MRT) sind nicht-invasive Bildgebungsverfahren, welche bei onkologischen Fragestellungen verwendet werden. Mithilfe von PET ist es möglich unter Zuhilfenahme eines radioaktiv markierten Tracers biologische Prozesse auf der molekularen Ebene zu visualisieren. Bei der MRT werden anhand von magnetischen Feldern und deren unterschiedlichen Auswirkungen auf die verschiedenen Gewebearten anatomische und funktionelle Bilder mit einem hohen Weichteilkontrast erzeugt. Eine Kombination dieser beiden Bildgebungsmodalitäten kann genutzt werden, um eine Verbesserung der onkologischen Bildgebung zu ermöglichen in Form einer besseren Diagnose, individuell angepasster Therapieplanung sowie einer genaueren Beobachtung der Therapieantwort.

Die Kombination von PET und MRT wird auch für die Bildgebung von Brustkrebs genutzt, die am häufigsten auftretende Krebsart bei Frauen. Um hierbei die MRT-Bildqualität zu verbessern, wird eine spezielle Hochfrequenz (HF) Spule für die Brust eingesetzt. Die PET-Bildgebung wird derzeit hingegen noch mit Ganzkörper PET/MRT-Systemen durchgeführt. Nachteilig daran sind die Einschränkungen hinsichtlich der Ortsauflösung und der Sensitivität, welche durch das in dieser Arbeit vorgestellte Brust PET/MRT-Insert, einem eigenständigen PET-Scanner für die Brust, verbessert werden sollen.

Hierfür wurde ein rudimentäres Design für das Insert erarbeitet, welches die Integration in die HF-Spule, die Anforderungen an die PET-Detektoren und den simultanen Betrieb innerhalb des Ganzkörper PET/MRT-Scanners beinhaltet. Weiterhin wurde das Konzept von Ereignissen, die koinzident zwischen beiden PET-Systemen auftreten, eingeführt. Hieraus ergibt sich das Potenzial einer Identifikation von kleinen Metastasen im Bereich des Brustkorbs und der Achsel.

Als mögliche PET-Detektoren und Systemelektronik bieten sich die Hamamatsu PET-Module (Hamamatsu Photonics K.K., Hamamatsu, Japan) aufgrund ihrer hohen Performanz, Modularität und Möglichkeit zur kompakten Integration an. Umfangreiche Tests wurden durchgeführt, um zu bewerten, ob sich die PET-Module zur Realisierung des Brust PET/MRT-Inserts nutzen lassen. Zunächst

wurde gezeigt, dass ein konstanter Betrieb über einen längeren Zeitraum und Temperaturbereich möglich ist. Da die verfügbaren Szintillationskristalle für die PET-Module zu groß gewesen wären, um eine hohe Ortsauflösung mit dem PET/MRT-Insert zu erreichen, wurde in dieser Arbeit ein Detektor mit dazugehöriger Signalauswertung entwickelt welcher ermöglicht 1.5 mm große Kristalle auszulesen.

Des Weiteren wurde der Betrieb der PET-Module innerhalb des MRT-Scanners untersucht. Die Integration eines PET-Systems in einen MRT-Scanner kann zu elektromagnetischen Störungen der Magnetfelder führen. Zusätzlich muss das PET-System den starken magnetischen Feldern des MRT-Scanners standhalten, welche zu Störungen in dessen Leitungen und innerhalb dessen Elektronik führen können. Da die PET-Module ursprünglich nicht für einen Einsatz innerhalb eines MRT-Scanners vorgesehen waren, mussten im Rahmen dieser Arbeit dahingehend Änderung durchgeführt werden. Deren Einfluss auf eine Kompatibilität des PET und MRT-Systems wurde stetig mithilfe von speziellen Testsequenzen und eigens dafür entwickelten Auswertemethoden der PET-Daten getestet, welche Rückschlüsse auf die Störung durch einzelne Komponenten des MRT-Scanners zuließen. Die gegenseitige Beeinflussung von PET und MRT konnte ausreichend minimiert werden durch das Verlegen eines Teils der Elektronik außerhalb des MRT-Raumes, einer HF-Abschirmung der Detektoren, einer gefilterten Spannungsversorgung sowie einer optischen Signalübertragung.

Zusammenfassend wurden im Rahmen dieser Arbeit fundamentale Aspekte für die Entwicklung des Brust PET/MRT-Inserts für den parallelen Betrieb innerhalb eines Ganzkörper PET/MRT-Scanners erarbeitet. Aufbauend auf dieser Arbeit ist es möglich weitere Entwicklungen und Simulationen des Komplettsystems durchzuführen. Des Weiteren sind die Ergebnisse aus dieser Arbeit nicht nur für die Entwicklung des Brust PET/MRT-Inserts relevant. Vielmehr können sie auch auf andere PET-Systeme übertragen werden, wie beispielsweise zur Kleintier- oder Hirnbildgebung, und geben allgemein Aufschluss darüber, wie ein Betrieb von PET-Detektoren innerhalb eines MRT-Scanners ermöglicht werden kann.

Table of Contents

1 Introduction

Breast cancer is the most commonly diagnosed cancer as well as the leading cause of cancer death for women. An estimated 2.1 million newly diagnosed cases of female breast cancer were reported in 2018. In Germany, one out of every eight women will develop breast cancer over the course of her lifetime. [1] Despite this negative trend, in recent years, mortality rates have decreased (i.e., increased chances of survival). Advances in therapy and early diagnosis are expected to contribute to this more positive trend. [2], [3] One area that has had a meaningful impact on this trend is the continuously evolving field of imaging in oncology. Noninvasive, in-vivo imaging technologies have a great potential to aid diagnoses, including the identification, localization, and staging of tumors, as well as treatment planning and therapy monitoring and have thus become indispensable within the clinical routine. [4] For oncology in general and breast cancer in particular, two advanced medical imaging modalities are of utmost interest in addition to the conventional X-ray-based mammography: positron emission tomography (PET) and magnetic resonance imaging (MRI).

PET has the potential to detect cancer based on alternated biochemical and molecular processes within tumor tissues. The exceptionally high sensitivity of PET allows for the detection of molecules in the picomolar range. [5] Before PET imaging, a radioligand, also known as the tracer, is injected into the patient and accumulates inside the body based on its specific chemical properties. One example is the frequently used analog of glucose, ^{18}F-fluorodeoxyglucose (FDG), which can be used to monitor the increased glucose metabolism that occurs in most types of tumors. The β^+ decay of the radioactive isotope ^{18}F, which involves the emission of a positron, is used to localize the tracer molecules in the body. In this process, the emitted positrons are measured indirectly by the detection of two simultaneously emitted back-to-back gamma rays, which result from positron-electron annihilation. A more detailed description of PET can be found in Chapter 2.1.

In contrast to PET, which lacks resolving morphology, MRI or the widely used X-ray computed tomography (CT) can gather high-resolution anatomic information.

The major advantages of MRI are its high soft tissue contrast, radiation-free operation, and potential to provide functional information, such as diffusion and perfusion imaging or magnetic resonance spectroscopy. [6] MRI scanners operate by employing a strong magnetic field to align nuclear spins. Hydrogen nuclei are widely used for MRI, as they are abundant in the human body. A second radiofrequency magnetic field can be applied to excite the nuclear spins. The relaxation of these spins to a lower energy changes the net magnetization, which in turn can be measured by the receiver of the MRI scanner. A brief overview of the MRI operation principles is presented in Chapter 2.2.

It should be noted that MRI and PET are not limited to the field of oncology and are highly beneficial in numerous other clinical applications, such as in the fields of neurology and cardiology. [7] In order to exploit the complementary information provided by the two imaging modalities, combined whole-body PET/MRI scanners, which offer simultaneous imaging, were first introduced for preclinical purposes and later found a wide application in the clinical field. [8]–[10] For the specific topic of this thesis—breast imaging—the synergy of simultaneous PET and MRI benefits several fields.

The fusion of PET and MRI provides accurate morphological and functional data while offering the advantages of each individual modality. As such, dynamic contrast-enhanced MRI is the most sensitive tool for breast cancer screening and features a high sensitivity ranging up to 98–100 %. [11] PET breast imaging has demonstrated an increased specificity compared with MRI [12], [13] and a high sensitivity for axillary and internal mammary nodal metastasis [14], [15]. The combination of the complementary sensitivity and specificity of both modalities will help improve diagnostic accuracy for breast cancer. [16]

The improved accuracy of PET/MRI has been demonstrated by a decrease of false-positive exams compared to standalone breast MRI, which is not always able to differentiate benign from malignant lesions. [16], [17] Furthermore, studies have reported that radiologists feel more confident assessing lesions through hybrid PET/MR imaging. Finally, the improved diagnostic accuracy of breast cancer may lead to a reduction of unnecessary breast biopsies. [11], [17] Combined PET/MRI is also sensitive to a characteristic specific to the breast: most malignant breast cancers show high grades of intratumoral heterogeneity. Research has shown that a combination of the multiparametric information acquired by simultaneous PET/MRI enables breast tumors to be classified, which in turn further helps to improve the diagnosis and can be applied in individualized therapy planning. [18]

Current clinical PET/MRI scanners are designed for a wide range of applications and are not solely used for breast imaging. To improve the quality of breast imaging, multichannel radiofrequency breast coils were introduced into combined PET/MR imaging. These coils resulted in an increase in the soft tissue contrast and spatial resolution of MR images of the female breast. [19], [20] However, regarding the PET modality, breast imaging was not improved by the breast-specific MR coils. The purpose of this thesis is to introduce the concept and development of a breast PET/MRI insert, which, in a simplified manner, can be thought of as a miniaturized PET scanner specifically designed for the breast and integrated into a whole-body PET/MRI scanner. The principal motivation for a breast-specific PET insert is to increase the image quality and sensitivity. First, a better image quality with higher resolution helps identify smaller structures, improving lesion detection and enhancing the accuracy of tumor classification. Second, the proximity of the PET insert to the breast naturally yields a higher sensitivity due to the high solid angle coverage, which can either be used to further improve the image quality or the patient’s comfort by reducing the scan time. The general system design of the PET insert, together with considerations on the integration into the RF coil and interaction with the whole-body PET/MRI scanner, are described in Chapter 3.

Furthermore, the focus of this thesis involves the development and evaluation of the PET detectors and PET system electronics dedicated to the breast insert. As a basis for the breast insert, the C13500 series PET modules (Hamamatsu Photonics K.K., Hamamatsu, Japan) were chosen, as they offer superior, state-of-the-art performance in combination with modular technology, enabling the high flexibility mandatory for the design process and prototyping of a breast PET insert. Chapter 4 addresses the work related to the general operation of the PET modules. This work mainly involves the software-based processing of PET event data with respect to performance optimization, stability over time, and varying temperature conditions.

The commercially available PET modules from Hamamatsu were designed for use in clinical whole-body PET scanners; hence, the detectors, including the size and dimension of the scintillation crystals and the photosensor, had to be modified for the breast insert to achieve higher spatial resolution and sensitivity. Chapter 5 describes the development of a customized prototype detector for the breast insert. For this purpose, a light sharing approach was used, which required changes to event data processing and a comprehensive evaluation of different hardware and software settings to obtain a PET detector with high overall performance.

A major difficulty with designing the breast insert is that it needs to be operated inside an MRI scanner while simultaneously performing MR imaging. [21], [22] In general, the high static magnetic field strength, which is, for example, 3 T for the Biograph mMR (Siemens Healthineers, Erlangen, Germany), has such a severe effect on the PET system that without the development of solid-state photosensors, the combined PET/MRI scanners that are now used for clinical routine would have never been feasible. [23]–[25]

While the detectors used in this work are composed of these solid-state photosensors, a wide range of complications arise in assuring mutual compatibility between the PET system and the MRI scanner. In addition to functioning in the scanner's static magnetic field, the PET system must operate robustly and consistently while withstanding the harsh conditions of the switching magnetic field, including the rapid changes of the local magnetic field strength (gradients) and the transmission of powerful radio frequency (RF) waves, which are essential processes of MRI scans. Furthermore, the stable performance of the MRI scanner needs to be guaranteed while the PET insert operates inside the MRI scanner's bore. The electromagnetic interference that could originate from the PET modules and the magnetic field inhomogeneity caused by magnetic susceptibility differences potentially distort the MRI scanner's sensitive operation principles and eventually cause artifacts in the MR images. [26]–[28] Chapter 6 addresses the problems associated with the PET system's MRI compatibility in further detail. A comprehensive evaluation of the simultaneous operation of the PET modules inside the Biograph mMR was conducted to address these issues. This evaluation involved several iterations of hardware modifications of the entire PET system setup, especially the detector front-end and the transmission lines. Furthermore, a variety of specially tailored MRI test sequences were used to expose the PET insert to a maximum stress level and accurately test that the MRI scanner properly operated in the presence of the PET system.

In summary, the work conducted in this thesis covers the mandatory steps for developing a breast PET/MRI insert for a clinical whole-body PET/MRI scanner.

2 PET/MRI Physical Principles and Technology

2.1 Positron Emission Tomography

2.1.1 β+ Decay and Positron-Electron Annihilation

A proton-rich radionuclide gains stability either through electron capture, where a proton of the nucleus interacts with an orbital electron and forms a neutron accompanied by a neutrino, or by β+ decay. The latter is the predominant effect that is observed for radionuclides used for PET imaging. [29] The decay equation

$$p \rightarrow n + e^{+} + \nu_{e}$$

describes the process, where a proton p is converted to a neutron n and accompanied by the emission of a positron e^{+} and neutrino ν_{e}. [29] β+ decay reduces the atomic number Z of the parent nuclide P by one and yields a new daughter nuclide D, as described by

$${}^{A}_{Z}P \rightarrow {}_{Z-1}^{\;\;A}D + e^{+} + \nu_{e} \, ,$$

where A is the total number of nucleons. [30] The nature of radioactive decay is represented by a certain statistic that can be described by the decay law

$$N(t) = N_{0}e^{-\lambda_{d}t},$$

where N_{0} is the number of radioactive atoms at t=0 and N is the remaining number of radioactive atoms after a time t. [31] λ_{d} is the decay constant that is specific to the radionuclide and can be used to define the half-life time

$$T_{1/2} = \frac{ln(2)}{\lambda_{d}} \, ,$$

in which half of the original number of radioactive atoms have undergone radioactive decay. [31] The decay process can be graphically illustrated, as Figure 1 shows, with the decay scheme of $^{18}\mathrm{F}$.

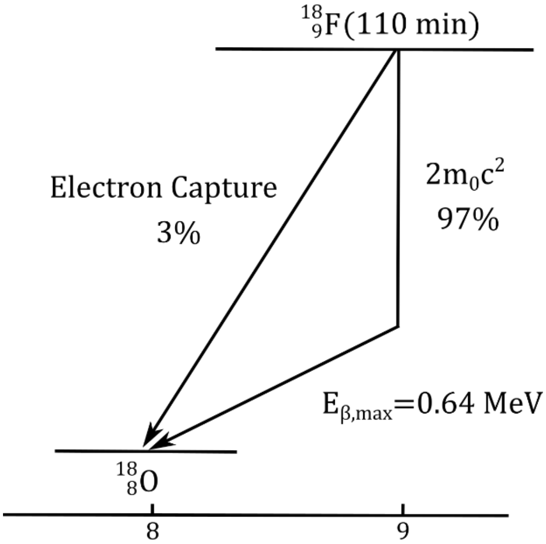

Figure 1: Decay scheme of ^{18}F to ^{18}O with probabilities for electron capture and β⁺ decay. Adapted and modified from [30].

A minimum energy of 1.022 MeV, which is twice the electron or positron rest energy of 511 keV, is necessary for β^+ decay. Furthermore, one electron mass must be added to the proton to form the neutron, and a second electron mass is necessary due to the ejected positron. The maximum energy of the positron $E_{\beta^+,max}$ after the β+ decay depends on the radionuclide and is shown for common positron emitters in Table 1.

Table 1: Common positron emitters used in PET with their respective half-life, the maximum energy of the emitted positron, and the range of the emitted positron in water. Adapted from [32].

Radionuclide	Half-life	$E_{\beta^+,max}$ [MeV]	Max. β^+ range in water [mm]	Average β^+ range in water [mm]
^{11}C	20.4 min	0.97	3.8	0.85
^{13}N	10 min	1.20	5.0	1.15
^{15}O	2 min	1.74	8.0	1.80
^{18}F	110 min	0.64	2.2	0.46
^{68}Ga	68 min	1.90	9.0	2.15
^{82}Rb	75 s	3.35	15.5	4.10

The positron passes through the surrounding material, and its energy is reduced through multiple interactions with the orbital electrons of surrounding atoms until its energy approaches the rest energy. A higher $E_{\beta^+,max}$ requires more interactions to reach the rest energy and as such increases the positron's range in the material. Furthermore, high-density materials increase the probability of interactions that reduce the positron's energy and therefore result in a lower positron range. [29], [31] A low positron range is highly important, as it defines the lower limit of the intrinsic spatial resolution of the PET system. [33]

Once the positron approaches its rest energy, it combines with an electron. This process is called positron-electron annihilation and is illustrated in Figure 2.

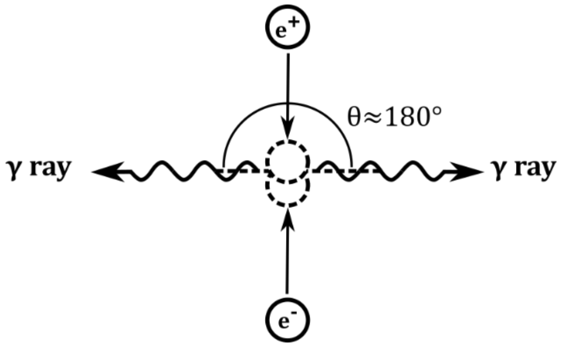

Figure 2: Annihilation of an electron with its counterpart, a positron, resulting in two gamma rays propagating in opposite directions. Adapted and modified from [31].

It is assumed that both particles are at rest for the recombination. Due to the laws of momentum and energy conservation, two gamma rays are produced, each with an energy of 511 keV (the rest energy of an electron), that propagate in almost opposite directions. It is possible that the positron retains a small portion of its kinetic energy before the annihilation process; the residual momentum is transferred to the two gamma rays and results in an angle between the trajectories of the two gamma rays that differs from 180°. [29], [31] This acollinearity angle, with a mean of 0.2° full width at half maximum (FWHM), translates into a degradation of the intrinsic spatial resolution of the PET system, depending on the scanner's bore size. [33]

2.1.2 Interactions of Photons with Matter

The effects that occur when gamma rays propagate in an absorber material cannot be described by their classic wave-like character. Due to wave-particle duality, the gamma rays can be represented by photons, and both terms are used interchangeably in this thesis. The three major types of interactions between these photons and matter are described by the photoelectric effect, Compton scattering, and pair production. [31], [34]

2.1.2.1 Photoelectric Effect

A photoelectric absorption takes place when an incident gamma ray transfers all of its energy $E_{\gamma 0}$ to a bound shell electron of an absorber atom. This process, known as the photoelectric effect, is illustrated in Figure 3.

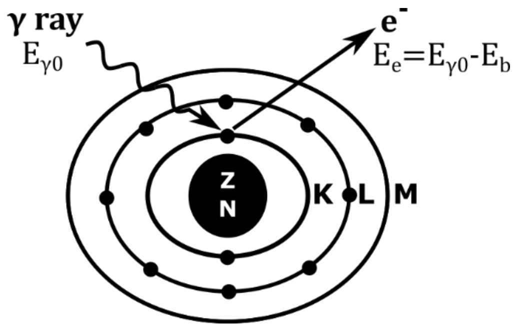

Figure 3: Depiction of the photoelectric effect, where an incident gamma ray transfers its energy and ejects a K shell electron. Adapted and modified from [29].

During this process, the gamma ray disappears completely, and the photoelectron is ejected from its orbital shell. [34] The energy of the photoelectron E_e can be described by

$$E_e = h\nu - E_b = E_{\gamma 0} - E_b \,,$$

where h is Planck's constant, ν is the frequency of the incident gamma ray and E_b is the binding energy of the orbital shell electron. [34] The photoelectric effect always requires the nucleus of the absorber atom; hence, it is not possible for this process to take place with a free unbound electron. [34] The photoelectric effect appears predominantly with K shell electrons, with a contribution of approximately 20 % from the L shell and a negligible contribution from the higher shells. [29]

The probability that a gamma ray will undergo the photoelectric effect can be described by the cross section σ_{pe} in approximation with the formula

$$\sigma_{pe} \sim \frac{Z^n}{E_{\gamma 0}^{3.5}} \,,$$

where n lies between 4 and 5. [31] It can be concluded that the photoelectric effect most likely occurs for low gamma ray energies and materials with a high atomic number Z. The fact that the probability increases rapidly with the atomic number is also the reason why high Z materials are used for scintillators and shielding in PET imaging. [31]

2.1.2.2 Compton Scattering

Compton scattering occurs when a gamma ray interacts with the outer shell electron, which has an atomic binding energy of E_b of an absorber atom, and the initial energy of the gamma ray is partially transferred to the electron. Figure 4 depicts this inelastic collision, which results in the ejection of an unbound Compton electron *e-* with an energy E_e. [29], [34]

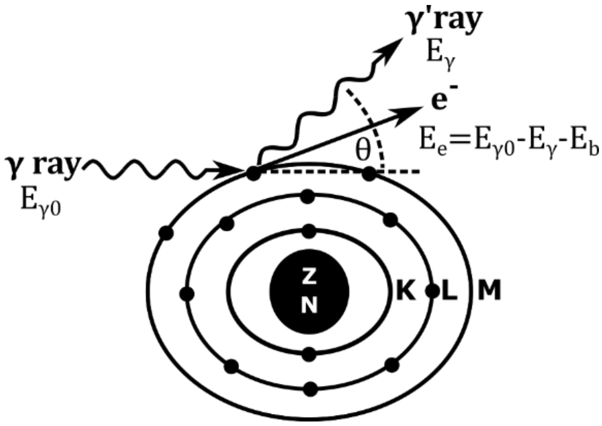

Figure 4: Process of Compton scattering, with the incident gamma ray, ejected outer shell electron, and scattered gamma ray at an angle θ. Adapted and modified from [29].

As a result of this process, the photon is deflected from its initial trajectory. The laws of conservation of momentum and energy explain the reduced energy of the Compton scattered photon E_γ, which can be described with the following formula

$$E_\gamma = E_{\gamma 0}\left(1 + \frac{E_{\gamma 0}}{m_0 c^2}(1 - \cos\theta)\right)^{-1},$$

where m_0 represents the mass of an electron at rest and *c* the speed of light in a vacuum. E_γ depends on the energy of the gamma ray before the collision $E_{\gamma 0}$ and the scattering angle θ between the direction of the incident photon and the scattered photon. [31] According to Klein and Nishina, the angular distribution of the scattering angle can be described by the differential cross section $\frac{d\sigma_c}{d\Omega}$ and the following formula

$$\frac{d\sigma_c}{d\Omega} = Zr_0^2\left(\frac{1}{1+\alpha(1-cos\,\theta)}\right)\left(\frac{1+cos^2\,\theta}{2}\right)\left(1+\frac{\alpha^2(1-cos\,\theta)^2}{(1+cos^2\,\theta)[1+\alpha(1-cos\,\theta)]}\right),$$

where r_0 is the classical electron radius and α=$E_{\gamma 0}/m_0c^2$. The differential cross section is related to the probability that an incident photon will be Compton scattered at an angle θ. [34] In Figure 5, the distribution is shown graphically.

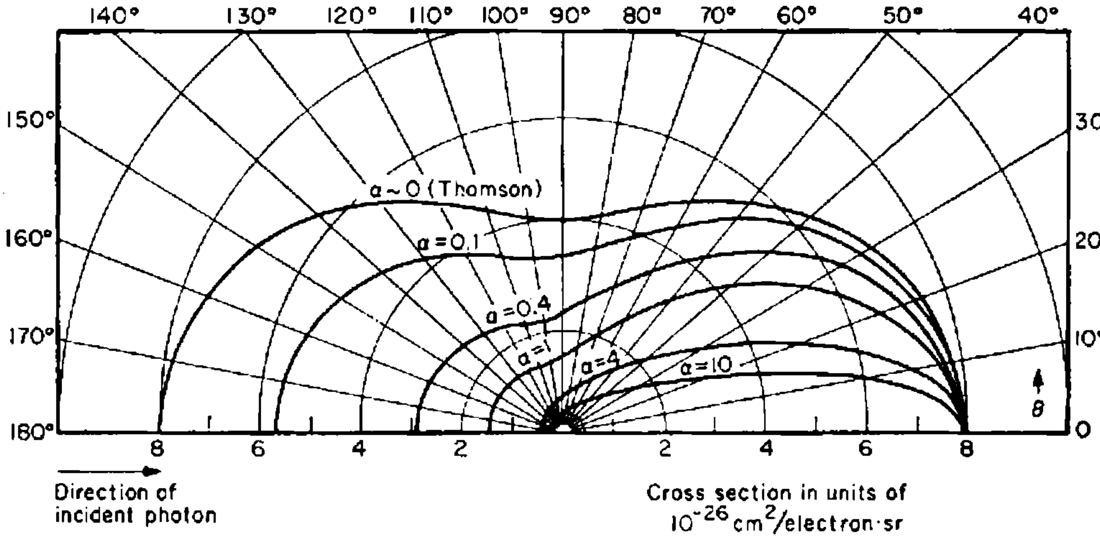

Figure 5: Polar plot of the cross section for incident photons Compton scattered at an angle θ. The different curves relate to different energies of the incident photon. Adapted and modified from [35].

The gamma ray energy of interest for PET is 511 keV and corresponds to α=1. It has been shown that photons with this energy are likely to be forward scattered (θ<90°). [34]

2.1.2.3 Pair Production

Pair production requires a minimum energy of 1.022 MeV (two times the 511 keV rest energy of an electron). Figure 6 demonstrates how the incident gamma ray disappears after interacting with the nucleus of the absorber atom. An electron-positron pair is generated with a kinetic energy of $E_{e,p}$, which is half of the excess energy above 1.022 MeV of the incident photon with an energy of $E_{\gamma 0}$. Pair production can be thought of as the inverse process to annihilation, with the difference that it always requires an atomic nucleus. [31]

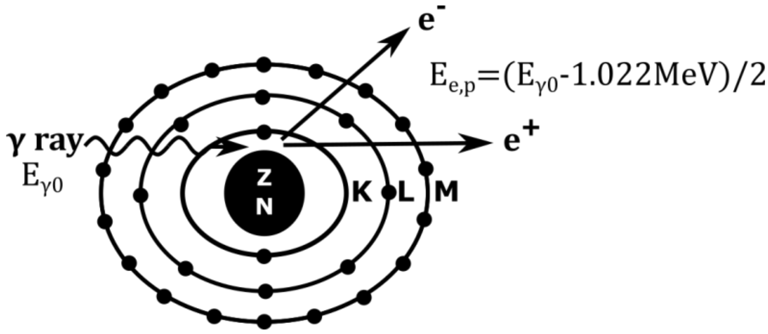

Figure 6: Process of pair production transforming an incident gamma ray into a free electron and positron. Adapted and modified from [29].

The relationship between the cross section for pair production σ_p and the atomic number of the nucleus Z can be described by [31]

$$\sigma_p \sim Z^2.$$

All three of these interactions between photons and matter are statistical processes and hence have a certain probability of occurrence. The likelihood that each process will occur highly depends on the photon's energy and the atomic number of the absorber (Figure 7).

For high Z absorber materials and relatively low energies, the photoelectric effect is the dominant mechanism over Compton scattering. However, pair production is the predominant effect for relatively high energies (>10 MeV) and materials with a high atomic number. [29]

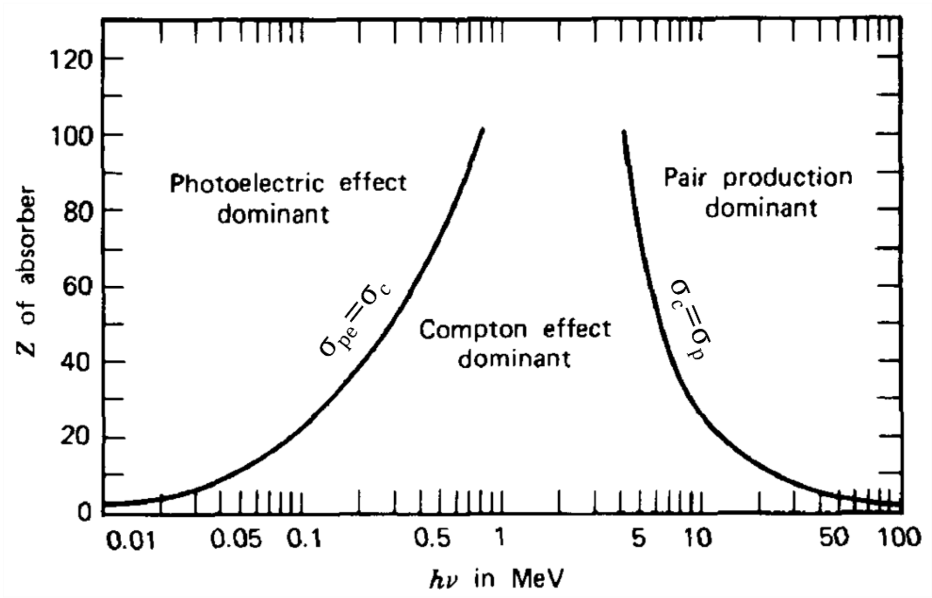

Figure 7: Graphical illustration of the likelihood of the photoelectric effect, Compton scattering, and pair production over the photon energy and for different atomic numbers. The two curves mark the Z and photon energy values where the cross sections ($\sigma_{pe}, \sigma_c, \sigma_p$) of two neighboring effects are equal. Adapted and modified from [36].

2.1.3 Inorganic Scintillators for Gamma Ray Detection

In general, scintillators are used to convert ionizing radiation to photons in the visible or ultraviolet spectrums. Multiple scintillator variants exist, such as liquid, solid, gaseous, organic, inorganic, crystalline, and non-crystalline scintillators. The gamma ray energy of 511 keV and high detection efficiency make inorganic single-crystal scintillators the most suitable choice for PET applications. [37]

The incident 511 keV gamma rays interact with the scintillator through either the photoelectric effect or Compton scattering and produce a photoelectron or a Compton scattered electron, respectively. As these electrons travel through the scintillator material, a portion of their energy is transferred to electrons in the valance band of the scintillator atoms. If this energy exhibits the band gap energy E_g, the electron is elevated from the valance band to the conduction band and effectively creates a positively charged hole in the valance band, as illustrated in Figure 8. [31], [34]

In a pure crystal, the de-excitation of the electron in the conduction band to the valence band results in a scintillation photon with an energy above the visible range due to a high E_g. Therefore, a small number of impurities, called activators, are added to the inorganic scintillation crystal in order to create luminescence centers in the crystal lattice.

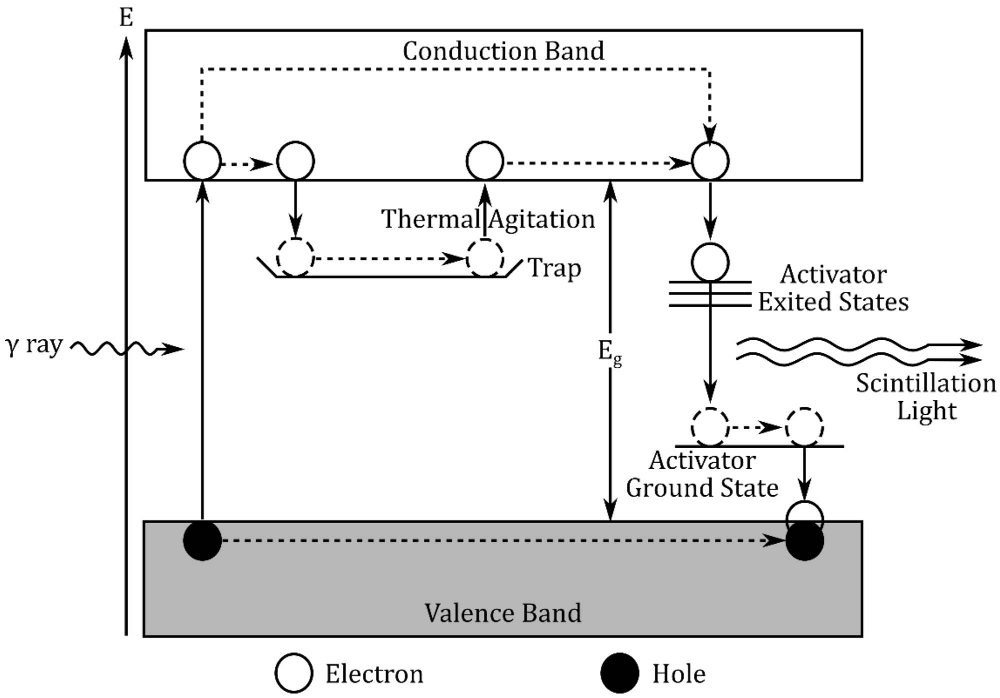

Figure 8: Principle of scintillation with successive states for the electron and the hole in the band model for an inorganic scintillation crystal. Adapted and modified from [31], [34].

Thus, the energy band structure of the scintillator is modified in a manner such that energy states, called activator states, are formed in the forbidden band between the conduction band and the valence band. An excited electron in the conduction band may now fall into the activator state, subsequently emitting scintillation light in the visible range on its way to the activator ground state before finally recombining with the hole in the valence band. [34], [38]

Excited electrons may also get trapped in a metastable energy state below the conduction band (Figure 8). After a period ranging from µs to hours, the electron is elevated back to the conduction band (e.g., by thermal agitation) and may also undergo the previously described scintillation process. The resulting delayed photons constitute the resulting phosphorescence. [31], [39] A comparison of the properties of different scintillators that are commonly used in PET is shown in Table 2.

Table 2: Inorganic scintillators: NaI(TI) = thallium-doped sodium iodide; BGO = bismuth germanium oxide; LSO = lutetium oxyorthoscilicate; YSO = yttrium orthosilicate; GSO = gadolinium orthosilicate; BaF_2 = barium fluoride. Adapted and modified from [38].

Property	NaI(TI)	BGO	LSO	YSO	GSO	BaF_2
Density [g/cm³]	3.67	7.13	7.40	4.53	6.71	4.89
Effective *Z*	50.6	74.2	65.5	34.2	58.6	52.2
Mean free path $\boldsymbol{\lambda_m}$ [cm]	2.88	1.05	1.16	2.58	1.43	2.20
Decay constant $\boldsymbol{\tau_d}$ [ns]	230	300	40	70	60	0.60
Light output [photons/keV]	38	6	29	46	10	2
Wavelength $\boldsymbol{\lambda}$ [nm]	410	480	420	420	440	220
Intrinsic energy resolution [%]	5.8	3.1	9.1	7.5	4.6	4.3
Index of refraction	1.85	2.15	1.82	1.80	1.91	1.56
Hygroscopic	Yes	No	No	No	No	No
Attenuation coefficient $\boldsymbol{\mu_t}$ [cm^{-1}]	0.34	0.95	0.87	0.39	0.70	0.45

The performance of a PET detector depends strongly on choosing the appropriate scintillator material, the most crucial properties of which are a high stopping power, a fast decay time, a high light output, and a low intrinsic energy resolution. [38]

A high stopping power requires a high atomic number for a large photoelectron cross section. [37] To further characterize the stopping power, the attenuation of a photon beam entering a material (e.g., a scintillator) is specified by the formula

$$I = I_0 e^{-\mu_t x},$$

where I_0 is the initial intensity of the photon beam before entering the material and I is its intensity at the depth x. The total linear attenuation coefficient μ_t depends on the material and the energy of the incident photon. [31] Furthermore, a more concise parameter to characterize the stopping power, the mean free path, can be derived from

$$\lambda_m = \frac{1}{\mu_t},$$

which can be interpreted as the depth where approximately 63 % of the incident photons have stopped in the scintillation crystal. [31]

A high light output in photons per keV of the absorbed photon is necessary for the photo detector to maintain a high signal-to-noise ratio. As such, a high encoding ratio, or the ratio of the number of crystals per channel in the photosensor that can be readout via light sharing, is increased. As a result, small scintillation crystal sizes can provide PET systems with a high spatial resolution. Another benefit of a high light yield is that the PET detector has an improved energy resolution, which can be used for Compton scatter rejection. [31], [38] The energy resolution of a PET detector is affected not only by the light output but also by the intrinsic energy resolution of the scintillator. Inhomogeneities in the impurities in the scintillator material and a non-uniform light output cause the intrinsic energy resolution to degrade. [38] The scintillation decay time τ_d defines the scintillation pulse, which can be described by the biexponential equation

$$L = L_0\left(e^{-t/\tau_d} - e^{-t/\tau_r}\right).$$

Here, L is the intensity of light at time t, L_0 the maximum height of the pulse, and τ_r the rise time constant. [31] Low scintillator decay times lead to short pulse durations, enabling PET systems with a high count rate. Moreover, the accuracy of the time measurement can be increased with low scintillation decay times, leading to a low number of random events. [38], [39] Finally, the refractive index of the scintillator material should be similar to that of the coupling material between the scintillator and the photo detector in order to avoid reflections, and scintillator materials should be transparent for visible light. [37]

2.1.4 Photosensors

For further processing, the relatively weak light output of a scintillator must be amplified and converted into an electrical signal. Two different types of photosensors, which are designed specifically for this task, are introduced in the following sections.

2.1.4.1 Photomultiplier Tube (PMT)

A photomultiplier tube (PMT) mainly consists of a photocathode and an electron multiplier structure encapsulated inside a glass vacuum tube (Figure 9). Incident photons may undergo the photoelectric effect by hitting the photocathode's absorber material and release photoelectrons. These electrons are accelerated by an electrical field and eventually collide with the first electrode, which is referred to as a dynode. Due to secondary electron emission, the energy deposition of the original electron at the dynode material leads to a reemission of more than one electron. [34]

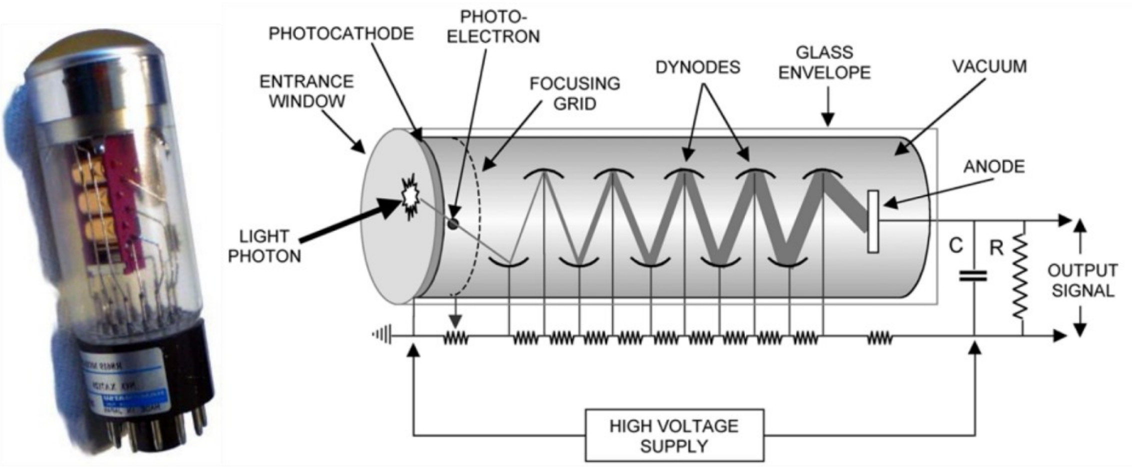

Figure 9: Principle of electron multiplication with multiple dynodes between the photocathode and the anode. Adapted from [40], [41].

The secondary electrons are then accelerated towards the subsequent dynode and release even more electrons after their collision. This process is repeated for all dynodes within the PMT. The electric potential between dynodes is thereby increased with each successive dynode to ensure that a positive electrical field accelerates the electron flux. When the electrons finally enter the anode, the resulting current corresponds to a gain in the order of 1×10^6 based on the multiplication process. [31], [34]

One disadvantage of PMTs is the high operation voltage, in the order of kV, which is needed to support the high voltage potentials of the dynodes. Furthermore, the trajectories of the electrons are influenced by magnetic fields, and PMTs are bulky devices. [34]

2.1.4.2 Semiconductor Detectors

Photo detectors can be constructed with semiconductor materials, such as silicon or germanium. In comparison to PMTs, semiconductor detectors are not sensitive to magnetic fields and allow for the combination of PET and MRI. [42] Another advantage of semiconductor detectors is their relatively small dimensions. [43]

The basic operation principle can be described as follows: incident photons interact with the semiconductor material by the physical processes described in section 2.1.2. As a result, the excitation of electrons from the valance band to the conduction band creates electron-hole pairs, which can be moved under the influence of an electrical field. [34] This is a required property for the detection process, as described in the following section.

2.1.4.2.1 Avalanche Photo Diode (APD)

Conventional photo diodes are inefficient in terms of generated charge carriers per incident photon. Avalanche photo diodes (APD) utilize impact ionization, where the initial electron is accelerated in an electric field and generates secondary electron-hole pairs along its trajectory, as illustrated in Figure 10.

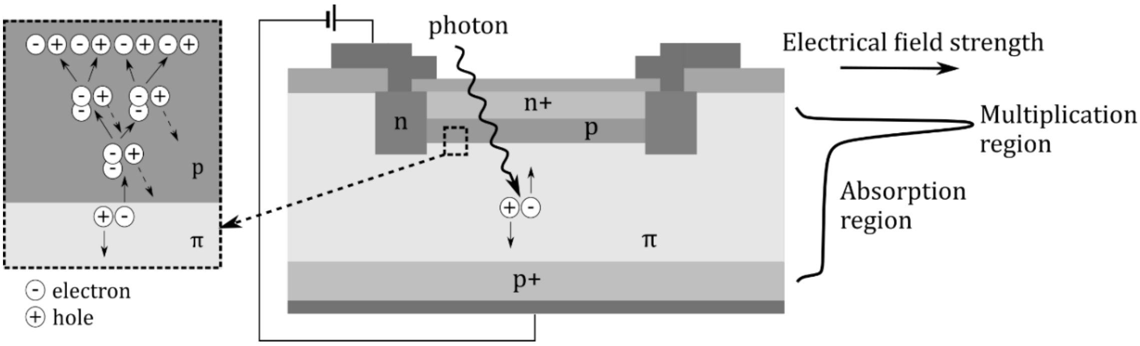

Figure 10: Structure of a reach-through type APD with differently doped layers (the "+" sign indicates a high doped region and "π" a low doped or intrinsic region), an avalanche of charge carriers, and an electrical field strength profile. Adapted and modified from [31], [43], [44].

The secondary electrons create more charge pairs, eventually resulting in an avalanche of charge carriers, known as a macroscopic current flow. Accordingly, gain factors of up to a few hundred are typical. [31], [34] The structure of the APD is optimized to enhance detection and amplification efficiency. Using differently doped layers in the APD, together with a high reverse bias voltage, results in an electric field profile across the layers of the APD (Figure 10). Two different zones in the depletion region can be defined according to their electrical field strength: the absorption region and the multiplication region. [43] The electrical field strength, and therefore the APD's current flow and gain, increases strongly with the amplitude of the reverse bias voltage V_{Bias}, as shown in Figure 11A. If the bias voltage operation point is below the breakdown voltage V_{BR}, a linear relationship between the incident photons and the current is observed, and the APD operates stably. If the applied voltage is increased above the breakdown voltage, the holes undergo impact ionization, and the charge carrier multiplication becomes self-sustaining. [34], [45] Normal APDs are not designed to operate in this region, called the Geiger mode.

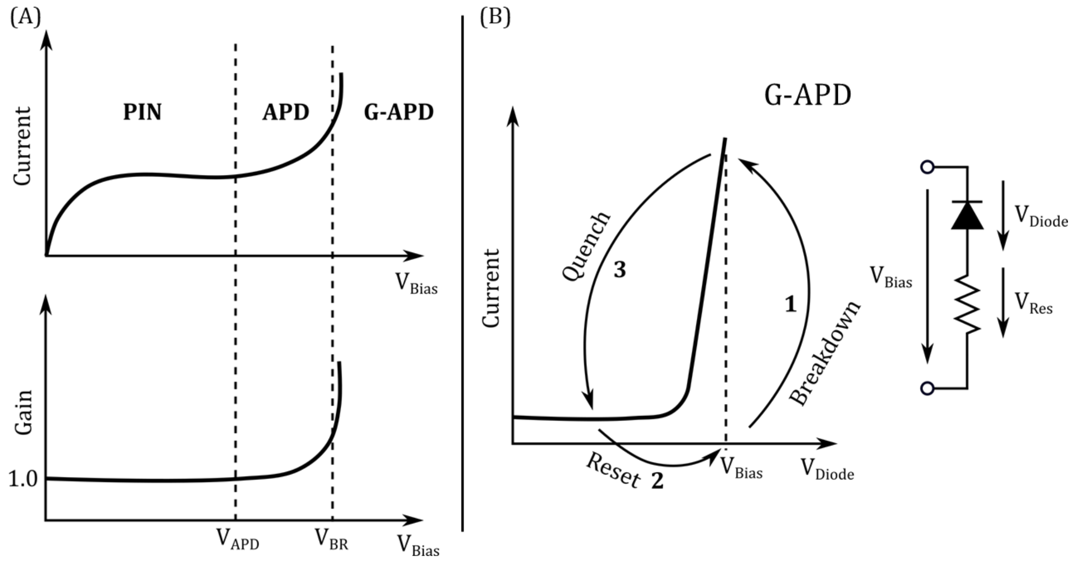

Figure 11A: Current and gain over bias voltage for different operational regions of photo diodes. An electric field strength exceeding 3×10⁵ V/cm in the multiplication region is necessary to operate the photo diode in the Geiger mode. A very thin multiplication region of ~1 µm accomplishes this via the application of only a few tenths of volts as bias voltage. Figure 11B: For the Geiger mode APD (G-APD), a detection cycle consisting of breakdown, quenching, and reset (recharging of the photo diode) is illustrated. Adapted and modified from [43], [46].

2.1.4.2.2 Silicon Photon Multiplier (SiPM)

Special Geiger mode APDs (G-APDs) use quenching to lower the electrical field and stop the self-sustaining avalanche of charge carriers. One technique is passive quenching, in which a resistor in series to the photodiode stops the avalanche (Figure 11B). The current of the avalanche causes a voltage drop over the resistor V_{Res}, which lowers the voltage at the photodiode V_{Diode}. This action stops the avalanche and returns the G-APD to quiescent mode; hence, the G-APD is ready to trigger the next incident photon. [34]

The gain of G-APDs can be as high as 1×10^5 to 1×10^7, and therefore even a single incident photon can produce a very high output signal. [45] It is not possible to distinguish between one or multiple incident photons. An array configuration of multiple G-APDs is used to overcome this lack of proportional amplification of the original number of incident photons (Figure 12A). [34]

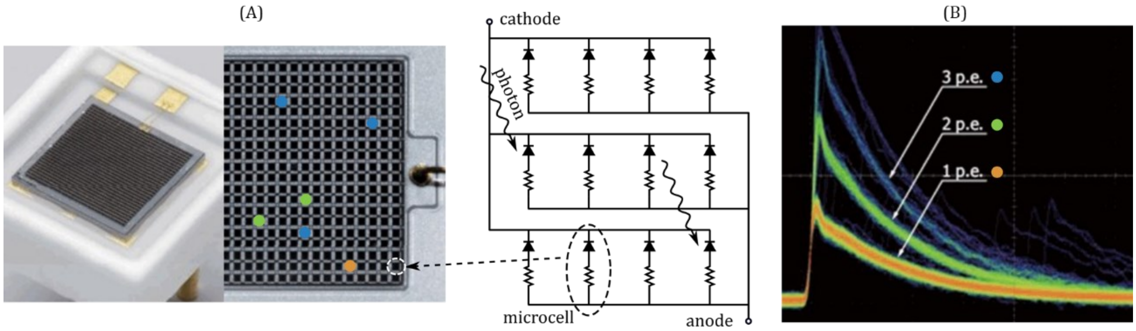

Figure 12A: Picture of a multi-pixel photon counter showing the array structure of the G-APD microcells. Figure 12B: The output signals of the photosensor are shown for up to three simultaneously detected photons. Adapted and modified from [47], [48].

The silicon photon multiplier (SiPM) consists of G-APD microcells. Each microcell, which is measured in tens of µm and referred to as a pixel, is used to trigger one incident photon. As an SiPM consists of multiple pixels, another term for SiPM is multi-pixel photon counter (MPPC). The parallel arrangement of these microcells results in an output signal that is proportional to the number of cells that underwent an avalanche, as Figure 12B shows. [47]

The structure of an SiPM, as well as the underlying physical properties of the photon detection, hamper the detection of every photon that hits the photosensor. The percentage of the number of detected photons with respect to the total number of incident photons is given by the photon detection efficiency (PDE), which is described by the formula

$$PDE(\lambda, V_{bias}) = QE(\lambda) * AIP(V_{bias}) * FF \ ,$$

where QE is the quantum efficiency that defines the probability that a photon enters the device and creates an electron-hole pair, which is a function of the wavelength λ of the photon. [47] The avalanche initiation probability AIP increases with a higher electrical field strength and is therefore dependent on the operation voltage V_{bias} of the SiPM. Furthermore, the PDE is influenced by the fill factor FF, which is defined as the fraction of photosensitive area with respect to the total geometric area of the SiPM. [34]

Another effect that limits an SiPM's photon detection capability, especially when a high number of photons is present, is its finite dynamic range, which is given by the formula

$$N_{fired} = M\left(1 - e^{-\frac{PDE * N_{ph}}{M}}\right).$$

The finite number of microcells M explains the difference in the number of incident photons N_{ph} from the number of microcells that triggered an avalanche (N_{fired}). [47] When the number of incident photons increases, the probability that a microcell will be hit by more than one photon also increases, as a scintillation light pulse of an lutetium oxyorthosilicate (LSO) crystal consists of approximately 15,000–25,000 photons/511 keV. [49] These additional hits on microcells that are already fired no longer contribute to the overall output signal. SiPMs with a large cell size, which have a low number of microcells, especially suffer from this saturation, as Figure 13 demonstrates.

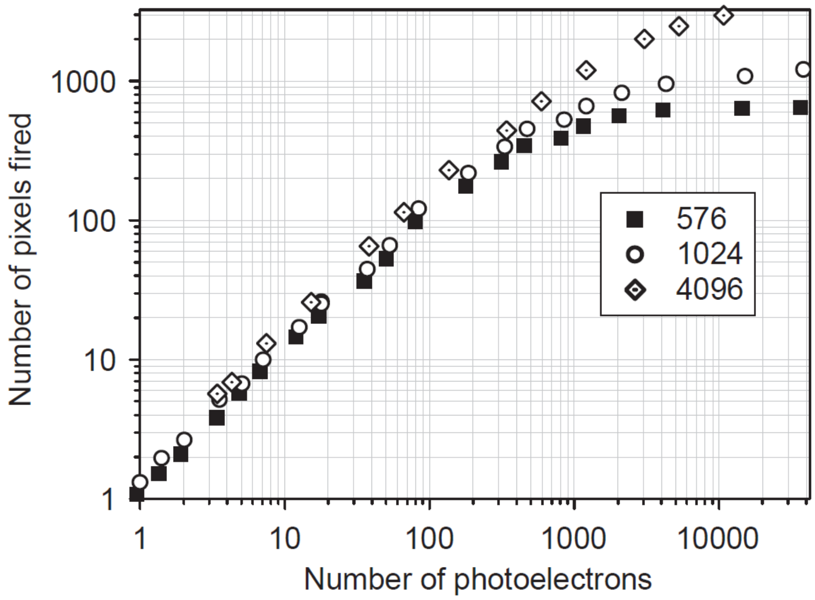

Figure 13: Number of micro cells of an SiPM that triggered an avalanche as a nonlinear function over the number of photoelectrons generated by incident photons. The curves are shown for SiPMs with 576, 1024, and 4096 microcells/mm^2. Adapted from [50]*.*

The gain of an SiPM is proportional to the overvoltage, which is defined as the difference between the voltage at which the SiPM is operated and its breakdown voltage. [47] The breakdown voltage is not constant but rather a linear function of temperature, as larger charge carrier mobility and higher ionization rates are observed at decreased temperatures. [51], [52] Conclusively, the gain of an SiPM decreases at higher temperatures. To account for the temperature sensitivity of the gain, either the SiPM is operated at a constant controlled temperature or a gain compensation circuitry is used.

2.1.5 Operation Principle of a PET Scanner

PET imaging is used to study and visualize human physiology with the detection of probes labeled with positron-emitting radionuclides. The synthetic compartment of a radionuclide (see Table 1 for examples) attached to a molecule of biological interest is referred to as a radiotracer. The most widely used tracer in clinical oncology, FDG, is used here as a representative to briefly explain how tracers function in PET. [53] Glucose metabolism is increased in rapidly growing tumors, which leads to an increased accumulation of the glucose analog FDG in the tumor. [54], [55] The tumor, or any regions with an increased uptake of the tracer, will show a high accumulation of the tracer's radionuclide. The distribution of the radionuclide, and as such of the tracer in the body, can be visualized by tomographic imaging, as described in the following section.

A PET scanner can detect the radiation from a tracer's radioactive isotope since the physical processes involved in PET yield two simultaneous back-to-back gamma rays, as shown in Figure 14 and explained in section 2.1.1. From this collection of unsorted events, electronic collimation is used to extract the desired gamma ray pairs. Here, since a gamma ray pair is detected in coincidence (i.e., at nearly the same time), a line can be drawn between two opposing detectors that represents the gamma ray emission path, also referred to as a line of response (LOR). The number of these lines crossing a particular volume in the body is proportional to its amount of radioactivity and as such to the tracer uptake. Finally, the set of lines acquired for a PET scan is reconstructed into a tomographic image through mathematical reconstruction algorithms. [41], [56] The PET scanner's detection mechanism and the steps necessary to generate the final image are described more comprehensively in the following section.

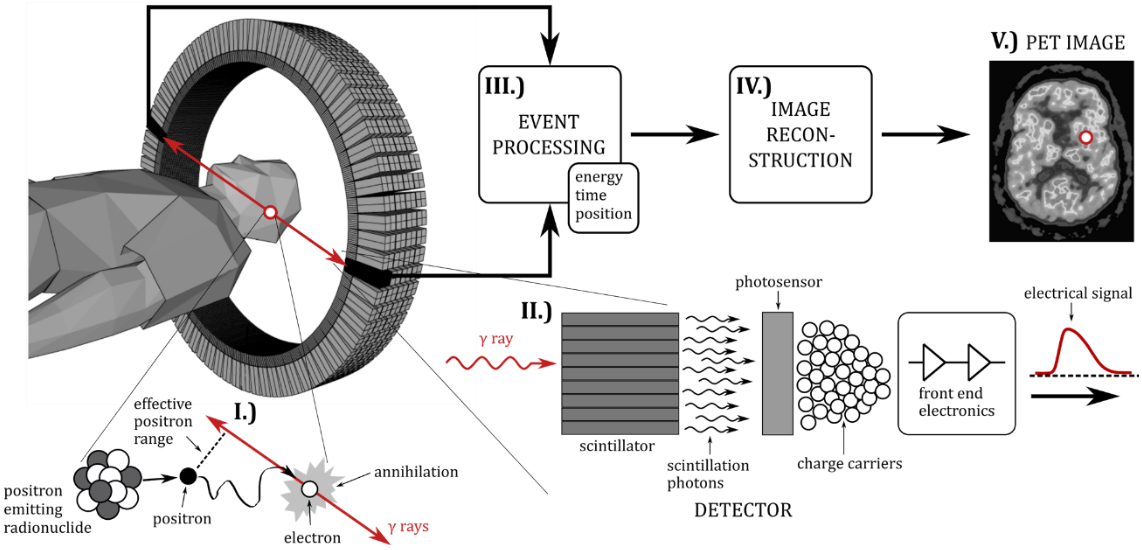

Figure 14: Simplified operation principle of a PET scanner for a single event showing gamma ray emission and detection with subsequent event processing and image reconstruction that depicts the tracer distribution. Adapted and modified from [25], [41], [57].

During the emission process, a positron is emitted based on the β+ decay of the tracer's radioisotope, as described in section 2.1.1. The positron transfers energy while it travels through the surrounding tissue and finally annihilates with an electron. The distance the positron travels depends on the medium and its energy and therefore on the isotope (e.g., 0.38 mm RMS [root mean square] positron range for $^{18}\mathrm{F}$ in water). [58], [59] The resulting 511 keV gamma rays propagate at an angle of approximately 180° with respect to each other and hit two opposing radiation detectors in a detector ring (Figure 14).

One limitation of PET is that the location of the positron-electron annihilation is detected rather than the position of the positron decay. [60] Furthermore, the non-collinearity of the emitted gamma rays introduces an error in the estimation of the annihilation point, which increases with the diameter of the PET scanner's bore.

The detection chain, as shown in Figure 14, starts when the 511 keV gamma ray enters the PET detector's scintillation crystal and is converted to multiple photons of lower energy, as described in section 2.1.3. As an example, an LSO scintillator yields approximately 15,000 photons with an energy of 2.95 eV corresponding to a wavelength of 420 nm per 511 keV gamma ray. [61] The scintillator block is typically not solid but pixelated, as the spatial resolution of the PET system scales with the crystal size, meaning a smaller crystal size corresponds to a higher spatial resolution. [33] It is possible to decrease the number of photosensors for a single detector block to a minimum of four by a weighted centroid position algorithm. [62]

The scintillation photons are further converted to electrical charge carriers and amplified by the photosensor, as described in section 2.1.4. The resulting charge is typically sent to a preamplifier with a charge sensitive configuration (i.e., integration of the transient current pulse) to produce a voltage proportional to the charge. Subsequent amplifier stages may be utilized for additional gain or to shape the signal to suit the signal processing. One measurement aims to extract the information of the energy of the incident gamma ray from the signal. Conventionally, this process is done by measuring the signal pulse height. [34] Another method, referred to as the time-over-threshold (ToT), is more efficient given the complexity of the electrical components, as only the amount of time the signal stays above a certain voltage threshold is measured. [63]

Another measurement of interest is the gamma ray's time of arrival. A time stamp is assigned to the signal pulse to gather this information. Several timing pick-off methods exist; however, the most direct is the leading edge triggering method, in which the time is measured as the leading edge of the signal pulse crosses a certain threshold voltage. [34]

The energy and time of arrival are used to classify the detected gamma ray as one of the four event types shown in Figure 15.

Coincident events that occur nearly at the same time, originate from the same annihilation event, and propagate along a linear path through the body are used to reconstruct the annihilation position. Known as true events, these coincident events have an energy of 511 keV. The difference in the time of arrival between the gamma rays is due to their different flight times. However, measuring the exact energy and time of arrival is not possible due to the statistical nature of the physical processes in the scintillator and photosensor and the noise and quantification errors of the electronics. The accuracy of the energy measurement is expressed by the energy resolution and the timing accuracy by the coincidence resolving time (CRT). To account for the detector's measurement uncertainties, an interval for the energies called the energy window is introduced, and a maximum value for the time stamp difference of two coincident events is given, known as the coincidence time window.

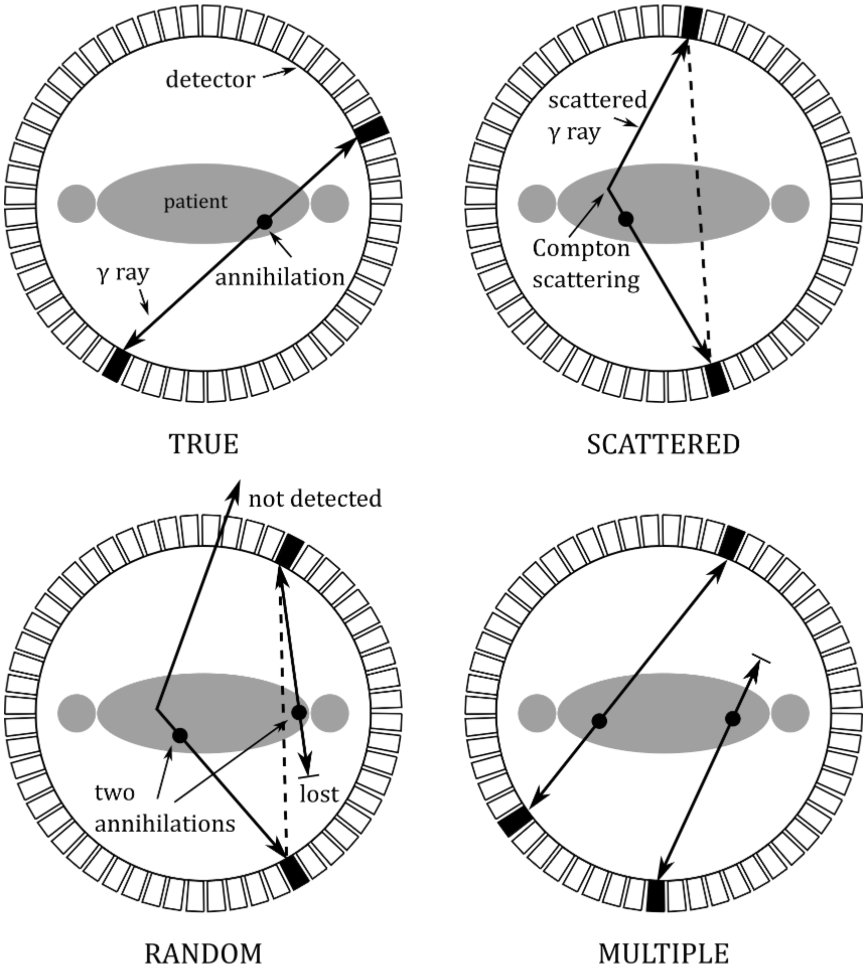

Figure 15: Event types in PET, where the slashed line between the black detector blocks corresponds to the assigned line of response if no energy or time discrimination is applied. Adapted and modified from [38], [60].

In addition to true events, scattered events can occur when at least one gamma ray undergoes Compton scattering in the body, the scanner materials, or the patient handling system, such as the patient's bed. The gamma ray is thus deflected from its original trajectory and loses part of its energy, as described in section 2.1.2.2. As such, the supposed annihilation position on the line between the two detectors does not match with the true annihilation position, which therefore introduces noise into the PET image. As the energy of Compton scattered gamma rays decreases, the assigned energy window can be used to lower the number of collected scattered events.

Furthermore, two gamma rays from two different annihilations can be detected, whereas their respective partner gamma rays originating from the same annihilation are not detected. The number of these random events that are falsely interpreted as true events can be reduced by using a tight coincidence time window.

If multiple events (i.e., three or more) are within the assigned energy window and occur within the coincidence time window, they are rejected, as their distinct origin cannot be determined. [38], [41], [60]

For an event pair, which is assumed to be a true event, an LOR is assigned between both opposing detectors (Figure 16 left).

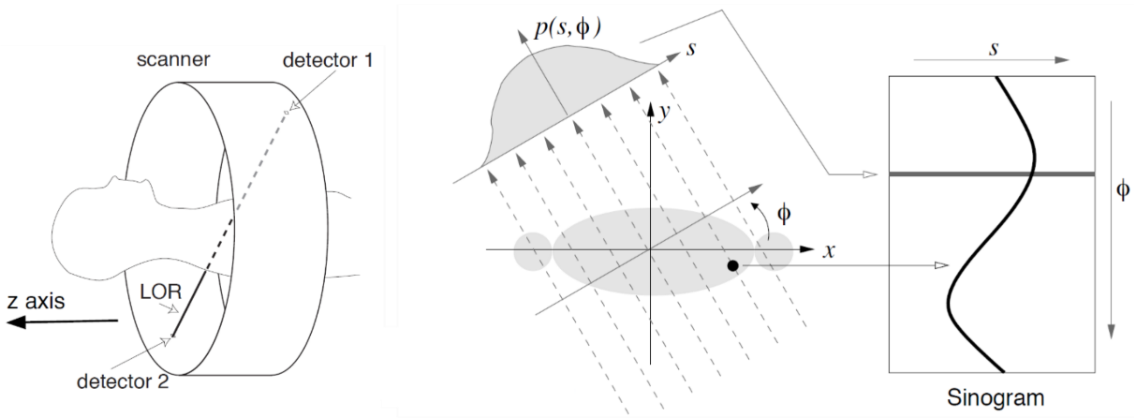

Figure 16: Left: PET ring detector with a line of response originating from a coincident event. Right: Projections by integration along all parallel LORs for a fixed angle ϕ are stored in a sinogram (a single annihilation site is mapped to a sine wave in the sinogram domain). [60] *Adapted and modified from* [64].

LORs are assigned for all events recorded during a PET scan and sorted into a sinogram (Figure 16 right). Each sinogram's pixel value corresponds to the total number of events recorded along a single LOR. [65] Each LOR is defined by the radial variable s, which is the distance between the LOR and the center of the coordinate system (detector ring), and the angular variable ϕ, which specifies the orientation of the LOR. [38] The sorting of all of the LORs is called projection $p(s, \phi)$, also known as X-ray transform, and is analogous to a Radon transform in 2D. [64] Hereby, all projections for $0 \leq \phi < 2\pi$ are used to generate a sinogram that represents all acquired events of a PET scan.

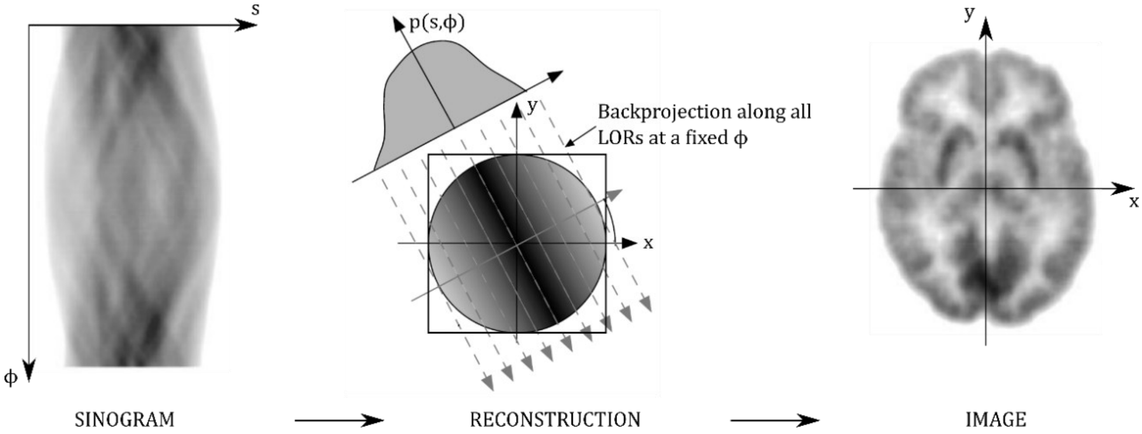

Figure 17: Simplified image reconstruction via a back projection of the sinogram data of a slice of a human brain to create the PET image. Adapted and modified from [64], [65].

One method for reconstructing images of the projections is to create a linear superposition of the back projections for each detector pair, as shown in Figure 17. [41] Re-weighting (i.e., filtering in the Fourier domain) can account for oversampling in the center of the coordinate system. This method is referred to as filtered back projection (FBP). [64]

In addition to analytic approaches, iterative reconstruction methods, such as the ordered subset expectation maximization (OSEM) algorithm, utilize successive iterations to find an image that is most consistent with the data. [41] To increase the sensitivity and image quality, 3D PET data acquisition can be performed, allowing for oblique angled LORs between detector rings. The reconstruction methods must be adapted accordingly. [41]

2.1.6 Time of Flight

Time of flight refers to the time a gamma ray needs to travel from the annihilation point to the PET detector, as shown on the left side of Figure 18.

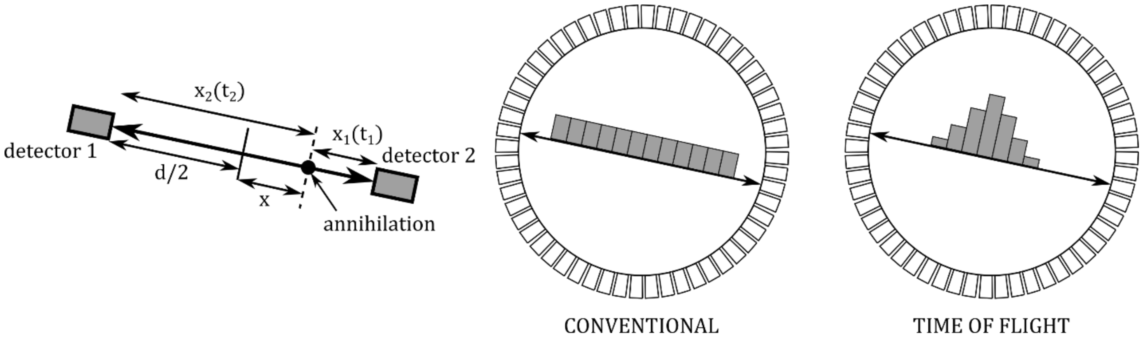

Figure 18: Left: Distances a coincident gamma ray pair travels from the annihilation point to the PET detectors. Middle: Conventional PET system, which is not able to define the annihilation point along the LOR. Right: Time-of-flight PET system, which determines the annihilation point along an LOR with uncertainty due to the limited time resolution. Adapted and modified from [66].

The measured difference in the respective time of arrival of each gamma ray can be translated into the annihilation point on the LOR by the following formula (adapted from [66]):

$$x = x_2 - \frac{d}{2} = x_2 - \frac{x_2 + x_1}{2} = \frac{x_2 - x_1}{2} = \frac{t_2 - t_1}{2} c \,,$$

where x is the distance from the center of the PET scanner's bore with a diameter d, x_1 and x_2 are the distances the two gamma rays traveled in a time t_1 and t_2, and c is the speed of light in a vacuum.

The time of flight information is used by conventional PET scanners to determine whether two events originated from the same annihilation and were detected within the assigned coincidence window. In addition to differentiating the time of arrival for each gamma ray, time-of-flight (TOF) PET scanners use a more precise time measurement to further improve the image quality and system performance. [67] If the arrival times of the gamma rays could be measured with perfect accuracy, the exact position of the annihilation event along the LOR could be determined according to the previous equation. This information would make tomographic reconstruction algorithms obsolete. [68] However, the components of the PET detectors, which incorporate scintillators, photo detectors, and processing electronics, limit the accuracy of the time measurements. [69] This finite time resolution leads to an uncertainty Δt in the measurement of the time difference between the gamma ray arrivals. This timing uncertainty translates to an FWHM position uncertainty Δx, as described by the formula

$$\Delta x = \frac{\Delta t}{2} c \,. \text{ [67]}$$

A time resolution of less than 50 ps is necessary to obtain a sub-centimeter position resolution; however, no PET scanner currently features such an accurate time resolution. [69]

Lower time resolutions are nonetheless beneficial, as they can improve the image reconstruction: for example, in conventional PET systems, the pixels used for back projection along an LOR are incrementally increased by the same amount (Figure 18 middle). However, with TOF PET systems, each pixel of the LOR is increased by the probability that the annihilation point is located at that pixel. For a TOF PET scanner to benefit from this Gaussian weighting, the position uncertainty determined by the time resolution (e.g., ~7.5 cm for 500 ps CRT) must be shorter than the emission line source (e.g., ~20 cm for the brain). [70]

Adapted TOF reconstruction algorithms can make further use of this additional positioning information and lead to the following advantages of TOF PET systems. The signal-to-noise ratio (SNR) for TOF (SNR_{TOF}) is proportional to the non-TOF SNR ($SNR_{non-TOF}$) by the relationship

$$SNR_{TOF} = \sqrt{\frac{D}{\Delta x}} SNR_{non-TOF} \,,$$

where D is the effective diameter of the imaged object and Δx is the position uncertainty. [71] Therefore, the gain in the SNR for TOF systems increases with both patient size and improved time resolution. Furthermore, the SNR is proportional to the square root of the noise equivalent counts (NEC) [67], as demonstrated by the formula

$$SNR \propto \sqrt{NEC} \,.$$

In turn, the number of events recorded during a PET scan with the noise equivalent count rate (NECR) given by the formula

$$NECR = \frac{T^2}{T + S + R},$$

where T is the true coincident event rate, S the scattered event rate, and R the random event rate. [67] In summary, the gain in the SNR and thus in the NEC can be interpreted as a virtual increase of valid events and of sensitivity. One possible application of TOF systems is that the radiotracer dose can be reduced while maintaining the same image quality as for non-TOF systems. Alternatively, the patient's comfort and imaging workflow can be improved by reducing the scan time without degrading the image quality. [71] Furthermore, the TOF information can be used to compensate for the absence of some LORs due to the incomplete angular coverage resulting from dedicated PET scanner geometries. [72]

2.1.7 Depth of Interaction

As PET scanners use scintillation crystals with a finite stopping power, the interaction of a gamma ray within a crystal is not likely to occur at the crystal surface but rather at a certain depth within the crystal. In addition, the reconstruction algorithm commonly assigns an LOR to the center of the front of the crystal. [73] Figure 19 (left) illustrates an annihilation point at the center of the field of view (cFOV) and the correct LOR assigned to the annihilation. However, if the annihilation position is radially off-center from the cFOV, the gamma ray might penetrate through several scintillation crystals before finally stopping in a crystal at a certain depth (Figure 19 left). [33] Consequently, the LOR is falsely assigned to the front surface of the final crystal, resulting in an incorrect estimation of the annihilation point.

This effect is referred to as the parallax error, which is caused by the radial elongation of the crystal profile. The parallax error increases with crystal length and for annihilation points close to the transaxial edge of the field of view (FOV). [43]

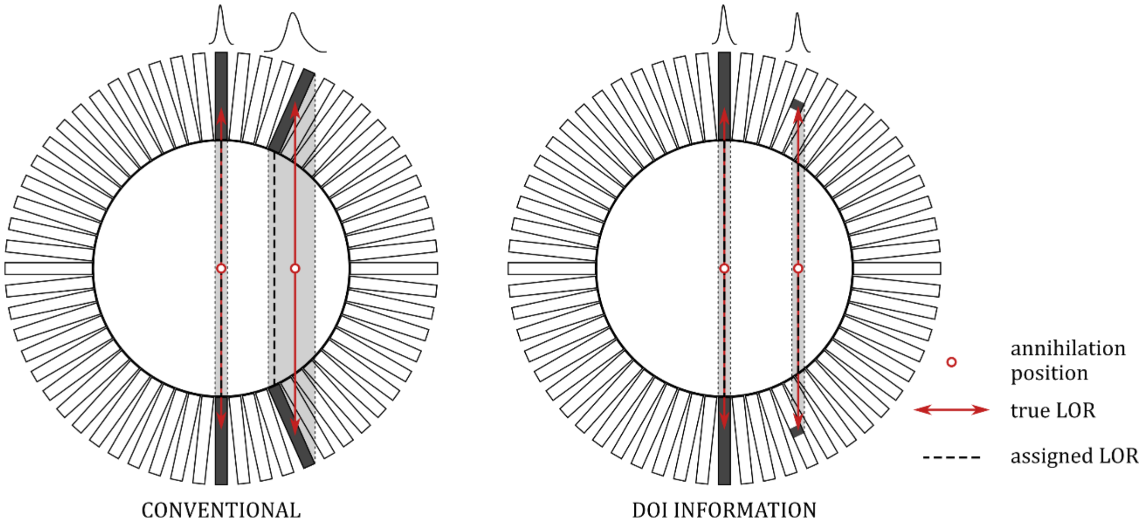

Figure 19: Example of two independent events with different annihilation positions and corresponding assigned lines of response for two PET system types. Left: Conventional PET system. Right: PET system capable of acquiring depth of interaction information. Adapted and modified from [73].

The magnitude of this uncertainty is described by a Gaussian distribution with an FWHM of

$$R_{DOI} = \frac{Lr}{\sqrt{r^2 + R^2}}$$

where r is the radial offset from the center of the FOV, L is the mean penetration depth of the gamma ray (depending on gamma ray energy and crystal type), and R is the radius of the detector ring. [43] The radial spatial resolution degrades with this error, especially for small diameter systems. [33]

One technique to overcome this issue is to determine the depth of interaction (DOI) of the gamma ray in the crystal. As shown in Figure 19 (right), this information can be used to correct for the parallax error and maintain a constant spatial resolution across the entire FOV.

PET detectors that are capable of measuring the DOI can be sorted into two categories, depending on whether they record discrete or continuous DOI information. The phoswich detector represents one common design for discrete DOI data acquisition and consists of two layers of different scintillator materials (Figure 20 left). [74] As the decay time varies with the material of the crystal, observing the differences in pulse shapes allows for the layer of interaction to be identified.

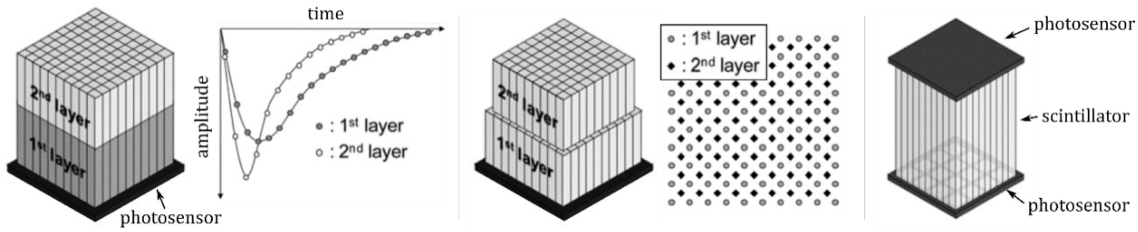

Figure 20: Different detector designs capable of acquiring DOI information. Left: A phoswich detector with pulse signals for the first and second crystal layer. Middle: Stacked crystal layers with half crystal offset and corresponding crystal position map. Right: Photosensor readout at the top and the bottom of a scintillation crystal. Adapted and modified from [73].

A second approach for measuring DOI is to have identical crystal arrays stacked on top of each other with a relative offset of one-half of a crystal pitch in the x and y directions (Figure 20 middle). [75] The DOI information can then be extracted from the 2D crystal position map, as the centroid of light dispersion shifts with the offset of the crystal arrangement. [73] Both designs (Figure 20 left and middle) can be extended to multiple layers, although the DOI resolution is always limited by the amount and thickness of the scintillator layers. [76]

One design capable of acquiring continuous DOI information and provides a fine DOI resolution is the dual-sided readout approach, as shown in Figure 20 (right. Two opposing photosensors are used for the readout of a single crystal block, and the ratio of the corresponding pulse signals is used to calculate the depth of interaction. [77] This DOI ratio needs to be mapped to an interaction depth in the crystal that is typically expressed in mm. It is possible to perform this so-called DOI calibration for detectors that are already assembled in a PET system. [78]

2.2 Magnetic Resonance Imaging

In general, magnetic resonance imaging (MRI) exploits different RF fields in a static magnetic field to alter and detect the precession of hydrogen spins in different tissues of the human body. The effects utilized for nuclear magnetic resonance (NMR) are enhanced with spatial encoding of the RF signal to enable radiological imaging. [79] The underlying physical effects and technological principles are described in the following sections. For this purpose, the focus is on hydrogen ^1H, as it is the most abundant nucleus used for MRI since human tissue is largely composed of hydrogen-containing water. However, other nuclei, such as ^{31}P or ^{13}C, can be used in other contexts to investigate energy or pyruvate metabolism, respectively. [80]

2.2.1 Static Magnetic Field B_0: Manipulation of the Net Magnetization

The intrinsic spin angular momentum of a positively charged nucleus (a single proton for ^{1}H) causes a magnetic field known as magnetization or the magnetic momentum M, as shown in Figure 21 (left).

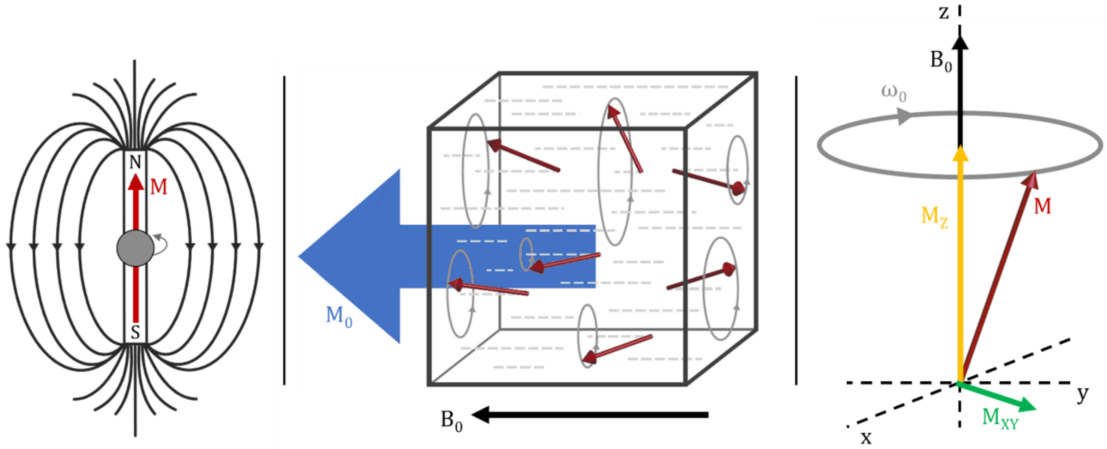

Figure 21: Left: Illustration of magnetic field lines and magnetic momentum oriented parallel to the spin axis of the rotating nucleus. Middle: Alignment of magnetization of the spins parallel and antiparallel to the external magnetic field. The excess of parallel orientated magnetizations of the spins causes a net magnetization M_0 of the volume of interest. Right: Magnetization vector components with precession, i.e., the trajectory of the magnetization vector describes a cone along the z-axis and B_0 field direction. Adapted and modified from [81], [82].

In the absence of an external magnetic field, the magnetizations of the spins are distributed randomly and therefore no net magnetization M_0 exists, which is the fundamental physical property necessary for acquiring an RF signal for imaging. The application of an external static magnetic field B_0 causes the magnetization of the spins to form a parallel or antiparallel alignment along the B_0 field lines (Figure 21 middle). [80] The parallel orientation of the spins has a lower energy than the antiparallel orientation and is therefore slightly preferred. The number of protons for each energy level is given by the Boltzmann distribution

$$\frac{N_{upper}}{N_{lower}} = e^{\frac{-\Delta E}{kT}},$$

where N_{upper} and N_{lower} are the number of protons in the upper and lower energy levels, respectively, k is the Boltzmann's constant 1.381e-23 JK^{-1}, and T the temperature. [81] The separation between the energy levels ΔE is directly proportional to the applied static magnetic field. For example, at B_0 = 1.5 T and T = 310 K (average body temperature), the ratio between protons in the lower energy level and higher energy levels is 1.000004. [83] This excess causes a polarization of the tissue with a net magnetization in the direction of the B_0 field (Figure 21 middle). [81]

The manipulation and measurement of this net magnetization are used in MRI to distinguish between different tissues of the human body based on their proton density. For example, the magnetization of a typical adult head of approximately 20 µT is small in comparison to the static magnetic field of a 1.5 T MRI scanner. [83] To be able to measure this small magnetization, it is necessary to alter the magnetization to be different to the direction of the B_0 field, as described in the following section. To understand how magnetization is measured, the underlying physical effects of nuclear magnetic resonance must be explained. Figure 21 (middle) demonstrates that the magnetizations of the spins do not assume a fully parallel or antiparallel orientation along the B_0 field due to their precession along the B_0 field vector. The influence of the B_0 field on the spin angular momentum of the protons leads to the precession of the magnetization vector M (Figure 21 right). [81]

The precession angular frequency ω_0 for M (and for the spin axis of the proton) is given by the Larmor equation

$$\omega_0 = \gamma B_0 \,,$$

where γ is the gyromagnetic ratio of approximately 2.7×10^8 rad/s/T for a hydrogen proton and B_0 the strength of the static magnetic field of the MRI scanner. [79] The scalar frequency can be calculated with the same equation by replacing γ with $\gamma/2\pi$ = 42.57 MHzT^{-1}. [83] For example, in the magnetic field of a 3T MRI scanner, the Larmor frequency is 127.71 MHz. The magnetization vector M can be divided into two components, one in the xy-plane, resulting in the transverse magnetization M_{xy}, and one on the z-axis along the static field direction, resulting in the longitudinal magnetization M_z (Figure 21 right).

2.2.2 Time Variant Magnetic Field B_1: RF Signal Generation

The phase of the magnetization vectors is randomly distributed for all spins, as shown in Figure 22 (top).

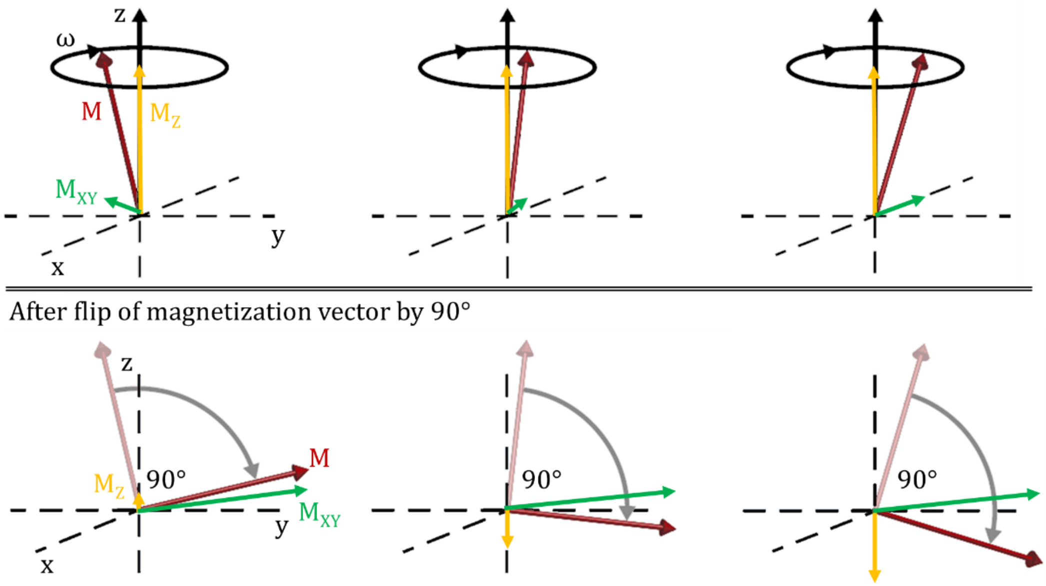

Figure 22: Top: Three different magnetization vectors M with the same precession frequency ω and different phases. M_{xy} is the transverse magnetization, and M_z is the magnetization along B_0. Bottom: The same magnetization vectors after a rotation via a flip angle of 90°. Adapted and modified from [82].

The vector sum of all transverse magnetization vectors M_{xy} equals zero, and therefore no transverse net magnetization exists. As transverse magnetization is required to generate the RF signal, each magnetization vector is flipped by an angle of example 90° (Figure 22 bottom), which results in a net transverse magnetization that can be detected.

The macroscopic net magnetization is now used instead of the microscopic distribution of the individual magnetization vectors. Figure 23 (left) demonstrates that the net magnetization M_0 only has a longitudinal component along the z-axis before rotating 90° in the transverse xy-plane. An external magnetic field that oscillates orthogonally to the B_0 field and is applied as a short RF pulse is used for the rotation. When the frequency of this applied field matches the Larmor frequency of the protons in the static magnetic field, the resulting resonance enables an energy transfer. [80]

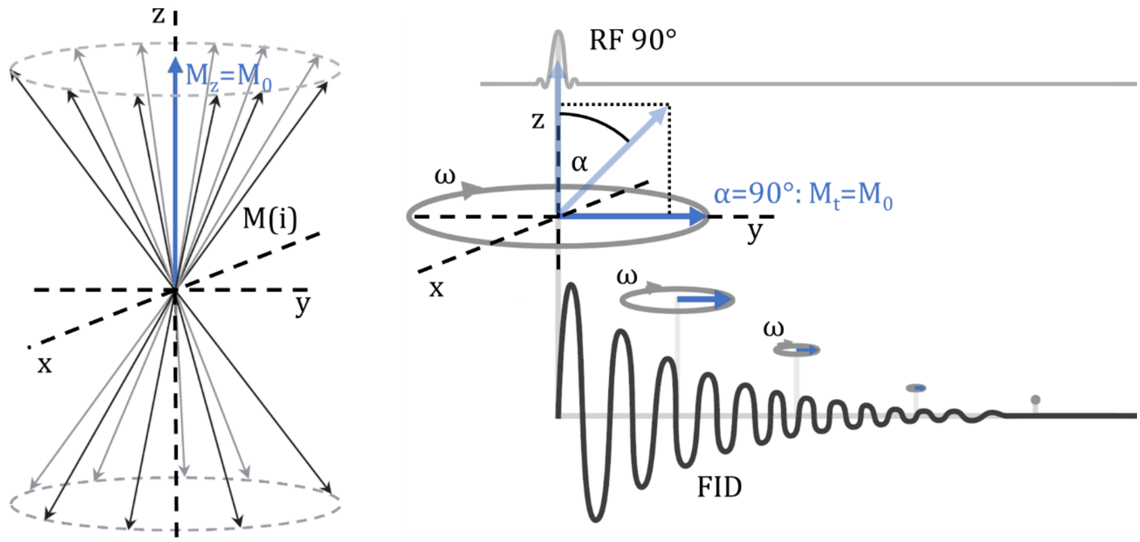

Figure 23: Left: Net magnetization M_0 composed of the average of the magnetization M(i) for multiple protons, with i = 1:n and n is the number of protons. Right: Applying an RF pulse leads to a flip of the net magnetization M_0 by the flip angle α. For an 90° RF pulse, the transverse magnetization M_t equals the net magnetization M_0 before the application of the pulse. Furthermore, the progression of the free induction decay (FID) signal over time is shown, which is caused by the magnetic field of the transverse net magnetization and oscillates with the frequency ω. Adapted and modified from [82], [83].

This excitation of the protons causes the net magnetization vector to be rotated by the flip angle α according to the following formula [83]

$$\alpha = \gamma B_1 t_p \, ,$$

where B_1 is the strength of the RF magnetic field, γ the gyromagnetic ratio, and t_p the duration of the RF pulse. An RF transmission coil is used to generate a circularly polarized B_1 field for the RF pulse. [83] The standard RF transmission coil for clinical whole-body MRI scanners is the RF body coil (Figure 24). After the application of the RF pulses, the transverse net magnetization M_t precesses at the Larmor frequency in the xy-plane (Figure 23 right). The resulting time variant magnetic field, which is perpendicular to the B_0 field, induces a voltage in the MRI scanner's receiver coil. The progression of the induced voltage over time results in the RF signal (Figure 23 bottom right). The signal oscillates at the Larmor frequency with an initial magnitude proportional to M_t and exhibits an exponential decay referred to as the free induction decay (FID). The decay of the

FID signal corresponds to a decrease in the transversal net magnetization over time and can be used to measure the so-called relaxation.

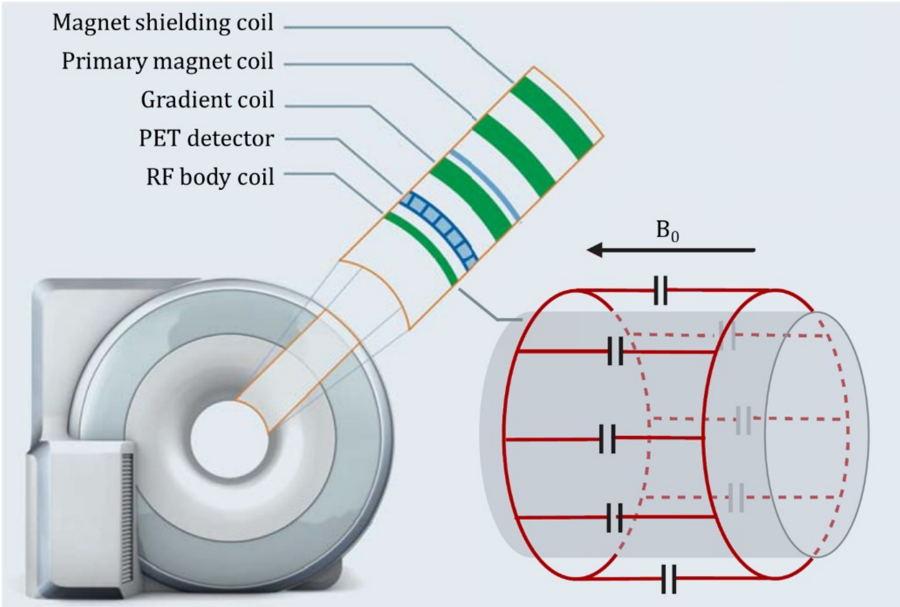

Figure 24: Schematic drawing of a PET/MRI Scanner (Biograph mMR) with dedicated MR coils. A birdcage RF transmission coil is commonly used for the MRI scanner's RF body coil to generate the basic RF pulse. Adapted and modified from [83], [84].

The corresponding transmitted energy is dissipated through two processes: longitudinal and transverse relaxation. [80]

<u>Longitudinal "spin-lattice" relaxation (T_1)</u>

Longitudinal relaxation describes the proton's return from the higher energy configuration caused by the RF pulse to the lower energy configuration of the resting state once the RF pulse is turned off. Principally, the excited protons transfer their energy to the surrounding environment, known as the lattice. [80], [81] The recovery of the longitudinal magnetization M_z to M_0 follows an exponential growth process, with the exponential time constant T_1 (Figure 25). It is of particular interest for MRI that T_1 is proportional to the probability that spins are able to transfer their energy to the lattice. This probability depends on the lattice: a sparse and limited lattice corresponds to a long T_1, and a more complex lattice results in a short T_1. [80]

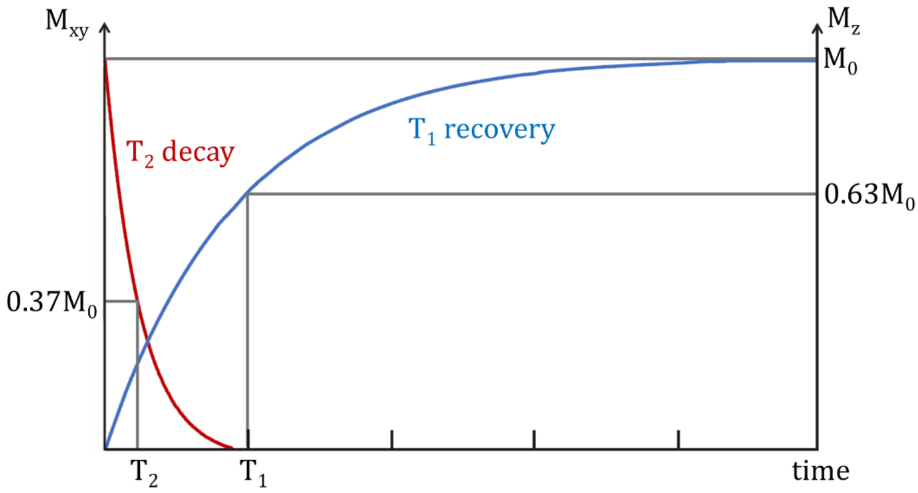

Figure 25: Recovery of the longitudinal magnetization M_z with the exponential time constant T_1 after the RF pulse is turned off. Simultaneously, the transverse magnetization M_{xy} decays with the exponential time constant T_2. Adapted and modified from [83].

Thus, this relationship can be used to distinguish between different tissues, as shown in Table 3.

Table 3: Representative approximate values of the relaxation times T_1 and T_2 for hydrogen components of different human body tissues at B_0 = 1.5 T and 37°C. Adapted and modified from [79].

Tissue	*T1* [ms]	*T2* [ms]
gray matter (GM)	950	100
white matter (WM)	600	80
muscle	900	50
cerebrospinal fluid (CSF)	4500	2200
fat	250	60
blood	1200	100-200

In order to investigate the effects related to T_1, it is necessary to measure the longitudinal recovery of M_z; however, this cannot be done by measuring M_z directly, as it does not contribute to the RF signal. Instead, the method illustrated in Figure 26 is used to take an indirect measurement of M_z. Here, a second RF pulse is applied after a considerably short time, referred to as the repetition time (TR), when M_z has only partially recovered to M_0. As previously mentioned, the RF pulse flips the magnetization vector so that the new transverse magnetization equals the previous longitudinal magnetization. With this method, it is possible to retain the value of the partially recovered M_z through the measurement of M_t. It should be noted that in order to use this principle to measure T_1, a sequence that involves multiple measurements with different TRs is necessary. [80]

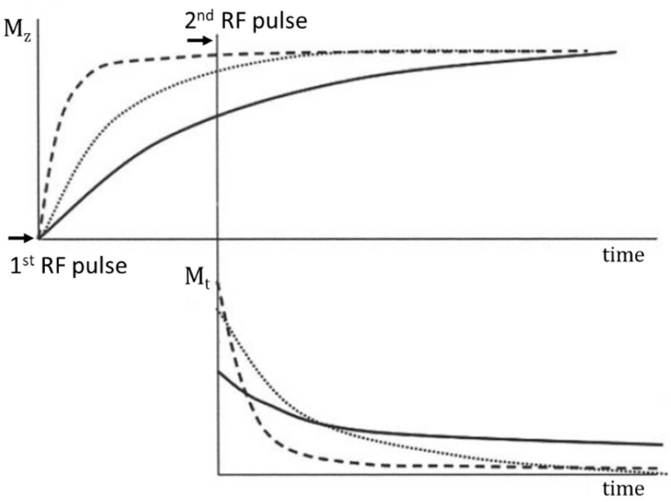

Figure 26: Principle of the recovery of longitudinal magnetization M_z at different rates after the application of an initial first RF pulse. The second RF pulse, which is applied at TR, flips the partially recovered longitudinal magnetization into the transverse plane. Each line corresponds to tissues with a different longitudinal recovery constant T_1. Adapted and modified from [80].

<u>Transverse relaxation</u>

After the RF pulse is applied, the phases of the spins are in coherence, which yields the maximum transverse net magnetization M_t. When the RF pulse is turned off, the spins are in the process of dephasing, which leads to a continuous decrease of M_t. [83] The reason spins dephase can be explained as follows. Each spin is exposed to an individual local magnetic field, which is composed of the applied magnetic field B_0 and the magnetic fields created by the neighboring spins. The variations of the local fields result in different local precession frequencies, which eventually causes the transverse magnetization vectors M_{xy} to fan out over a time that is analogous to the loss of phase coherence (i.e., dephasing).

Transverse relaxation can be further divided into random, irreversible (T_2), and recoverable (T_2') effects as follows.

“Spin-spin” relaxation (T_2)

As previously stated, spin-spin interactions are one cause of dephasing. Two adjacent freely moving protons are exposed to a slightly higher or lower magnetic field as they become closer to each other. The Larmor frequencies are adjusted to match the new magnetic field, and each proton will dephase with respect to its precessional frequency. When they move apart, both protons retain their original precessional frequency; however, the phase difference acquired during the spin-spin interaction remains. [83] The exponential decay of M_t due to this effect is described by the spin-spin relaxation time T_2 (Figure 25). Table 3 shows that T_2 is shorter for solid materials than for liquids and always shorter than T_1 for the same tissue. [79]

Apparent spin-spin relaxation: T_2*

An additional source for the loss of transverse phase coherence is the local change of the magnetic field caused by the scanner and the patient themselves. On the one hand, imperfections in magnet manufacturing result in nonuniformities of the static B_0 field. On the other hand, differences in magnetic susceptibility will distort the local magnetic field near the interface between different tissues. Both effects lead to a local difference in the Larmor frequencies of the spins, which causes the spins to dephase and eventually exponentially decreases M_t with the decay constant T_2'. [81]

The total transverse relaxation decay constant T_2* of M_t is composed of the two transverse decay constants T_2 and T_2' according to the formula [79]

$$\frac{1}{T_2^*} = \frac{1}{T_2} + \frac{1}{T_2'}.$$

It is possible to recover the loss in M_t introduced by the heterogeneity of the magnetic field (i.e., neutralizing the effects of $T_{2'}$).

A method called spin echo uses RF pulses with a flip angle of 180° to invert the phase of the spins. In short, the spins with a lower precession frequency (slow spins) are “behind” (in terms of phase difference) the spins with a higher precession frequency (fast spins) after the 90° RF pulse is switched off. The application of the 180° RF pulse at half of the echo time (*TE*) shifts the slow spins "ahead" of the fast spins by exactly the previous phase difference. After another time *TE*/2, the fast spins catch up with the slow spins, nearly recovering the net magnetization M_t at the time *TE*. The remaining loss of M_t is now solely due to the effect of T_2. A repetition of the spin echoes is used to extract T_2 from the received RF signal. [80]

The previously described longitudinal and transverse relaxation mechanisms are physical principles independent of each other and are present over the total acquisition time of an MRI sequence. Conclusively, an RF signal always contains a mixture of each effect inherent to longitudinal and transverse relaxation. However, a proper manipulation of the spins by an MRI sequence, as described in section 2.2.4, can be used to increase the effective influence of a specific relaxation process on the RF signal by suppressing the influence of other relaxation effects. The resulting images, called weighted MR images, have different contrasts, providing anatomical, morphological, or functional information.

It should be noted that proton density-weighted images can also be acquired. Tissues with a high proton density have a high net magnetization, which results in a higher amplitude of the RF signal in comparison to tissues with a lower proton density. [83] In terms of relaxation, MRI sequence parameters are used to minimize T_2 relaxation (short *TE*) at maximal magnetization (long TR).

2.2.3 Gradient Fields: Spatial Encoding

The previous sections described how the RF signal based on nuclear magnetic resonance is formed and detected. This approach is sufficient for the spectroscopy of small samples; however, to acquire 3D images, it is necessary to localize the RF signal. This localization is performed by a specific interaction between the components of an MRI scanner's gradient system.

For this interaction to occur, three orthogonal linear magnet field gradients are required, which are generated by dedicated gradient coils, as Figure 27 shows for the gradient in the y direction. [83]

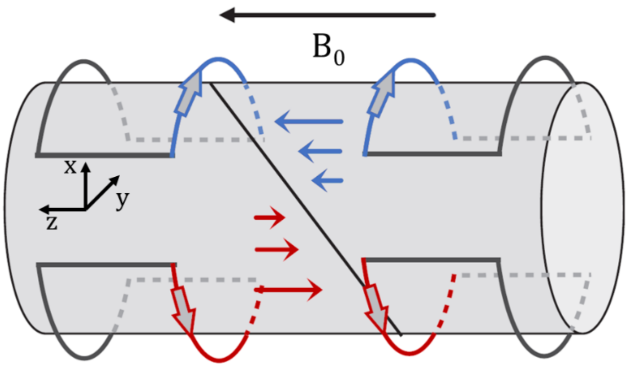

Figure 27: Saddle coil for the generation of the gradient field in the y direction. The current flows in opposite directions but with equal magnitude through the coils. The magnetic field strength decreases with the distance to the source of the magnetic field and conclusively leads to a magnetic field gradient. The x and z gradients are generated analogously with a separate saddle coil and a Helmholtz coil, respectively. Adapted and modified from [83].

Figure 28 shows the effective magnetic field strength B_{net} along the z direction, representing the superposition of the static magnetic field strength B_0 and the gradient field strength G_z along the z direction.

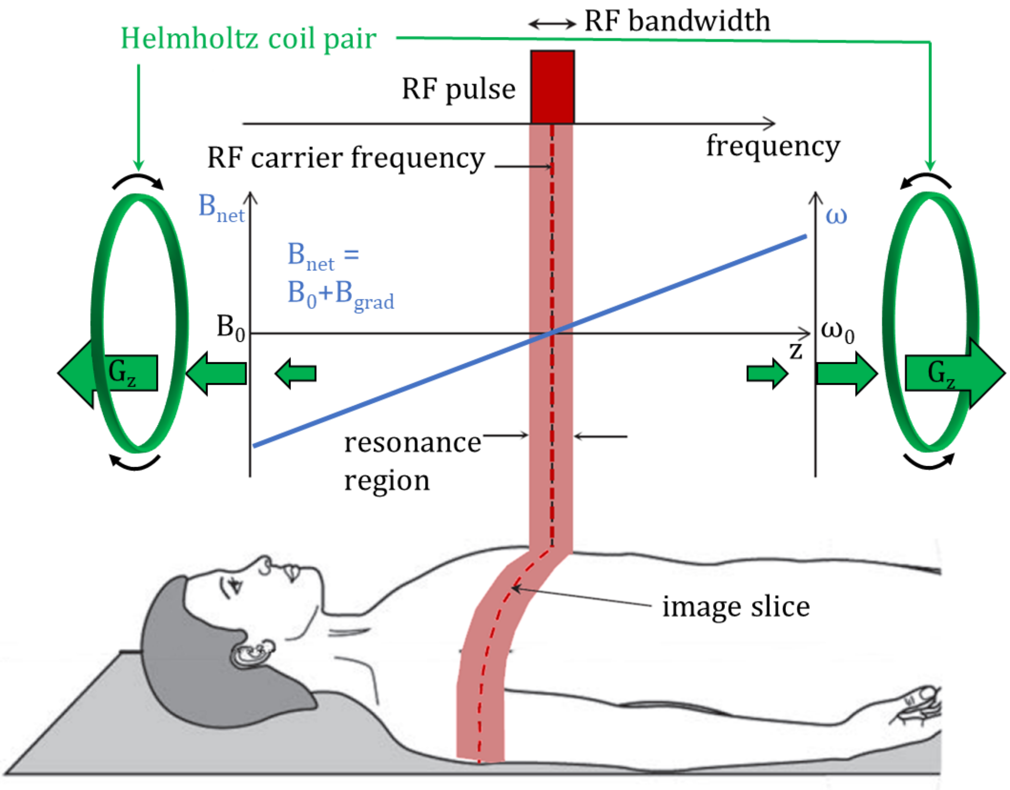

Figure 28: Helmholtz coil pair to generate the gradient G_z along the z direction. The linear change of the net magnetic field strength B_{net} along the z-axis results in a proportional change in the Larmor frequency ω of the spins. An applied RF pulse leads to the excitation of a resonance region with the corresponding Larmor frequency bandwidth, which in turn generates the RF signal from a transverse imaging slice. Adapted and modified from [80], [83].

Slice selection: slice-selective gradient G_{ss}

Turning on the slice-selective gradient G_{ss} exposes the protons in the body to different magnetic field strengths due to the gradient field, which leads to a precession at different Larmor frequencies. Figure 28 demonstrates that in the isocenter of the scanner and gradient field, the Larmor frequency ω_0 matches the static magnetic field strength B_0. The increase of B_{net} on the right of the isocenter results in higher precessional frequencies of the spins ω.

Applying an RF pulse with only one frequency component at ω_0 would lead solely to an excitation of the protons in the body that are located at the isocenter. This excitation at a single frequency would result in an infinite thin coronal slice and therefore provide spatial location in one direction. In practice, the RF transmitter is not able to create an RF pulse at a single frequency; instead, the RF pulse has a certain bandwidth. This transmission bandwidth leads to an excitation of all spins in a certain resonance region in the body with a finite thickness (Figure 28). [80] After the RF pulse is switched off, only the excited resonant spins from this imaging slice induce the RF signal, as described in the previous section.

Switching (i.e., turning on and off) the individual gradient fields G_x, G_y, and G_z selects the sagittal, coronal, and transverse imaging slice, respectively. A combined switching of the gradients can also create oblique angles for the imaging plane. In general, a gradient with a steeper slope and an RF pulse with a narrower bandwidth result in a thinner imaging slice.

The image slices must be further divided into volume elements (voxels) in order to generate the voxel-based MR images. For this purpose, a two-step process that includes the switching of two additional gradients establishes the in-plane localization of the spins along both remaining dimensions.

In-plane localization for dimension I: frequency-encoding gradient G_{FE}

Once the slice-selective excitation is performed, G_{ss} is switched off. As only the static magnetic field B_0 remains, each spin in the body precesses again with ω_0. However, only the excited spins from the resonance region contribute to the RF signal with their net transverse magnetization. If, at that time, a frequency-encoding gradient G_{FE} in another direction is switched, such as G_x, the precessional frequency of the spins is encoded according to the gradient along the x-axis in the specific image slice. As the RF signal is a composition of the signals inherent to this resonance region, the RF signal itself contains a mix of these frequencies. The Fourier transform can then be used to separate each frequency component along with its corresponding amplitude and thus determine the net magnetization of the tissue spatially encoded in the x-direction in the transverse image slice.

Processing the received RF signal involves sampling the analog signal to enable the conversion to digital values. Moreover, processing the signal represented in the digital domain requires the discrete Fourier transform (DFT). [80] In terms of computational expense, a number of single frequency components, which can be expressed by a power of two, is preferable and explains the commonly used dimension size of 64, 256 or 512 pixels for MR images. [83]

In-plane localization for dimension II: phase-encoding gradient G_{PE}

Finally, to determine the comprehensive localization of the RF signal, a phase-encoding gradient G_{PE} is used for the remaining dimension. After the G_{SS} is turned off, all spins precess at the Larmor frequency ω_0. If a gradient is switched, such as G_y in the y direction, a linear change in the precessional frequency of the spins along the direction of the gradient can be observed. Spins located at the isocenter are exposed to a gradient field of zero magnitude, thus precessing with ω_0 due to the static magnetic field strength. Moving away from the isocenter of the gradient in the positive direction, for example, causes the spins to be exposed to a net magnetic field strength B_{net}, which is higher than B_0. As these spins precess at higher frequencies, dephasing occurs, which changes linearly in magnitude according to the distance of the spins from the isocenter. If the phase-encoding gradient is turned off again, the precessional frequency of the spins returns to ω_0; however, the change in phase remains. As dephasing is strongest for spins located at the edges of the gradient field, their potential contribution to the net transverse magnetization is the lowest, as is their contribution to the overall RF signal. In turn, the spins located closer to the isocenter experience a smaller amount of dephasing and thus potentially contribute more to the net transverse magnetization.

However, it is not possible to extract the information of the amount of dephasing that occurs along the gradient axis by applying a single phase-encoding gradient G_{PE}. Therefore, G_{PE} is applied several times using different magnitudes. Figure 29 provides an example of three different magnitudes of G_y. Furthermore, Figure 29 demonstrates that two phase-encoding gradients with different magnitudes such as M1 and M3 lead to different slopes of ω across the gradient direction and correspond to a different slope for the change in phase. Observing this change allows for spatial encoding: the spins located at the edge of the gradient field (e.g., Figure 29 position c) experience a large change in the phase difference between the application of phase-encoding gradients with different strength. The change in phase difference becomes smaller for spins located closer to the isocenter and ultimately becomes zero at the isocenter.

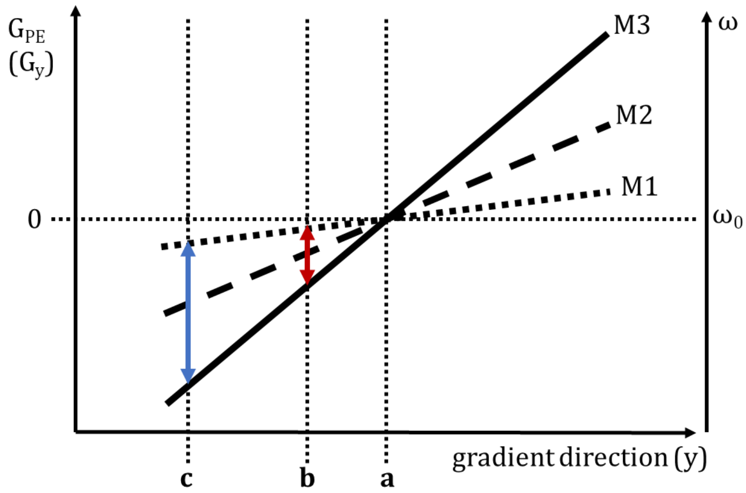

Figure 29: Progression of three phase-encoding gradients with different magnitudes M1, M2, and M3. The difference in precessional frequency due to two gradient fields of different magnitude is dependent on the distance of the spins to the isocenter (position a). The absolute difference in ω and thus the amount of dephasing is higher for position c at the edge of the gradient field than for position b, closer to the isocenter. Adapted and modified from [80].

The rate of change in the phase difference can be used to localize the transverse net magnetization along the direction of the phase-encoding gradient. To make use of this localization technique, the MR sequence, as visualized in Figure 30 (left), must be repeated for different magnitudes of G_{PE} without changing G_{SS} or G_{FE}. The individual RF signals for each repetition are sampled, processed, and stored in what is known as the k-space. The first DFT along the dimension of frequency is used to determine the localization, enabled by the frequency-encoding gradient as previously described. A second DFT along the dimension of the rate of change in phase difference then leads to the localization of the RF signal according to its phase difference from the isocenter, as Figure 30 shows (right). [80], [81] In summary, a precisely timed and repeated application of the RF pulses, G_{SS}, G_{FE}, and G_{PE} is used to generate the MR image (Figure 30 right). During this process, the brightness of each pixel indicates the RF signal intensity. [83]

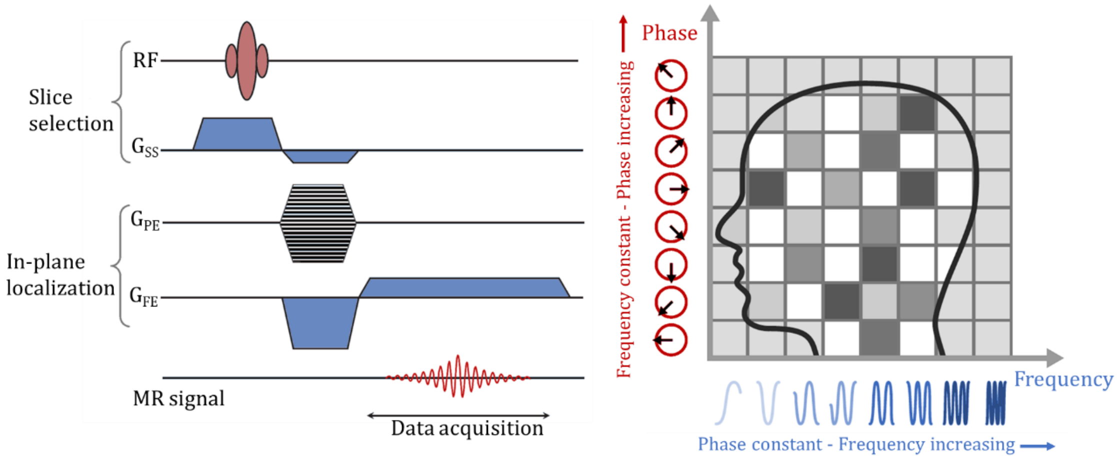

Figure 30: Left: Basic gradient-echo MR imaging sequence with all three gradients, which are used for slice selection and localization encoding. The adverse dephasing introduced by the switching of G_{SS} and G_{FE} is encountered by compensatory gradient lobes. [85] *Right: Visualization of the concept behind a pixelated MR image of a single slice with frequency-encoding in the x direction and phase-encoding in the y direction. Adapted and modified from* [82], [83].

2.2.4 Spin Echo Sequence

One example of an MRI sequence is the commonly used single spin echo sequence. Figure 31 shows that the 90° RF excitation pulse is applied simultaneously with the slice selection gradient G_{SS}. Section 2.2.2 previously described how the net transverse magnetization induces an RF signal, which decays due to T_2* effects. Furthermore, applying a 180° RF pulse causes the spins to rephase, therefore leading to maximum net magnetization after a time duration TE/2, which is equal to the time between the 90° RF pulse and the 180°

RF pulse. As this method flips the spins 180° to recover the maximum RF signal, it is called the spin echo. Accordingly, the time between the application of the excitation pulse and the sampling of the spin echo is termed the echo time (*TE*).

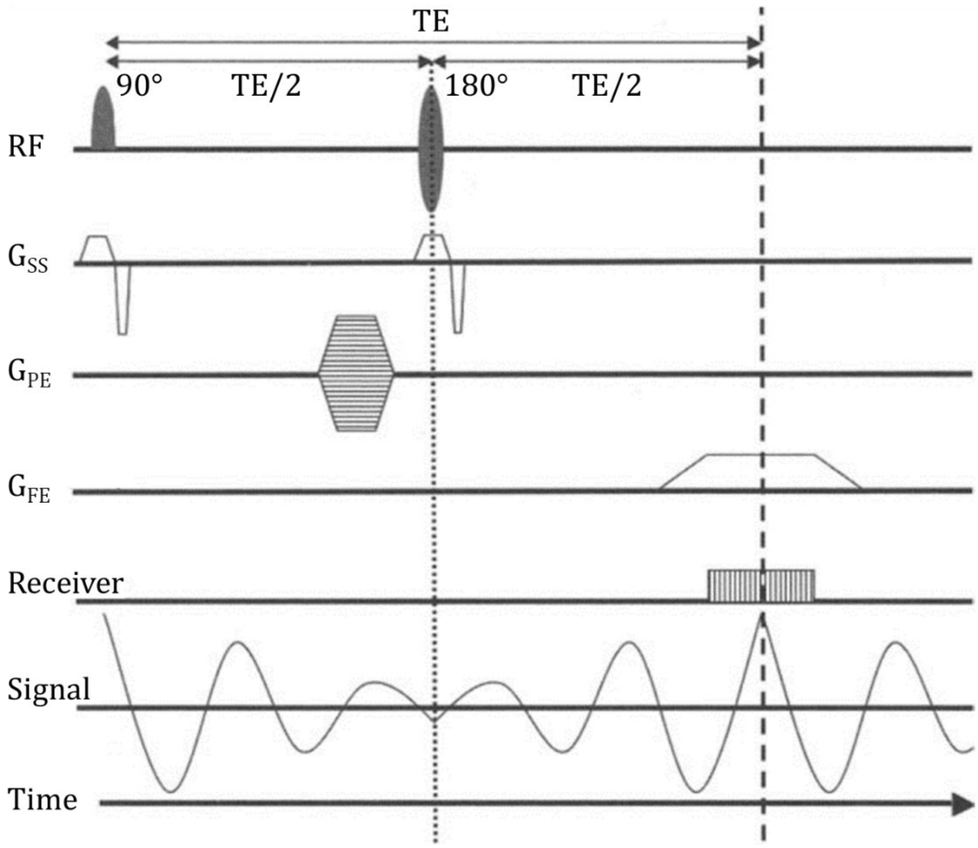

Figure 31: Diagram of a spin echo sequence with recovery of the initial RF signal after the echo time TE. The horizontal stripes of G_{PE} correspond to successive repetitions of this sequence with different magnitudes of G_{PE}. The vertical lines in the row of the receiver are used to visualize the discrete sampling of the signal. Adapted and modified from [80].

A gradient echo sequence in turn uses a change in the polarity of the gradients to recover the maximum RF signal. Further components of the spin echo sequence diagram in Figure 31 include the phase encoding gradient G_{PE} and the frequency encoding gradient G_{FE} that determines in-plane localization, as described in the previous section. Localization via phase encoding requires multiple repetitions of the sequence section shown in Figure 31 with different magnitudes of G_{PE}. The time interval between two successive RF excitation pulses is known as the repetition time (TR). [80], [81]

3 PET Insert System Design

The physical principles and technologies in the field of PET and MRI as described in the previous chapter, provide the basis for the design of the breast PET insert, which will be explained in more detail in this chapter. In addition, this chapter discusses the concept of combining both modalities and explains the PET detector and system hardware requirements. Finally, this chapter demonstrates why combining a PET insert with a whole-body PET/MRI scanner is beneficial by introducing the concept of mixed coincidences and considering their advantages in breast imaging.

3.1 Integration of the PET Detectors in a Radio Frequency Coil for Dedicated Breast Imaging

In order to simultaneously perform breast PET and MR imaging, it is necessary to combine the technical components involved in both modalities. To achieve the maximum PET signal detection sensitivity and image resolution, the local MR RF coil and the PET insert must be as close to the breasts as possible. The 4-channel coil BI 320-PA-SI (NORAS MRI products, Höchberg, Germany), as shown in Figure 32, is commercially available and routinely used for breast imaging inside 1.5T and 3T Siemens MRI scanners. [86]

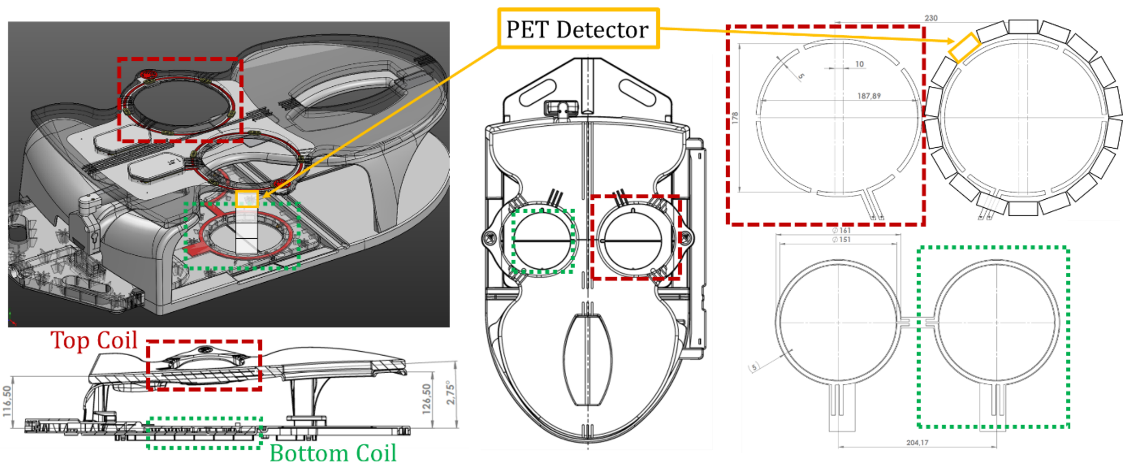

Figure 32: Rendered image of the 4-channel breast coil and technical drawings with dimensions of the coil elements. The position of the PET detectors is shown as an example of a cylindrical geometry of the insert and only for one coil pair. Image courtesy NORAS MRI products.

The dimensions of the four coils and their distances have already been optimized to suit the anatomy of the typical female breast. Therefore, our approach integrates the PET insert into the breast coil, placing the PET detectors between the top and bottom coils (Figure 32 top left). One potential geometry uses multiple rings of PET detectors with a diameter larger than the top coil, as shown for a single ring in Figure 32 (top right). Finally, a stack of multiple detector rings forms a cylindrical insert for each breast. Different arrangements for the PET detectors are possible and will be discussed in section 3.3.

An important aspect to consider when integrating the PET insert into the breast coil is the shielding of the PET detectors to enable MRI compatibility. As these highly conductive shielding boxes are close to the coil's elements, they can change the coil's inductive properties and hence necessitate retuning the RF coil to the Larmor frequency and impedance matching. [80]

3.2 PET Detector Considerations

Design considerations for the PET breast insert were mainly driven by the question of how to increase the PET image quality of the breast region. One of the main components that directly influences the image quality is the intrinsic spatial resolution of the PET system, which in turn is mainly determined by the size of the scintillation crystals. As the insert aims to improve the resolution compared to the whole-body PET scanner, it is necessary to choose a crystal size smaller than the $4.0 \times 4.0\ mm^2$ currently used for clinical PET scanners, such as the Biograph mMR. In this work, the initial size of the scintillation crystals was set to $1.51 \times 1.51 \times 10\ mm^3$, as described in Chapter 5. The crystal size itself limits the lowest achievable intrinsic spatial resolution to half of the crystal's width. However, several other factors, such as the positron range, gamma noncollinearity, the accuracy of determining the crystal position, parallax error, and the choice of the reconstruction algorithm, can further degrade the spatial resolution. [33] Comprehensive Monte Carlo-based simulations performed with the simulation toolkit Geant4 (Geant4 Collaboration) or GATE (OpenGATE Collaboration) are required to make a precise statement on the spatial resolution at different positions across the PET insert's field of view.

While it is preferable to use smaller crystal widths for the purposes of spatial resolution, it is also important to ensure that every single crystal records a sufficient number of events to enable accurate image corrections and optimal image reconstruction. Furthermore, it is necessary to ensure that the identification of a single crystal is still possible on the hardware level of the detector. Whereas the process of identifying the crystals is straightforward when the crystals and MPPCs are directly coupled (i.e., the size of a single crystal matches the size of a single MPPC), a light sharing approach has the advantage of using fewer channels, as described in section 5.1.1. The reduction in channels means fewer PET electronics are necessary, which is more cost-effective and helps integrate the PET insert into the limited space around the RF breast coil. Chapter 5 verifies that the $1.51 \times 1.51\,mm^2$ crystals can be resolved by light sharing on an MPPC with a $3 \times 3\,mm^2$ photosensitive area. The MPPC array on a single detector had a dimension of 8×8 (i.e., 64 individual channels), as a single electronics unit—called signal processing board—is capable of processing 72 channels. Again, further simulations are required to find the optimum dimension of the scintillation crystal block and hence the MPPC array dimension. In theory, it is possible to use a non-square scintillator block to make use of each processing channel or to use scintillator blocks of smaller dimensions to process more than one block with a single signal processing board.

The initial length of the scintillation crystals was set to 10 mm based on the following considerations: the rather small diameter of the PET insert is prone to suffer from the parallax error as described in section 2.1.7, which causes the spatial resolution towards the transaxial edge of the FOV to degrade. This effect increases with the scintillation crystal’s length. Nevertheless, the probability of stopping and detecting a gamma quant inside the scintillation crystal also increases with its length and thus increases the sensitivity of the PET system. While a high-sensitivity PET system has an acceptable signal-to-noise ratio and requires less scan time and a smaller radiation dose, it must be capable of achieving a high event count rate. Additionally, the detectors of the PET insert are close to sources of unspecific tracer uptake, such as the heart and liver, which further expose the PET detectors to an increased single events rate. Therefore, to determine the optimum length of scintillation crystals, simulations and hardware tests need to be performed that address the maximum count rate and the potential gain of various DOI methods, as described in section 2.1.7.

3.3 Geometric Design and PET System Electronics Considerations

Section 3.1 previously mentioned that a potential geometric design for the breast PET insert consists of two separate cylinders. In total, three different design approaches were considered, as shown in Figure 33. This work aimed to construct an insert with a high solid angle coverage while allowing for the insert's practical integration into the RF coil.

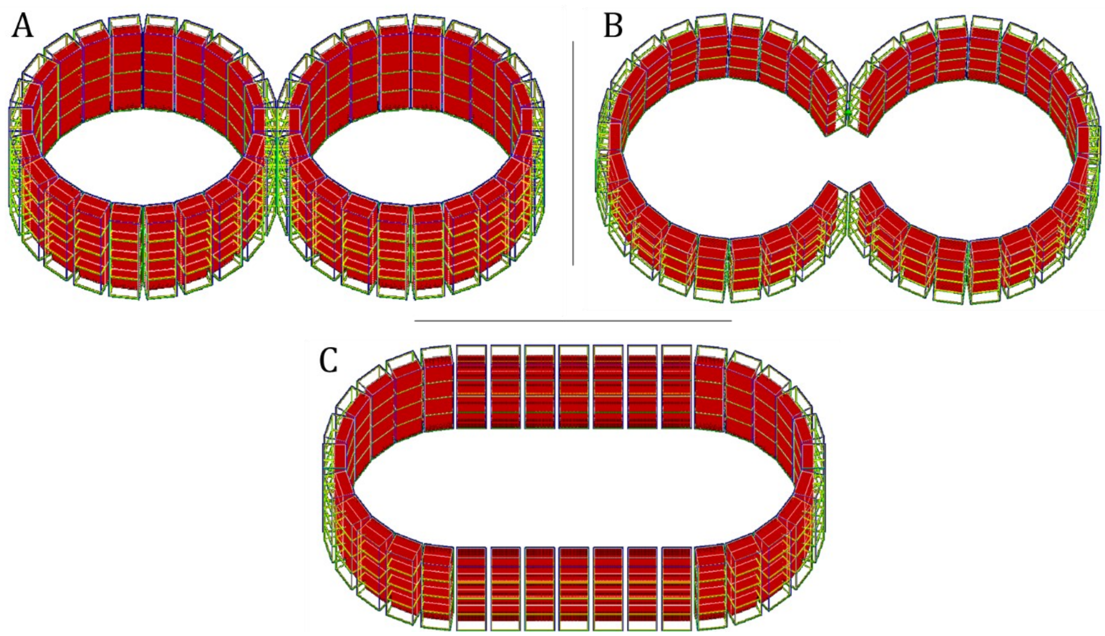

Figure 33: Different geometric designs for the breast PET insert, with four PET rings and 25.4×25.4×10.0 mm^3 scintillation crystal blocks shown in red. The total number of single PET detectors is 176, 152, and 144 for designs A, B, and C, respectively. Image courtesy of Christian Pommranz.

The performance trade-offs of the individual designs are beyond the scope of this thesis and will be evaluated by comprehensive simulation and reconstruction studies. However, the initial specifications indicate that the PET electronics must meet the following requirements: first, a superior integration capability and low power consumption are necessary due to the limited space for the breast PET insert. Second, the PET electronics must be highly scalable in terms of the number of detectors, including a different number of PET scanner rings, to enable the different designs. Last, the development of different detector prototypes (i.e., MPPC array and scintillator configurations, DOI capability) requires adjustable electronics that can be tailored to the specific design and offer a processing of the single event data.

Based on these considerations, the C13500-4075LC-12 PET module and C13500 series back-end electronics (Hamamatsu Photonics K.K., Hamamatsu, Japan) were chosen for the breast PET insert (see section 4.1.1). This PET module consists of a PET detector, including signal amplification, processing, and digital data communication. Figure 34 (left) demonstrates that, theoretically, an infinite number of these PET modules and thus single PET detectors can be connected in a daisy chain to be read-out by the back-end electronics.

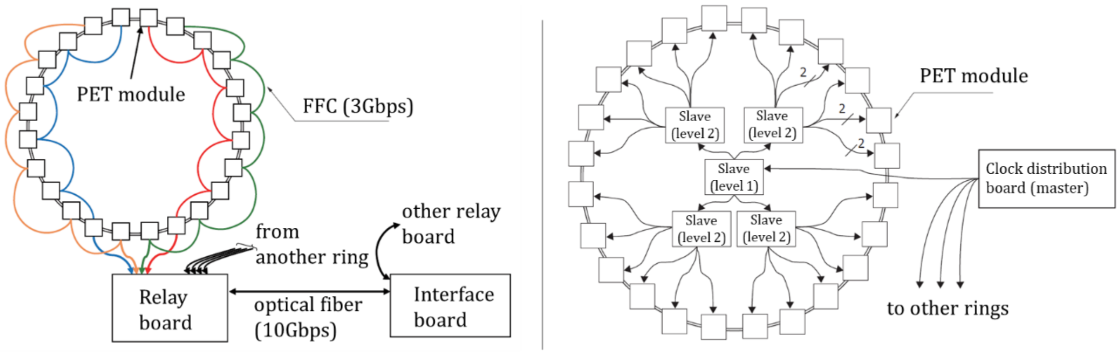

Figure 34: Left: Block diagram of the daisy chain of the data signal from multiple PET modules inside a single ring of PET detectors. Right: Block diagram of the clock signal's distribution to multiple PET modules by a master-slave implementation of clock distribution boards. Adapted and modified from [87].

The only constraint is that the copper-based flexible flat cable (FFC) connection and the optical fiber connection have a data rate limitation of 3 Gbps and 10 Gbps, respectively.

Furthermore, it is possible to use a daisy chain of relay boards and multiple interface boards. Therefore, the system electronics should be chosen to account for the maximum expected count rate, depending on the event data format. In addition to a connection for data transfer, each PET module should have a clock signal, which can also be provided for any number of PET modules by arranging the 16 channel clock distribution units into a master-slave configuration, as shown in Figure 34 (right). This high grade of scalability is accompanied by a low power consumption of 1.3 W per signal processing board and a superior time resolution, which can be used for TOF applications. More precisely, a CRT of 280 ps has been observed for a detector with a 4.14×4.14×20.00 mm^3 lutetium fine silicate (LFS) scintillator and a 4×4 mm^2 MPPC with a 75 µm pixel pitch (no CRT has yet been reported for scintillation crystals with a dimension of 1.51×1.51mm^2). [87] In addition, this CRT value allows for a narrow coincidence acceptance window, which reduces the random event rate. Reducing the random event rate is of high value, especially for the breast insert, as the unspecific uptake of nearby organs might result in a high random event rate.

Finally, two remaining issues should be addressed to make the PET modules suitable candidates for the PET insert. First, it has yet to be proven that the MPPC and electronics of a customized detector can successfully resolve crystal sizes smaller than 3 mm (the smallest crystal size commercially available for the PET modules), as stated in section 5.2.2. Second, the PET modules should be modified and tested to ensure the proper operation of the PET breast insert inside the MRI scanner without mutual distortion, as described in Chapter 6.

3.4 Simultaneous PET Insert Operation with a Whole-Body PET/MRI Scanner

For the classification of breast cancer and subsequent treatment guidance, the tumors located directly in the breast tissue are not the only ones of interest. An essential part of the staging process involves observing any metastasis and propagation of cancer cells in the sentinel lymph nodes, as the axillary lymph nodes (Figure 35 right) are located outside of the breast. [88], [89]

If the entire FOV was solely dependent on the PET insert, it would not be possible to image regions outside of the breast. The concept proposed in this thesis relies on coincidences between the PET insert and the whole-body PET scanner to overcome this issue. Figure 35 (left) demonstrates that this method allows for LORs that penetrate the thorax as well as the axilla and conclusively enables the molecular imaging of these regions.

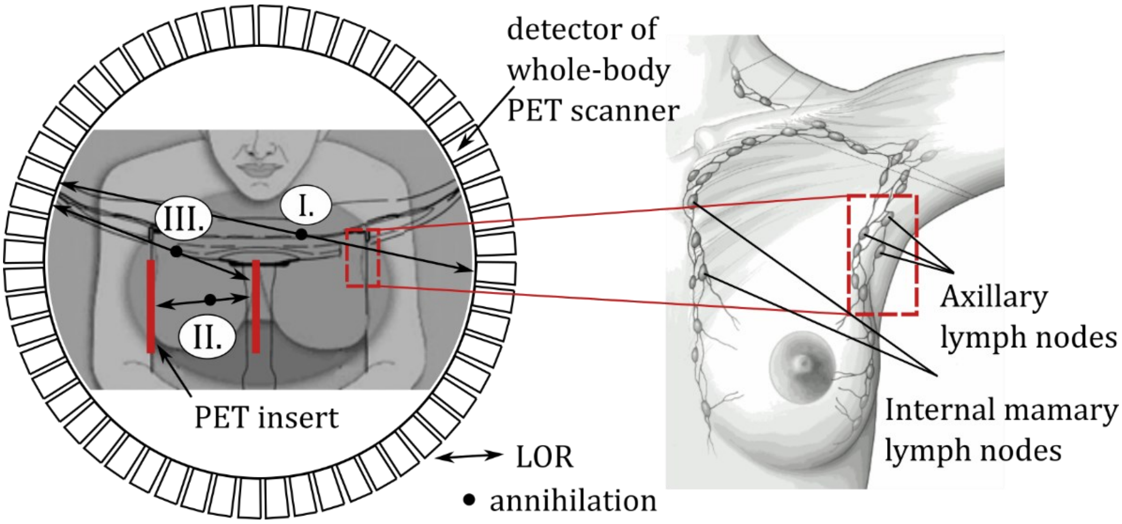

Figure 35: Left: Setup for simultaneous operation of the breast insert and the whole-body PET scanner. The LORs of three different types of coincident events, which are named external (I), internal (II), and mixed (III) events, are shown. For illustration purposes, only the cylindrical insert for the right breast is shown. Right: Location of lymph nodes close to the breast, which are used for diagnosis. Adapted and modified from [90], [91].

Furthermore, the two individual PET systems and their combination produce three different types of coincident events, as shown in Figure 35 (left).

I. External coincidences between the whole-body PET scanner's detectors

These detected events do not differ from those of the current whole-body scanner with no PET insert installed, except that a reduced number of LORs cross the voxels that are located in the volume of the PET insert due to the high stopping power of the insert's scintillation crystals. The transverse and axial resolution of 4.3 mm, which was measured at a radial offset of 10 mm from the center of the FOV, is excepted to remain stable. [92]

II. Internal coincidences between the PET insert's detectors

The PET insert can only detect true coincidences from annihilations that occur inside the breast. The insert's scintillation crystals are 1.51×1.51 mm^2 in size and hence smaller than the 4.0×4.0 mm^2 crystal size of the whole-body PET scanner. [93] The smaller size of these crystals leads to an increased LOR density, a finer sampling, and thus a higher spatial resolution across the insert's FOV.

III. Mixed coincidences between the detectors of the PET insert and the whole-body PET scanner

Regions in the body, such as the axilla, in which an annihilation event can result in an LOR between the whole-body PET scanner and the PET insert, are assigned a spatial resolution value between the individual intrinsic spatial resolutions of both systems. This is due to the much smaller crystal size of the PET insert compared to the crystal size of the whole-body PET scanner.

The following discussion provides an estimation of the intrinsic spatial resolution, or the resolution limitation defined by the crystal width, for a system with two different crystal sizes. First, this section considers the crystal size's general impact on the spatial resolution. In addition, this section determines the coincidence response function, or the rate of coincident events detected for a point source moved along the axis parallel to the surface of two scintillation crystals, as shown in Figure 36.

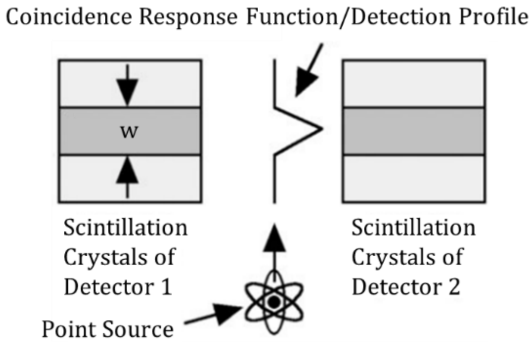

Figure 36: Coincidence response function with the characteristic triangular shape for two scintillation crystals with the same width w. The relevant crystal pair is depicted with a darker color and irrelevant crystals with a brighter color. Adapted and modified from [33].

The FWHM of the coincidence response function, which is termed the detection profile, is used to determine the intrinsic spatial resolution. For the example shown in Figure 36, where the point source is located in the middle between two scintillation crystals of the same width, the intrinsic spatial resolution is half of the crystal width.

This concept can be extended to analyze detection profiles not only at the center position between two opposing scintillation crystals but also at multiple positions along the axis between both crystals (Figure 37 left).

The detection profiles, which are not at the center position between both crystals, have a trapezoidal shape. Furthermore, the FWHM of these profiles increases as they move towards one of the crystals. Based on these considerations, the FWHM of the detection profiles is investigated for scintillation crystals of different widths (Figure 37 middle).

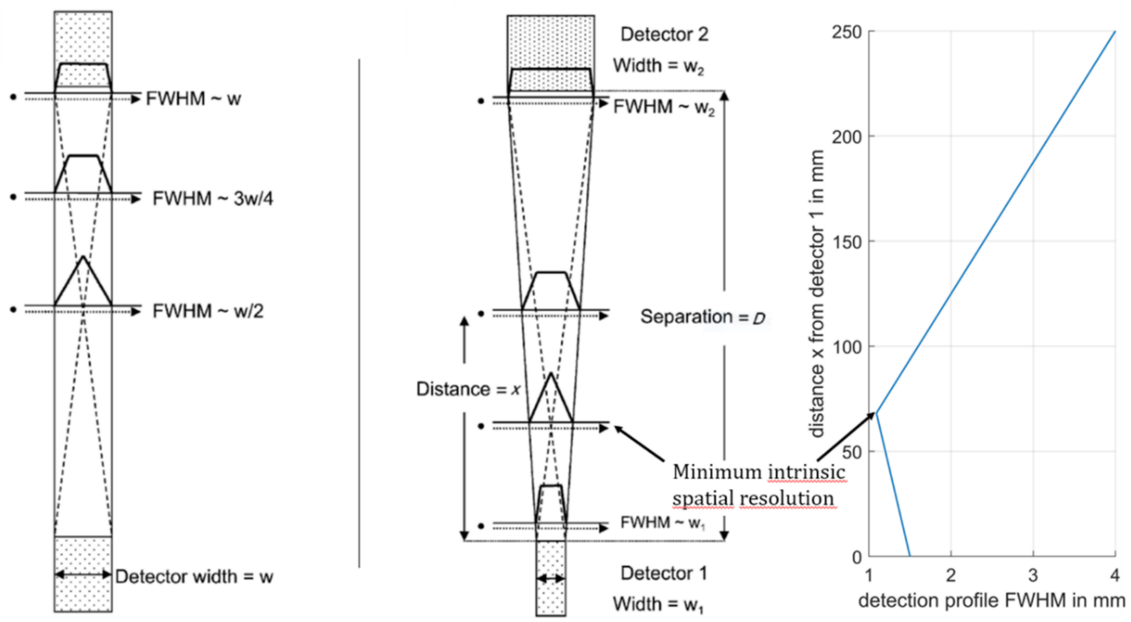

Figure 37: Left: Detection profiles for different distances between the radiation point source and the two scintillation crystals of the same size. The intrinsic spatial resolution is determined by the FWHM of the profiles. Adapted and modified from [94]. *Middle: Analogs for two crystals of different sizes, where the detection profiles indicate that the optimum intrinsic spatial resolution is closer to the smaller crystal. Adapted and modified from* [94]. *Right: Calculated theoretical FWHM of the detection profiles over the distance x in regard to the position of the detection profile from detector 1. The crystal width is set to 1.5 mm for detector 1 and 4.0 mm for detector 2, and the distance between both detectors is set to 250 mm.*

The corresponding intrinsic spatial resolution is equal to the FWHM of the profiles R_{det}, which can be described by

$$R_{det} = \frac{(D - x) \cdot w_1 + x \cdot w_2 + |(D - x) \cdot w_1 - x \cdot w_2|}{2 \cdot D},$$

where D is the distance between the crystals of both detectors and w_1 and w_2 are the crystal width of detectors 1 and 2, respectively. [94] Furthermore, x represents the distance from the crystal in detector 1 to the position of the radiation source. The intrinsic spatial resolution is not only dependent on the crystal size of both

PET systems but also on the distance between crystal pairs. Figure 37 (right) shows the relationship between the intrinsic spatial resolution and the distance to detector 1 for a crystal pair with a distance of 250 mm and crystal widths of 1.5 mm and 4.0 mm for detector 1 and detector 2, respectively. In this example, the lowest intrinsic spatial resolution is 1.1 mm and occurs on the LOR at a distance of 68.2 mm from the PET insert's crystal.

In summary, the integrated breast PET insert will provide the highest resolution for imaging the breast itself and improved resolution for regions with coincidences between the whole-body PET scanner and the insert, while the resolution of the whole-body PET scanner for the rest of the body will remain unchanged.

3.5 Discussion and Conclusion: PET Insert System Design

Section 3.1 discussed the integration of the PET insert into the RF coil. If the shielding boxes are placed next to each other with no gap between them, it could be more difficult for the RF waves, which are transmitted from the whole-body MRI scanner, to penetrate the breast tissue. As a result, the magnetization's required rotation is hindered, preventing the effective MR imaging of the breast. Further simulations on RF wave propagation and tests with the shielding enclosures arranged based on the structure of the PET insert should be conducted to determine whether the MRI scanner can still be properly operated.

The results of these tests might indicate that a gap is required between the detectors, which in turn might decrease the sensitivity of the PET insert. Furthermore, it might be necessary to reduce the thickness of the shielding layer, and consequently, the PET modules may not be adequately shielded against the RF distortion introduced by the MRI scanner.

Both problems can be solved by replacing the receive-only RF coil. A combined transmitter and receiver, called a transceiver coil, can generate RF waves locally inside the PET insert and thus minimize changes to the B_1 excitation field introduced by the shielding enclosures. [95]

Sections 3.2 and 3.3 introduced an initial design for a detector and rudimentary designs for the geometries of the breast PET insert. These designs might change for the final PET insert; however, they establish a reasonable starting point for further tests and simulations. In general, simulation and detector development should go hand in hand to achieve optimum system performance with respect to hardware limitations while considering the spatial limitations given by the anatomical shape of the breasts when enclosed in the PET insert. For this purpose, it is sensible to begin with an existing RF breast coil, which is designed to fit the average human female breast, although the RF coil might be redesigned for the final breast PET/MRI insert.

Section 3.4 demonstrates that the intrinsic spatial resolution improves because the crystals of the whole-body PET scanner and the PET insert differ in size. This calculation is possible when the front crystal surfaces of two opposing detectors face each other directly (Figure 37 middle). However, this is not the case for potential LORs of mixed coincident events, which are detected by both the breast insert and the whole-body PET. The gamma rays of the mixed coincident events do not enter the front of the PET insert's crystal surface but enter laterally at a certain angle, resulting in gamma ray interaction at a certain depth inside the scintillation crystal. Therefore, the spatial resolution of mixed coincident events depends on the detector's capability of determining the depth of interaction and its corresponding accuracy.

In addition, factors such as the noncollinearity of the emitted gamma rays or the isotope- and medium-dependent positron range further degrade the final resolution of the image reconstruction. [94] Hence, further comprehensive simulations should be performed in order to evaluate changes in the spatial resolution and understand the gain in performance for coincidences between both PET systems.

To physically enable coincidence detection between the PET insert and the whole-body PET scanner, it is necessary to synchronize the event data of both systems. Section 6.6.1 shows that the clock signal of the whole-body scanner can be fed externally to the PET insert to ensure clock synchronization over time. However, future research should focus on implementing combined coincidence processing.

4 Operation of the PET Modules

The previous chapter noted that the PET detectors and system electronics, which are based on the Hamamatsu C13500-4075LC-12 PET modules, are one component of the PET insert's system design. This chapter describes these modules and their corresponding back-end electronics and considers their internal signal processing, which enables a digital representation of the detected PET events. Furthermore, this chapter introduces the binary data format of the PET events. It should be noted that the "16 Byte Compton firmware" was used for the measurements discussed in this chapter and in Chapter 6; however, the "32 Byte Compton firmware" was used to account for the modified hardware detailed in Chapter 5. Representing the PET events with this data format requires a special post-processing method, which this chapter describes in more detail. In addition, this chapter demonstrates a correction method for improving the accuracy of the PET modules' timing measurements. In addition, this chapter further analyzes the effects of temperature on the PET modules and solutions to account for this issue by a temperature compensation of the photo sensor's bias voltage and appropriate air cooling.

4.1 Material and Methods

4.1.1 Hamamatsu PET Module and Back-end Electronics

Figure 38 provides an overview of a PET detector setup with two detectors using the C13500-4075LC-12 PET module and C13500 series back-end electronics (Hamamatsu Photonics K.K. Hamamatsu, Japan).

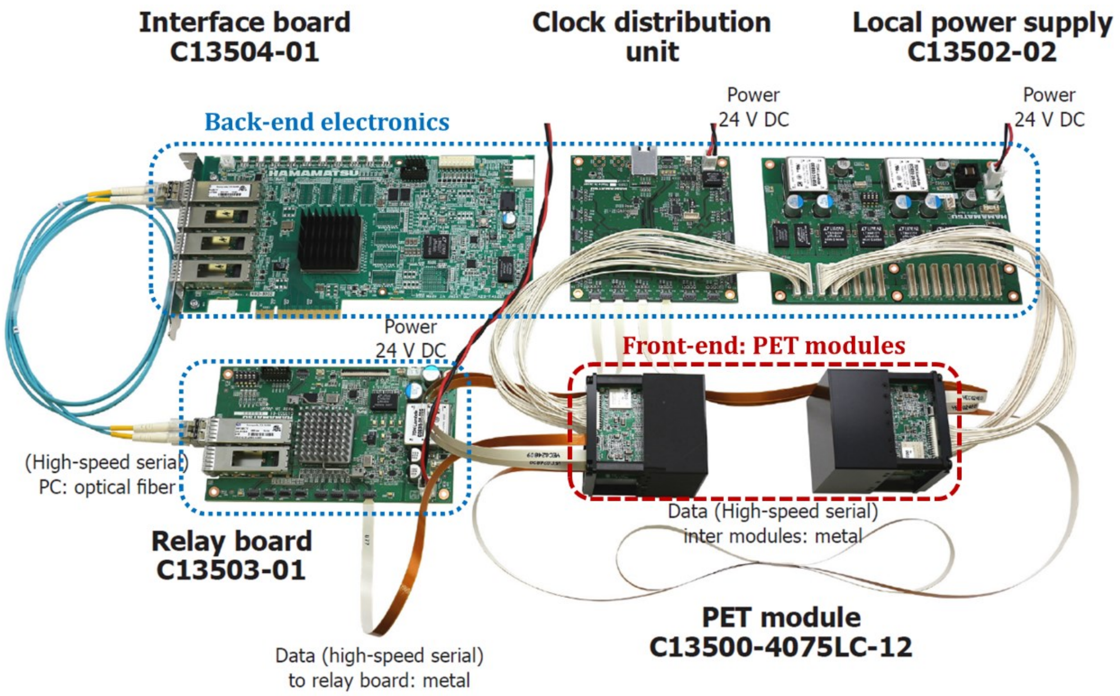

Figure 38: C135000-4075LC-12 PET module and C13500 series back-end electronics by Hamamatsu. Adapted and modified from [87].

The functionality and connection between the front-end and the back-end are shown in a simplified manner in the block diagram in Figure 39.

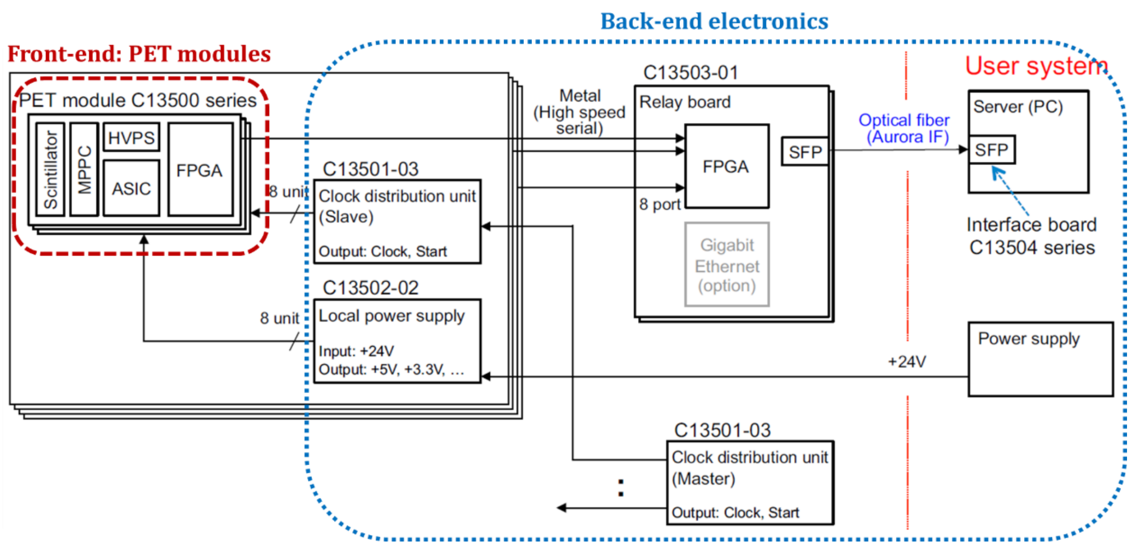

Figure 39: Block diagram visualizing the link between the PET modules and the building blocks of the back-end electronics. Adapted and modified from [96].

The PET modules are known as the front-end, as they represent the first stage and are responsible for gamma ray detection and event preprocessing.

The second stage is referred to as the back-end electronics and consists of multiple building blocks used for the power supply, setting and communicating with the PET modules, and event processing. The functionality of these building blocks is as follows: the local power supply C13502-02 is used for powering the PET modules and most of the boards of the back-end electronics. The clock distribution unit C13501-03 feeds the clock signal to the front-end and ensures synchronization between each PET module and the back-end electronics. The relay board C13503-01 is responsible for two-way communication between the front-end and the back-end. For example, the relay board transfers the setting for the operation voltage of a PET module's MPPC. Furthermore, the relay board collects the data stream from each PET module, processes the data (e.g., energy discrimination), and finally transfers the data to the interface board C13504-01. This board is connected via a peripheral component interconnect (PCI) to a PC that stores the raw binary event data stream.

A more detailed view of the components of a C13500-4075LC-12 PET module (standard configuration) is shown in Figure 40 (left). It consists of a 12×12 LFS scintillator array with crystal dimensions of $4.14 \times 4.14 \times 20\ mm^3$. The 12×12 MPPC array has a photosensitive area of $4 \times 4\ mm^2$ per channel and a pixel pitch of $75 \times 75\ \mu m^2$. In addition, the module includes two signal processing boards, each capable of processing 72 channels, as illustrated in Figure 40 (right).

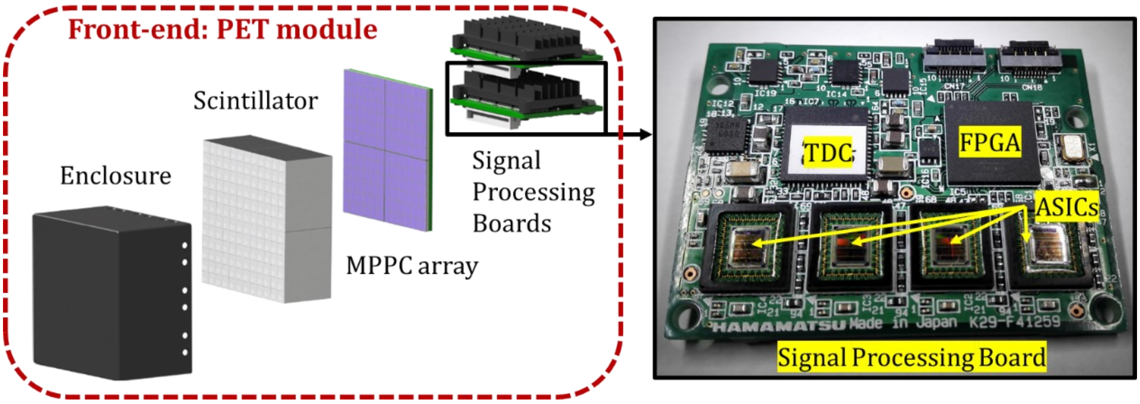

Figure 40: Left: Exploded view of a PET module with a light tight aluminum enclosure. Right: Top view of the signal processing board. Adapted and modified from [87].

The main components of a signal processing board include four application-specific integrated circuits (ASICs), a field-programmable gate array (FPGA), a time-to-digital converter (TDC), and a high voltage power supply (HVPS) unit (located at the bottom of the signal processing board in Figure 40, right).

The HVPS is used to supply a temperature-stabilized operation voltage to the MPPC. A single ASIC can handle up to 18 MPPC channels, as illustrated in Figure 41.

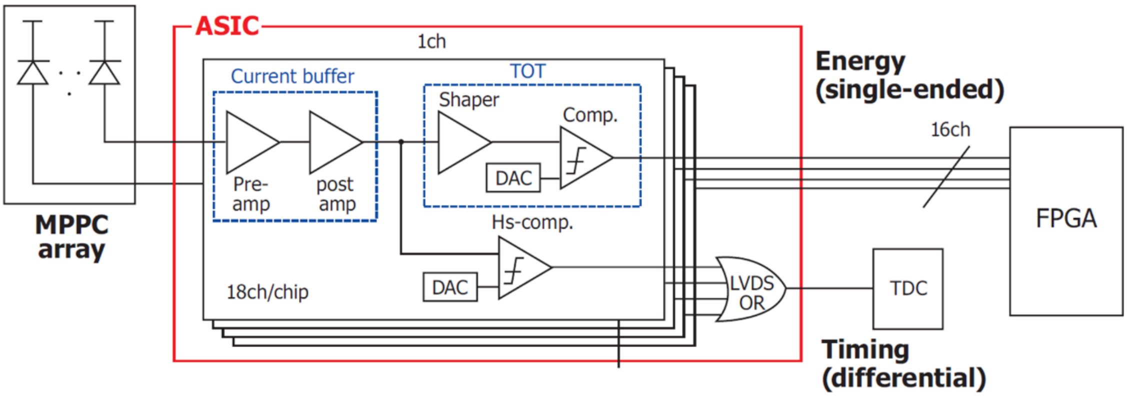

Figure 41: Block diagram visualizing the main components of the ASIC and its connections to the MPPC, FPGA, and TDC. Adapted and modified from [87].

The first stage of the ASIC is the current buffer, which outputs an amplified signal that is split into two paths. In the first path, the signal's time-over-threshold (ToT) is generated to measure the energy of the incident gamma ray. Each ToT signal is further sampled by the FPGA with a 4 ns granularity to determine the value of the energy.

The second path uses the output signal of a comparator, which can be related to the incident gamma ray's time of arrival. The TDC is subsequently used to generate the time stamp with a granularity of 15.0602 ps. However, as the TDC is limited to 4 input channels, the ASIC's 18 timing channels are first combined by an OR gate (a digital logic gate that implements logical disjunction). The event data (e.g., board number, ASIC channel, energy, time) is finally transferred to the back-end electronics by the FPGA.

Unless otherwise stated, the PET modules used for the measurements in this thesis have the following custom modifications in comparison to the C13500-4075LC-12 PET modules (standard configuration):

- The scintillator block dimension, MPPC array, and number of signal processing boards are reduced by a factor of two, resulting in:
  - a 6×12 channel MPPC array
  - a 6×12 scintillator array
  - a single signal processing board for one detector block (MPPC array + scintillator array);
- The heatsink, which is mounted to the signal processing board, has been removed;
- The 125 MHz oscillator chip on the signal processing board has been removed;
- The HVPS C11204-02 (inductor voltage boost) has been replaced with the C11204-04 (external voltage boost).

4.1.2 General Coincidence Measurement Setup

A general setup for measuring coincident events can be seen in Figure 42.

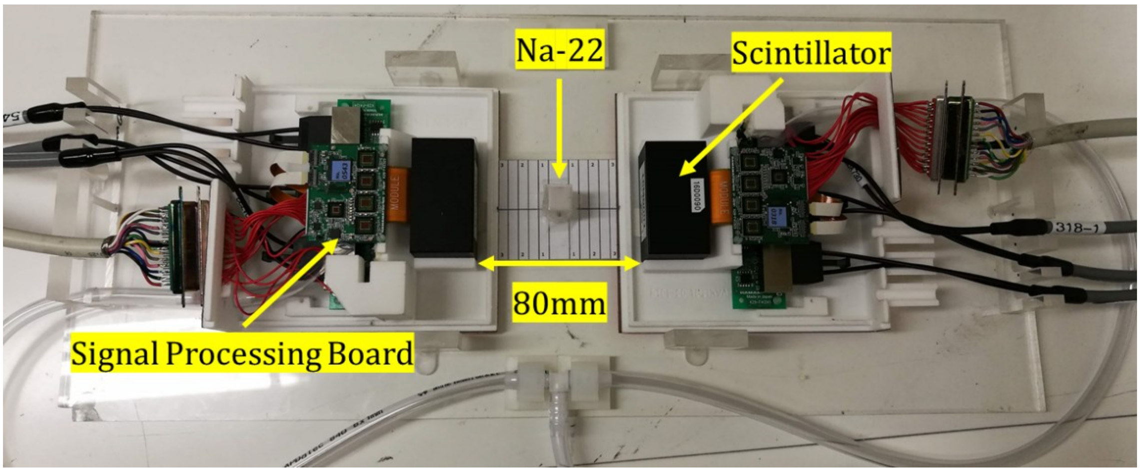

Figure 42: Setup with two opposing PET modules and an Na-22 source for the acquisition of coincidence events. The PET modules are encapsulated in boxes to enable the cooling airflow to circulate. The airflow is delivered by compressed air connected to the transparent tubes.

The detector blocks of both PET modules are facing each other, and an Na-22 point source is centered between the modules with a distance of 40 mm to each scintillator block. If not otherwise stated, the following settings apply to all subsequent measurements: in total, 1×10^6 single events are acquired with an energy window of 100 ns to 800 ns (ToT). The overall operational voltage is set to 56.22 V at 25°C, which was adjusted by the ASICs for each MPPC channel to account for their different breakthrough voltages. The temperature compensation of the HVPS is set to 54 mV/°C.

Post-processing of the binary file that stores the single events was done using a PC. The “16 Byte Compton firmware”, (see section 4.1.3) necessitates a special treatment of real events that are represented by more than one data event. Therefore, an algorithm was used to merge certain data events in order to create a digital representation of the PET events, as described in section 4.1.3. Furthermore, a coincidence timing window of 20 ns was used to select coincident events. The timing spectrum was generated by energy discriminated coincident events, where only events with an energy between ±1σ around the photo peak of the assigned crystal were considered. The energy of one data event was equal to the sum of all four energy registers (*Energy1-4*), as described in section 4.1.3.

4.1.3 16 Byte Compton Firmware Event Data Processing

Events acquired with the “16 Byte Compton firmware” are saved in a 16 byte data format, as shown in Figure 43. The number of the signal processing board attached to this block was used to identify the scintillator block in which the event was registered. With the *TDC_ch* register, which corresponds to the ASIC number, and the ASIC channel register *Ch1-4*, the corresponding MPPC channel of interaction can be determined. Gamma rays that stop in a single crystal and fire only the corresponding directly coupled MPPC channel result in register values for *Ch1* and *Energy1*, while the register values *Ch2-Ch4* and *Energy2-3* remain zero. Three additional energy/channel pairs were stored in one data event to account for inter-crystal scatter (i.e., the gamma ray is Compton scattered between the crystals of a pixelated scintillator block).

■ Compton firmware data format (Binary, 16 byte / event)

Symbol	Symbol	Description
Data [127:0]	Blank [2:0]	Blank
	Board_No [9:0]	Board number
	TDC_ch [1:0]	Channel of TDC
	OVF_CT [31:0]	1.28us resolution timing data (Over flow counter of TDC_coarse)
	TDC_coarse[9:0]	1.25ns resolution coarse timing data
	TDC_fine [6:0]	15.0602ps resolution fine timing data
	Blank [0]	Blank
	Ch1 [6:0]	MPPC channel (1st energy value)
	Energy1 [7:0]	4ns resolution energy data (1st)
	Ch2 [6:0]	MPPC channel (2nd energy value)
	Energy2 [7:0]	4ns resolution energy data (2nd)
	Ch3 [6:0]	MPPC channel (3rd energy value)
	Energy3 [7:0]	4ns resolution energy data (3rd)
	Ch4 [6:0]	MPPC channel (4th energy value)
	Energy4 [7:0]	4ns resolution energy data (4th)
	Blank [2:0]	Blank

Figure 43: Registers of a single data event for the data format of the 16 Byte Compton firmware [97].

Figure 44 (left) shows the energy signals for an inter-crystal scatter scenario that results in firing five different MPPC channels connected to the same ASIC.

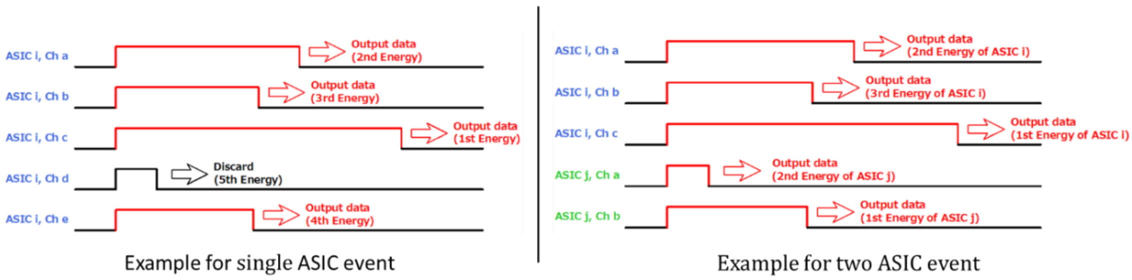

Figure 44: ToT energy signals from a single gamma ray for ASIC numbers i and j and channel numbers a–e. Left: Only MPPC channels connected to a single ASIC are fired. Right: MPPC channels connected to two different ASICs are fired. Adapted and modified from [97].

The four highest energy values and their corresponding MPPC channel number are stored in descending order, with the highest energy value stored in the registers *Energy1* and *Ch1*. Lower energy values, such as the fifth energy value in Figure 44 (left), are discarded.

Figure 44 (right) depicts a second scenario in which an inter-crystal scatter occurs between the crystals placed on two different MPPCs connected to two different ASICs. In this example, one data event stores the first ASIC's three energy/channel pairs. Another data event stores the second ASIC's two energy/channel pairs. Hence, a PET event, which corresponds to an incident gamma ray, can be represented by more than one data event.

Theoretically, the maximum number of data events that represent a PET event is equal to the number of ASICs connected to a single scintillator block. Practically, only a negligible fraction of the gamma rays are scattered over a number of crystals not covered by two ASICs. Therefore, for the data processing in this thesis, no more than two data events were used to represent a PET event acquired by the "16 Byte Compton firmware" data format.

4.1.4 Measurements for Determining the Optimum Compton Time Window

Section 4.1.3 noted that a single PET event can be expressed by multiple data events. Figure 45 further explains this process, illustrating a 6×12 MPPC array and directly coupled crystals separated into four sections.

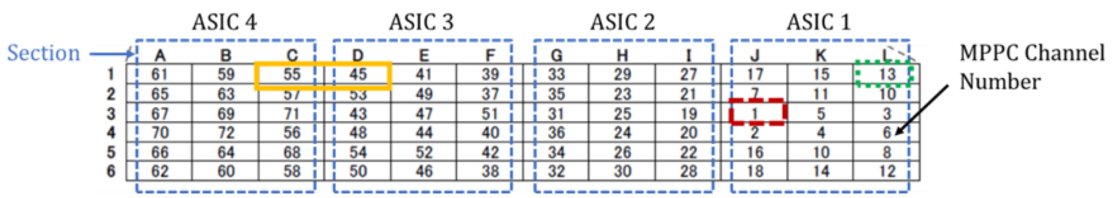

Figure 45: Illustration of the connection between MPPC channel numbers and assigned ASICs. The yellow box serves as an example of a PET event, which is represented by two data events. A gamma ray stopped at a crystal placed on MPPC channel 55 is Compton scattered into the neighboring crystal (inter-crystal scatter) placed on top of MPPC channel 45. As MPPC channel 55 is assigned to ASIC 4 and MPPC channel 45 is assigned to ASIC 3, both ASICs provide an individual data event; thus, two data events are used to represent a single PET event.

Each of these sections is associated with 18 channels on one ASIC. Inter-crystal scatter between two different sections (e.g., the interaction shown by the yellow box in Figure 45) results in two data events in the event data stream for a single real interaction.

In order to merge these two data events into a single event, a so-called Compton time window is applied. Single data events from one PET module that have a time stamp difference less than or equal to this time window are merged into a single event. The MPPC channel number for this event is set to the *Ch1* register of the first of the two events in the data stream. The energy is the sum of the four energy registers of both data events.

The optimal value of the Compton time window is important to achieve an accurate representation of the real gamma ray interactions represented by the digital data events. For instance, if the value of the Compton time window is too large, data events that do not originate from the same PET event would be falsely merged. On the other hand, if the value of the Compton time window is too small, data events that originate from the same PET event are not merged and would be treated as two individual PET events.

The following analysis aims to determine the optimum Compton time window. In contrast to the coincidence time window, which is affected by the timing performance of both detectors, the Compton time window applies to the data acquisition of a single PET detector. For this reason, the setup described in section 4.1.2 was used; however, only one detector acquired the events, as it is not necessary to perform coincidence measurements to determine the optimum Compton time window.

The following analysis was performed to investigate the impact of different Compton time window values on the energy spectra of the MPPCs and thus the directly coupled scintillation crystals. First, as an example, the single-channel energy histograms were acquired for MPPC channel 1 and MPPC channel 13 for Compton time window values of 0 ns, 1 ns, 10 ns, 100 ns, and 1000 ns. Second, the total block energy histogram of all of the MPPC channels was determined for a smaller range of Compton time window values between 0.00 ns and 10.00 ns with a step size of 1.25 ns, which corresponds to the granularity of the *TDC_coarse* register (Figure 43). Along with a qualitative comparison of the shape of the energy histograms, the mean value and standard deviation of all energies from each data set were calculated for the quantitative analysis.

In addition to investigating the effect of multiple Compton time windows on the energy histograms, the impact of the Compton time windows on the number of merged data events was examined. For this process, the percentage of merged data events with respect to all single data events (before the merge according to the Compton time window) was calculated for Compton time window values between 0.00 ns and 10.00 ns, with a step size of 0.05 ns.

4.1.5 Measurements for Evaluating the Influence of the Time Skew Correction on Timing Performance

In order for the Hamamatsu PET modules to achieve the best timing accuracy, two corrections must be applied concerning time stamp acquisition.

First, a calibration is required to account for the TDC's nonlinearity. The manufacturer performs this calibration, and the correction values are stored for each signal processing board in a lookup table and are accounted for as the FPGA processes the time stamps.

Second, the time skew, which applies to each individual MPPC and ASIC channel, must be corrected. This time skew originates from the interplay of each source that affects the timing signal and the determination of each event's time stamp. As such, manufacturing process variations in the scintillation crystals and MPPCs result in different analog timing signals and correspond to an individual channel time skew. Furthermore, according to the manufacturer, each ASIC can introduce a constant delay of up to 200 ps due to process variation. In addition, the MPPC channels connected to the ASICs have different signal trace lengths, also causing a constant delay in the timing signal.

To correct for the channel based time skew, first a calibration coincidence measurement needed to be performed, which enabled the acquisition of timing histograms for all MPPC channels. For this reason, the distance between the radiation source and the scintillators of the PET detectors was increased (Figure 42) to enable the acquisition of multiple LORs between the two PET detectors. The distance between both detectors was set to 20 cm, and 75×10^6 single events were acquired for the time skew correction according to the guidelines of the manufacturer, with a 400 kBq Na-22 point source. This calibration data set was provided to the manufacturer, who used an iterative maximum likelihood method based on their process standards to determine the individual channel time skew. A total of 144 time skew correction values were then stored in a lookup table for the FPGA and applied during signal processing.

To investigate the influence of the time skew correction on timing performance, a coincidence timing histogram was generated with a Gaussian fit to determine the

FWHM CRT with the setup mentioned above, first without and then with the time skew correction.

4.1.6 Setup for Evaluating the Operating Temperature Range and the HVPS Temperature Compensation

The HVPS component on the signal processing board of the PET modules is used to supply the MPPC's bias voltage (Figure 46 left).

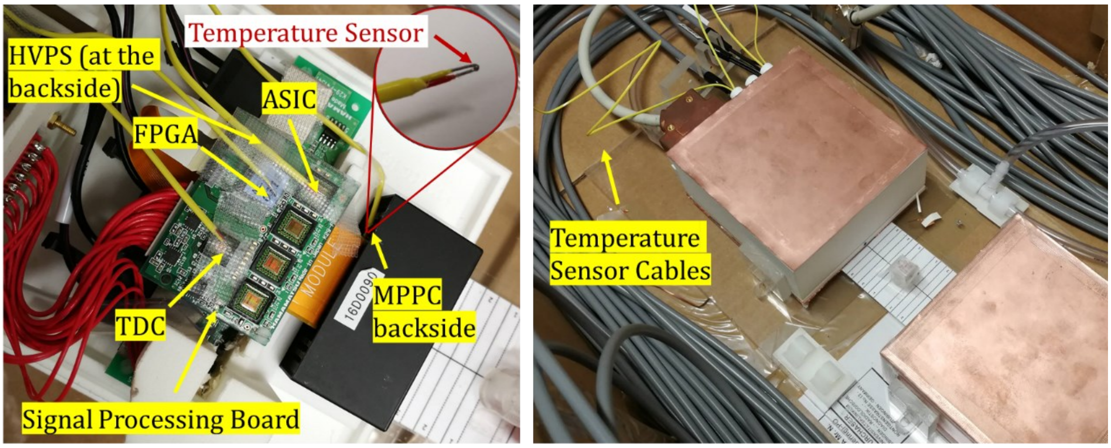

Figure 46: Left: The four temperature sensors (at the end of the yellow cables) attached on top of the TDC, FPGA, and ASIC and on the back of the MPPC. Right: Measurement setup with PET detectors inside closed boxes to enable the cooling airflow to properly circulate.

As the gain is temperature dependent, a temperature compensation mechanism is built in by the manufacturer. The temperature of the MPPC is measured with a temperature sensor integrated circuit, and based on this temperature value, the bias voltage supplied by the HVPS is continuously adjusted.

In order to evaluate whether temperature compensation can account for the changes in temperature that occur during the PET modules' normal operation, the following measurements were performed. The MPPC temperature was monitored by a type K thermocouple temperature sensor (Figure 46 left). It should be noted that the temperature of the MPPC could not be measured directly, as the aluminum housing prevents access to the top side of the MPPC. Alternatively, the closest position to the MPPC is at the back of the printed circuit board (PCB) on which the MPPC is mounted; therefore, the true MPPC temperature is likely to differ from the measured temperature. In addition, the temperatures of the ASIC, FPGA, and TDC on the signal processing board were measured with the thermocouple temperature sensors to determine whether the supplied air cooling is sufficient to prevent these components from overheating.

The measured temperature values were logged over a period of 480 minutes in one second intervals with an Extech SDL 200 (Extech Instruments, Nashua, NH, USA) at a precision of ±(0.4 %+1°C). During the measurement, the PET modules were cooled by airflow while encapsulated in boxes that were used for RF shielding (see section 6.4.1). Figure 46 (right) depicts the measurement setup. As section 4.1.2 described, the conditions also apply to the measurements performed with this setup; however, only the PET data from the detector with the attached temperature sensors were processed. The activity of the Na-22 source was 409 kBq.

The average photo peak position of the scintillation crystal energy histograms is proportional to the gain of the MPPC and is thus used as an indicator of the MPPC's operational stability across changes to temperature and time. To this end, PET data sets were recorded over a measurement time of 480 minutes. As the highest temperature changes occurred at the beginning of the measurement and reached a steady state towards the end of the measurement, the frequencies that determine when PET data sets are acquired were set accordingly. In the first 60 minutes, PET data sets were acquired every 2 minutes. In the following 60 minutes, the interval between measurements was increased to 5 minutes, then further increased to 15 minutes for the following 60 minutes, and for the last 3 hours, the interval between measurements was 60 minutes.

In addition to analyzing the average photo peak positions over the measurement time, the correlation between the photo peak positions and the temperature measured at the back of the MPPC was analyzed.

The results of this analysis were reported to the manufacturer. Based on these results, a firmware change was required for the temperature compensation mechanism to function properly. In order to verify the stability of the photo peak position over time with the new firmware, the previously described measurement setup was used; however, the temperature was not monitored, as the new firmware did not affect the temperature of the components over the measurement time. In addition, the measurement time was increased to 21 hours to validate the stability of the temperature compensation over a longer period.

4.1.7 Setup for Evaluating the Impact of the Cooling Conditions on the Performance of the PET Modules

Section 4.2.3 reports that the new firmware, which is capable of compensating for temperature effects, allows for the MPPC to experience a constant gain over the operation time. In addition to this feature, the effect of cooling the PET modules was evaluated. In order to monitor the temperature for this setup, no external temperature sensors (see section 4.1.6) were used; however, a built-in temperature sensor (see Figure 47) was used.

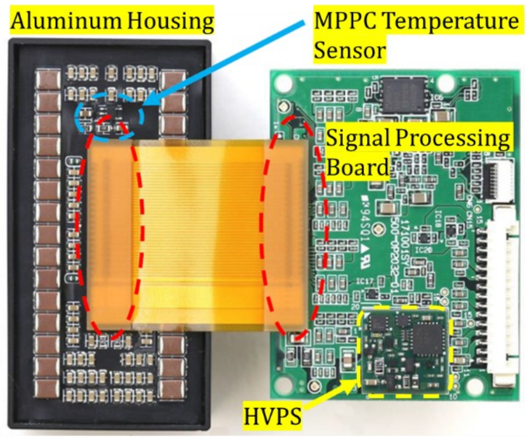

Figure 47: MPPC temperature sensor integrated circuit mounted at the back of the PCB on the MPPC. The measured temperature value is used internally by the HVPS temperature compensation mechanism to adjust the bias voltage of the MPPC. Modified and adapted from [97].

The readout of this sensor was performed using software provided by the manufacturer, which was not available for the temperature measurements described in section 4.1.6.

Thus, it was possible to record the temperature, which was then used for the HVPS temperature compensation, for each measurement. Figure 47 demonstrates that the MPPC temperature sensor is not located directly at the MPPC but at the back of the PCB, where the MPPC is mounted. As a result, the measurement is an approximation of the actual MPPC temperature: the sensor was exposed to direct airflow, while the MPPC was encapsulated by the aluminum housing. The measurements were performed with the setup as described in section 4.1.2 using a 392 kBq Na-22 source with three different cooling conditions. The pressure of the airflow was set to 1.0 bar or 0.5 bar, or no cooling was applied, and the corresponding measurements were labeled as *high airflow*, *medium airflow,* and *no airflow*, respectively. A PET data set was acquired every 30 minutes over a period of 120 minutes, and the MPPC sensor temperature was recorded accordingly.

The average photo peak position and average energy resolution of one detector's single crystal energy histograms were determined to evaluate the PET modules' stability at different cooling conditions with regard to energy-related performance. In addition, to evaluate the stability of measurements concerning timing accuracy, the peak position of the Gaussian fit of the timing histogram was determined, as was the CRT across various temperatures for different airflow measurements.

4.2 Results

4.2.1 Optimum Compton Time Window to Account for Compton Scattered Events

As Figure 48 (left) shows, the energy histogram for MPPC channel 13, which corresponds to a corner crystal (Figure 45 green box), does not change substantially for different Compton time windows. This is in accordance with a mean energy value of 436.0 ns±45.7 % and 439.2 ns±46.1 % for Compton time windows of 0 ns and 1000 ns, respectively. This finding can be explained by the fact that the scattered gamma rays must penetrate at least two crystals to reach a second section, which results in a low probability that PET events represented by two data events correspond to corner crystals. However, for the crystal corresponding to MPPC channel 1 at the edge of two sections (Figure 45 red box), the energy spectra in Figure 48 (right) show a high variation for different Compton time windows. In this instance, Compton time windows of 0 ns and 1000 ns had a mean energy value of 474.1 ns±50.0 % and 483.8 ns±37.8 %, respectively. This result can be explained by the increased probability of PET events represented by two data events, as a gamma ray can be scattered directly to the neighboring crystals of another section and thus a different ASIC.

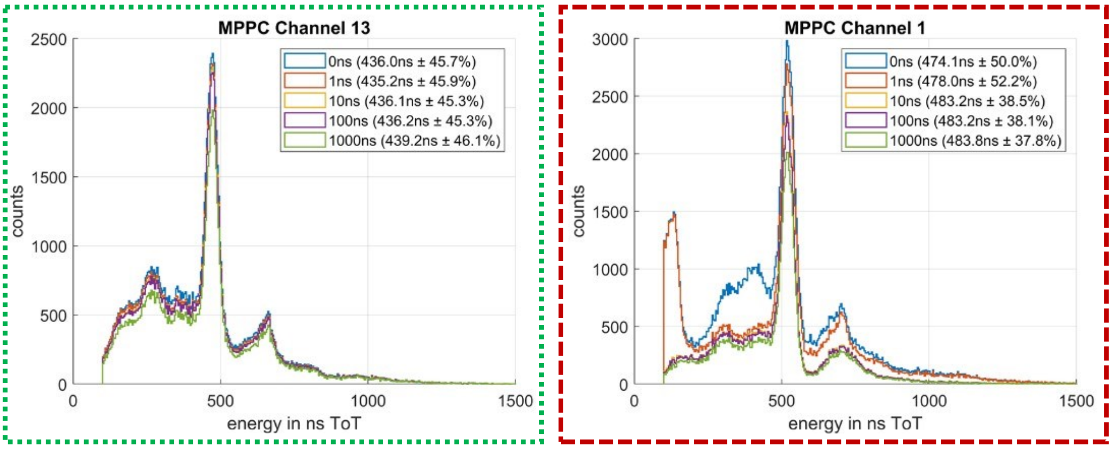

Figure 48: Single crystal energy histograms for Compton time windows between 0 ns and 1000 ns (with mean energy value and standard deviation in brackets). Left: MPPC channel 13 corresponding to a corner crystal in the scintillator block. Right: MPPC channel 1 corresponding to a crystal at the edge to the crystals associated with a second ASIC.

Figure 48 (right) demonstrates that for a Compton time window with a value of 10 ns, the energy histogram differs from those with Compton time windows of 0 ns and 1 ns; notably, the peak for energies below the photo peak is eliminated. For Compton time windows of 0 ns and 10 ns, counts at the peak position of 120 ns reduce from 1.4×10^3 counts to 0.2×10^3 counts, respectively. The reason the Compton time window values of 0 ns and 1 ns have a higher probability of events in the region below the photo peak can be explained as follows. Some of the corresponding data events in this region are falsely treated as PET events, whereas they are only one part of a Compton scattered event and thus have only a fraction of the total energy of the PET event. The energy spectra do not show the spurious peaks in the lower energy region for Compton time window values above 10 ns. Therefore, the data processing algorithm, which uses the Compton time window method to merge data events, sufficiently corrects for these false annotations.

Additionally, to narrow the interval for the search of the optimum value for the Compton time window, the total block energy histograms were calculated for Compton time windows below 10.00 ns (Figure 49 left).

The energy spectra reveal changes in Compton time window values below 7.50 ns, especially in the region with energies lower than the photo peak energy.

Hence, Compton time windows larger than 7.50 ns did not reveal changes in the shape of the energy histograms.

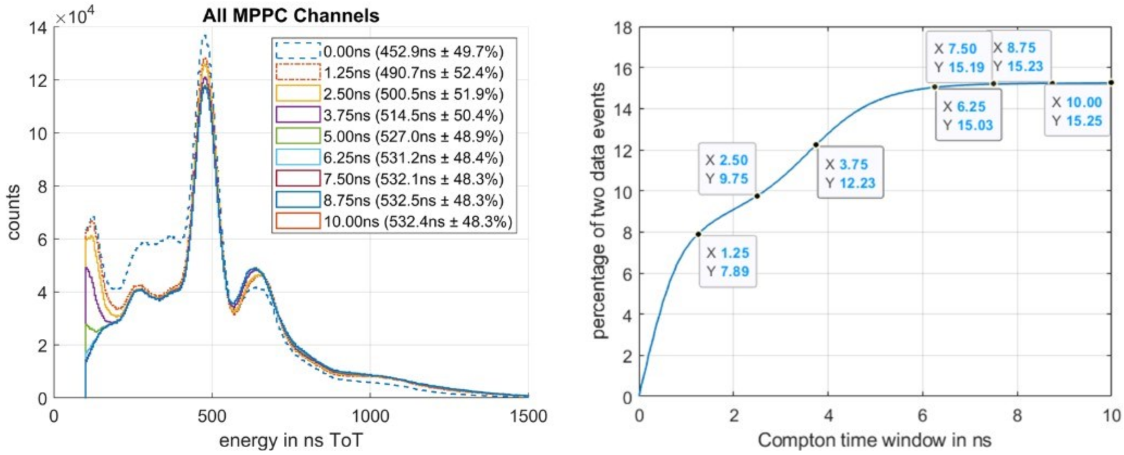

Figure 49: Left: Total block energy spectra for Compton time windows between 0.00 ns and 10.00 ns (with mean energy value and standard deviation in brackets). Right: Dependency of the fraction of two data events from all single data events on the Compton time window.

Furthermore, the percentage of events that are represented by two data events was calculated for Compton time windows between 0.00 ns and 10.00 ns, as illustrated in Figure 49 (right). The percentage strongly increases for low Compton time window values and becomes saturated for values above 7.50 ns at 15.19 %. A value of 8.75 ns (with a percentage of two data events of 15.23 %) was selected to merge the majority of data events that originate from a single PET event. A higher value would result in the false merger of two subsequent data events in the data event stream, which correspond to two independent PET events.

4.2.2 Influence of Time Skew Correction on the Timing Performance

In Figure 50, the timing spectra reveal that the CRT improves from 352 ps to 261 ps without and with the time skew correction, respectively.

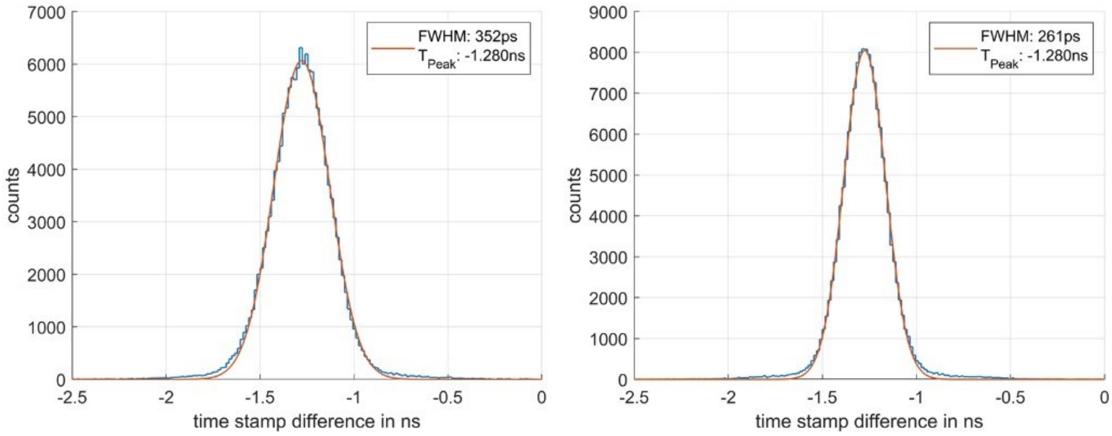

Figure 50: Timing spectra acquired with the coincidence setup in Figure 42, with a distance of 20 cm between the PET detectors. Left: Without time skew correction applied. Right: With time skew correction applied.

4.2.3 The Operating Temperature Range and the HVPS Temperature Compensation

Figure 51 (left) shows the response of the four temperature sensors after turning on the PET modules for a period of 480 minutes.

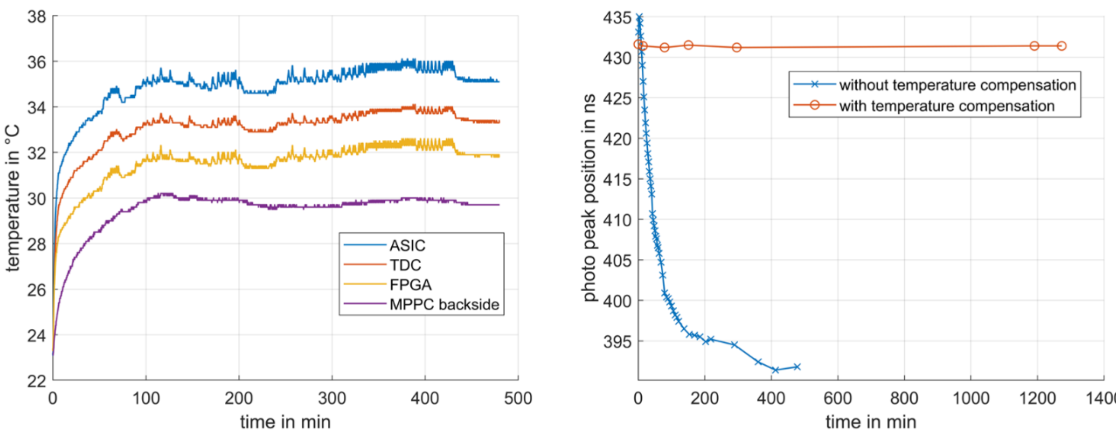

Figure 51: Left: Temperature measured over time by sensors mounted on different components of the PET module. Right: Average photo peak position across time with and without using the firmware for temperature compensation.

The temperature of all four components was 23.1 °C at the start of the acquisition. The subsequent temperature increase was strongest for the ASIC, followed by the TDC and the FPGA and lowest for the temperature sensor at the back of the

MPPC. The temperature increase peaked at 34.9 °C, 33.2 °C, 31.6 °C, and 29.9 °C 100 minutes after turning on the PET module at the ASIC, TDC, FPGA, and the back of the MPPC, respectively. At these temperatures, the PET modules still operate reliably. Therefore, the supplied air cooling effectively prevents these components from overheating.

However, the average photo peak position decreased over time without temperature compensation (Figure 51 right). This result can be explained by the graph in Figure 52, which shows the correlation between the measured temperature at the back of the MPPC and the photo peak position.

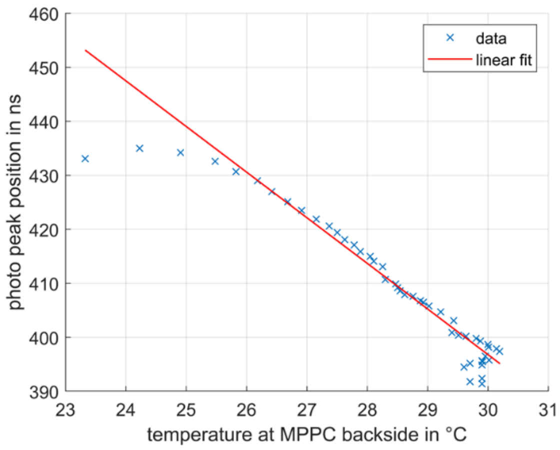

Figure 52: Average photo peak position over the temperature measured at the back of the MPPC. For the linear fit, the two lowest temperatures were excluded.

It is assumed that this measured temperature is proportional to the temperature of the MPPC array. As such, an increase in temperature results in an increase in the photo sensor's breakdown voltage. As the bias voltage remained constant despite temperature changes, the overvoltage, or the difference between the bias voltage and the breakdown voltage, decreased at higher temperatures. According to the manufacture's specifications, the MPPC's breakdown voltage increases linearly at 54 mV/°C. Correspondingly, the MPPC's gain decreases at higher temperatures, which is reflected by the linear photo peak's decrease of -8.5 ns/°C as the temperature changes (Figure 52). A high coefficient of determination of 0.96 indicates that the data is well approximated by a linear progression.

The new firmware provided by the manufacturer is able to account for the change in temperature by adjusting the MPPC's bias voltage by 54 mV/°C. This temperature compensation stabilized the photo peak position at 431.39±0.15 ns for 21 hours, as shown in Figure 51 (right, orange curve).

4.2.4 The Impact of the Cooling Conditions on PET Module Performance

The temperature measured by the MPPC temperature sensor shows a comparable trend for the cooling conditions with *no airflow* and *medium airflow* (Figure 53).

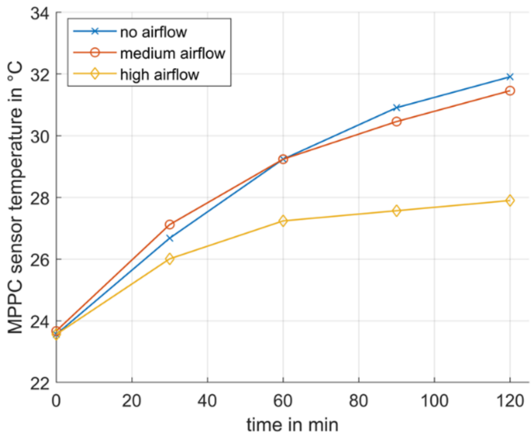

Figure 53: Temperature measured by the MPPC temperature sensor over 120 minutes for three different cooling conditions.

Accordingly, after 120 minutes, the average temperatures are comparable for *no airflow* and *medium airflow* at 28.46±3.38 °C and 28.39±3.10 °C, respectively. The same holds true for the minimum and maximum temperatures of 23.56°C and 23.67°C and 31.91°C and 31.46°C for *no airflow* and *high airflow*, respectively. In contrast, cooling with a *high airflow* resulted in a lower average temperature of 26.46±1.77 °C with a smaller fluctuation, indicating greater temperature stability: the changes in temperature over time (23.56°C to 27.90°C in 120 minutes) are smaller in comparison to the two other cooling conditions.

Figure 54 (left) shows that *no airflow* had the highest photo peak position with an average of 444.1±5.6 ns, which decreased to 434.6±3.0 ns for *medium airflow* and 426.6±0.9 ns for *high airflow*.

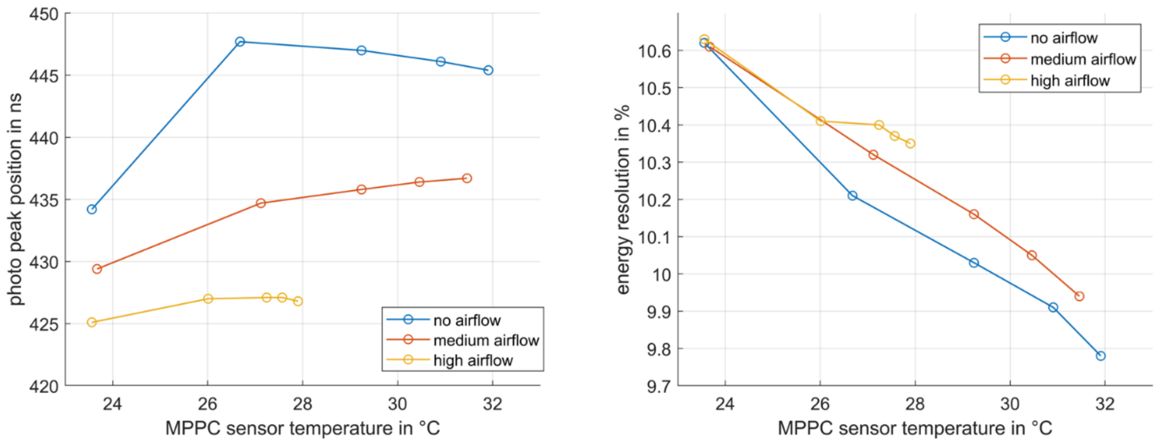

Figure 54: Left: Average photo peak position over temperature as measured by the MPPC temperature sensor for three different cooling conditions. Right: The corresponding relationship between the average energy resolution, temperature, and cooling conditions.

The most stable progression of the photo peak position and thus of the MPPC gain during temperature changes was achieved with *high airflow* cooling. As shown in Figure 54 (right), the average energy resolution across a temperature range of 23.56°C to 31.91°C was 10.1±0.3 %, 10.2±0.3 %, and 10.4±0.1 % for *no airflow*, *medium airflow,* and *high airflow*, respectively.

Following the same methodology used to evaluate the energy-related performance parameters, the timing peak position and CRT were calculated to determine the stability of the timing measurements (Figure 55).

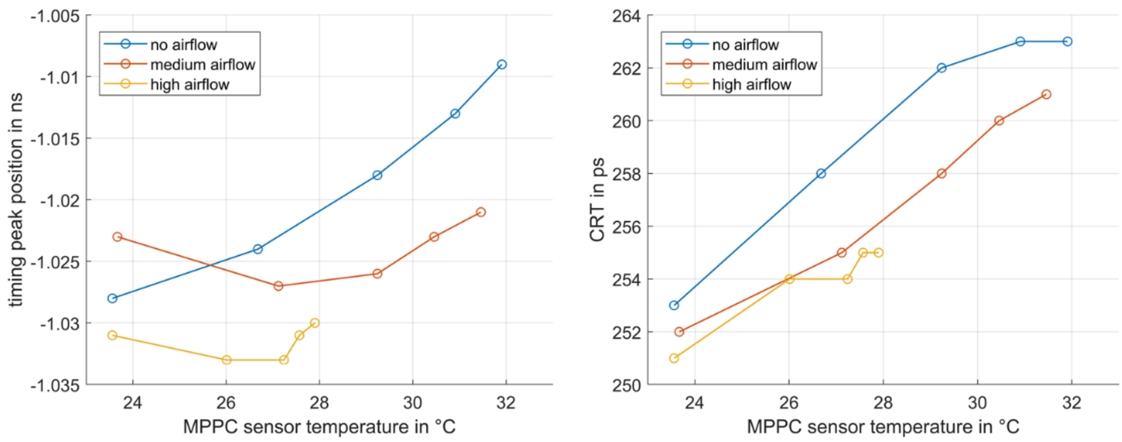

Figure 55: Left: Average timing peak position over temperature measured by the MPPC temperature sensor for three different cooling conditions. Right: The corresponding relationship between CRT, temperature, and cooling conditions.

High airflow cooling resulted in the smallest variation of the timing peak position, with a standard deviation of 0.001 ns (mean -1.032 ns), which increased to

0.002 ns (mean -1.024 ns) for *medium airflow* and was the highest at 0.008 ns (mean -1.018 ns) for *no airflow*. Accordingly, the best CRT with the smallest variation over temperature was achieved with *high airflow*, with 254±2 ps. The CRT degraded to 257±4 ps for *medium airflow* and further degraded to 260±4 ps with *no airflow*.

4.3 Discussion and Conclusion: Operation of the PET Modules

The PET modules' method for acquiring event data might cause a single PET event to be represented by multiple data events since multiple ASICs can be involved in the signal processing of a single PET event. A method that used the temporal differences between individual data events was used to merge the individual data events and thus regain the information concerning the original PET event. Section 4.2.1 showed that for the setup used in this thesis, a Compton time window of 8.75 ns yields reasonable results for the energy spectrum while maintaining a low probability that two independent PET events will be incorrectly merged.

Section 4.2.2 showed that correcting for the channel-dependent time skew improved the CRT by 91 ps. Furthermore, it should be noted that the peak position of the timing histogram T_{peak} in Figure 50 is -1.28 ns instead of 0.00 ns, which is the expected value of the setup when the radiation source is centered between the two detectors. According to the manufacturer, this offset is caused by a skew of the 50 MHz reference clock that measures the timing information. More specifically, this skew originates from the photonic integrated circuits and the long optical fibers of the reference clock line used for optical transmission (see section 6.3.1).

As section 4.2.3 demonstrated, the PET modules' components, such as the ASIC, TDC, FPGA, and MPPC, can be kept in a reasonable temperature range, with a maximum temperature of 36.1°C. The temperatures inside of the PET modules' shielding enclosures reach a steady state after approximately 100 minutes. However, the gain of the MPPC was affected by temperature changes, which was shown by the change of the photo peak position in the energy histogram with increased temperature. A new firmware provided by the manufacturer compensated for the temperature-dependent change in the MPPC's breakdown voltage, and thus the gain was stabilized, as demonstrated over a period of 21 hours.

The CRT and peak position of the timing histogram were examined with respect to temperature for three cooling conditions to determine the potential effects of temperature on the photo peak position and energy resolution (section 4.2.4). The photo peak position was 426.6±0.9 ns with *high airflow* cooling and decreased by 3.9 % in comparison to *no airflow* at 444.1±5.6 ns. In theory, the temperature compensation of the HVPS should set the bias voltage depending on the temperature and thus yield the same gain and photo peak positions for all measurements. An explanation for the effect of the cooling-dependent gain is illustrated in Figure 56.

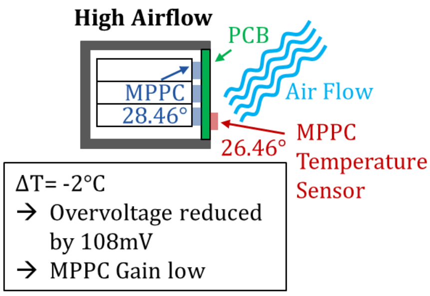

Figure 56: Simplified structure of the detector block showing the location of the MPPC and the MPPC temperature sensor. The real temperature of the MPPC cannot be measured, and therefore theoretical combinations of MPPC temperature and the temperature of the MPPC temperature sensor are shown. The difference between both temperatures ΔT is dependent on the airflow cooling, and the impact of the HVPS temperature compensation on the applied overvoltage and thus the gain is also illustrated.

The sensor that measured the temperature for the temperature compensation is located on the back of the PCB on which the MPPC is mounted. As such, the actual temperature of the MPPC differs from the measured temperature. Furthermore, the MPPC temperature sensor was exposed to the airflow, and thus the measured temperature was lower during *high airflow* cooling (26.46±1.77°C) than during *no airflow* (28.46±3.38°C). As the MPPC was encapsulated inside the aluminum housing, it was not directly exposed to the airflow. The difference in MPPC temperatures with and without cooling is assumed to be lower than for the temperatures recorded by the MPPC temperature sensor outside of the aluminum enclosure. As the difference between MPPC temperature and the temperature of the MPPC sensor is lower with *no airflow*, the overvoltage (the difference between bias voltage and breakdown voltage) is accordingly higher. A higher overvoltage results in a higher gain, explaining why the gain is higher without than with cooling.

However, regarding the results in section 4.2.4, the small variation of the photo peak over temperature for *high airflow* cooling is of more importance than the relatively small decrease in gain. This conclusion applies to the energy resolution as well, which was 10.1±0.3 % and thus lowest during *no airflow*. However, the standard deviation is smaller during *high airflow* cooling (10.4±0.1 %).

High airflow cooling resulted in the best CRT of 254±2 ps with the lowest temperature variation. It is assumed that temperature-related factors, such as an increased MPPC dark count rate, influence the accuracy of the PET events' time stamps and thus the CRT.

The variation of the timing peak position was lowest at -1.032±0.001 ns during *high airflow* cooling and increased to -1.018±0.008 ns during *no airflow*. As previously stated, the timing peak position is dependent on the optical transmission components, which were also located inside the shielding enclosure and thus benefited from airflow cooling. The timing peak was -1.018 ns instead of -1.280 ns, as reported in section 4.2.2, because the optical fibers, which are used for the clock transmission between the measurements, were changed.

In summary, cooling affects energy and timing-related measurements. Moreover, a *high airflow* cooling of 1.0 bar is favorable for this setup, as it results in the lowest variations (i.e., the greatest stability of the performance parameters).

5 Customized PET Detector Based on the Hamamatsu PET Electronics

The previous chapter described the structure and operation of the standard commercially available Hamamatsu C13500-4075LC-12 PET modules. The insights gained by these investigations with respect to the internal signal processing, data communication, and processing the PET event data enabled the construction of the customized detector, including all features of the standard PET modules, which is introduced in this chapter. The reason for this development was that the potential designs for the detectors for the breast PET insert were not commercially available by the manufacturer. As this chapter describes, the customized PET detector enables the readout of an individual MPPC and scintillator block configuration by interfacing with the signal processing board and back-end electronics of the PET modules.

It should be noted that the MPPC array for the customized PET detector has a dimension of $3\times3\,mm^2$ and a $50\times50\,\mu m^2$ pixel size to account for the dedicated assemblies required for a breast PET insert, whereas the standard MPPC array with $4\times4\,mm^2$ and $75\times75\,\mu m^2$ pixel size was used for the measurements discussed in Chapters 4 and 6.

First, this chapter describes the structure of the customized detector and the associated “32 Byte Compton firmware”, which was used to account for the modified hardware. Next, the chapter considers how crystal identification is performed by a light sharing approach and examines the underlying data processing. Furthermore, the chapter explains how the ASIC settings were adjusted to enable the readout of the customized MPPC array and scintillator configuration. Finally, the chapter examines how different ASIC gain settings with and without a light guide impact crystal identification and energy-related performance parameters, such as the energy resolution and photo peak position.

This chapter aims to demonstrate that a customized scintillator block and MPPC configuration readout is possible and to determine the optimum ASIC settings and light guide configuration.

5.1 Material and Methods

5.1.1 Structure of the Customized PET Detector

The PET modules' scintillator array initial crystal size of 4.14×4.14×20 mm^3 (see section 4.1.1) had to be decreased to enhance the spatial resolution of the PET detectors for the breast PET/MRI insert. The setup described in section 4.1.1 relied on a direct coupling, in which one scintillation crystal aligns with the area of one MPPC channel. However, the customized PET detector used a light sharing approach in order to minimize the number of MPPC channels (Figure 57).

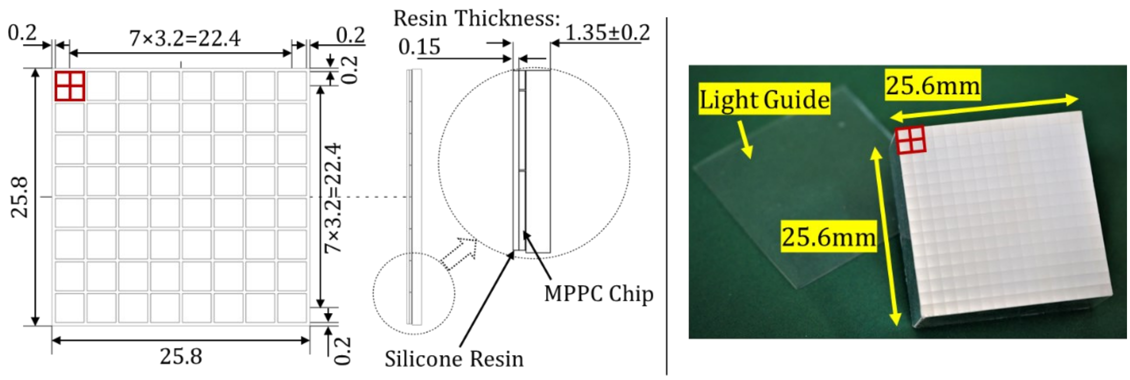

Figure 57: Left: Technical drawing of the MPPC array used for the customized PET detector with light sharing. Adapted and modified from [98]*. Right: Crystal block used for the customized PET detector with its corresponding dimensions and epoxy light guide.*

The 8×8 MPPC array S14161-3050HS-08 (Hamamatsu Photonics K.K. Hamamatsu, Japan) with a 50×50 µm^2 pixel pitch was coupled to a 16×16 scintillation array. The dimensions were designed in such a way that four scintillation crystals align with the 3.0×3.0 mm^2 photosensitive area of one MPPC channel. The scintillation array consists of 1.51×1.51×10 mm^3 LSO crystals with an Enhanced Specular Reflector (3M, St. Paul, MN, USA) for crystal separation. The MPPC array was placed next to the temperature sensor LM94021 (Texas Instruments, Dallas, TX, USA) on the MPPC adapter PCB (Figure 58). The 64 anodes of the MPPC array were connected with signal traces of matched lengths to the ASIC channels on the signal processing board. A common operation voltage of 40.71 V at 25°C (2.70 V above the breakdown voltage) was applied for all MPPC channels, as the variation of the breakdown voltage across the MPPC channels was 38.01 V±0.02 V.

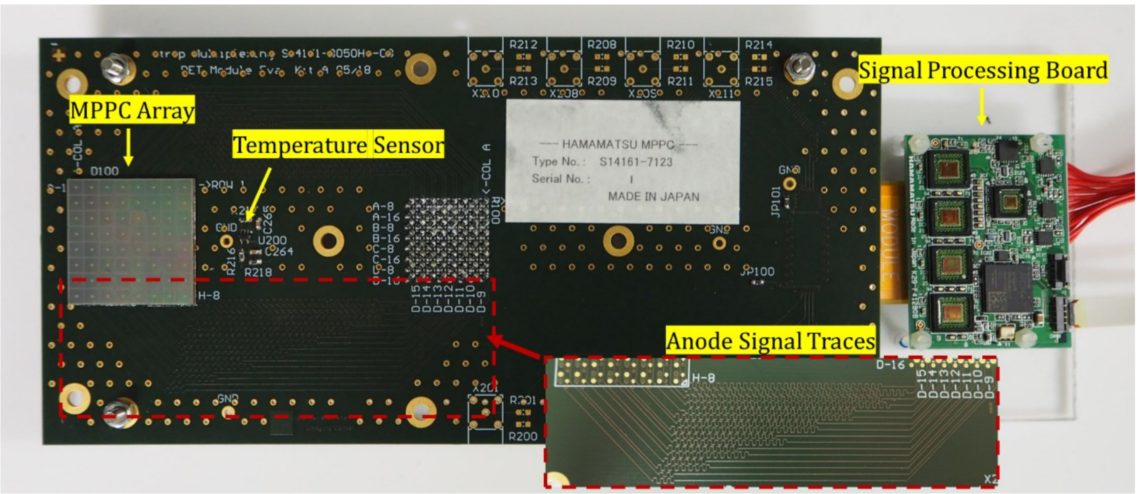

Figure 58: MPPC adapter PCB for the readout of a customized MPPC array and scintillation block configuration with the standard signal processing board.

Furthermore, the customized detector used a temperature compensation of 54 mV/°C, as described in section 4.1.6. As Figure 59 shows, the standard PM4.1 version of the PET modules (Hamamatsu Photonics K.K. Hamamatsu, Japan) was used for the signal processing board and the back-end electronics without any of the modifications described in section 4.1.1.

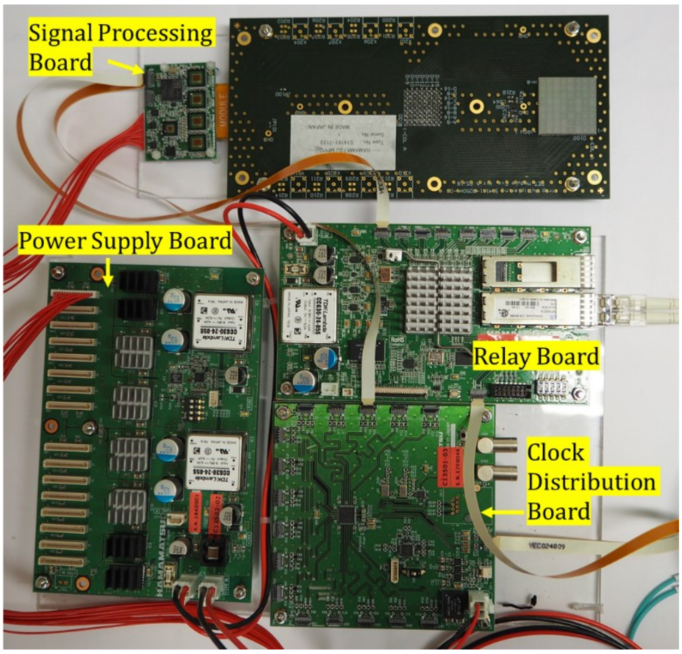

Figure 59: Standard PM4.1 back-end electronics with C13501-03 clock distribution board, C13502-02 power supply board, and C13503-01 relay board.

5.1.2 Event Data Processing for 32 Byte Compton Firmware for Light Sharing

Only the four highest energies of a single data event were stored with the "16 Byte Compton firmware" (see section 4.1.3). For the customized PET detector, a data format with 32 bytes was used instead, enabling the storage of all recorded energies of a data event from one ASIC (Figure 60).

■ **Compton firmware data format (Binary, 32 byte / event)**

Name	Size [bit]	Description
Blank	3 (MSB)	Blank
Board_No	10	Board number
TDC_ch	2	Channel of TDC
OVF_CT	32	1.28us resolution timing data (Over flow counter of TDC coarse)
TDC_coarse	10	1.25ns resolution coarse timing data
TDC_fine	7	15.0602ps resolution fine timing data
Blank	1	Blank
ch	7	MPPC channel (which has the highest energy value)
Energy1	8	Ch(TDC_ch x 18 + 1) 4ns resolution ToT energy data
Energy2	8	Ch(TDC_ch x 18 + 2) 4ns resolution ToT energy data
Energy3	8	Ch(TDC_ch x 18 + 3) 4ns resolution ToT energy data
Energy4~17	···	Ch(TDC_ch x 18 + 4~17) energy data
Energy18	8	Ch(TDC_ch x 18 + 18) 4ns resolution ToT energy data
Blank	40	Blank

Figure 60: Registers of a single data event for the data format of the 32 Byte Compton firmware [99].

Figure 61 demonstrates that a single ASIC can read out two neighboring rows on the MPPC array, using 16 of the 18 ASIC channels. For each data event, a column of 18 energy values for the channels of the specific ASIC is generated during binary data post-processing. A single PET event can generate multiple data events when the scintillation light of the incident gamma ray spreads across MPPC channels that are connected to different ASICs. This phenomenon is described in section 4.2.1, and the same optimized time window of 8.75 ns was used for the customized PET detector. The example data stream in Figure 61 illustrates which data events are within the assigned time window and therefore merged into a single PET event.

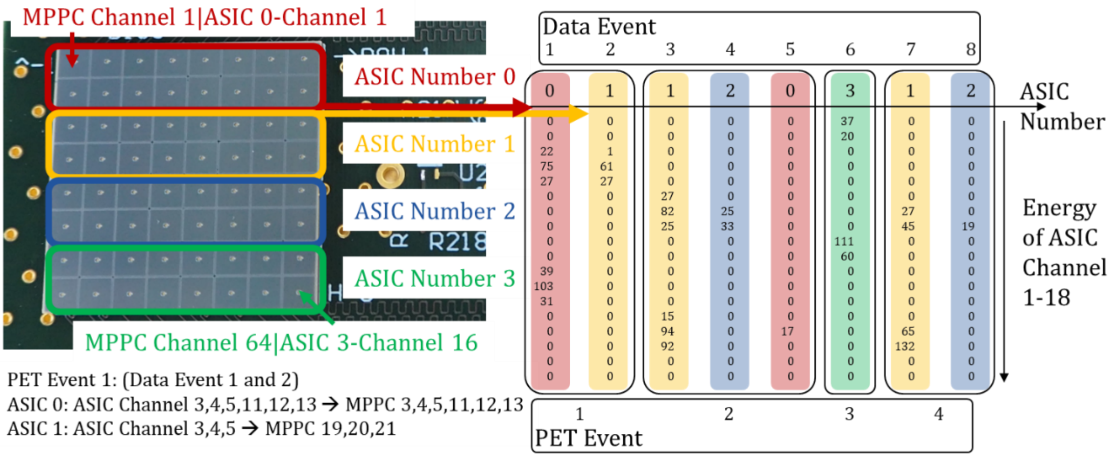

Figure 61: Assignment of the MPPC channels to the ASICs with an example data stream of eight data events with the corresponding energies values of the ASIC channels. The data events are merged into four PET events based on the difference in their time stamps.

The channel number of the MPPC $Ch_{MPPC}(i)$ for event i can be determined according to the following formula:

$$Ch_{MPPC}(i) = 16 * (n_{ASIC}) + Ch_{ASIC}(i) + 1\ ,$$

where n_{ASIC} is the number of the ASIC (from 0 to 3) and $Ch_{ASIC}(i)$ is the corresponding channel of the ASIC connected to the MPPC (from 0 to 15).

5.1.3 Crystal Position Identification

As previously described, four crystals share the photosensitive area of one MPPC channel. Using the light output directly below the crystal's surface makes it impossible to determine in which of the four crystals the interaction occurred. Thus, an epoxy layer between the bottom surface of the scintillation crystals and the MPPC functions as a light guide for the scintillation photons. This layer enables the scintillation photons to form a light cone that spreads across multiple MPPC channels (Figure 62).

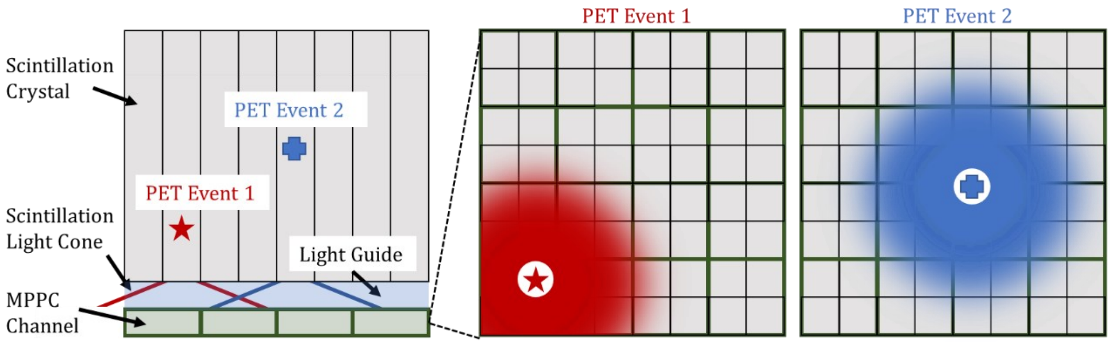

Figure 62: Left: Schematic illustration of the interaction of the gamma rays from two different PET events inside the crystal block. Right: Light spread of the scintillation photons across multiple MPPC channels, with the center of the light cone located at the position of the crystal where the interaction with the incident gamma ray occurred.

The positions of the fired MPPC channels and the amount of energy deposited in each channel allow for the 2D positioning of the initial gamma ray interaction. First, the x position of a fired MPPC channel x_{MPPC} is calculated according to the formula

$$x_{MPPC}(Ch_{MPPC}) = (Ch_{MPPC} - 1) \ mod \ 8 \, ,$$

where the MPPC channel $\mathrm{Ch_{MPPC}}$ is calculated by the equation presented in section 5.1.2. The expression “fired MPPC” indicates that a sufficient number of photons hit the MPPC and generated recorded energy data for that MPPC. Accordingly, the y position of the fired MPPC channel is calculated by

$$y_{MPPC}(Ch_{MPPC}) = \lfloor (Ch_{MPPC} - 1)/8 \rfloor \, .$$

With these calculated x and y positions, it is possible to map a single fired MPPC to the coordinate system (Figure 63 left).

Furthermore, to obtain the position of the crystal, it is necessary to calculate the fractional position in this coordinate system by using the positions of all fired MPPCs and their corresponding recorded energies for one PET event. In addition, the total energy E_{total} of a single PET event i is calculated according to

$$E_{total}(i) = \sum_{j=1}^{n} E(j) \, ,$$

where $E(j)$ is the energy acquired by a single fired MPPC, and j and n represent the total number of fired MPPCs.

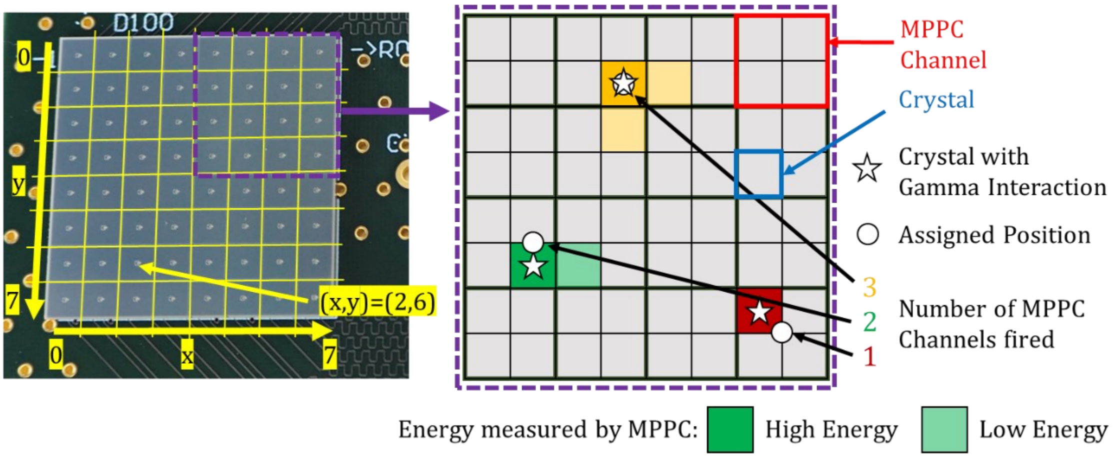

Figure 63: Left: X and y coordinate system for positioning a PET event in the MPPC array of the customized PET detector. Right: Schematic illustration of three independent and subsequent gamma interactions in three different crystals, as represented by the stars. Examples are given for events where the energy and light spread of the detected scintillation photons fire 1 (red), 2 (green), or 3 (orange) MPPC channels. The intensity of the color corresponds to the energy measured by the fired MPPC channel. The circle represents the weighting of the different fired MPPC channel positions for each event with the corresponding measured energy results in the assigned position.

Finally, all of the positions of a single PET event recorded on the MPPC channels were weighted with their respective energies. Normalizing the summed weighted MPPC x positions with the total energy yields the x position of the PET event i, as described by the formula

$$x(i) = \frac{1}{E_{total}(i)} \sum_{j=1}^{n} x_{MPPC}\big(Ch_{MPPC}(j)\big) * E(j)\ .$$

Accordingly, the y position of the PET event is calculated by the formula

$$y(i) = \frac{1}{E_{total}(i)} \sum_{j=1}^{n} y_{MPPC}\big(Ch_{MPPC}(j)\big) * E(j)\ .$$

For this setup, the light cone from the scintillation crystals spreads across multiple MPPC channels. However, the number of photons might be too low to record energy data. The number of photons in the MPPC channels decreases as the distance to the center of the light cone increases and for events with a low energy of the incident gamma ray. The number of fired MPPC channels varies for each

PET event; therefore, the minimum number of fired MPPC channels necessary to extract the x and y position of a PET event must be determined. Figure 63 (right) shows a schematic illustration of a 4×4 MPPC array with an 8×8 crystal array as well as three individual PET events.

For the first event (red), it is assumed that only a single MPPC channel was fired. The assigned position for this event would be the center of the MPPC channel below the crystal. This would also be the case for the other three crystals placed upon that MPPC channel. Thus, it is not possible to accurately determine the crystal's position (i.e., crystal identification) with only a single MPPC channel fired.

The same holds true for the second PET event (green), where only two MPPC channels are fired. In this example, it is only possible to identify the x position of the PET event.

To identify the y position, three MPPC channels must be fired, as shown for the third PET event (yellow). However, if three MPPC channels located on the same axis are fired, it is not possible to accurately determine the crystal's position. Therefore, a minimum of three fired MPPC channels that are not all are located in the same row or column are necessary to identify the crystal's position. With the customized PET detector used in this thesis, the majority of the recorded events resulted in more than three fired MPPC channels, thus fulfilling the criteria for crystal position identification. However, as the remaining events could not be assigned to a crystal position, they could not be used and were thus discarded. The ratio between valid (i.e., a crystal identification is possible) and invalid events depends on the PET modules' gain settings as well as the scintillation crystals and light guide (see section 5.2.4).

5.1.4 Single Detector Measurement Setup

As Figure 64 shows, the customized PET detector setup was operated in a light tight enclosure, which was temperature stabilized at 20±0.3°C. The scintillation crystal block (described in section 5.1.1) was used and wrapped with polytetrafluoroethylene tape, not covering the top and bottom surfaces of the crystal block. For the measurement setup, a 340 kBq Na-22 point source was centered to the top surface of the crystal block at a distance of 75 mm. In the configuration without a light guide, silicone optical grease (BC-630, Saint-Gobain Crystals, Hiram, OH, USA) was used to couple the scintillation crystal block and the MPPC array.

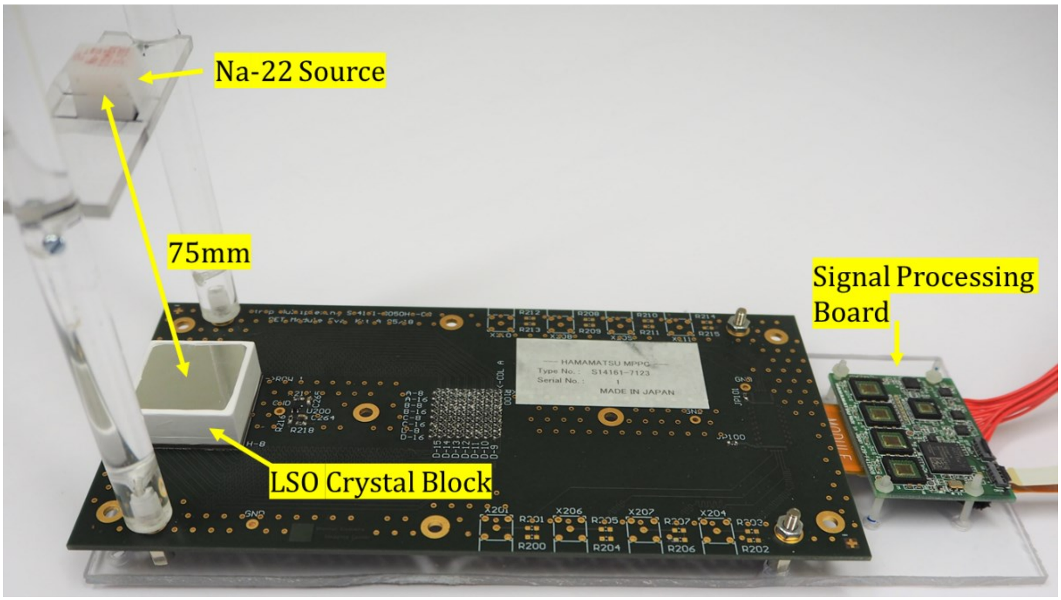

Figure 64: Measurement setup for the customized PET detector based on the Hamamatsu PET electronics.

The second test setup used a customized light guide made from a silicone rubber compound (RTV615, Momentive, Waterford, NY, USA) with the dimensions 25.6×25.6×0.5 mm^3 (Figure 57 right).

The performance of the PET electronics was adjusted with the register settings in the *PM4AsicCtrl for PM4.1 Ver. 1.0.5.0* software (Hamamatsu K.K., Hamamatsu, Japan). The gain of the ASICs on the signal processing board was adjusted by changing the *LG_PullUp* register. The recorded data events were preprocessed by the FPGA on the signal processing board, where the setting of the *Energy Range Minimum* register was adjusted to the lowest possible value of 1. All events with an energy ToT value equal to or higher than 4 ns were recorded in order to avoid discarding low energy events from the event data stream. Furthermore, in the FPGA settings, the *Time Info Comparison Maximum* register was changed to a value of 400. This register set the maximum allowed temporal duration between the first energy signal and the following energy signals of the fired MPPC channels on a single ASIC, thus mapping the signals to a single data event. If not otherwise stated, 1×10^6 single data events were acquired for each measurement. After the data events were merged to the PET events according to the 8.75 ns window, they were discriminated by the number of fired MPPCs per PET event. Only events with more than two MPPCs fired with the MPPCs not being in the same row or column were used for further evaluation.

A 2D histogram of the x and y positions was then generated, calculated as described in the previous section. This 512×512 pixel histogram, known as a flood map, allowed for crystal identification. Figure 65 demonstrates how the flood map is separated into sections corresponding to the positions of the individual crystals by Voronoi cells.

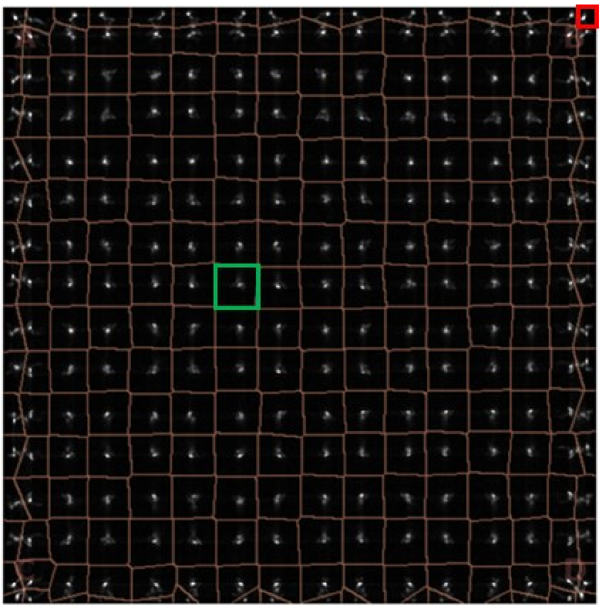

Figure 65: 2D histogram of x and y positions for the 16×16 scintillation block and Voronoi cells (orange), defining the area of each crystal. The area of a center and corner crystal are marked in green and red, respectively.

Finally, using the x and y positions, the event can be pinpointed to a specific Voronoi cell and therefore to a specific crystal. The position profile along one crystal row and one crystal column was evaluated to determine how accurately crystals were identified in the different configurations (Figure 66 left). The crystal positions were manually mapped to the brightest spots along the specific row and column, and a band with a width of nine pixels was used along the interpolated path between the crystal positions. The mean of the nine pixel values (i.e., the number of counts) for each x and y position was calculated for the row and column, respectively. The corresponding position profile graphs were used to calculate the peak-to-valley ratio (PVR), a figure that verifies the crystal identification's accuracy. In this way, the mean ratio of each peak and its two neighboring valleys was calculated. For peaks corresponding to the corner crystal, only one neighboring valley exists and, therefore, only one valley was used to calculate the PVR.

An evaluation of the energy values for all events of each crystal is obtained through the generation of a histogram with a bin width of 4 ns visualizing each energy spectrum. A Gaussian fit was used to identify the photo peak position and determine the FWHM energy resolution (ERES) for each crystal.

5.2 Results

5.2.1 Flood Maps and Total Block Energy Histograms of Discriminated Events

As section 5.1.3 stated, events in which less than three MPPCs are fired are not suitable for precisely identifying the crystal's position. Therefore, only events with more than two fired MPPCs were used to generate the flood map in Figure 66 (left).

Figure 66 (right) shows the energy histogram of each PET event acquired using the configuration with no light guide and the lowest gain setting of *LG_PullUp*=0.

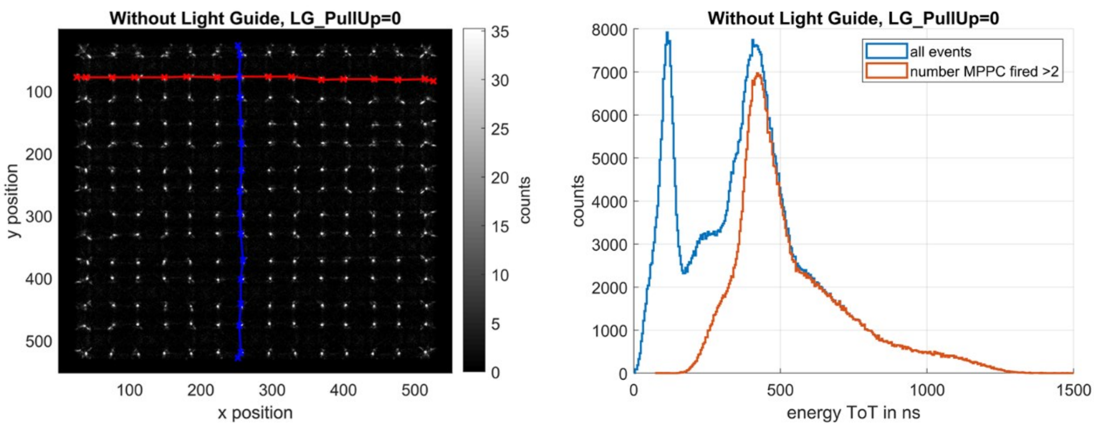

Figure 66: Configuration without light guide and gain register LG_PullUp=0. Left: 2D position histogram flood map for crystal identification. Right: Total block energy spectrum of all events and events with more than two MPPCs fired.

The corresponding discriminated energy spectrum in Figure 66 (right) demonstrates that multiple MPPCs are not fired for low energy events in particular. With the low gain setting, a noticeable number of events needed to be discarded (see section 5.2.4 for a detailed comparison of the fraction of qualified PET events). The flood map reveals that crystals at the outer rows and columns have fewer events than the other crystals. This finding is demonstrated by the fainter brightness of the spots located at the outer positions of the 2D position histogram.

By increasing the gain with a setting of *LG_PullUp*=1, the outer crystals also had an increased number of counts (Figure 67 left).

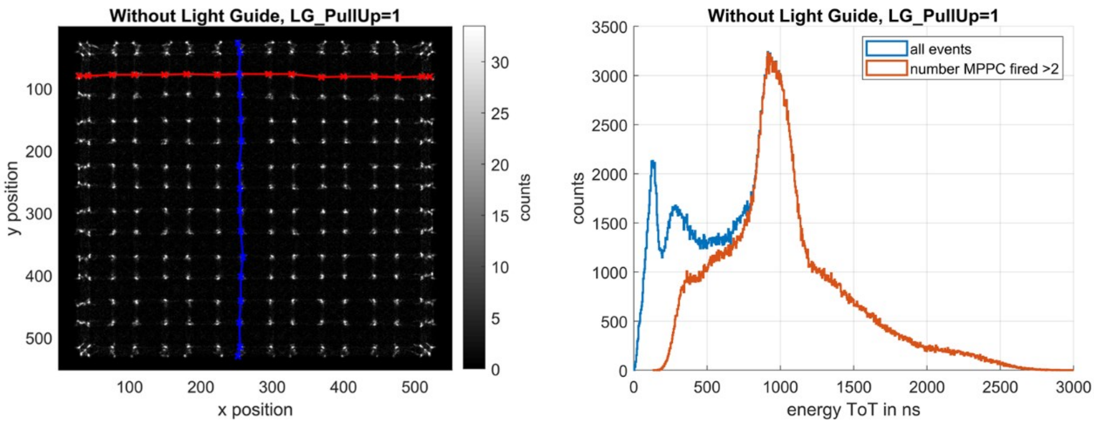

Figure 67: Configuration without light guide and gain register LG_PullUp=1. Left: 2D position histogram flood map for crystal identification. Right: Total block energy spectrum of all events and events with more than two MPPCs fired.

With an increased gain, the outer MPPCs had a higher mean number of MPPCs fired per event, and as such, fewer events for the outer crystals were discarded. This concept is also shown in Figure 67 (right), in which only a small fraction of low energy events did not result in at least two fired MPPCs.

Further increasing the gain setting to *LG_PullUp*=2 led to no significant improvements in the flood map in Figure 68 (left). Instead, crystals at the outer rows and columns were prevented from separating from their neighboring crystals located closer to the center. Section 5.2.2 presents a quantitative analysis to explain the process of crystal identification for each setup in more detail.

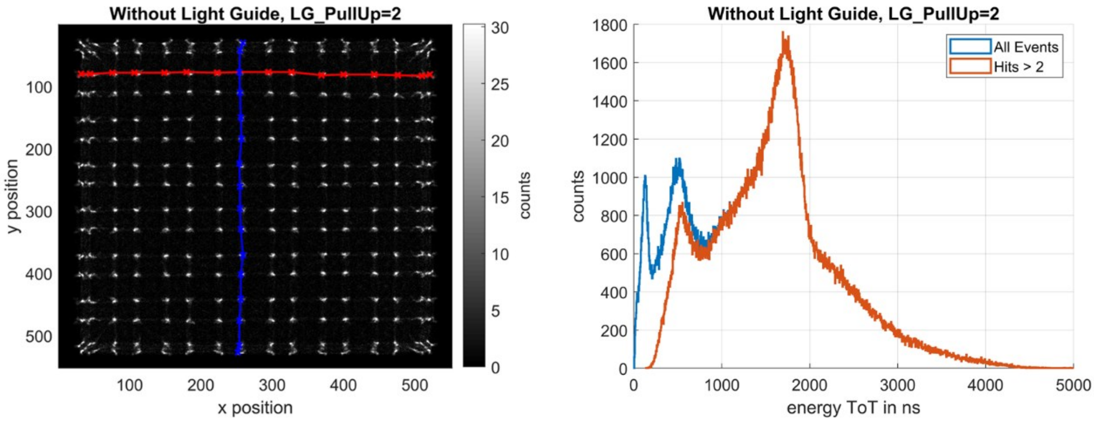

Figure 68: Configuration without light guide and gain register LG_PullUp=2. Left: 2D position histogram flood map for crystal identification. Right: Total block energy spectrum of all events and events with more than two MPPCs fired.

It should be noted that the total block energy spectra for the different *LG_PullUp* values appear to be determined by a larger number of events for the low *LG_PullUp* values (e.g., Figure 66), as the maximum y-axis count value is 8000 for *LG_PullUp*=0 in comparison to a maximum y-axis count value of 1800 for *LG_PullUp*=2 (Figure 68). The reason for this discrepancy is that the measured ToT energy values increase with the *LG_PullUp* gain register value, which is shown as the photo peak shifts towards higher ToT energy values for higher values of *LG_PullUp* while the granularity of the ToT measurement remains at 4 ns. As such, the measured energies of the events are distributed over a wider range in the energy spectra acquired with higher *LG_PullUp* values. As the bin width of the histograms remained constant at 4 ns for all measurements, the number of bins increased for higher *LG_PullUp* values, and the number of counts in each bin decreased accordingly.

The use of the light guide results in an optimized flood map (Figure 69 left), which is comparable to the same gain setting of *LG_PullUp*=1 with no light guide. Therefore, a closer investigation was performed to identify the optimal settings and configuration for the customized PET detector readout. This investigation is discussed in the following sections.

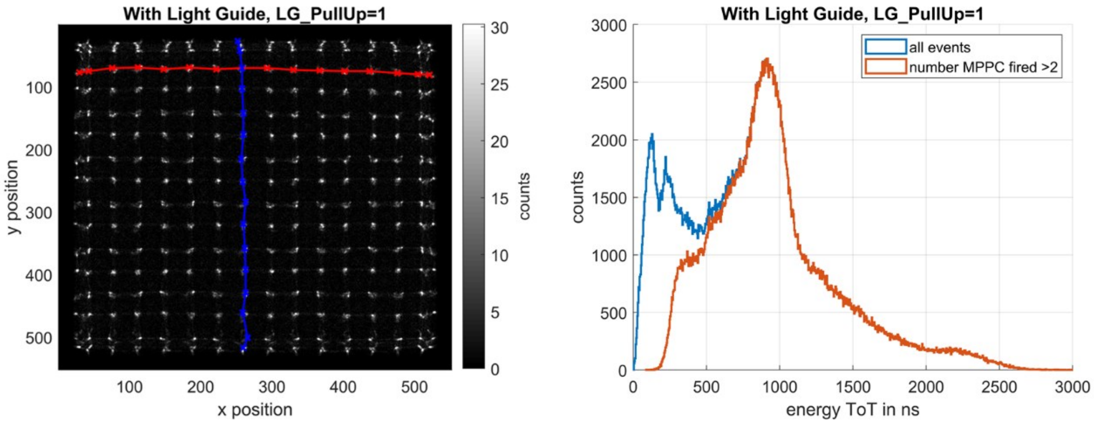

Figure 69: Configuration with 0.5 mm-thick RTV615 light guide and gain register of LG_PullUp=1. Left: 2D position histogram flood map for crystal identification. Right: Total block energy spectrum of all events and events with more than two MPPCs fired.

5.2.2 Position Profiles of Crystal Row and Column

As the flood maps in Figure 66–Figure 69 (left) show, crystals at row three (red) and column eight (blue) were analyzed and also evaluated according to their position profile. Figure 70 (left) demonstrates that for a low gain setting of *LG_PullUp*=0, the position profiles of this column and row reveal 14 and 15 distinct peaks, respectively.

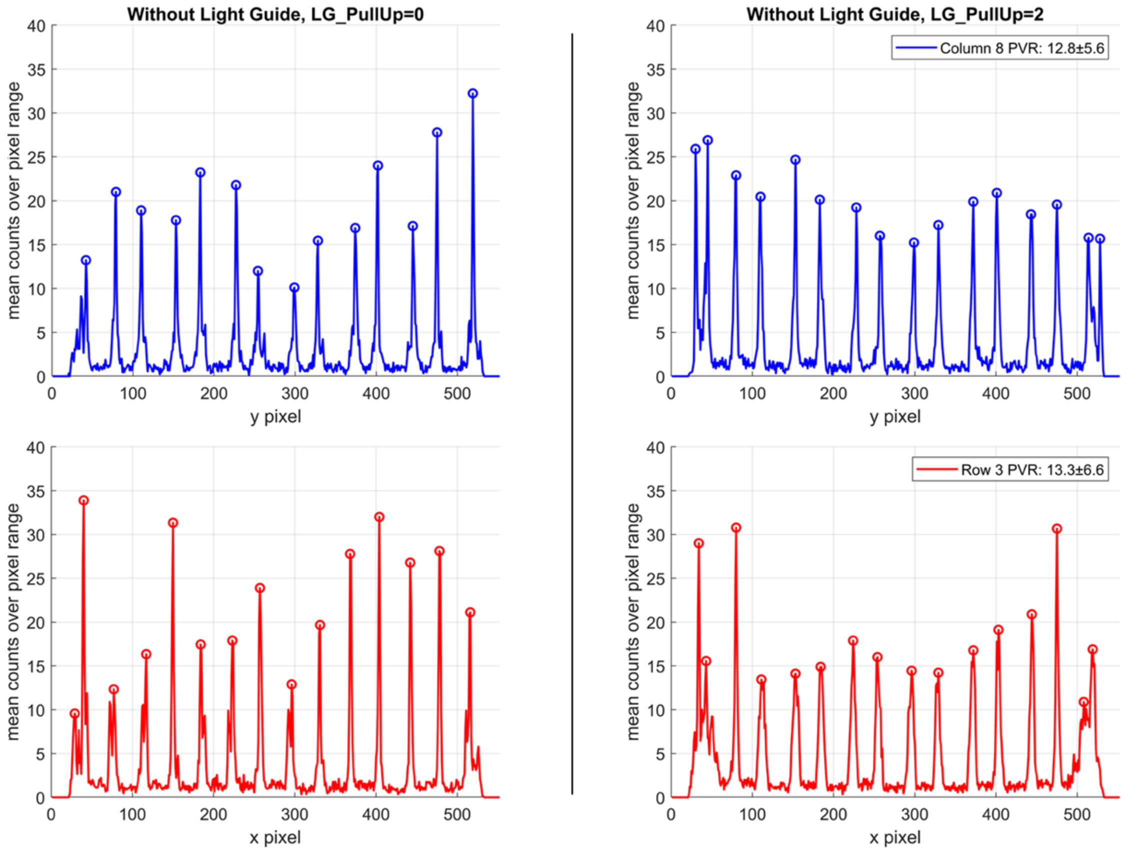

Figure 70: Position profiles of column 8 (top, blue) and row 3 (red, bottom) without light guide. Left: Low gain setting of LG_PullUp=0 (no PVR was determined, as not all 16 crystals in the column and row could be identified). Right: High gain setting of LG_PullUp=2.

For a detailed identification of each crystal, 16 peaks should be identified, as Figure 70 (right) shows for the high gain setting of *LG_PullUp*=2. This finding was also verified by a high PVR of 12.8±5.6 and 13.3±6.6 for the row and column, respectively.

This high PVR was maintained at 16.9±7.2 and 13.0±6.4 even at a medium gain setting of *LG_PullUp*=1 with no light guide (Figure 71 left). Furthermore, the separation between the two peaks at the edge of the row was better for the medium gain setting than the high gain setting. The use of the light guide (Figure 71 right) also yields accurate crystal identification. However, compared without a light guide, the PVR of the column and row slightly decreased to 13.4±5.6 and 10.9±5.3 for the column and row, respectively.

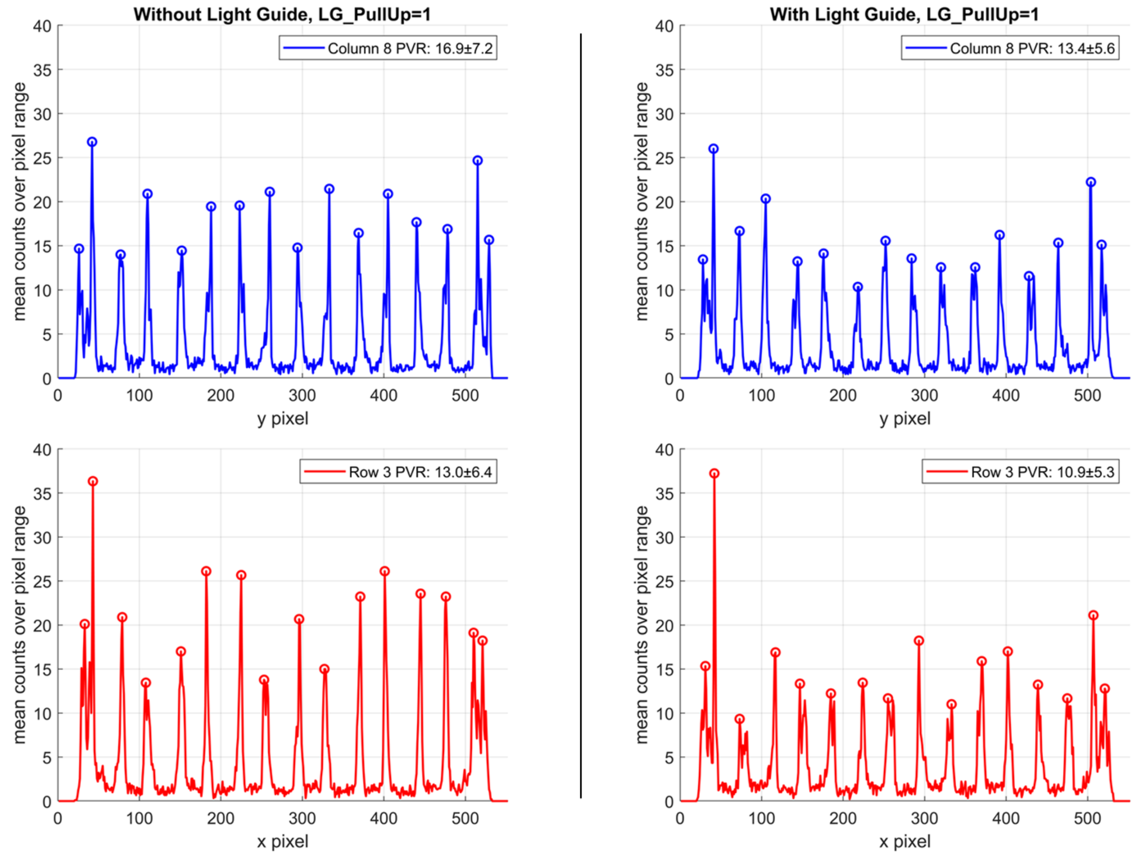

Figure 71: Position profiles of column 8 (top, blue) and row 3 (red, bottom) with a medium gain setting of LG_PullUp=1. Left: Without a light guide. Right: With a 0.5 mm RTV615 light guide.

5.2.3 Single Crystal Energy Spectra for Different ASIC Gain Settings and Light Guide Configurations

Figure 72 depicts the energy spectra of one crystal at the center and one at the edge of the crystal block using different gain settings and light guide configurations.

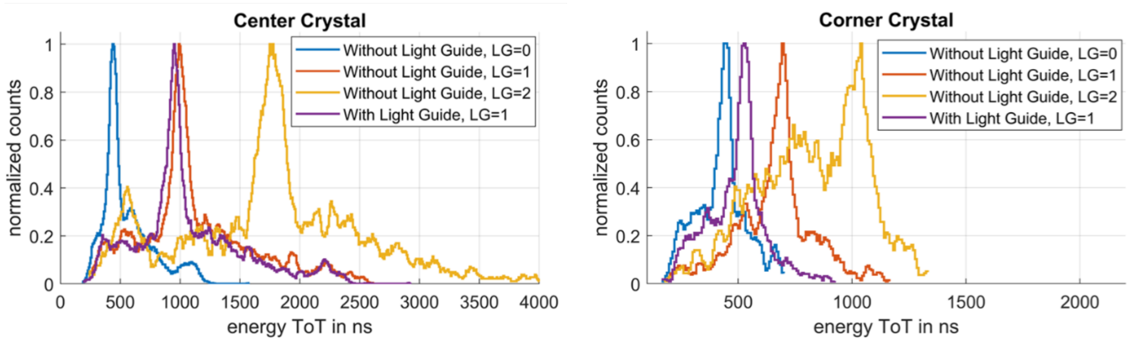

Figure 72: Single crystal energy spectra for different light guide and ASIC gain settings (register LG_PullUp abbreviated by LG). Left: Comparison of the energy spectra of a center crystal. Right: Comparison of the energy spectra of a corner crystal.

As expected, the energy spectra of the center crystal demonstrated increased photo peak energy with an increased ASIC gain setting. The resulting photo peak position without the light guide was 438.1 ns, 998.1 ns, and 1768.1 ns, with corresponding *LG_PullUp* values of 0, 1, and 2, respectively. At a gain setting of 1, the light guide caused the photo peak position to decrease slightly to 946.3 ns.

A direct comparison of the energy spectra of the center and the corner crystals demonstrates that the energy spectra of the corner crystals shift towards lower energy values. This finding can be quantified by observing the photo peak positions of 998.1 ns and 686.7 ns (*LG_PullUp*=1, no light guide), 946.3 ns and 524.5 ns (*LG_PullUp*=1, with light guide), and 1768.1 ns and 1012.9 ns (*LG_PullUp*=2, no light guide) for the center and the corner crystals, respectively. As expected, crystals at the edge or corner of a block detect fewer scintillation photons. In general, a smaller number of the scintillation photons at the corner of the scintillation block encounter the MPPC surface, thus triggering fewer MPPC pixels than the crystals at the center of the block. The light guide increases this effect, and fewer scintillation photons of the scintillation photon cone strike the photosensitive area of the MPPCs, as shown in Figure 62. Thus, smaller energy values were acquired in comparison to the setup without the light guide.

The photo peak position with no light guide and a setting of *LG_PullUp*=0 was 438.1 ns and 439.4 ns for the center and the corner crystal, respectively. It was expected that the photo peak position would be higher for the energy histogram of the center crystal than for the corner crystal. However, for a center crystal at this low gain setting, the threshold to trigger an MPPC is also so low that the spread of the light cone only triggered a small number of MPPCs. The average number of MPPC hits was calculated for an energy window of 5 % around the photo peak position, resulting in an average number of hits of 3.33 and 3.31 for the center crystal and the corner crystal, respectively. As a comparable number of MPPCs contribute to the energy signal for the corner and center crystals, it is reasonable that the corresponding energy signals (i.e., photo peak positions) are also comparable.

5.2.4 Overview of Performance Parameters for Different ASIC Gain Settings and Light Guide Configurations

Table 4 lists the mean number of fired MPPCs per event without a light guide and with *LG_PullUp* values of 0, 1, and 2 as 3.2±1.7, 5.0±2.5, and 6.7±3.3, respectively.

Table 4: Performance parameters for different ASIC gain settings and light guide configurations. The mean value and standard deviation of the number of fired MPPCs per event are listed, as well as the mean value and standard deviation of the individual crystal photo peak position in the energy histogram with the corresponding FWHM energy resolution and the peak-to-valley ratios (PVR). Events with more than two fired MPPCs are considered valid events. The best and worst performance parameters are marked in green and red, respectively.

LG_PullUp	Light Guide	Number fired MPPCs	Valid Events [%]	Photo Peak [ns ToT]	Energy Resolution [%]	PVR (Column 8)	PVR (Row 3)
0	none	3.2±1.7	61.2	433.8±34.1 *	16.2±3.7 *	-	-
1	none	5.0±2.5	80.5	942.3±96.8	15.9±2.8	16.9±7.2	13.0±6.4
2	none	6.7±3.3	88.1	1615.9±212.6	16.4±2.5	12.8±5.6	13.3±6.6
1	0.5 mm RTV615	5.2±2.7	81.1	869.3±130.5	16.2±2.9	13.4±5.6	10.9±5.3

**) For LG_PullUp=0, no identification of the outer column and row crystals was possible. The photo peak position and energy resolution are calculated based on the remaining 196 crystals.*

The number of fired MPPCs per event increased with the increase in the *LG_PullUp* settings because, for a high gain, fewer photons are needed to overcome the threshold to trigger an event. The number of valid events, which can be used to generate a flood map and can be mapped to a single crystal, also increased with the ASIC's gain, as demonstrated by the number of valid events for *LG_PullUp* settings of 0,1, and 2 at 61.2 %, 80.5 %, and 88.1 %, respectively. The number of valid events is comparable for the configurations with and without the light guide, at 81.1 % and 80.5 %, respectively.

Table 4 reveals that the photo peak position approximately doubles with each increase of *LG_PullUp* by a value of 1, as the mean photo peak positions are 433.8±34.1 ns, 942.3±96.8 ns, and 1615.9±212.6 ns for *LG_PullUp* settings of 0, 1, and 2, respectively. The photo peak position at a gain of 1 was higher for the setup without a light guide and showed less variation than the setup with a light guide, which corresponded to a photo peak position of 869.3±130.5 ns.

The energy resolution for the configuration without a light guide was 16.2±3.7 %, 15.9±2.8 %, and 16.4±2.5 % for *LG_PullUp* values of 0, 1, and 2, respectively. The setup with a light guide and *LG_PullUp*=1 had a comparable energy resolution of 16.2±2.9 %. Hence, the energy resolutions were approximately in the same range for all configurations; however, the best measured energy resolution of 15.9±2.8 % was achieved with a medium gain setting of *LG_PullUp*=1 and no light guide.

Section 5.2.3 reported that when *LG_PullUp* was set to 0, the crystals at the edges of the scintillator block could not be resolved, and as such no PVR was calculated. For the remaining measurements with an *LG_PullUp* value of 1 or 2, high PVR values were achieved, as described in section 5.2.3 and shown in Table 4. However, the best PVR value, and thus the greatest possibility of crystal identification, was achieved by the configuration with no light guide and a setting of *LG_PullUp*=1, with a PVR of 16.9±7.2 and 13.0±6.4 for column 8 and row 3, respectively.

5.3 Discussion and Conclusion

This chapter considered the readout of a custom configuration using a 3.0 mm×3.0 mm MPPC, a scintillation crystal block with a crystal size of 1.51×1.51×10 mm^3, and the Hamamatsu PET electronics. The “32 Byte Compton firmware”, which stores the energies of all of the MPPC array’s channels for each PET event, was used to perform a light sharing readout method for crystal identification. In addition, the threshold in the FPGA, which must be exceeded in order to record the energy of a data event, was set to the lowest possible value of 1. This was done in order not to discard low energies that correspond to photons at the spread of the light cone and are required for position identification via light sharing.

When the gain of the ASIC was too low (i.e., a register *LG_PullUp* of 0), it was not possible to resolve the crystals at the edge of the scintillation block, as the amplitudes of the analog signals from this low scintillation photon yield were too low to trigger the corresponding MPPCs. However, with the medium and high gain settings of the ASIC (i.e., an *LG_PullUp* of 1 and 2), it was possible to identify every scintillation crystal position in the corresponding flood maps. This finding was confirmed by the PVR values of a representative column and row of 16.9±7.2 and 13.0±6.4 and 12.8±5.6 and 13.3±6.6 for *LG_PullUp* settings of 1 and 2, respectively.

In addition, the photo peak position of 942.3±96.8 ns for the medium gain setting (*LG_PullUp*=1) is much lower than the photo peak position of 1615.9±212.6 ns for the high gain setting (*LG_PullUp*=2). This can be translated to an average analog signal that is approximately twice as long for the high gain setting. To avoid an increased dead time and thus maintain a high count rate performance, the medium gain setting of *LG_PullUp*=1 is preferred for the MPPC and scintillator configuration.

Using a 0.5 mm-thick epoxy light guide did not result in any performance improvements compared using optical grease to couple the scintillator block and the MPPC array. This finding was quantitatively confirmed by the fraction of valid events of 81.1 % and 80.5 %, the photo peak position of 869.3±130.5 ns and 942.3±96.8 ns, and the energy resolution of 16.2±2.9 % and 15.9±2.8 % for the setup with and without the light guide, respectively. Furthermore, slightly decreased PVR values of 13.4±5.6 (column) and 10.9±5.3 (row) were observed for the setup with a light guide in comparison to the values of 16.9±7.2 (column) and 13.0±6.4 (row) for the setup without a light guide. Based on these observations and the fact that a light guide leads to a more complex assembly, the configuration without a light guide is more optimal.

It should be noted that the number of valid events with respect to all recorded events is 80.5 % for the optimum setting for the measurement with *LG_PullUp*=1 and no light guide. The remaining 19.5 % of the acquired data events were not used to further process the PET events, as they could not be assigned to a single crystal; however, they still contributed to the data rate. Figure 67 (left) demonstrates that events with fewer than three triggered MPPC channels have lower energies than the photo peak position. Therefore, the true coincident events used for PET image reconstruction will not be affected. However, if a scatter correction is implemented based on this firmware and detector configuration, further evaluation will be required to determine whether a scatter correction of the low energy events would contribute to improved sensitivity. The data rate could be lowered by preprocessing the event data in the FPGA, which discards low energy events before data transmission to the relay board.

Finally, it should be stated that the timing performance has not yet been observed, as only one detector was available at the time the measurements were taken for this thesis. However, the setup can be extended to use a second detector for coincidence measurements. Furthermore, the ability of this customized setup to make correct time stamps has already been proven, as merging the data events to the PET events requires accurate event time stamps.

6 MRI Compatibility of the PET Modules

The previous chapter demonstrated the readout of a custom configuration using the MPPC array and the scintillation crystal block, which is a prerequisite for using the Hamamatsu PET modules to develop a breast PET/MRI insert. Furthermore, it is important to avoid mutually distorting the operations of the PET modules and the MRI scanner. However, MRI compatibility could not be achieved with the commercially available version of the PET modules, as they were not designed to operate inside an MRI scanner. Hence, several modifications to the PET modules and corresponding shielding were made.

This chapter identifies critical aspects of the PET modules' operations that impede MRI compatibility and consequently discusses possible solutions for enabling the distortion-free operation of the PET and the MRI scanner. In order to verify the MRI compatibility, a comprehensive analysis of the PET event data was performed, and special MR test sequences were used to evaluate the performance of the MRI scanner. Multiple modifications to the PET system, including the connection between the PET modules, RF shielding, and filter, were implemented to achieve full MRI compatibility.

This chapter will focus on how each modification separately impacts MRI compatibility. As such, the results of the different test setups in each section were used to implement an improved iteration of the PET modules in the successive section. Along with improving the physical components, the test procedures and data analysis were also refined. Some of the measurements and analyses described in the first sections were performed qualitatively to identify MRI incompatibility, which was sufficient for deciding how the PET modules should be further modified. However, all of the analyses and evaluations were performed quantitatively to verify the final versions of the PET modules and are given at the end of this chapter.

It should be noted that the customized PET detector described in section 5.1.1 was not used for the MRI compatibility tests, as the development of the detector and the work towards the MRI compatibility were performed at the same time. However, as MRI compatibility is not dependent on the configuration of the MPPC array and scintillation crystals, it is acceptable to use the standard MPPC array with a 4 mm×4 mm and 75×75 μm^2 pixel size and 6×12 LFS scintillation crystals 4.14×4.14×20 mm^3 in size, as described in section 4.1.1. Whereas the MPPC array and scintillation crystal block remained the same for all measurements this chapter discusses, the remaining hardware of the PET modules was changed. In sections 6.1 and 6.2, a version of the PET modules was used with a signal transmission via copper cables, which was introduced in section 4.1.1. In the remaining sections, a version of the PET modules with improved MRI compatibility and a signal transmission via optical fibers was used, as described in section 6.3.1. An overview of the various MRI compatibility setups and corresponding tests is illustrated on the following page.

Setup	A	B	C	D	E	F
Changes to Previous Setup	• None	• Back-end Electronics Outside MRI Scanner Room	• Data Transmission Via Optical Fiber • Aluminum Shielding	• Moderate RF Shielding (Copper 18µm) • Second Module for Coincidence Measurements	• Improved RF Shielding	• Filter at the Front-End • Clock Synchronization • Breast Coil
Number of PET Modules	2	2	1	2	2	2
Data Transmission	Copper Cables	Copper Cables	Optical Fibers	Optical Fibers	Optical Fibers	Optical Fibers
Shielding	None	Copper 35 µm (not soldered)	Aluminum 2 mm	Copper 18 µm (not soldered)	Copper 18 µm (soldered)	Copper 18 µm (soldered)
Filter	None	None	Wall of the MRI Room	Wall of the MRI Room	Wall of the MRI Room	Wall of the MRI Room + Front-End
RF Coil used	None	Body Coil (Transmit+Receive)	Body Coil (Transmit+Receive)	Body Coil (Transmit+Receive)	Body Coil (Transmit+Receive)	Body Coil (Transmit) + Breast Coil (Receive)
Time Skew Correction	no	no	no	yes	yes	yes

MRI→PET	• Static Field (Functionality) ✗	• Static Field (Quantitative) ✓
		• RF Distortion (Functionality) ✗
		• Gradient Distortion (Functionality) ✗
			• Gradient Distortion (Functionality) ✓
			• RF Distortion (Functionality) ✓
			• RF Distortion (Event Time Stamps) ✗
				• Gradient Distortion (Quantitative) ✓
				• RF Distortion (Event Time Stamps) ✗
					• RF Distortion (Event Time Stamps) ✗*)
					• RF Distortion (Event Energy) ✗
						• RF Distortion (Quantitative) ✓
						• RF Distortion (detailed Investigation in RF On Phase):
						  • Event time stamps ✓
						  • Event energy ✓
						  • Event count rate ✓

PET→MRI	• None	• RF Distortion (Qualitative) ✗	• RF Distortion (Qualitative) ✓	• RF Distortion (Qualitative) ✗ • B_0 homogeneity ✓ • B_1 homogeneity ✓ • Spin Echo ✓	• RF Distortion (Quantitative) ✓	• RF Distortion Breast Coil (Quantitative) ✓

✓ : passed
✗ : failed
Functionality: Possibility to acquire Event Data
Quantitative: (MRI→PET) Analysis of Performance Parameters
Quantitative: (PET→MRI) Analysis of RF Spectra Mean/Noise Level
*) Distortion significantly reduced, but still present

6.1 MRI Compatibility Test Setup A: Signal Transmission via Copper Cables and Back-end Electronics Located at the MRI Scanner

6.1.1 Material and Methods

The PET modules' MRI compatibility was evaluated to determine if it was possible to operate the PET modules in the static magnetic field of a 3T MRI scanner using a modified version of the C13500-4075LC-12 PET modules, as described in section 4.1.1. The front-end and back-end electronics were operated next to a 3T MRI scanner (Magnetom Prisma, Siemens, Erlangen, Germany). The laboratory power supply of 24 V (GPS-4303, GW Instek, Taipei, Taiwan) and 70 V (2400-C, Keithley Instruments, Cleveland OH, USA) were located outside of the MRI room to ensure that the static magnetic field of the MRI scanner did not distort them. The power supply cables and the optical fibers data between the relay board and interface board were fed through a waveguide located inside the wall of the MRI room (Figure 73).

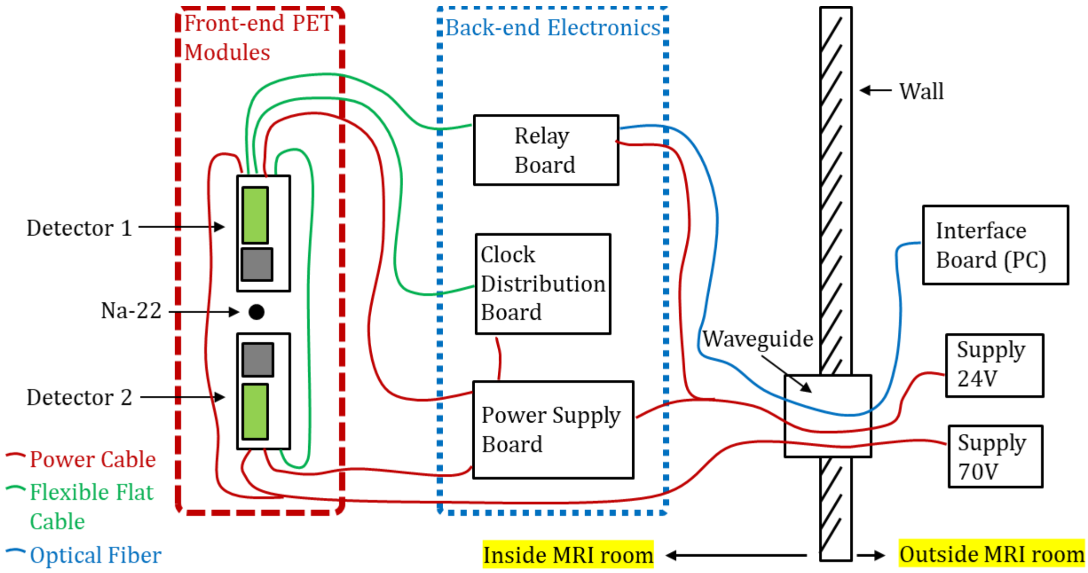

Figure 73: Block diagram of setup A with the front-end and back-end electronics of the PET modules placed inside the MRI room.

The front-end and back-end electronics of the PET modules were placed on the patient bed of the MRI scanner with a distance of 100 cm between them (Figure 74).

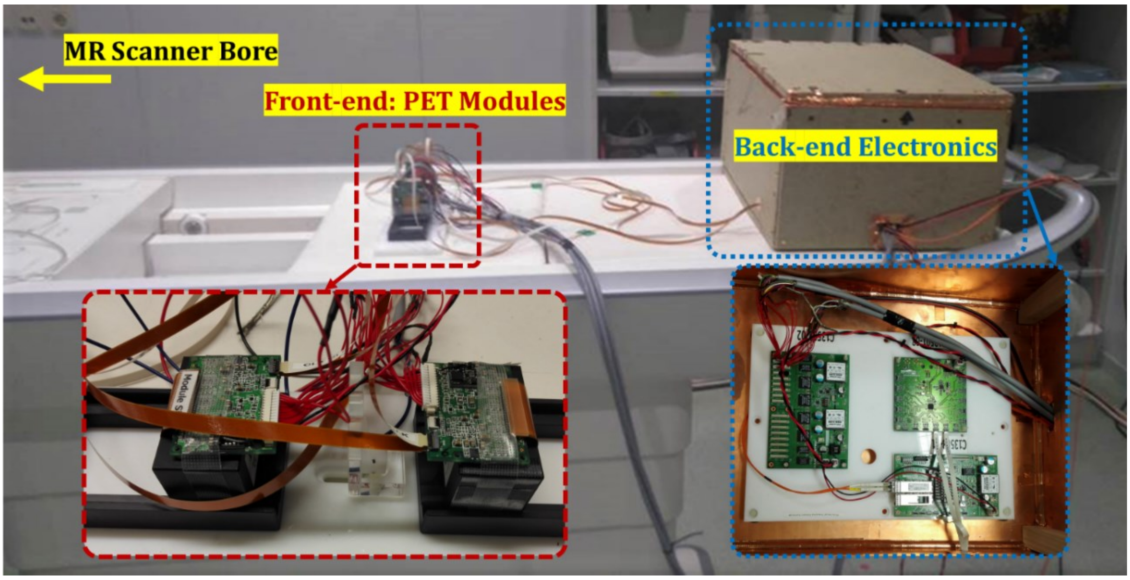

Figure 74: Setup with the front-end and back-end electronics of the PET modules placed on the patient bed of the MRI scanner. A 625 kBq Na-22 point source is centered between the two detectors.

Moving the patient bed varied the distance between the setup and the MR bore to determine the influence of the static magnetic field's strength on the PET modules. The possibility of operating the PET modules at two bed positions was evaluated (Figure 75).

For this proof-of-concept measurement, it was sufficient to evaluate whether a PET event acquisition was possible by having proper communication between the signal processing boards of the front-end and back-end electronics. More detailed quantitative analyses were performed for the test setups described in the following sections.

In the first position, the front-end and back-end electronics were 0 cm and 100 cm from the bore opening, respectively, whereas in the second position, they were at a distance of 105 cm and 205 cm, respectively. As Figure 75 only illustrates isomagnetic contours, a range for the B_0 field strength was assigned to each position of the electronics instead of a single value. Accordingly, the front-end was exposed to a B_0 field strength range of 200 mT to 3 T and 40 mT to 200 mT for the first and second positions, respectively. The back-end electronics were exposed to a B_0 field strength range of 40 mT and 200 mT and 5 mT and 10 mT for the first and second positions, respectively. The current drawn by the 24 V laboratory power supply was monitored to determine whether the PET modules' power supply was stable.

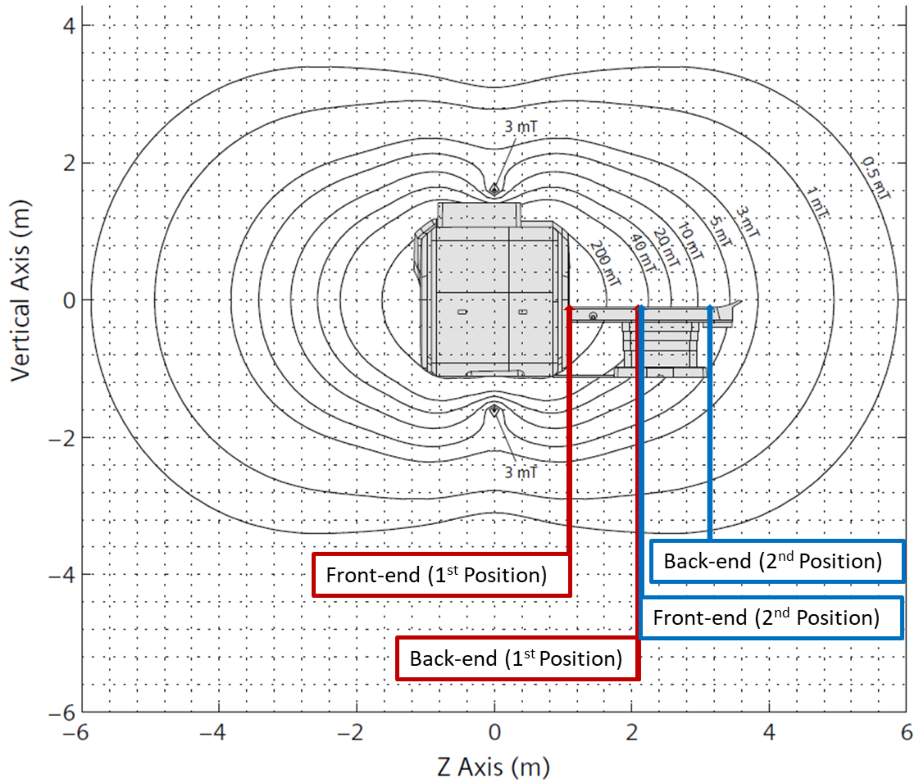

Figure 75: Side view of the spatial distribution diagram of the static magnetic B_0 field of the 3T Magnetom Prisma MRI scanner with iso-magnetic contours. The first and second positions of the front-end and back-end electronics of the PET modules with a distance of 0 cm and 105 cm between the front-end and the opening of the MRI bore are shown. Adapted and modified from [100].

6.1.2 Results

<u>Influence of the MRI on the PET Modules' Operation</u>

An operation of the PET modules based on the setup shown in Figure 74 was not possible for the first position, with the front-end placed directly at the opening of the MR bore. More specifically, communication with the signal processing boards of the front-end using the proprietary software of the manufacturer was not possible; hence, data acquisition was not possible. For this measurement, a fluctuation of the current between 0.2 A and 0.5 A of the 24 V power supply was observed.

In the second position, the distance between the front-end and back-end electronics to the MRI bore was increased, resulting in a reduced magnetic field strength and a normal operation of the PET modules (i.e., the acquisition of PET event data). The current drawn by the 24 V power supply remained constant at a value of 0.7 A, similar to the normal operational current without any exposure to a magnetic field.

6.1.3 Discussion and Conclusion

In setup A, the front-end and back-end electronics were located inside the MRI room to evaluate whether the PET modules fully operated when exposed to different static magnetic field strengths. The exact values of the B_0 field were not measured; instead, the interval of the values was determined by the spatial distribution diagram of the static magnetic field strength provided by the manufacturer (Figure 75). Therefore, a conservative approach is used in the following analysis, which assigns the magnetic field strength of the lower interval border to the corresponding measurement. The PET modules did not function when the front-end and back-end electronics were exposed to magnetic field strengths of 40 mT and 200 mT, respectively. As the current drawn by the 24 V power supply fluctuated between 0.2 A and 0.5 A, it is assumed that the voltage regulators on the power supply board of the back-end electronics were distorted by the static magnetic field. Furthermore, after increasing the distance between the setup and the opening of the MRI bore by 105 cm, the PET modules functioned at a lower static magnetic field strength of 5 mT and 40 mT for the front-end and back-end electronics, respectively. As previously explained, it is assumed that the impact of the static magnetic field on the back-end electronics prevented the PET modules from operating.

6.2 MRI Compatibility Test Setup B: Signal Transmission via Copper Cables and Increased Distance between Back-end Electronics and MRI Scanner

6.2.1 Material and Methods

The measurements described in the previous section revealed that the static magnetic field impeded the operation of the PET modules when the front-end and back-end electronics were placed at a distance of 0 cm and 100 cm from the opening of the MR bore, respectively. It is necessary that for the implementation of the PET insert to operate the front-end electronics, including the PET detectors, inside the MR bore. However, the back-end electronics do not necessarily have to be placed close to the MRI scanner. Thus, the back-end electronics were placed outside of the MRI room to prevent their distortion by the static magnetic field, gradient switching, or RF (Figure 76). According to the manufacturer's data sheet, the back-end electronics were within the 5-Gauss line (i.e., inside a region with a field strength larger than 0.5 mT). [100]

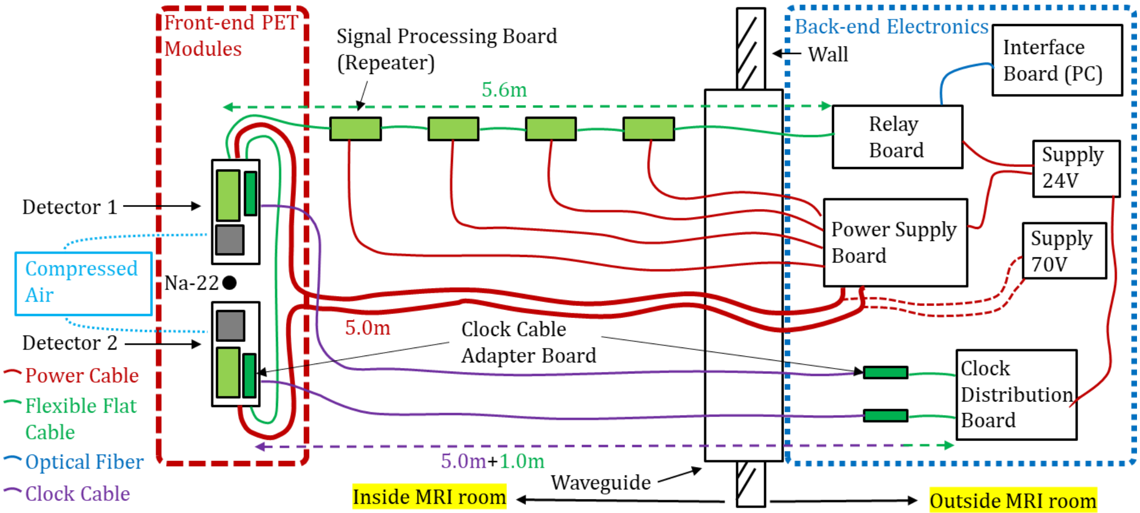

Figure 76: Block diagram of setup B with the back-end electronics of the PET modules placed outside of the MRI room. A daisy chain of four signal processing boards was used for the extension of the data transmission line.

To increase the distance between the front-end and back-end electronics so that the back-end electronics could be placed outside the MRI scanner room, the following modifications were required in comparison to setup A:

- Extension of the power cable between the detectors' signal processing board and the power supply board. A shielded 15×0.25 mm^2 cable of 5 m length (Unitronic LiYCY, Lapp, Stuttgart, Germany) was used.
- Extension of the clock line between the detectors' signal processing board and the clock distribution board. The FFC cable used for the transmission of the clock signal cannot be extended more than 1.15 m, and therefore a CAT6 patch cable of 5 m length was used for the clock cable. A custom-made adapter board was used for the connection between the FFC cable and the patch cable (Figure 77 top right). Four of these clock cable adapter

boards were used in total (one adapter board at the front-end and a second at the clock distribution board for each detector).

- Extension of the data transmission line between the detectors' signal processing board and the relay board. Data communication with a cable longer than 1.15 m was not possible due to the limitation of the data signal driver on the signal processing board. Therefore, the signal was refreshed by signal processing boards with customized firmware every 1.15 m, serving as repeaters of the data signal. This technique extended the total distance of the data transmission line to 5.6 m using four repeaters (Figure 76).

All of the cables between the front-end PET modules and the back-end electronics were fed through a waveguide in the wall of the MRI room. A single chain of repeater boards for the data communication line of detector 1 was sufficient to read out both detectors, as the data output of detector 2 was connected to detector 1. This daisy chain feature was implemented by connecting both detectors with a single FFC, as shown in Figure 76 (left; green line connecting both connectors).

Shielding boxes were used to prevent spurious radio frequency waves from the front-end PET modules from distorting the MRI scanner's receiver coil (Figure 77 lower right). Furthermore, the shielding boxes should prevent any RF distortion introduced by the MRI scanner's transmitter coil, which might distort the operations of the PET modules.

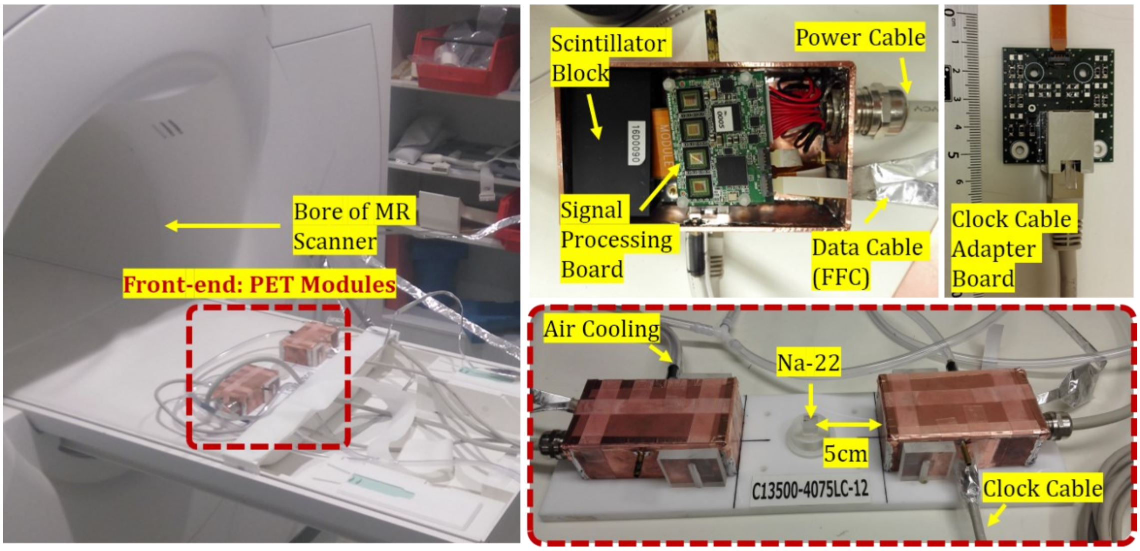

Figure 77: Setup with the front-end electronics of the PET modules placed on the patient bed of the MRI scanner. The back-end electronics are placed outside the MRI room. A single detector is encapsulated inside the shielding box together with the clock cable adapter board.

The shielding boxes were custom-made with a 1.6 mm-thick FR4 material and a 35 µm-thick copper layer on each side. To further minimize the effects of mutual RF distortion, all unshielded components, such as the FFC cables used for data transmission and the repeater boards, were wrapped in aluminum foil 30 µm in thickness. As the shielding boxes were closed, the potential heating of the PET module components was prevented by cooling with compressed air (Figure 77 bottom right).

First, it was determined whether the PET modules inside the MR bore could operate with the increased distance between the back-end electronics and the MRI scanner. As such, a measurement with the front-end of the PET modules at the center of the MR bore was performed and compared to a reference measurement outside of the MRI scanner room, with no static magnetic field present. The two opposing detectors of the front-end were each placed at a distance of 5 cm to a centered 600 kBq Na-22 point source (Figure 77 bottom right). In total, 1×10^7 single PET events were acquired for both detectors and each measurement. In order to quantitatively evaluate the impact of the static magnetic field on the PET modules, the PET event data were analyzed to characterize the PET detectors in regard to their FWHM energy resolution, photo peak position, single event count rate, and the FWHM CRT. In order to determine the coincident events for the timing histogram, only events detected within an energy window of ±1σ around the photo peak were considered in a coincidence time window of 520 ps.

The energy resolution and photo peak position were determined for each scintillation crystal by a Gaussian fit of the corresponding single crystal energy spectrum. It should be noted that for detector 1, only 36 of the 72 ASIC channels, and thus the scintillation crystals, were used for the analysis, as two of the four ASICs on the signal processing board were not functional (the damage occurred prior to the measurements described in this section and was not caused during these experiments with the MRI scanner).

Using this setup, two additional measurements were performed to evaluate the effects of the RF distortions caused by the MRI scanner on the PET modules and their sensitivity to the switching the gradients.

To examine the effects of the RF distortions from the MRI scanner on the PET modules, an *rf_pulse* sequence (see Appendix) was used with a pulse width (PW) of 1 ms, a duty cycle of 1 %, and a flip angle (FA) of 45°.

Similarly, the *grad_freepulse* sequence (see Appendix) was used to investigate the PET modules' gradient switching sensitivity. All three axis gradients were switched with a maximum gradient field strength of 10 mT/m, a ramp of 0.2 ms, and a slew rate of 50 T/ms^{-1}.

Finally, the *rf_noise_spectrum* sequence (see Appendix) was used to evaluate the influence of the RF distortion introduced by the PET modules on the MRI scanner's receiver coil. Two measurements were performed with the PET modules at a distance of 30 cm to the opening of the MR bore, as shown in Figure 77 (left). The first measurement was used as a reference without powering on the PET modules. The second measurement was performed while the PET modules were running.

6.2.2 Results

Influence of the MRI on the PET Modules' Performance

Normal operation of the PET modules (i.e., acquisition of the PET data) was possible when the front-end electronics were operated at the center of the MRI scanner and the back-end electronics were located outside of the MRI scanner room. Table 5 depicts the performance parameters when the front-end electronics were exposed to the MRI scanner's static magnetic field and the reference measurement was taken outside of the magnetic field. For detector 2, the energy resolution of 8.4±0.8 % and the photo peak position of 420.8±27.2 ns measured inside the MRI bore is comparable to the reference measurements of 8.3±0.8 % and 409.0±26.4 ns, respectively. For detector 1, the energy resolution of 9.6±0.6 % decreased within the static magnetic field in comparison with the reference measurement of 10.2±0.7 %. This difference of 0.6 % in the energy resolution is assumed to be unrelated to the presence of the static magnetic field but rather due to small changes in the cooling conditions of the MPPC under different airflow conditions (see section 4.2.4) and the finite accuracy of the Gaussian fits in the energy spectra used to determine the energy resolution. This would also explain the slightly lower photo peak position of 409.0±26.4 ns for the measurement in the MRI bore in comparison with the reference measurement of 420.8±27.2 ns.

Table 5: Performance parameters for a reference measurement outside the magnetic field and for a measurement with the PET modules operating at the center of MRI bore with the following abbreviations: D1,2: detector 1,2; photo peak: center position of the Gaussian fit in the single crystal energy spectrum; CRsingle: single event count rate for one detector; CRT: block-to-block coincidence resolving time for ±1σ energy discriminated events.

Condition	Energy Resolution (D1) [%]	Energy Resolution (D2) [%]	Photo Peak (D1) [ns ToT]	Photo Peak (D2) [ns ToT]	CRSingle (D1) [kcounts/s]	CRSingle (D2) [kcounts/s]	CRT [ps]
Reference outside magnetic field	10.2±0.7	8.4±0.8	420.8±27.2	491.8±24.8	20.8	43.0	269
Exposed to static magnetic field	9.6±0.6	8.3±0.8	409.0±26.4	487.1±24.1	21.8	43.3	267

The single event count rate remained stable within the measurement accuracy for detector 2 with 43.3 kcounts/s, in comparison with the reference measurement of 43.0 kcounts/s. Furthermore, for detector 1, the single event count rate was 21.8 kcounts/s when the PET modules were exposed to the static magnetic field and 20.8 kcounts/s for the reference measurement. This rather small increase of 4.8 % compared to the reference measurement was not due to the influence of the static magnetic field, as detector 1 and detector 2 were exposed to the same magnetic field strength, and detector 2 did not show any variation. Small changes in the measurement setup, such as different cooling conditions, or a small change in the alignment between the scintillation crystal block of detector 1 and the radiation source, likely caused this slight variation.

The static magnetic field did not affect the process of assigning time stamps to the PET events, as the CRT was 267 ps for the measurement at the center of the MRI bore, which was comparable to the reference measurement of 269 ps outside of the magnetic field.

When both measurements were taken with either the RF distortion or the gradient switching sequence, the PET modules did not function properly, as it was not possible to acquire PET event data.

Influence of the PET Modules on the Performance of the MRI Scanner

Figure 78 (left) illustrates spurious spikes in the RF noise spectrum when the PET modules are placed at a distance of 30 cm to the opening of the MRI bore. The fact that this distortion is present even when the PET modules were not powered on indicates that the cables, which were fed through the waveguide to the back-end electronics outside the MRI room, propagate RF distortions. Figure 78 (right) shows the RF noise spectrum for the same setup with the PET modules switched on. The increased magnitude and change of the RF noise spectrum indicates that the radiated RF noise by the PET modules' front-end and back-end electronics was not sufficiently isolated. It should be noted that the raw data of the RF noise spectra could not be extracted from the files. Therefore, only the images of the RF noise spectra were available for these measurements, which do not allow for a quantitative analysis. However, for subsequent measurements using PET modules with improved MRI compatibility, the raw data was saved, allowing for a further quantitative analysis of the RF noise spectra, as described in sections 6.5.2 and 6.6.2.

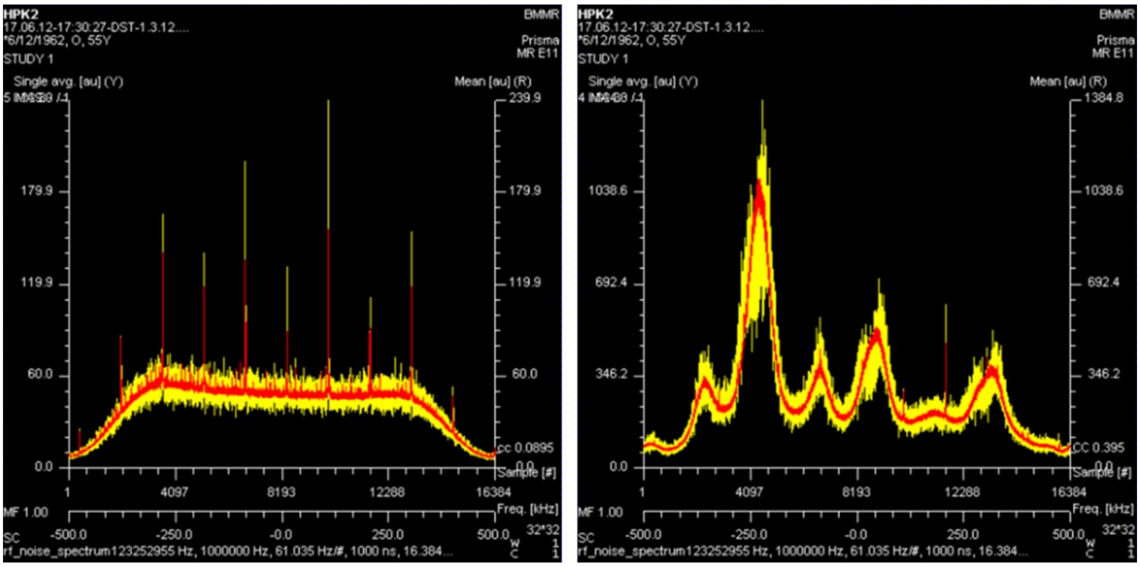

Figure 78: RF noise spectra for setup B placed at a distance of 30 cm from the MRI bore. Left: PET modules switched off. Right: PET modules switched on.

6.2.3 Discussion and Conclusion

To verify whether the impact of the static magnetic field on the back-end electronics prevented the PET modules from operating, the back-end electronics were moved outside of the MRI room for setup B, whereas the front-end remained exposed to the static magnetic field. This setup allowed the PET modules to operate; hence, the back-end electronics are prone to distortions caused by the static magnetic field and were therefore placed outside of the MRI room for subsequent measurements. However, the front-end electronics were not affected by the static magnetic field, as the performance of PET modules did not degrade when they were operated at the center MRI bore compared to a reference measurement outside the magnetic field.

Switching the gradients with a slew rate of 50 T/ms^{-1} hindered the operation of the PET modules. It is assumed that the large ground loops formed by the six separate power cables for the detectors and repeater boards (Figure 76) were prone to voltage induction due to the gradient switching. Therefore, the daisy chain of repeater boards should be removed to enable MRI compatibility. To maintain the extended distance between the PET modules' front-end and back-end electronics, a solution that used data communication via optical fibers (see section 6.3.1) was used for the next iteration towards MRI compatibility of the PET modules. The use of optical fibers further mitigates the effects of RF distortion on the PET modules, preventing spurious RF wave coupling on the data communication lines. These fibers are necessary, as section 6.2.2 reported that RF pulses transmitted by the MRI scanner can prevent the PET modules from operating.

Further improvements to the detectors' shielding box and the filter for the power cables should be performed to increase the PET modules' RF robustness. In addition, these modifications might also mitigate the RF distortion introduced by the PET modules on the MRI scanner.

6.3 MRI Compatibility Test Setup C: Signal Transmission via Optical Fibers and Single PET Module with Strong RF Shielding

6.3.1 Material and Methods

The PET modules and back-end electronics described in section 4.1.1 were modified with the EVAKIT01 (Hamamatsu Photonics K.K., Hamamatsu, Japan) components to enable the transmission of the clock and data signal via plastic optical fibers (Figure 79).

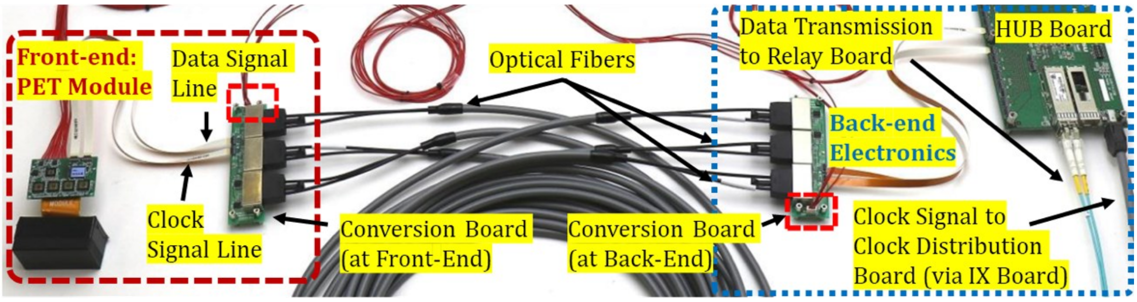

Figure 79: EVAKIT01 components for signal transmission via plastic optical fibers. Modified and adapted from [97].

One optical fiber transferred the clock signal, and the other two optical fibers maintained two-way data communication between the front-end PET modules and the back-end electronics. The signal processing board used a different firmware for data communication, whereas the MPPC and scintillator block remained unchanged. Two conversion boards were used to interface between the FFC cables and the optical fibers. One conversion board was located at the front-end coupled to the signal processing board and the other one at the back-end, which was connected to the HUB board. The HUB board was used to transfer the clock signal via the IX board from the clock distribution board and to establish data communication between the conversion board and the relay board. Figure 80–Figure 82 illustrate all of the components and connections.

Figure 80 depicts MRI combability test setup C, which uses optical fibers to extend the distance between the front-end PET module and the back-end electronics. In addition to MRI compatibility test setup B described in section 6.2, an additional low-pass filter (DaFid, Siemens Healthineers, Erlangen, Germany) was used for PET modules' power supply cable with the intention of minimizing distortions on the power supply line.

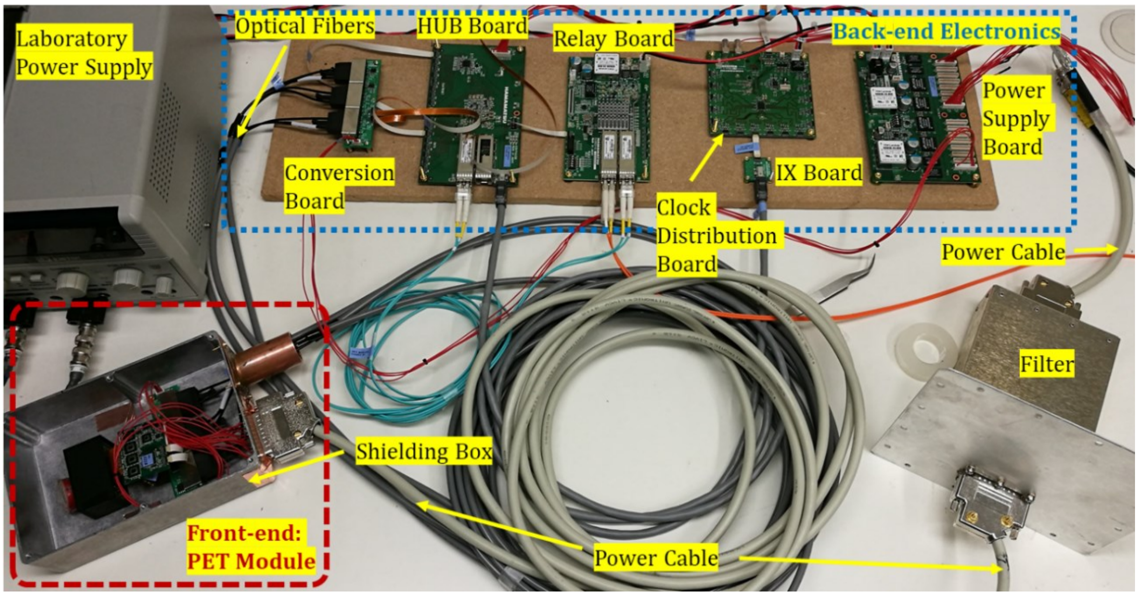

Figure 80: Components for MRI compatibility test setup C with a single PET module with strong RF shielding and optical fiber signal transmission.

The filter was mounted on the wall of the MRI room, and the shielding braid of the 5 m-long power supply cable was connected via the shell of the DSUB connector to the grounded metal plate inside the wall (Figure 81 right).

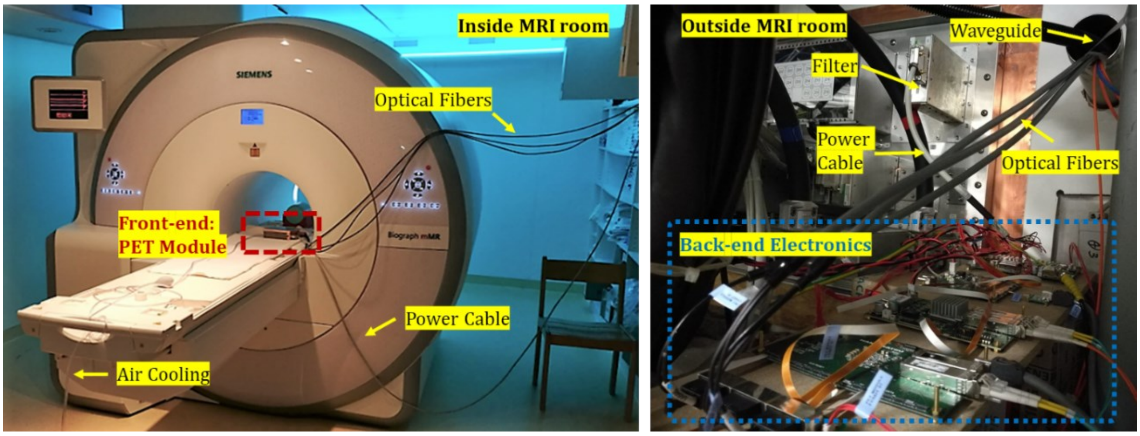

Figure 81: Left: Front-end PET module encapsulated in the shielding box inside the bore of the Biograph mMR with connecting cables to the back-end electronics. Right: Filter and waveguide outside the MRI room with the back-end electronics of the PET module.

The second connection between the front-end PET module and the back-end electronics was established with 5 m-long optical fibers, which were fed through a waveguide inside the wall of the MRI room, as shown in Figure 81 (right) and Figure 82.

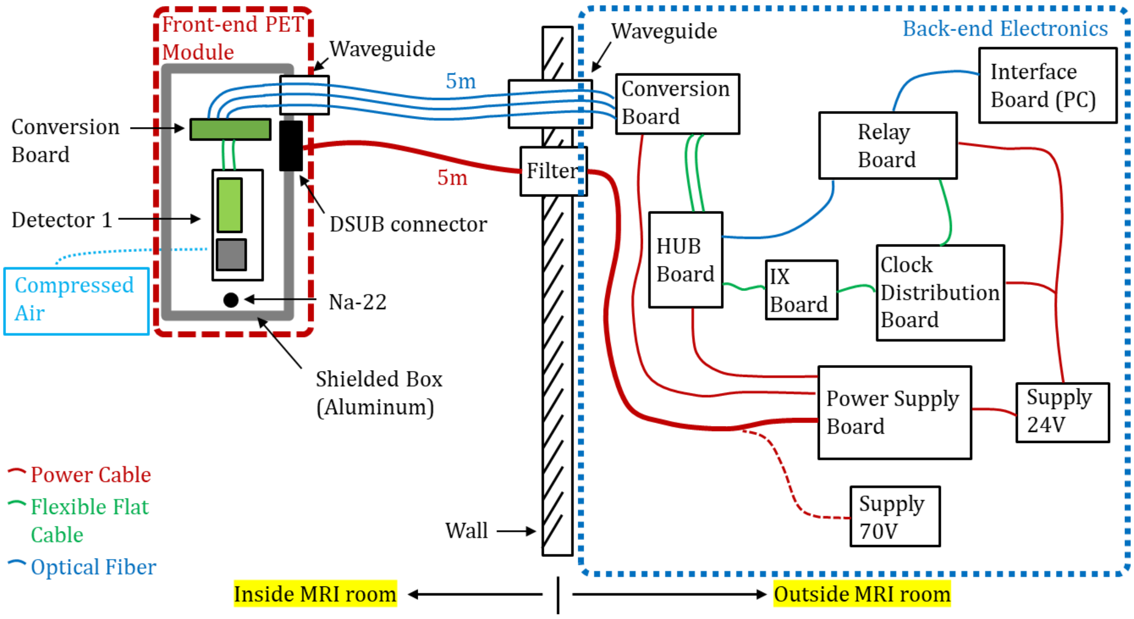

Figure 82: Block diagram of setup C with signal transmission between a single PET module inside the aluminum shielding box and the back-end electronics via optical fibers.

The PET module was placed inside the Biograph mMR (Figure 81 left). The front-end PET module was encapsulated inside an RF shielding box (Figure 83 right) with a thickness of 2 mm made from the aluminum alloy ADC12. The optical fibers were fed into the shielding box through a copper waveguide together with the tube for air cooling (Figure 83 left). The shielding of the power cable was connected to the shielding box via the shell of the DSUB connector. A 500 kBq Na-22 point source was centered at a distance of 2.5 cm to the scintillator block. All measurements were performed with the PET module located at a distance of 30 cm to the center of the MRI bore (Figure 81 left).

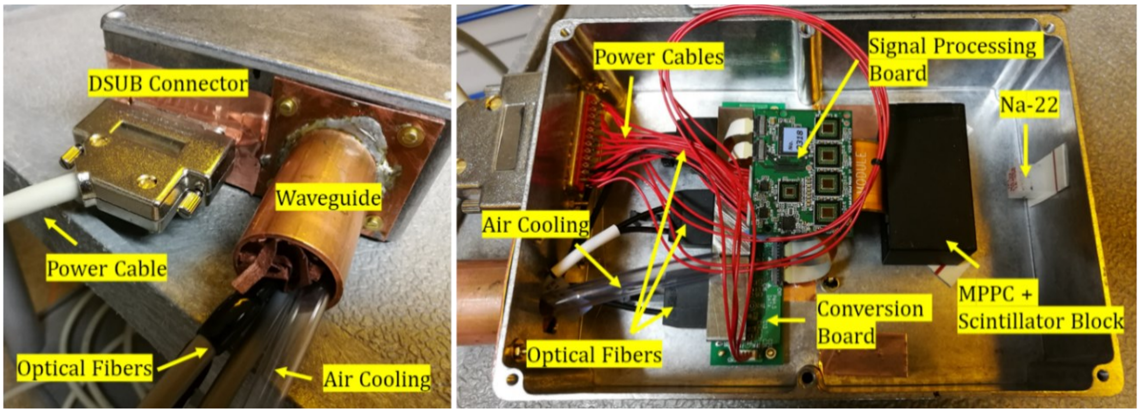

Figure 83: Left: Connection of power supply lines via DSUB connector to the shielding box and signal transmission via optical fibers fed through a waveguide. Right: Components of the front-end PET module encapsulated in the aluminum shielding box.

The previous section demonstrated that gradient switching and the transmission of RF pulses distorted the PET modules, preventing PET data acquisition. In order to verify whether the change from a copper-based transmission line to optical fibers prevents this distortion, two measurements with their respective MR test sequences were performed.

The first test ascertained whether PET data could be acquired while switching all three axis gradients via a *grad_freepulse* sequence with a maximum gradient field strength of 20 mT/m, a ramp of 0.3 ms, and a slew rate of 66.7 T/ms^{-1}.

Second, to evaluate whether RF distortion can impede data acquisition, an *rf_pulse* sequence of FA = 720°, PW=1 ms, and TR=104 ms (duty cycle 0.95%) was used for two measurement conditions, one with the shielding box closed and one with the lid of the shielding box removed. These measurements determined whether the PET modules could operate without the shielding. It should be noted that only qualitative results are reported that allow for a statement whether the data acquisition of the PET modules is possible. A more detailed quantitative analysis of the PET performance was performed for the setups described in sections 6.4–6.6. For the measurements described here, two PET detectors were available, which is necessary for coincidence measurements to evaluate the timing performance.

Another RF pulse sequence was applied to take a measurement with the shielding box closed using a more moderate power *rf_pulse* sequence of FA=180°, PW=1 ms, and TR=105 ms (duty cycle 0.95%). In addition, the start of the *rf_pulse* sequence was delayed by 9 s from the start of the PET event data acquisition. Thus, the PET events acquired in the first 9 s were not exposed to RF distortion, whereas the remaining 1×10^7 events were recorded during RF pulse transmission. To evaluate the effects of the RF pulses on the PET event data, the progression of the time stamps over the event number was determined and compared for the two different acquisition conditions. In addition, a histogram of the time stamps of the PET events, which were acquired while the RF noise sequence was applied, was used to analyze the time stamp values with respect to a systematic distortion.

The previous section reported that RF distortions coupled on the copper cables that connect the PET modules' front-end and back-end electronics caused a distortion in the MRI scanner's RF receiving spectrum. For the setup used in this section, a power line filter was used, and the copper-based transmission lines were replaced with optical fibers. It was expected that these modifications would reduce the RF distortion introduced by the PET modules on the MRI scanner's RF receiver coil. To validate this theory, the spectra acquired by the *rf_noise_spectrum* sequence (see Appendix) were compared for a measurement taken while the PET modules were operating and a reference measurement without the PET modules installed.

6.3.2 Results

<u>Influence of the MRI on the Performance of the PET Modules</u>

The operation of the PET modules was still possible while switching all three axis gradients with a slew rate of 66.7 T/ms^{-1}. The same held true during the application of the 720° FA *rf_pulse* sequence when the shielding box was closed.

However, with the open configuration of the shielding box the RF distortion of the 720° FA *rf_pulse* sequence prevented PET event data acquisition.

The delayed 180° FA *rf_pulse* sequence did not stop the modules from operating, thus allowing to analyze the time stamp progression of the PET. Figure 84 (left) demonstrates that when no *rf_pulse* sequence is applied, the value of the time stamps increased with the event number (some jumps were visible; however, these jumps were not caused by the MR and were also observed for measurements outside the magnetic field, indicating the firmware used for these measurements caused the jumps).

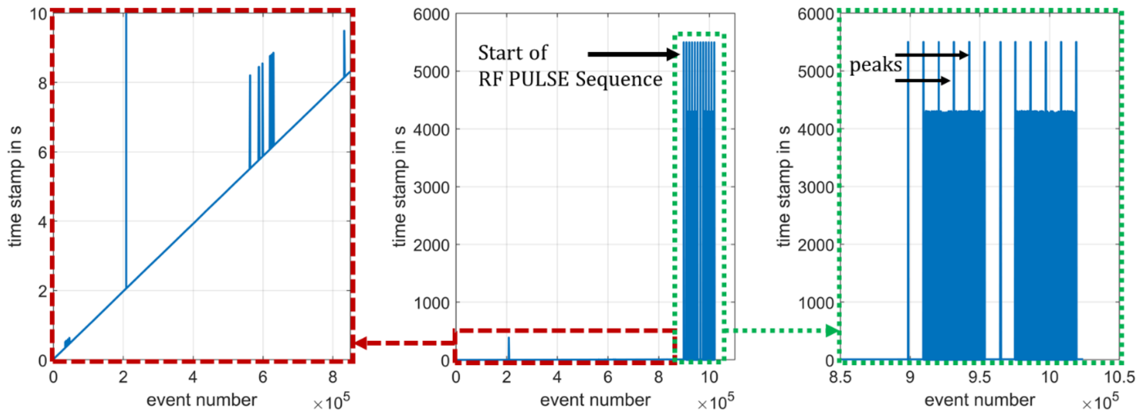

Figure 84: Time stamp progression of PET events for a 180° FA rf_pulse sequence applied 9 s after the measurement start time. Left: Events acquired in the time without the rf_pulse sequence. Middle: Events acquired over the total measurement time, including the rf_pulse sequence starting after 9 s. Right: Time stamps of events after starting the rf_pulse sequence.

Starting the *rf_pulse* sequence after 9 s heavily distorted the time stamps, which exhibited highly increased values (Figure 84 middle). The 12 peaks in Figure 84 (right) have a mean value of $5.4976\times10^3\pm0.0074$ s and a mean distance of $1.10\times10^4\pm128$ events. The mean count rate with this setup was 102.4 kcounts/s when no sequence was applied. Therefore, the peak distance corresponded to 107.4 ms, assuming that while the *rf_pulse* sequence was running, the count rate remained stable. The fact that this temporal distance is close to the repetition time of the *rf_pulse* sequence of 105 ms indicates a correlation between the *rf_pulse* on phase (i.e., the time slots in the *rf_pulse* sequence when RF pulses are transmitted) and the distortion of the event time stamps.

To assess whether the RF pulses caused a systematic distortion, a histogram of the time stamps during the application of the 180° FA *rf_pulse* sequence was made, as shown in Figure 85.

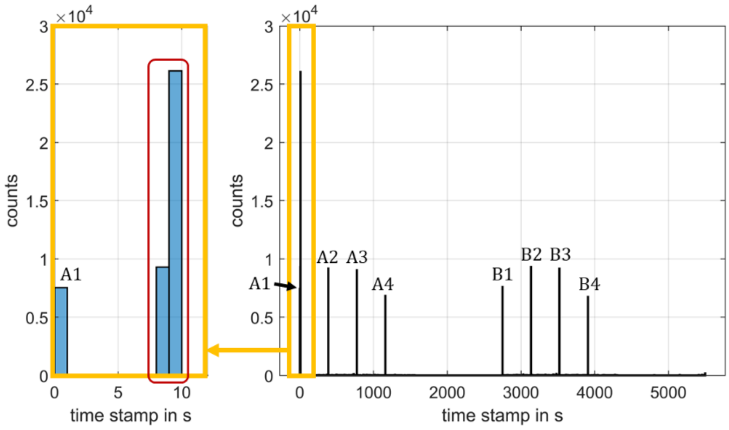

Figure 85: Histograms of time stamps acquired during the application of the 180° rf_pulse sequence. Left: Subpart of the histogram from 0 s to 12 s; the time stamps mapped to the bins in the red box are in the range of time stamp values that would be expected for a normal, i.e., distortion-free acquisition. Right: Total histogram with peak positions denoted A1–A4 and B1–B4.

Discrete peaks in the histogram are visible, which contain 53.1 % of all events acquired while the *rf_pulse* sequence was applied. Furthermore, the distance between neighboring peaks is 386.3±0.6 s and 386.5±0.6 s for A1–A4 and B1–B4, respectively.

<u>Influence of the PET Modules on the MRI Scanner's Performance</u>

No difference was observed between the RF noise spectrum while the PET modules were operating (Figure 86 left) and the RF noise reference spectrum with no PET modules installed (Figure 86 right). As described in section 6.2.2, a quantitative comparison was not possible. Due to the measurement procedure, images of the RF noise spectrum exist but not the raw data. A quantitative comparison was performed for the setups described in sections 6.5 and 6.6. However, a qualitative comparison was performed to determine whether replacing the copper-based transmission line with optical fibers and introducing the power filter mitigates the RF noise transmitted by the PET modules. The distortions visible in the RF noise spectra for the previous setup (Figure 78) were strongly reduced by the optical fibers and power filter (Figure 86 left).

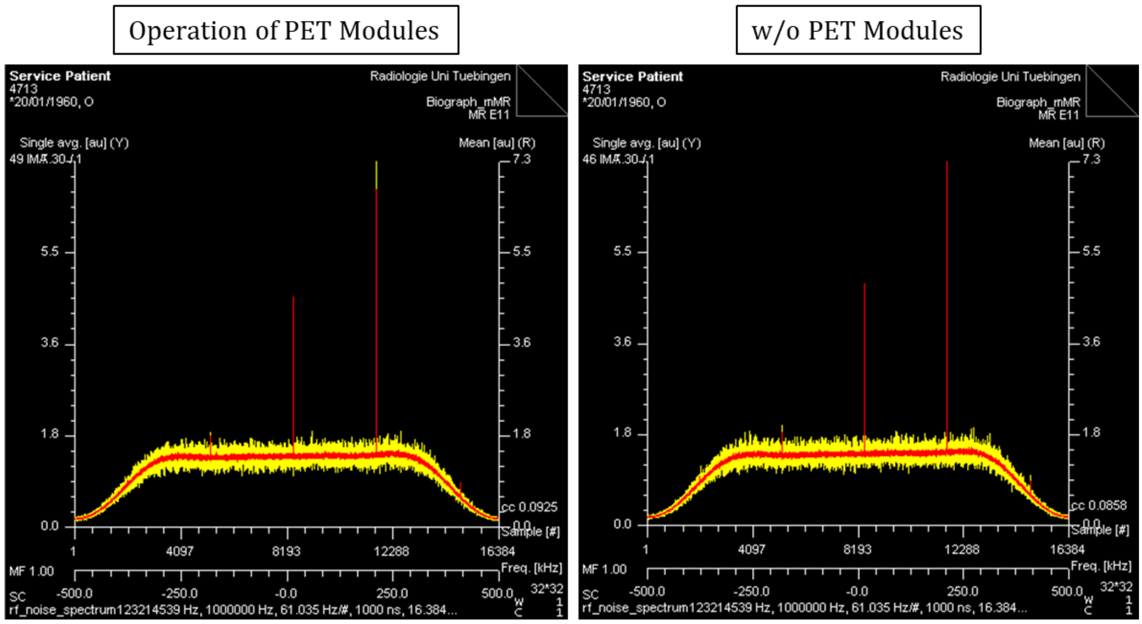

Figure 86: Left: Normal operation of the PET module encapsulated in the strong RF shielding box. Right: Reference RF noise spectrum without the PET module installed. The three spikes visible in both spectra are caused by a binning effect of the spectra.

6.3.3 Discussion and Conclusion

For setup B (see section 6.2), which used copper connections and a daisy chain of repeater boards, the PET modules could not operate when the MRI scanner's gradients were switched or RF pulse distortion was applied. However, with the optimized setup C, which uses a signal transmission via optical fiber and a filter for the power supply lines, the PET module functioned during gradient switching with a slew rate of 66.7 T/ms^{-1}. Furthermore, the module operated while a high power *rf_pulse* sequence with an FA of 720° was applied; however, this was only achievable while the PET module was inside a shielding box designed for strong RF shielding. The time stamps of the PET events were analyzed during RF pulse distortion with a FA of 180°. These time stamps showed distorted values of up to 5.4976×10^3±0.0074 s, which occurred approximately at the repetition time of the *rf_pulse* sequence. In addition, while the *rf_pulse* sequence was running, 53.1 % of the acquired PET events showed distorted time stamps distributed between eight discrete values, for which the lower and higher four time stamp values were 386.3±0.6 s and 386.5±0.6 s apart, respectively.

These observations were not due to the effect of the RF pulses on the analog PET signals used to determine the event time stamp. The discrete nature of the time stamp distortion indicates a systematic error within the time stamps caused by a distortion of a digital component used to determine the time stamps. As the TDC and FPGA are the two components of the signal processing board used for time stamp determination, it is assumed that either one or both components were sensitive to RF distortion. A more comprehensive analysis of the influence of RF pulse distortion on the timing measurement is discussed in sections 6.4.2, 6.5.2, and 6.6.2, which consider different RF power and duty cycles using setups with two PET modules for the coincidence measurements and further improvements to the filters and shielding.

The introduction of the optical fiber transmission and power filters helped to significantly reduce the distortion propagated by the cables connecting the front-end and the back-end electronics of the PET modules. While no quantitative evaluation was possible, the reduction of the *rf_noise* spectrum distortion on the body coil was qualitatively detectable in comparison to setup B, which did not have a filter and used copper cables instead of optical fibers. Setup C successfully minimized the RF noise introduced by the PET module on the MRI scanner. Sections 6.5 and 6.6 present a quantitative confirmation of this observation.

Setup C served as a proof of concept; however, it is impractical due to the thickness of the shielding box and the corresponding gradient transparency, which is not suitable for maintaining the normal operation of the MRI scanner. Therefore, the next step in making the PET modules MRI compatible required thinner and potentially less efficient RF shielding boxes. As previously shown, insufficient shielding resulted in PET event data distortions, which correlated to the RF distortion. Therefore, the next tests on MRI compatibility required a more detailed analysis of PET performance parameters with respect to the *rf_pulse* sequence. A coincidence setup with PET modules was used to precisely evaluate the potential degradation in timing accuracy.

6.4 MRI Compatibility Test Setup D: Signal Transmission via Optical Fibers and PET Modules with Moderate RF Shielding

6.4.1 Material and Methods

In comparison to the strong RF shielding used for setup C (2 mm-thick aluminum), the shielding for setup D was made from 18 µm-thick copper. The thin adhesive copper foils were placed on a customized structure laser sintered with PA 2200 (Jomatik, Tuebingen, Germany), as shown in Figure 87.

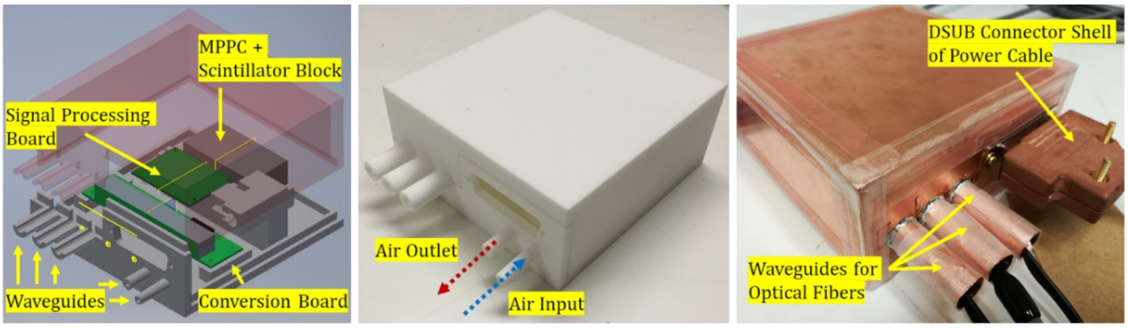

Figure 87: Left: Rendered model of the shielding box with a removable lid to enable the enclosure of the PET module components. Middle: Laser sintered shielding box structure with waveguides for air circulation. Right: Final shielding box with copper foil on the surface and the waveguides.

The waveguides and the edges of the shielding box were wrapped with adhesive 35 µm copper tape. The nickel the power cable DSUB connector and of its shell were removed (Lueberg Elektronik GmbH & Co. Rothfischer KG, Nuernberg, Germany) to improve MRI compatibility. Figure 88 illustrates the placement of the PET modules’ components and the routing of the power cables and optical fibers inside the shielding boxes. The two PET modules used the same components as setup C. A 446 kBq Na-22 point source was centered between both detectors, with a distance of 40 mm to each scintillator block.

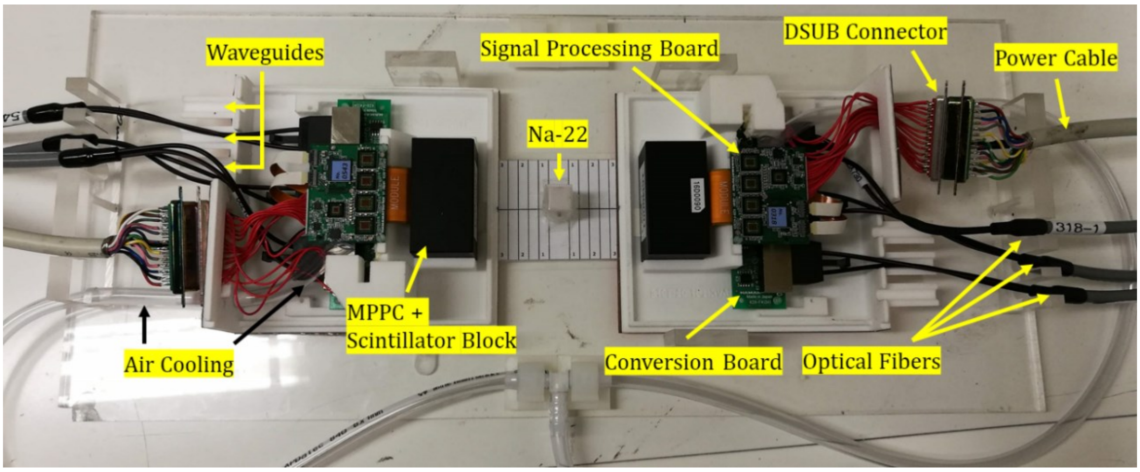

Figure 88: Setup D: Coincidence setup of two opposing EVAKIT01 PET modules. For visualization, the lid of the shielding boxes is not attached, nor is the shell of the DSUB power connector.

Figure 89 shows a block diagram of setup D, using optical fibers 10 m in length to allow the two opposing detectors to be placed at the center of the MRI bore. For the same reason, the power cable for each front-end PET module had to be extended to 6.5 m. The extension of the power cable and the corresponding increased wire resistance caused a drop of the supply voltages at the front-end of the PET modules. For the PET modules to operate properly, the supply voltages at the primary side of the longer power cable had to be increased, which was not possible with the C13502-02 power supply board (Hamamatsu K.K., Hamamatsu, Japan). Therefore, external power supplies (GPS-4303, GW Instek, Taipei, Taiwan) were used (Figure 89).

This setup was built to evaluate whether more moderate RF shielding was capable of preventing mutual distortion between the PET modules and the MRI scanner in comparison to the strong RF shielding described in section 6.3. Moreover, the use of a coincidence setup with two detectors allowed for potential degradations in the timing measurement accuracy to be observed.

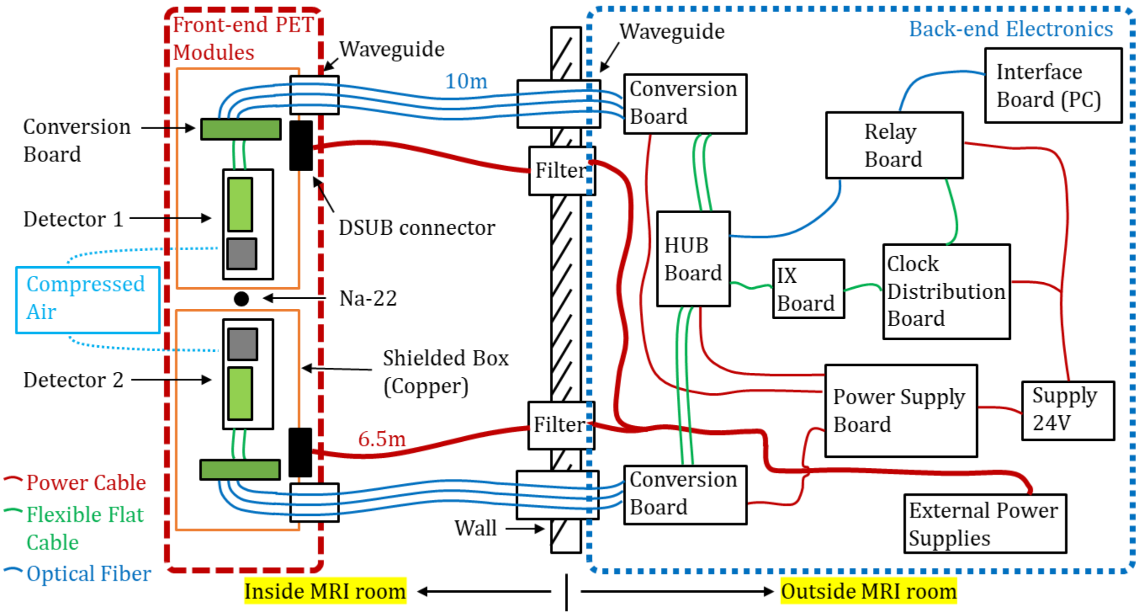

Figure 89: Block diagram of setup D with two coincident PET modules, data transmission via optical fibers, and front-end shielding boxes made upon a thin copper layer.

Figure 90 depicts the setup for testing MRI compatibility, which used a cylindrical phantom to evaluate the effects of the PET modules' operation on the MRI scanner.

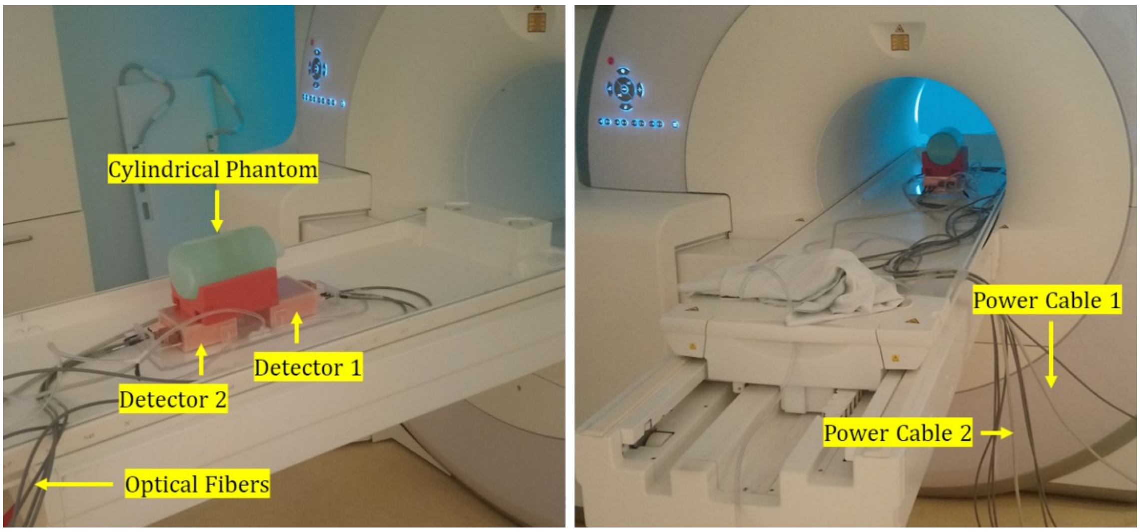

Figure 90: Coincidence setup of two PET modules inside 18 µm copper shielding boxes and the cylindrical phantom placed on top. Left: Position for visualization on the patient table outside the PET/MRI scanner. Right: Position for the measurement in the center of the bore of the PET/MRI scanner.

First, a reference measurement was taken with the detectors in the center of the MRI bore without applying any MR sequences (i.e., the PET modules were only exposed to the static magnetic field). Furthermore, three *grad_freepulse* sequences (see Appendix) were used to evaluate the effects of gradient switching on the PET modules, with a maximum gradient field strength of 20 mT/m and T_{ramp}=0.2 ms, 0.3 ms, and 1.0 ms corresponding to a slew rate of 100 T/ms^{-1}, 66.7 T/ms^{-1} , and 20 T/ms^{-1} and a duty cycle of 28.6 %, 37.5 %, and 66.7 %, respectively. A spin echo sequence with TR=400 ms, TE=12 ms, and FA=90°, was used to evaluate the impact of an imaging sequence on the PET modules.

For the PET data analysis, 1×10^7 data events were acquired. PET events for five MPPC channels on detector 1 and six MPPC channels on detector 2 were excluded from the calculation of the mean photo peak position and mean energy resolution due to their corrupted energy histograms. These corruptions likely originated from cracks in the scintillation crystals caused by the force placed on the scintillator blocks during their assembly in the shielding box and prevented the photo peak from being properly identified. For the quantitative analysis of the PET event data, typical performance parameters were evaluated to characterize the PET detectors, such as the FWHM energy resolution, photo peak position, single event count rate, coincidence event count rate, and the FWHM CRT. In order to determine the coincident events for the timing histogram, only events with an energy within an energy window of ±1σ around the photo peak were considered, with a coincidence time window of 120 ns. This high value for the coincidence time window allowed for the observation of potential distortions only visible for events acquired outside the common time window of two times the CRT. For these measurements, the time skew correction described in section 4.1.5 had not yet been applied. The energy resolution and photo peak position were determined for each scintillation crystal by a Gaussian fit of the corresponding individual crystal energy spectrum.

The potential distortion from transmitted RF waves on PET event time stamps was analyzed for an *rf_pulse* sequence with FA=90°, PW=1.0 ms, and TR=3.0 ms (duty cycle of 33.3 %). First, the coincidence timing histogram was analyzed for distorted values of the time stamp difference between detector 1 and detector 2. In the next step, the time stamps of the events from detector 1, which contribute to the distortion of the coincidence timing histogram, were determined, visualized in a histogram, and further analyzed, as described in section 6.4.2.

The impact of the PET modules on the MRI scanner was evaluated by comparing two measurements with the cylindrical phantom. A reference measurement without the PET modules installed was compared to a measurement with the PET modules operating and the cylindrical phantom placed on top of the shielding boxes, using the following MRI test sequences (see Appendix for sequence details):

- *field* sequence with TR=32 ms to evaluate the homogeneity of the static magnetic B_0 field;
- *rf_field* sequence to evaluate the homogeneity of the B_1 RF field;
- *spin echo* sequence, with TR=400 ms, TE=12 ms, and FA=90° to analyze potential distortions;
- *rf_noise_spectrum* to evaluate potential RF distortions in the receiving bandwidth of the MRI scanner.

6.4.2 Results

Influence of the MRI scanner on the PET Modules' Performance

Applying the gradient switching sequences with different T_{ramp} values and thus different duty cycles did not degrade any of the PET modules' performance parameters compared to the reference measurement, as shown in Table 6. However, applying a spin echo sequence caused a drop in the coincidence count rate from 2.13 kcounts/s to 1.83 kcounts/s in comparison to the reference measurement. The CRT degraded slightly from the reference measurement of 332 ps to 345 ps. The differences between the remaining performance parameters, such as energy resolution, photo peak position, and single event count rate, of the reference measurement and the spin echo sequence were within measurement accuracy.

Table 6: Performance parameters for different MR sequences with the following abbreviations: D1,2: detector 1,2; photo peak: center position of the Gaussian fit in the single crystal energy spectrum; CRsingle: single event count rate for one detector; CRCoin: coincidence count rate for a 120 ns time window; CRT: block-to-block coincidence resolving time for ±1σ energy discriminated events.

Test Sequence	Energy Resolution (D1) [%]	Energy Resolution (D2) [%]	Photo Peak (D1) [ns ToT]	Photo Peak (D2) [ns ToT]	CRSingle (D1) [kcounts/s]	CRSingle (D2) [kcounts/s]	CRCoin [kcounts/s]	CRT [ps]
Reference	10.5±0.6	10.1±0.5	443.9±29.6	434.1±26.5	33.2	34.4	2.13	332
grad_freepulse Tramp=0.2 ms	10.5±0.6	10.1±0.5	442.8±29.5	434.7±26.5	33.3	33.4	2.13	335
grad_freepulse Tramp=0.3 ms	10.5±0.5	10.1±0.5	443.7±29.6	435.1±26.6	33.2	34.4	2.12	339
grad_freepulse Tramp=1.0 ms	10.5±0.6	10.1±0.5	444.5±29.5	435.2±26.6	33.3	33.4	2.13	329
spin echo	10.6±0.6	10.4±0.5	442.9±29.5	434.2±26.5	33.5	34.8	1.83	345

Applying the 90° FA *rf_pulse* sequence led to spurious peaks in the coincidence timing histogram (Figure 91).

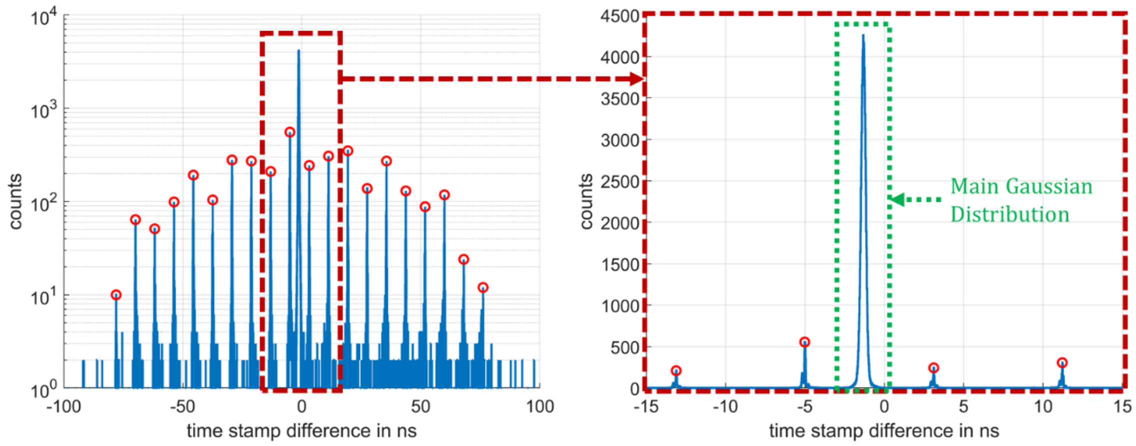

Figure 91: Distorted coincidence timing histogram for 90° FA RF pulses and a 120 ns coincidence time window. Left: Logarithmic presentation of the total histogram. Right: Linear representation between -15 ns and 15 ns for visualizing the main Gaussian distribution of the time stamp differences.

Figure 91 shows that the distance between the peak positions, as indicated with a red circle, was 8.115 ns±0.013 ns, and the inverse resulted in 123.23 MHz, which is close to the MRI scanner's Larmor frequency of 123.21 MHz .

The events with a time stamp difference that potentially led to the spurious peaks were analyzed. Specifically, the subgroup of events with a time stamp difference outside of the main Gaussian distribution of the coincidence timing histogram was examined to determine the time stamp difference that potentially caused the spurious peaks (Figure 92 left).

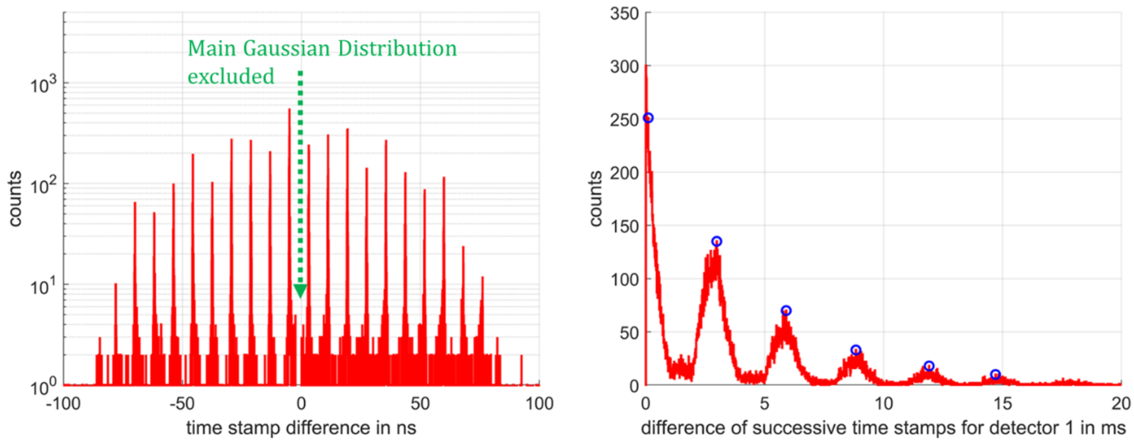

Figure 92: Left: Coincidence timing histogram of events with a distorted time stamp difference, which are selected for the analysis of the single event time stamps. Right: Difference of the successive single event time stamps from detector 1 for the selected events.

The histogram showing the difference in the time stamps between two successive events reveals a pattern that is not based on the Poisson distribution inherent to radioactive decay (Figure 92 right). The position of the peaks marked with blue circles was 2.92±0.11 ms, which is close to the 3 ms repetition time of the *rf_pulse* sequence.

<u>Influence of the PET Modules on the MRI Scanner's Performance</u>

Figure 93 (left) illustrates that the RF noise spectrum is strongly distorted when the PET modules were operated at the center of the MRI bore. This qualitative analysis reveals that RF distortion due to the PET modules occurred when the 18 µm copper shielding was used. More detailed and quantitative analyses were performed for the setups discussed in sections 6.5 and 6.6.

The homogeneity of the static magnetic field B_0 was evaluated using the *field* sequence (Figure 94A). A single interference line corresponds to a change in the B_0 field of 0.254 ppm, as described in the Appendix. When no PET electronics were installed, the B_0 field revealed an inhomogeneity of 1.27 ppm (Figure 94A left). Installing and operating the PET modules in the center of the MRI bore resulted in a single additional interference line (Figure 94A right). This line corresponds to a minor increase of 0.254 ppm to 1.524 ppm in the inhomogeneity of the B_0 field.

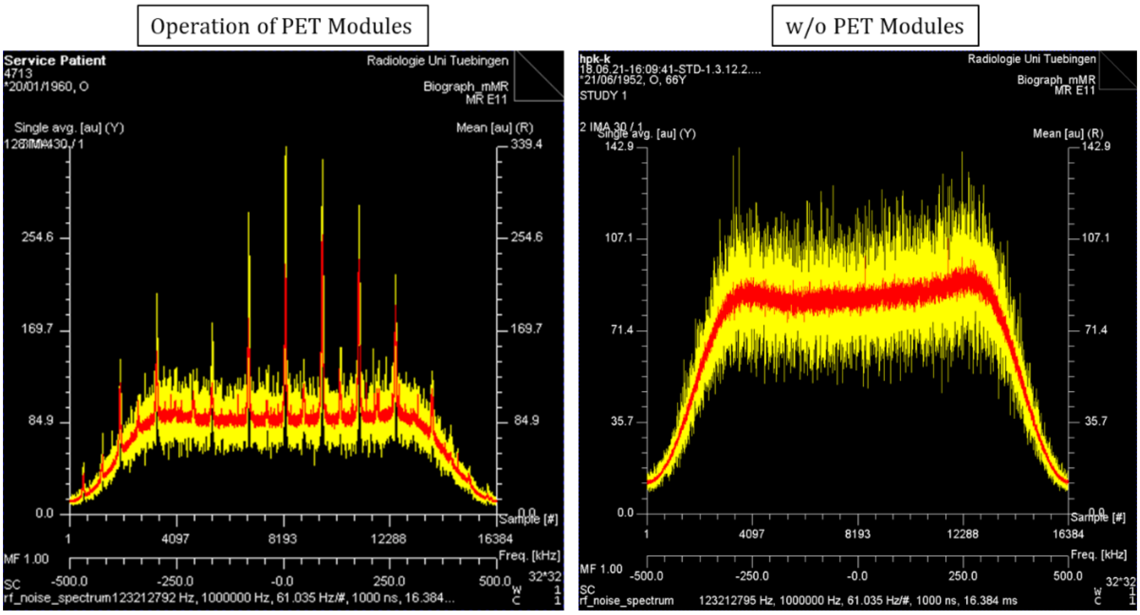

Figure 93: Left: Normal operation of the PET modules encapsulated in the copper shielding boxes. Right: Reference RF noise spectrum without the PET modules installed.

The homogeneity of the RF field B_1 was evaluated using the *rf_field* sequence (Figure 94B). In comparison to the reference measurement with neither PET module installed (Figure 94B left), two additional interference stripes were introduced (Figure 94A right) when the PET modules were operated in the center of the MRI bore. Conclusively, the two PET modules caused a change to the B_1 field of 12.5 % (6.25 % per additional interference stripe).

Figure 94C (right) depicts representative images acquired by the *spin echo* sequence used to evaluate the potential impact of the MRI scanner on the PET modules. No significant visual distortion was observed when the PET modules were operated inside the MRI bore compared to the reference measurement. This qualitative comparison serves as a proof of concept that imaging with a spin echo sequence while simultaneously acquiring data from the PET modules is feasible. A more quantitative analysis, such as examining the impact on the signal-to-noise ratio, is subject to investigation for a test setup that more closely resembles the final breast insert, including multiple detectors arranged according to the geometry of the insert.

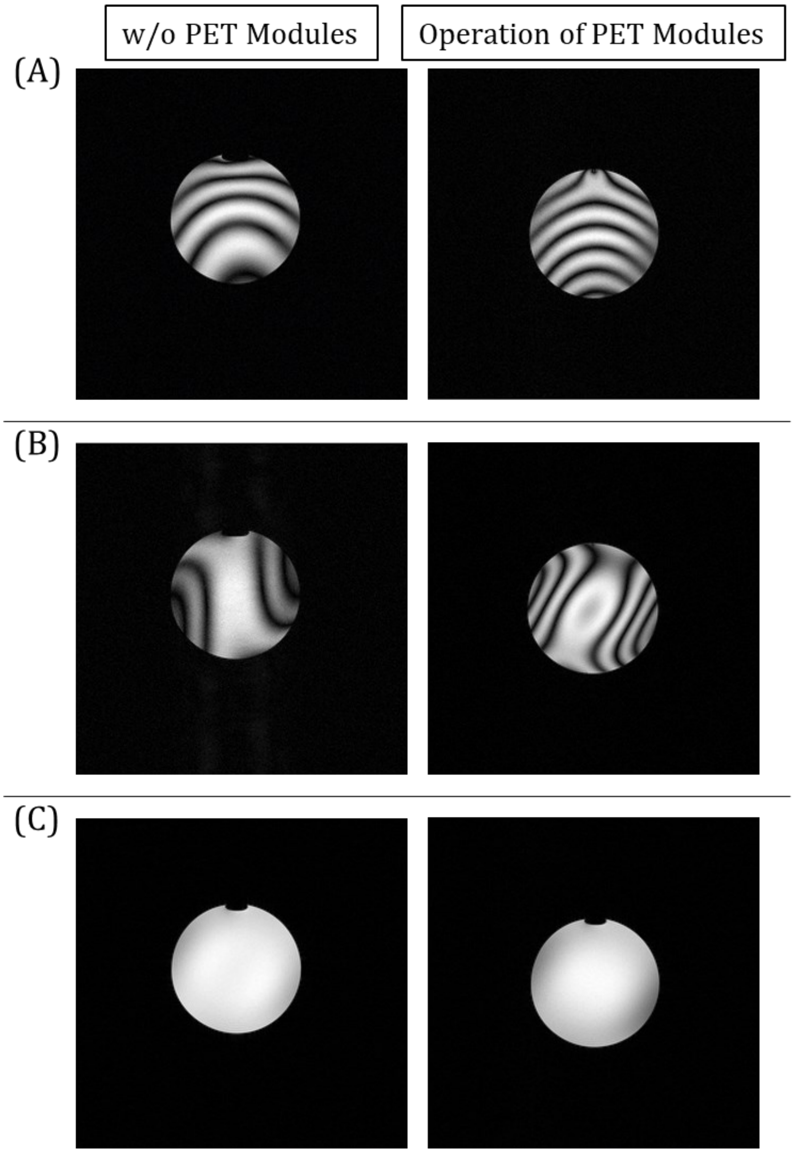

Figure 94: Images of the cylindrical phantom acquired with the field sequences (A), rf_field sequence (B), and spin echo (C). Left: Without the PET modules installed. Right: Normal operation of the PET modules encapsulated in the copper shielding boxes.

6.4.3 Discussion and Conclusion

Neither switching the gradients with a high slew rate of 100 T/ms^{-1} (with 28.6 % duty cycle) nor using a high duty cycle of 66.7 % (with 20 T/ms^{-1} slew rate) caused any performance degradation in the PET modules, including their energy or timing measurement accuracy. Furthermore, as the single event count rate and coincident event count rate were not affected by the application of the gradient sequences, it can be concluded that no spurious pseudo-events were triggered by the gradients and no PET events were consequently discarded.

However, RF pulses with a FA of 90° caused a distortion in the time stamp differences of coincident events. The probability for these spurious time stamp differences was highest for multiples of the inverse of the Larmor frequency. This indicates that RF distortion did not lead to a general malfunction of the components responsible for acquiring time stamps during the total measurement time. Instead, the time stamp distortions were related to the characteristic periodical signal shape of the RF pulses, as they would occur by coupling the RF waves with the signal processing board’s signal or supply traces, which affect the trigger point of the analog PET signal.

Furthermore, it is likely that the time stamps were distorted only during the phase when the RF pulses of the *rf_pulse* sequence were transmitted. This would be consistent with an increased probability of distorted time stamps at a distance of multiples of the repetition time of the *rf_pulse* sequences. Therefore, for the next MRI compatibility test setup described in the following section, a more comprehensive analysis was performed to determine how different RF pulse distortions impact the characteristics of the PET events.

It is possible to use a spin echo sequence while the two PET modules are operating. However, the timing performance was slightly degraded, as indicated by the increase of the CRT by 13 ps in comparison to the reference measurement. In addition, the coincidence count rate was reduced by 14.1 % in comparison to the reference measurement, indicating that this fraction of valid coincident PET events was not recorded. These degradations do not impede the operation of the PET modules; however, they would lead to a decrease in the sensitivity and image quality of the PET system. As a spin echo sequence involves several RF pulses and the performance degradations caused by the spin echo sequence are related to distortions of the PET event time stamps, it is assumed that this performance degradation was caused by an RF distortion.

A potential reason for this sensitivity to RF pulses might be that the PET modules were insufficiently shielded. This explanation can be confirmed by the heavily distorted RF noise spectrum that occurred with the 18 µm copper shielding, whereas no distortion was observed with setup C (section 6.3.2), which had a 2 mm-thick aluminum shielding. Therefore, the shielding was further improved for setup E, discussed in the following section, by soldering the edges of the copper layers, which are prone to the penetration of RF waves.

Furthermore, the inhomogeneity of the B_0 field increased when the PET modules were installed. However, this increase of 0.254 ppm is below the specific threshold of 0.5 ppm, which is the accepted value for MRI compatibility for the Biograph mMR in regard to B_0 inhomogeneity.

The inhomogeneity of the B_1 field also increased by 12.5 % because of the PET modules. For this test scenario, a variation of up to 10.0 % is the threshold to pass the MRI compatibility specifications. At the current stage of development, this slight excess of the threshold is tolerable, as it does not cause a severe degradation of the MRI scanner's performance. Changing the shielding and orientation of the PET detectors in the final insert with respect to the B_1 field will potentially decrease this inhomogeneity.

The B_1 and B_0 homogeneity were only tested for the two PET modules and their shielding boxes inside the MRI scanner. The purpose of these tests was to evaluate whether the introduced inhomogeneities were so severe that changes to the material, shielding, or components would be required already for a single module. The results showed that such changes are not mandatory. However, to guarantee the MRI compatibility of the total PET/MR breast insert, further tests on the structure of the total PET/MR insert, including the PET modules and the RF breast coil, should be performed.

6.5 MRI Compatibility Test Setup E: Signal Transmission via Optical Fibers and PET Modules with Improved Moderate RF Shielding

6.5.1 Material and Methods

In comparison to setup D, the shielding for setup E was improved by soldering the shielding boxes of the detectors at critical spots prone to leakage of RF waves (e.g., the joints between the copper tape and the 18 µm copper foil, the area around the DSUB connector, the overlapping copper tape of the waveguides). Figure 95 depicts a comparison between the former non-soldered version of the shielding box and the new soldered version.

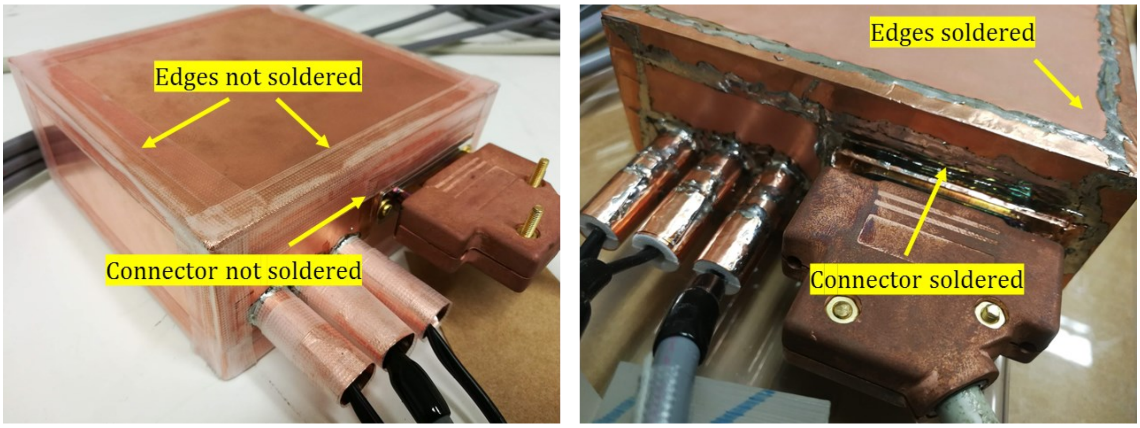

Figure 95: Shielding boxes for the PET modules with the 18 µm-thick copper layer. Left: Version without soldering used for setup D. Right: Soldered version used for setup E.

The arrangement of the back-end and the front-end electronics was the same as in setup D (Figure 89). The same holds true for the coincidence setup and the position of the front-end and back-end electronics, supply voltages, and cable connections. Due to decay, the activity of the Na-22 radiation source was 395 kBq during the test for setup E.

This section discusses the impact of RF wave coupling on the PET detectors' power cables. The power cable on detector 1 was routed in either a curved or straight position, with the curved position exposing a larger part of the power cable to the transmitted RF pulses and potentially leading to a stronger distortion of the PET modules by the RF waves. Both of the detectors' power cables were fed through the front side of the opening of the MR bore (Figure 96).

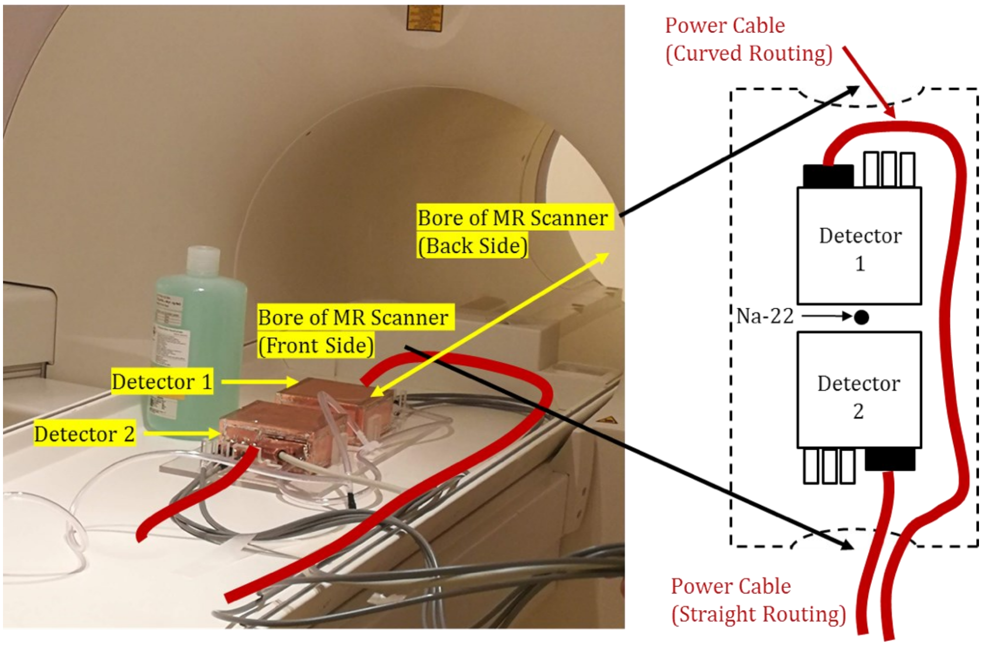

Figure 96: PET detectors with power cables fed in the same direction and the curved routing of the power cable of detector 1. For visualization, the setup is shown at a bed position outside of the MRI scanner; however, the measurements were performed with the setup at the center of the MR bore.

This configuration led to the curved routing of the detector 1 power cable. For the measurement with the straight cable (Figure 97), the detector 1 power cable was fed through the back of the MR bore.

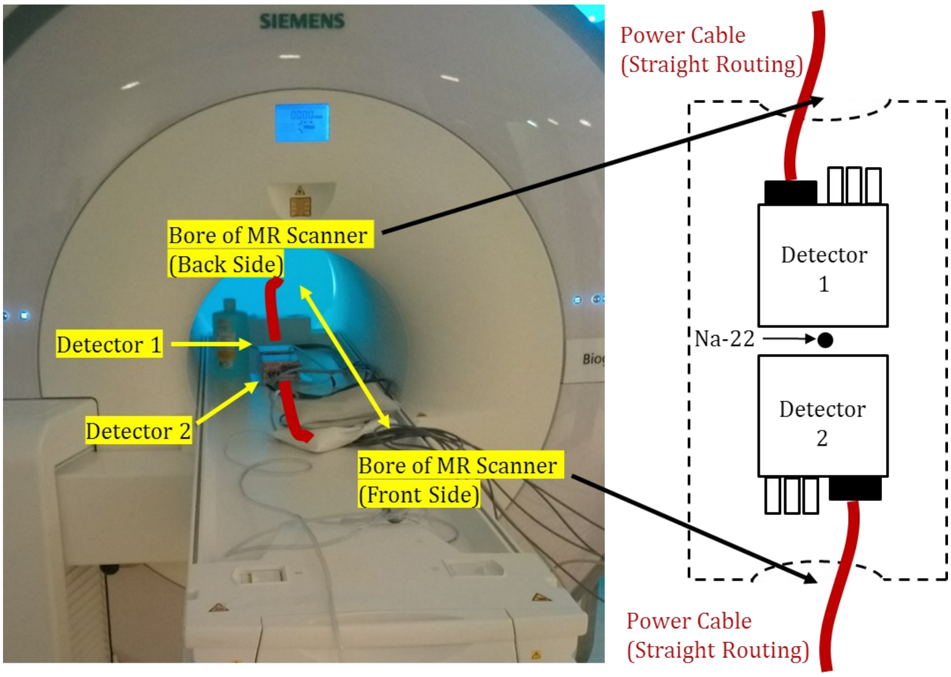

Figure 97: PET detectors with power cables fed in opposite directions and the power cable of detector 1 routed straight.

In total, 1×10^7 data events were acquired for both detectors, and the energy spectra, timing histograms, and CRT were observed, as previously described. For the measurements discussed in this section and the following section, the time skew correction was applied, as described in section 4.2.2. The following evaluations were performed:

1. The first test investigated whether the spurious spikes in the timing histogram caused by the previously reported RF-distorted the time stamps could be prevented with improved shielding. The timing histogram was acquired with the front-end electronics placed at the center of the MR bore and the detector 1 power cable curved while applying an *rf_pulse* sequence with FA=90°, PW=1 ms, and TR=3 ms.
2. Furthermore, for a more detailed analysis of the time stamps' RF pulses distortion, the timing histograms and CRT for both setups (with curved and straight routing) were compared for *rf_pulse* sequences with the following parameters:
   - FA=30°, TR=3 ms, PW=1.5 ms
   - FA=80°, TR=3 ms, PW=1.5 ms.

   In addition, to evaluate the effects of RF distortion on the energy values of the PET events, the energy spectrum for the total scintillator block of detector 1 was analyzed using different *rf_pulse* sequences and both power cable routings.
3. Potential distortions in the spectrum acquired by the *rf_noise_spectrum* sequence were evaluated during PET module operation by storing the raw data of these measurements, thus enabling a quantitative analysis of the spectra. The mean value and standard deviation of the long-term RF noise spectrum, as described in the Appendix, were calculated between the frequencies of 123.0 MHz and 123.4 MHz. The resulting mean values were compared to a reference measurement taken with the PET modules powered off.
4. In addition, a second test sequence called *rf_noise* was used to evaluate distortions in the RF receiving spectrum of the body coil. As described in the Appendix, this sequence uses a narrower bandwidth of 500 kHz and a

receiving spectrum used for the normal operation of the MRI scanner. As such, if the *rf_noise* sequence spectrum is not distorted, it can be concluded that the MRI scanner is operating normally.

In order to quantitatively analyze the spectra of the *rf_noise* sequence, a fit with a two-term Gaussian model of the RF power values over the total bandwidth was used, as shown in Figure 98 and described by the formula

$$f(x) = a_1 * e^{-\left(\frac{x-b_1}{c_1}\right)^2} + a_2 * e^{-\left(\frac{x-b_2}{c_2}\right)^2}.$$

The peak position of this distribution was used to quantify the mean value of the noise floor in the *rf_noise* sequence spectrum.

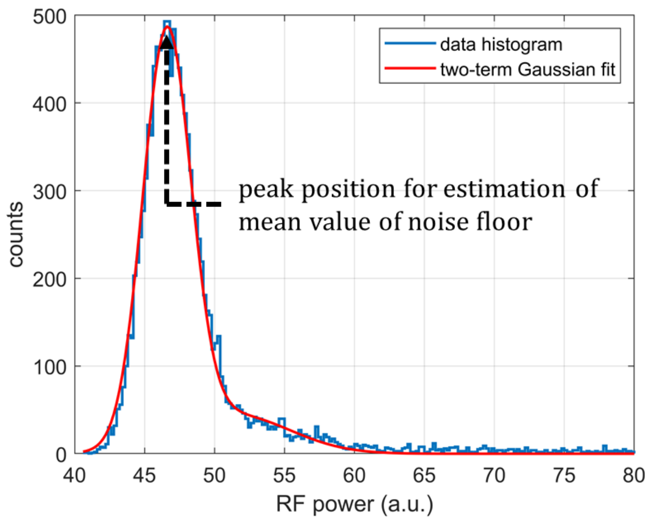

Figure 98: Two-term Gaussian fit of RF power values of the spectrum acquired with the rf_noise sequence.

The spectra of the *rf_noise* sequence and the corresponding mean values and standard deviations were acquired for setup D (Figure 95 left, non-soldered shielding boxes) and setup E (Figure 95 right, soldered shielding boxes) to evaluate the impact of the improved shielding on the RF distortion of the MRI scanner. The mean values and standard deviations were then compared to a reference measurement taken with the PET modules powered off.

6.5.2 Results

Influence of the MRI Scanner on the PET Modules' Performance

Figure 99 shows the coincidence timing histogram for operating the PET modules inside the soldered (setup E) and non-soldered shielding box (setup D) while an *rf_pulse* sequence with FA=90° is applied.

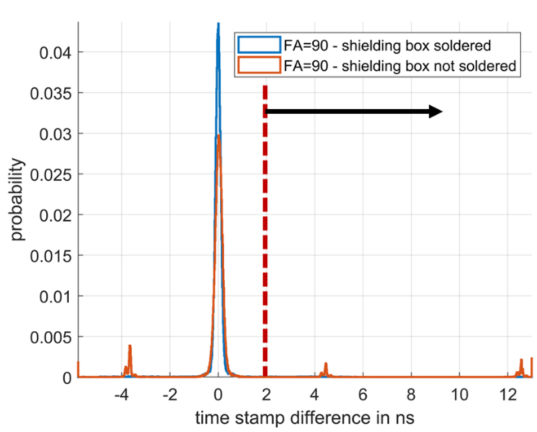

Figure 99: Coincidence timing histogram for the applied 90° RF pulses and different versions of the shielding boxes. Left: For an interval between -6 ns and 13 ns. Right: For an interval between 4 ns and 50 ns.

The spurious peaks caused by the distortion of the PET event time stamps were eliminated when using the soldered shielding box. Figure 100 (left) demonstrates different Gaussian distributions of the timing histograms of measurements taken with the PET modules inside the soldered shielding box while using different RF pulse sequences and power cable routings.

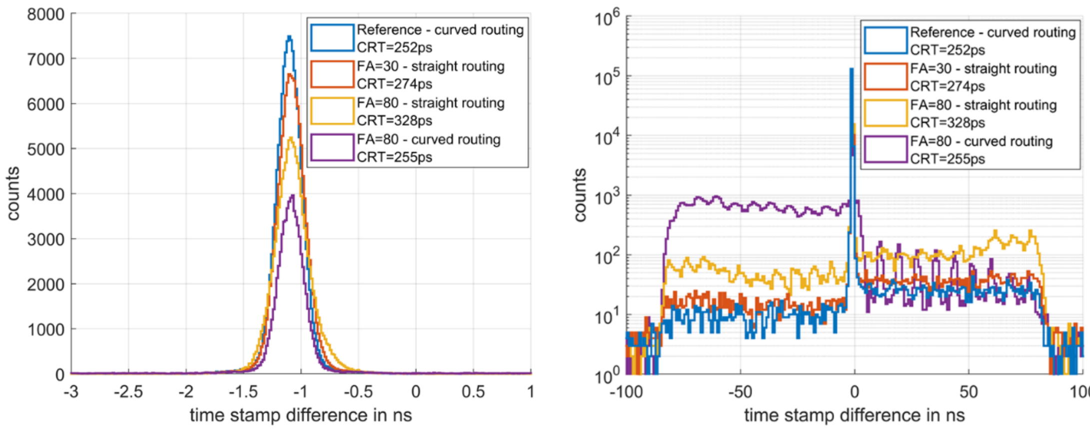

Figure 100: Coincidence timing histograms for different applied rf_pulse sequences and different routings of the detector 1 power cable. Left: Linear representation of the main Gaussian distribution (with 0.015 ns bin width). Right: Logarithmic representation between -100 ns and 100 ns (with 0.9 ns bin width).

The reference measurement with no RF pulses yielded a CRT of 252 ps. Applying the *rf_pulse* sequence with FA=30° and using a straight cable routing caused the CRT to degrade to 274 ps. An increase in the RF power with an *rf_pulse* sequence with FA=80° and a straight cable routing further degraded the CRT to 328 ps.

For RF pulses with an 80° flip angle and a curved detector 1 power cable, the CRT was 255 ps, which is comparable to the reference measurement CRT of 252 ps. This result seems counterintuitive at first, as the curved routing is assumed to be prone to a larger distortion by the RF pulses, hence yielding a degraded CRT in comparison to the reference measurement. However, the combination of curving the detector 1 power cable and applying 80° flip angle RF pulses increased the probability for time stamp differences located left of the main Gaussian distribution (Figure 100 right, purple). More precisely, the number of events with a time stamp difference of less than -2 ns is 51.6 times higher than the number of events in that range for the reference measurement.

These observations indicate that, while low power RF distortions resulted in a moderate variation of the time stamps, high power RF distortions caused a different type of error, with larger deviations in the time stamp differences.

The total block energy spectra (Figure 101) did not reveal any differences between the reference measurement and the measurement with an *rf_pulse* sequence with FA=30° (curved routing) and FA=80° (straight routing). However, the *rf_pulse* sequence with FA=80° distorted the energy values of the PET events with the curved cable routing, which is observed in the energy spectrum's spurious alternating pattern (Figure 101 right, yellow). A further increase of the flip angle to 90° diminished this effect and increased the width of the distribution around the photo peak (Figure 101 right, purple).

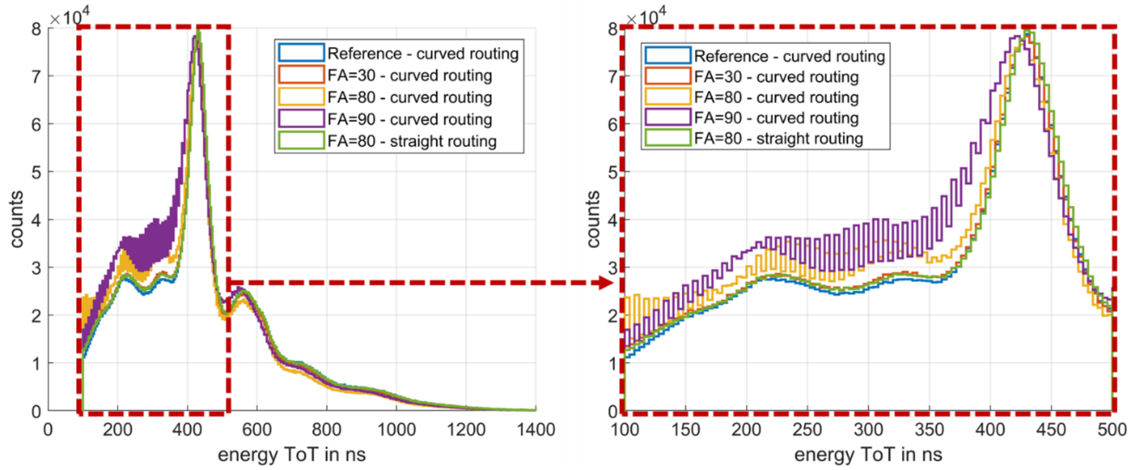

Figure 101: Energy spectra of the total scintillator block of detector 1 for different rf_pulse sequences and different power cable routings. Left: Interval between 0 ns and 1400 ns. Right: Interval between 100 ns and 500 ns.

<u>Influence of the PET Modules on the MRI Scanner's Performance</u>

It was previously reported that operating the PET modules inside the non-soldered version of the copper shielding boxes caused severe RF distortions visible in the RF noise spectrum.

Compared to the reference measurement with the PET modules powered off (Figure 102 left), the use of the soldered shielding boxes helped to maintain a clean RF noise spectrum while operating the PET modules (Figure 102 right).

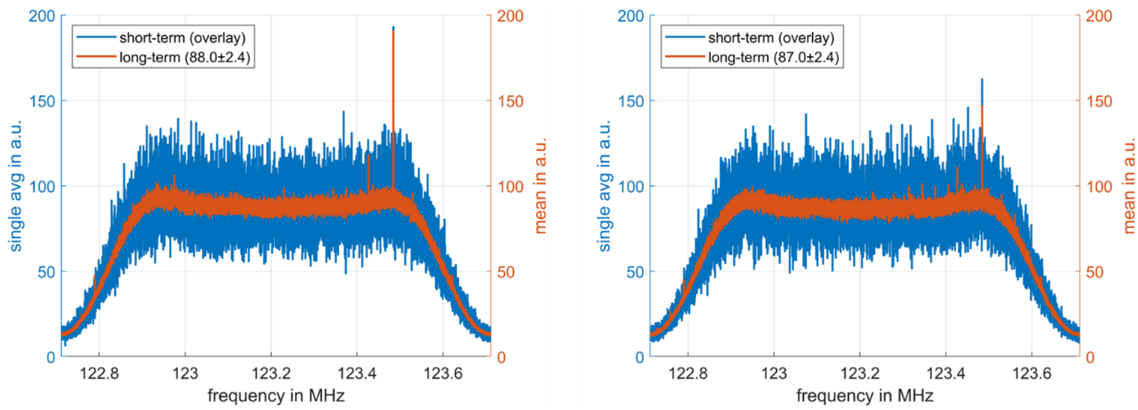

Figure 102: Left: Reference RF noise spectrum with the PET modules powered off. Right: Normal operation of the PET modules encapsulated in the soldered version of the copper shielding boxes.

The mean value for the RF noise spectrum was 87.0±2.4 while the PET modules were operating and is nearly identical to the reference spectrum mean value of

88.0±2.4. Hence, the soldered version of the copper shielding box sufficiently attenuates RF waves transmitted by the PET modules.

Furthermore, the spectrum acquired with the *rf_noise* sequence did not reveal any distortion when the PET modules were operated inside the soldered shielding boxes compared to the reference measurement (Figure 103).

Figure 103: Spectra acquired with the rf_noise sequence. The top and middle spectra were acquired with MRI compatibility test setup E and the bottom spectrum with setup D.

The mean value and standard deviation of the RF power values over the total spectrum remained stable at 46.0±1.6, in comparison to the reference measurement value of 46.2±1.6. The spectrum acquired while the PET modules were operating inside the non-soldered shielding boxes maintained a mean value of 46.6 and had an increased standard deviation of ±6.7. In addition, this spectrum suffered from severe distortions, as shown by the spurious spikes in Figure 103 (bottom).

6.5.3 Discussion and Conclusion

The soldered shielding increased the robustness of the PET modules against RF wave penetration, as the time stamp distortion, which previously caused spurious spikes in the timing histogram, was decreased. However, the CRT degraded with the power of the RF distortion (e.g., up to 76 ps for RF pulses with FA=80°). Therefore, the time stamps are still distorted, though not as strongly, as the degree of distortion is dependent on the power of the RF pulses.

Figure 104 depicts an explanation of the CRT degradation due to RF distortion.

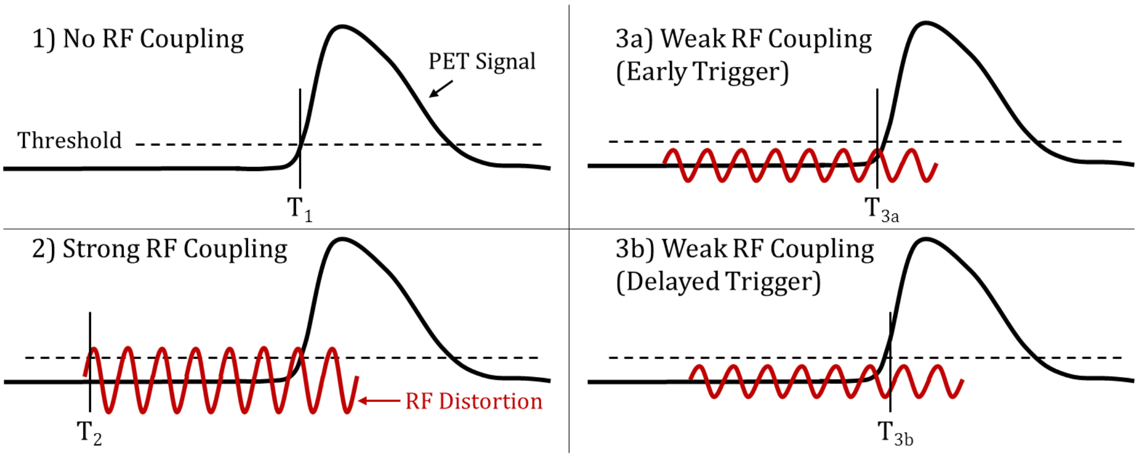

Figure 104: Simplified illustration of PET event time stamp T_x and superposition of RF distortion and PET signal. Case 1) reference time stamp T_1 without any RF distortions; case 2) strong RF coupling T_2<<T_1; case 3a) weak RF coupling T_{3a}; case 3b) weak RF coupling T_{3b}>T_1 (a different phase difference between the PET signal and RF distortion than for case 3a).

When no RF pulses are applied, the time stamp T_x of a PET event depends on the time when the PET signal reaches the timing threshold. An RF distortion can potentially affect this time stamp trigger circuit. This can be simplified as a superposition of the RF distortion, shown in Figure 104 (red) and the PET signal (black). The superposition signal reaches the threshold at a different time point and shifts the time stamp of the PET event.

If the coupled RF distortion is weak, a slightly lower T_{3a} or higher T_{3b} time stamp is created, depending on the phase difference between the RF distortion and the PET signal. Consequently, the main Gaussian distribution broadens, and thus the CRT increases.

Furthermore, a curved routing of the detector 1 power cable, together with applying an *rf_pulse* sequence with FA=80°, increased the probability of negative time stamp differences in the timing histogram. The time stamp difference is calculated as the time stamp of detector 1 minus the time stamp of detector 2. As such, the increased probability of observing negative time stamp differences can be explained by the lower values for the detector 1 time stamps due to RF distortion. A possible explanation for this behavior is illustrated in Figure 104 (bottom left). If the RF distortion is high enough to cross the timing threshold itself, the time stamp values of the PET events would be lower than for the test with no RF distortion. Applying the same *rf_pulse* sequence with FA=80° showed the effects of a weak RF coupling for the straight power cable routing, and the effects of a strong RF coupling for the curved routing. The distortion of the time stamps is thus due to a coupling of the RF pulses on the power cable. When curved, a larger part of the power cable is exposed to the transmitted RF waves, and it is assumed that this leads to stronger coupling of the RF waves than the straight routing. This assumption also explains why using a straight power cable and an *rf_pulse* sequence with FA=80° caused no distortions in the energy values of the PET events, whereas the energy values were heavily distorted using the same sequence and a curved routing of the power cable.

In order to mitigate the effect of noisy coupling on the power cable, filters at the front-end of the PET modules were used for the MRI compatibility setup described in the next section. In addition, a more detailed analysis of the PET events during the active phase of the *rf_pulse* sequence (i.e., when RF waves are transmitted) will be provided.

The spectra of the test sequences *rf_noise* and *rf_noise_spectrum* did not exhibit noticeable differences from those of the reference measurements when the PET modules were operating in the soldered shielding boxes. This finding is also verified by the mean spectra values of 46.2±1.6 and 46.0±1.6 for the *rf_noise* sequence and mean spectra values of 88.0±2.4 and 87.0±2.4 for the *rf_noise_spectrum* sequence, which correspond to the reference measurement and the test with the PET modules operating, respectively. These results are in sharp contrast to the tests using the non-soldered shielding boxes. Hence, spurious RF waves transmitted by the PET modules were able to penetrate the non-soldered shielding and affect the MRI scanner’s RF receiver, whereas the soldered shielding boxes prevented this occurrence.

Until this point, all MRI compatibility measurements with regard to RF distortion were performed with the MRI scanner's body coil. As the PET modules will be used for the breast PET/MRI insert, the following section considers a commercially available RF breast coil BI 320-PA-SI (NORAS MRI products, Höchberg, Germany) and how it responds to the RF distortion introduced by the PET modules.

6.6 MRI Compatibility Test Setup F: Signal Transmission via Optical Fibers and PET Modules with Front-End Filter and RF Coil for Breast Imaging

6.6.1 Material and Methods

In comparison to setup E, setup F used filters for the power lines located at the front-end of the PET modules. Hereafter, each of the five supply voltages (1.1 V, 1.9 V, 2.5 V, 3.3 V, 62 V) and the ground reference potential (GND) were filtered individually with a low pass filter (Figure 105 left).

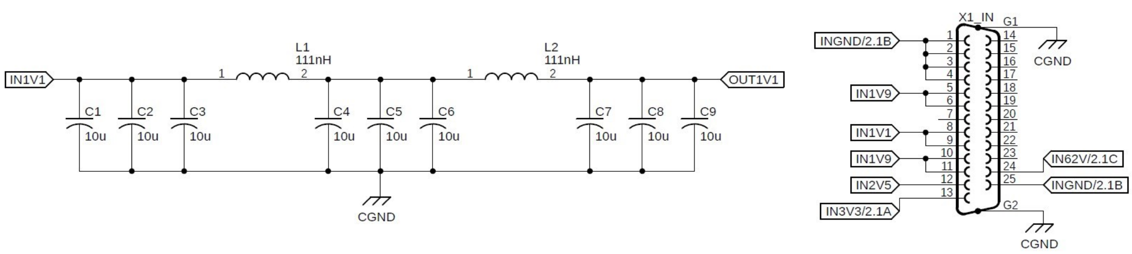

Figure 105: Left: Schematic of the filter circuit for one out of six supply voltages. Right: Schematic of the DSUB connector for the power input of the front-end (FE) filter board.

The six individual filter circuits were placed on the top and bottom sides of a PCB, as shown in Figure 106A/B. The filter board itself was placed inside an 18 µm-thick copper shielding box, comparable to the PET detectors' shielding box. For each PET module, a front-end filter was used that could serve as an optional interface between the power cable's connector and the DSUB connector of the PET module's shielding box. The chassis ground was connected for the connector shell of the power cable, the shielding box of the front-end filter, and the shielding box of the PET detector.

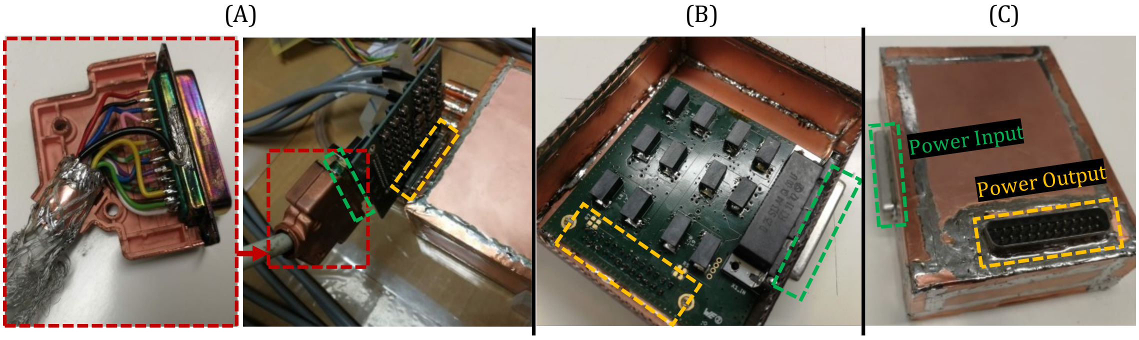

Figure 106A: Open connector shell of the power cable and front-end filter between the shielding box of the PET detector and the power cable (without the shielding box for visualization purposes). Figure 106B: Front-end filter placed inside the shielding box with the open lid for visualization. Figure 106C: Closed shielding box for the front-end filter with power input and output connectors.

Figure 107 illustrates the final setup, with both detectors in coincidence and mounted front-end filters.

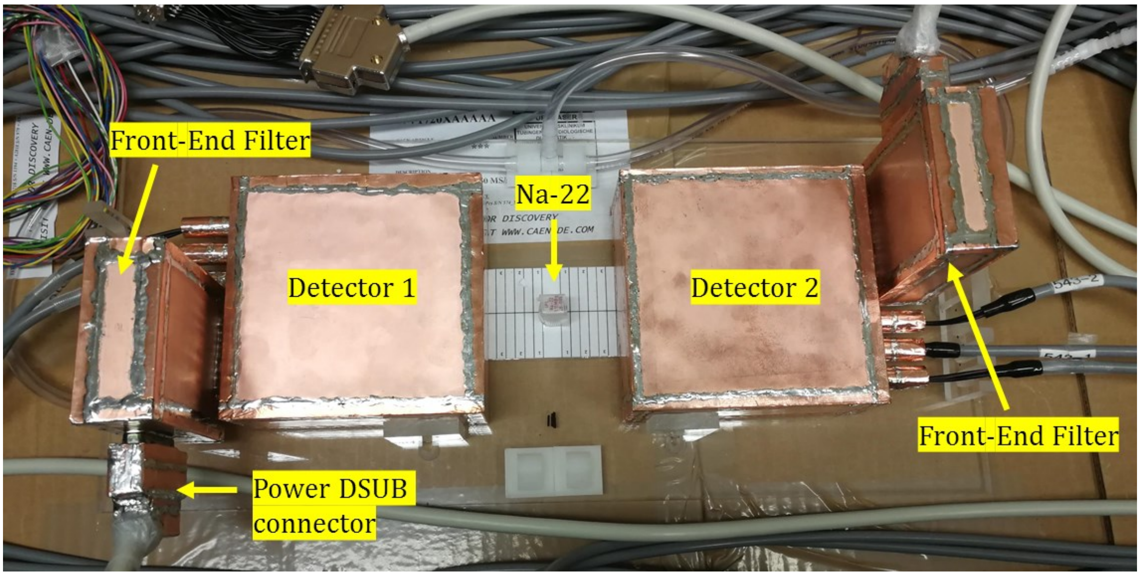

Figure 107: Coincidence setup with detectors inside 18 µm copper shielding boxes and mounted front-end filters inside shielding boxes with a centered 353 kBq Na-22 source.

Except for the front-end filters, no changes to the setup were done in comparison to setup E. Figure 108 shows the PET modules with the front-end filters and how the power cables were routed inside the MR bore.

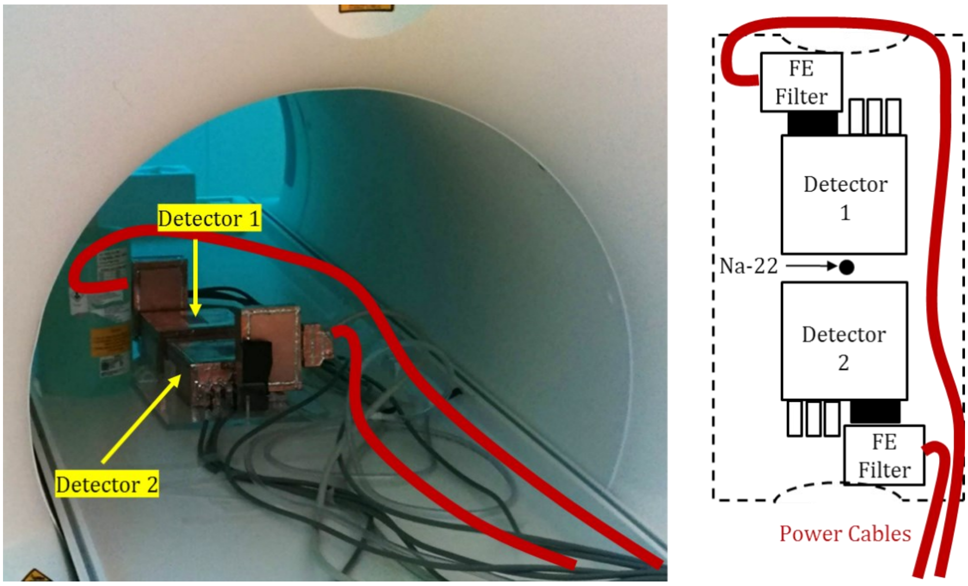

Figure 108: PET detectors with front-end filter boxes operated at the center of the bore of the Biograph mMR.

A possible synchronization between the PET modules and the MRI scanner was tested, as the PET modules' current clock signal with a frequency of 50 MHz is not supported by the MRI scanner's clock box (Figure 109).

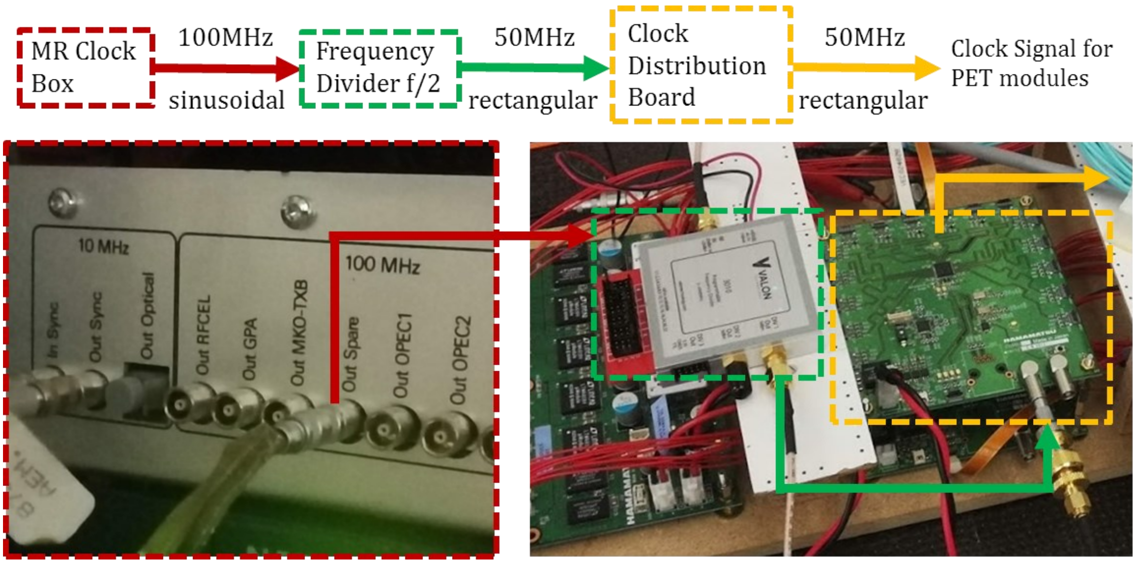

Figure 109: Signal chain for synchronizing the clock signal of the MRI scanner and the PET modules with the MR clock box, frequency divider, and clock distribution board.

Therefore, the MRI scanner's sinusoidal clock signal with a frequency of 100 MHz was converted to a rectangular 50 MHz signal by a frequency divider (3010A, Valon Technology, San Francisco, CA, USA). This 50 MHz signal was used as an input signal for the clock distribution board instead of the clock signal provided by the relay board.

Section 6.5.2 (setup E) explained that the energy and timestamp values of the PET events were distorted by applying the *rf_pulse* sequence, even with improved shielding. In addition, section 6.4.2 (setup D) reported that the distortion of the time stamps was related to the repetition time of the *rf_pulse* sequence, which gives rise to the following assumption: PET events were directly affected by the RF pulses. However, indirect distortion (i.e., lasting effects) during the time when no RF pulses were transmitted was not caused by the RF pulses. This section first considers the validity of this theory and provides a detailed analysis of the events in the RF on phase (i.e., the time slots in the *rf_pulse* sequence when RF pulses are transmitted). Next, this section discusses whether using front-end filters for the PET modules can prevent the RF distortion of the PET events.

In order to evaluate both of these objectives, the following steps were performed. It should be noted that all events acquired during the RF on phase could be extracted when the first RF pulse start point was known. From this point on, the fact that the RF pulses had a constant pulse width (PW) and were repeated based on the repetition time (TR) was considered. However, the *rf_pulse* sequence start point was not known, meaning it was not defined with respect to the time stamps of the PET event data stream. Therefore, an approach that extracts subgroups of events for each possible *rf_pulse* sequence start point was used.

An example of this approach is shown in Figure 110. Repeating stencils of the same width PW are used to select a subgroup of PET events, which are temporarily located inside these stencils with the start point $Sp(m=1)$. A second set of stencils is illustrated for a higher value start point $Sp(m=2)$. When the start point of the stencils eventually matches the start of the *rf_pulse* sequence, the corresponding subgroup of events is equal to the events that are acquired during the RF on phase.

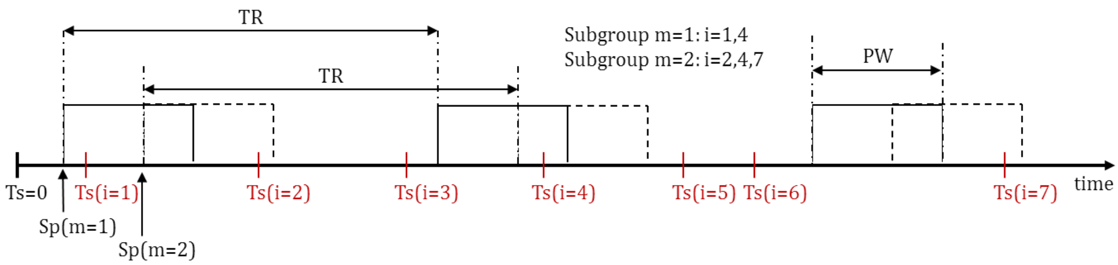

Figure 110: Visualization of the approach for extracting PET event subgroups based on repetitive stencils which mimic potential rf_pulse sequences. An example is shown for two subgroups of events for two different start points of the stencils. In this example, the PET events with the numbers 1 and 4 are assigned to subgroup 1, and the PET events with numbers 2,4, and 7 are assigned to subgroup 2.

The assignment of an event *i* to a subgroup with the start point *Sp(m)* was performed using the following formulas:

$$r(i) = \big(Ts(i) + Sp(m)\big)\%TR;\ r(i) \leq PW,$$

where *Ts(i)* is the time stamp of the PET event *i* and *r(i)* is the remainder for event *i*. If the remainder is less than or equal to *PW,* the event is assigned to the subgroup *m*. The start point *Sp(m)* is calculated by the following formula:

$$Sp(m) = \frac{TR}{N_{steps}} * (m-1),$$

where m=1:N_{steps} and N_{steps} is the total number of subgroups and defines the step size between the start points of two successive subgroups. N_{steps} is set to 100 for the data analysis presented in this section to enable an accurate identification of the subgroup of events in the RF on phase.

In total, 1×10^7 data events were acquired for both detectors, and the energy spectra, timing histograms, and CRT were observed.

PET data acquisition was performed with the *rf_pulse* sequence with FA=200°, TR=30 ms, and PW=1 ms without the front-end filters. The number of events in the 100 subgroups was determined for detectors 1 and 2. The progression of these counts in the subgroups over their corresponding start points was analyzed to identify the actual start point of the *rf_pulse* sequence. Figure 112 demonstrates that a drop in the progression of the counts in the subgroups is present, and the peak position of a Gaussian fit is considered the actual start point for the following analysis. With the start point for the *rf_pulse* sequence determined, the subgroup of events acquired during the RF on phase of the *rf_pulse* sequence was identified and analyzed. The following steps were performed first for the energy histograms of detector 1, and afterward for the coincidence timing histograms:

1. The energy values acquired during the RF on phase without front-end filters and with the 200° FA *rf_pulse* sequence were used to calculate a total block energy histogram for detector 1. This energy histogram was compared with the energy histogram of the remaining events acquired in the RF off phase and with an energy histogram of a reference measurement without the *rf_pulse* sequence applied.
2. The total block energy spectra of detector 1 with the installed front-end filter and the *rf_pulse* sequences with the following parameters:
   - FA=30°, TR=3 ms, PW=1.5 ms
   - FA=90°, TR=3 ms, PW=1 ms
   - FA=200°, TR=30 ms, PW=1 ms
   - FA=700°, TR=100 ms, PW=1 ms

   were compared to a reference block energy spectrum. The combination of a high power *rf_pulse* sequence (i.e., high flip angle) with a high duty cycle was not possible due to the MRI scanner's limitations. Therefore, the duty cycle was lowered with increasing flip angles by increasing the TR. The objective of this comparison was to validate whether the front-end filters could prevent a distortion of the energy values.

In addition, to verify whether the front-end filters helped prevent distortions of the PET event data, a quantitative analysis of the typical PET performance parameters was performed. For this analysis, the measurements with the previously mentioned four *rf_pulse* sequences were compared to a reference measurement with no MRI sequences applied.

It should be noted that the 200° FA and 700° FA *rf_pulse* sequences have a low duty cycle of 3.3 % and 1.0 %, respectively. As such, only a small fraction of the total number of acquired events is assumed to be distorted by the RF pulses. The contribution of these potentially distorted events to the overall energy and timing histograms and the PET performance parameters might be too low to cause a significant change. In order to verify that the front-end filters also prevent this small fraction of events from being distorted by the RF pulses, the events in the RF on phase were analyzed separately.

The progression of the subgroups over the corresponding start points for the 200° FA pulse sequence did not exhibit a drop in counts when the front-end filters were used (Figure 115). Therefore, it was not possible to identify the start point and thus the RF on phase for measurements using the front-end filters.

3. However, a different approach was used, which compares all of the individual total block energy histograms for detector 1 of the events of the 100 subgroups. Instead of the conventional energy histogram form (Figure 113), a color-coded histogram (Figure 116 left) was used to display multiple energy histograms in one image. Hereafter, each row corresponds to the total block energy histogram of the PET events of a subgroup. Inside each row, the position and the color of the pixel correspond to the bin position and bin value of the energy histogram, respectively. In order to validate this approach, the PET event data acquired during the 200° FA *rf_pulse* sequence without the front-end filters were analyzed. For this measurement, distortions were detected in the energy spectrum during the RF on phase, as shown in Figure 113; consequently, these distortions should also be visible in the color-coded histogram. In order to prove that the distortions in the form of a stripe-shaped artifact in the color-coded histogram (Figure 116 left) occurred during the RF on phase, the height of this stripe-shaped artifact was calculated using the following method. The counts of each energy histogram of an event subgroup were summed over a range from 100 ns to 380 ns. Accordingly, the counts of each timing histogram of an event subgroup were summed over a range from -50 ns to -2 ns. These summed energy histogram values were plotted against the start point of each subgroup, and a Gaussian fit was applied to this function. If the approach using the color-coded histogram can accurately identify distortions in the

RF on phase, the FWHM of the Gaussian fit should match the 200° FA *rf_pulse* sequence's pulse width of 1 ms. Finally, this approach should be used to investigate whether distortions in the energy values can be identified for the 200° FA and 700° FA *rf_pulse* sequences with the front-end filters installed.

In setup E, the shielding of the PET modules prevented a distortion of the MRI scanner's RF receiving spectrum; however, this measurement was performed with the body coil of the MRI scanner. In order to validate whether the shielding boxes are also capable of preventing the RF distortion of an RF breast coil, the setup illustrated in Figure 111 was used.

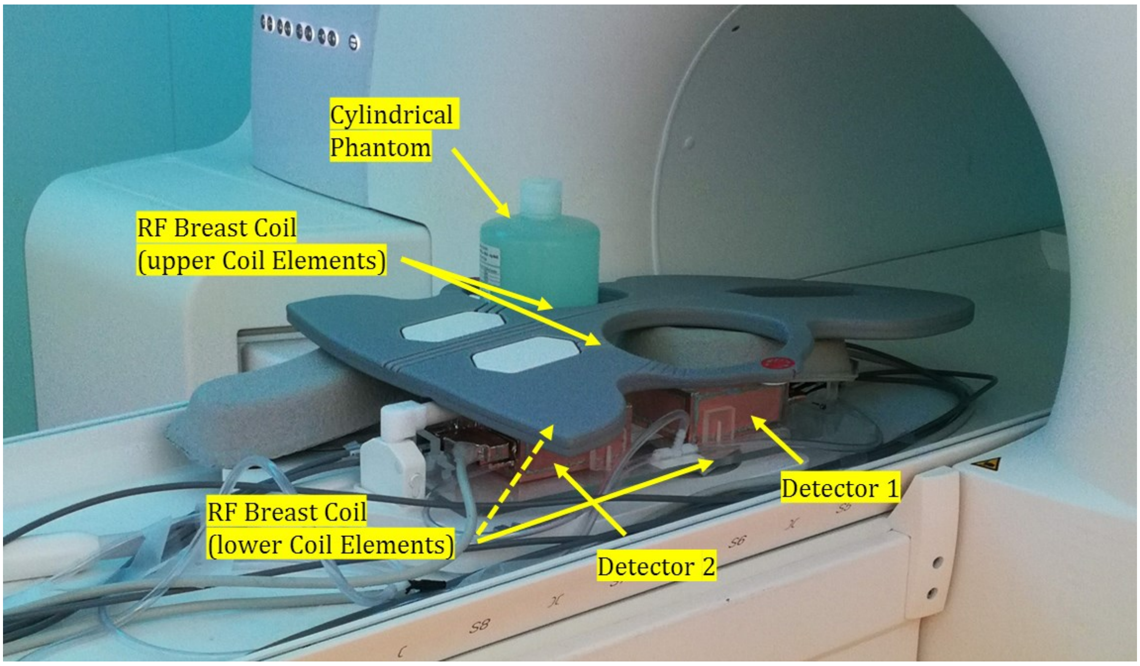

Figure 111: PET modules located between the upper and lower parts of the RF breast coil. The solid structure, which is necessary to carry the patient, was removed in order to place the PET modules close to the coil elements of the RF breast coil.

For this measurement, the RF breast coil described in section 3.1 was used to acquire the spectra with the sequences *rf_noise_spectrum* and *rf_noise,* as previously discussed. A comparison between the spectra and the corresponding mean values acquired by both test sequences was performed with the PET modules powered on and off, respectively.

6.6.2 Results

Influence of the MRI on the PET Modules' Performance

Two PET detectors without front-end filters were operated while the 200° FA *rf_pulse* sequence was applied, and the acquired PET events were sorted into subgroups. Figure 112 shows that the number of events in each of the subgroups is not stable for the 100 different subgroups.

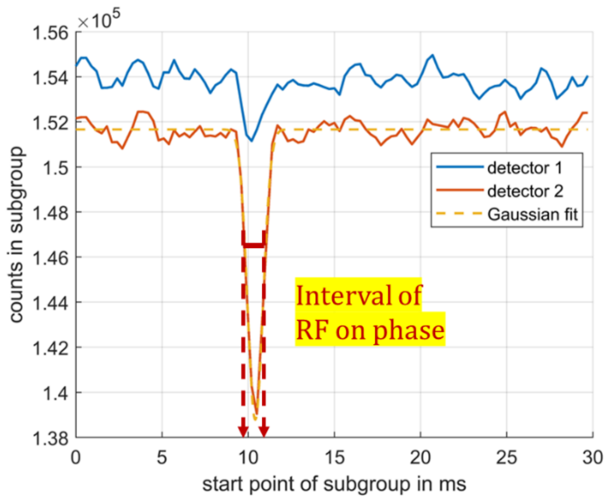

Figure 112: Progression of counts in the subgroups of the PET events acquired during an applied rf_pulse sequence with FA=200° and without front-end filters installed.

Instead, the counts in the subgroups decreased simultaneously for both detectors for an interval of 1.05 ms width (the FWHM of the Gaussian fit in yellow in Figure 112) around a start point of the subgroups of 10.5 ms. The decrease in the number of counts per subgroup was 1.8 % and 8.35 % for detector 1 and detector 2, respectively. These results were determined by calculating the ratio of the minimum of each graph in Figure 112 and the mean value of the counts in the subgroups for start point values located outside the interval between 5 ns and 15 ns. As the pulse width of the applied *rf_pulse* sequence was 1.0 ms, it is assumed that this interval corresponds to the RF on phase when RF waves are transmitted.

The PET events of the subgroup with the start point of 10.5 ms are referred to as events of the RF on phase, whereas all remaining events are called events of the RF off phase. In Figure 113, the detector 1 energy spectra for the events acquired in the RF on phase and in the RF off phase are compared to the reference spectrum with no *rf_pulse* sequences.

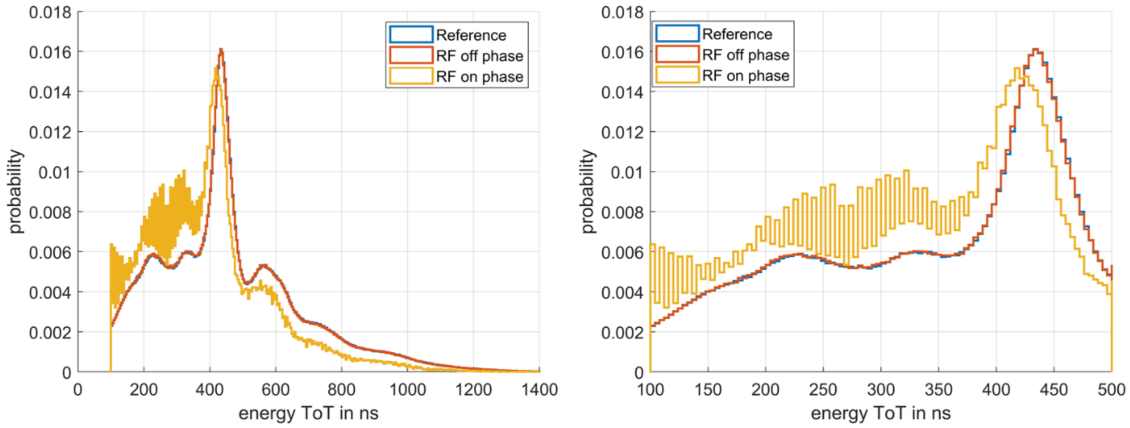

Figure 113: Total block energy spectra of detector 1 without front-end filters installed for the applied rf_pulse sequence with FA=200 (red and yellow) and without any RF pulses applied (blue). Left: For an interval between 0 ns and 1400 ns. Right: For an interval between 100 ns and 500 ns.

For the RF off phase, no difference to the reference energy spectrum was observed. However, during the RF on phase, the energy spectrum was strongly distorted, as shown by the alternating pattern left of the photo peak and the photo peak's shift of 16.2 ns in comparison to the reference measurement (Figure 113 right). These findings prove that distortions in the energy values of the PET event data do in fact only occur during the presence of RF pulses.

For the tests that used the front-end filters and the *rf_pulse* sequences with a flip angle of 30°, 90°, 200°, and 700°, the energy spectra of detector 1 did not differ from the reference spectrum (Figure 114).

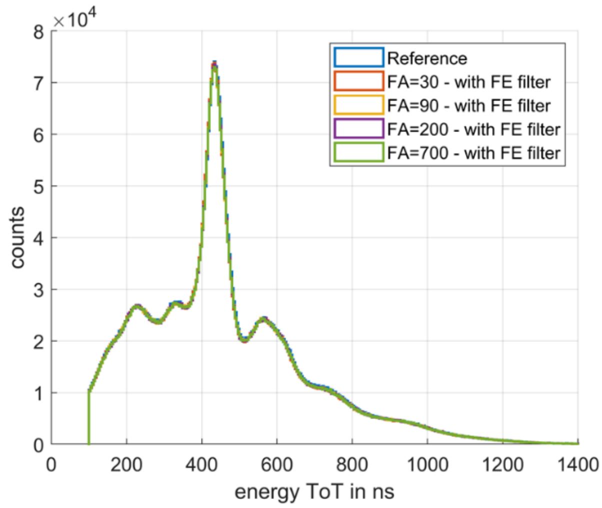

Figure 114: Total block energy spectra for detector 1 with installed front-end filter and the application of rf_pulse sequences with different flip angles.

In addition, the photo peak positions of the energy spectra and the energy resolution for each crystal were not affected by the applied *rf_pulse* sequences. The fact that the performance parameters were comparable to the reference measurement reinforces this finding (Table 7).

Table 7: Performance parameters for different applied rf_pulse sequences using front-end filters with the following abbreviations: D1,2: detector 1,2; photo peak: center position of the Gaussian fit in the single crystal energy spectrum; CRSingle: single event count rate for one detector; CRCoin: coincidence count rate for a 120 ns time window; CRT: block-to-block coincidence resolving time for ±1σ energy discriminated events.

Test Sequence	Energy Resolution (D1) [%]	Energy Resolution (D2) [%]	Photo Peak (D1) [ns ToT]	Photo Peak (D2) [ns ToT]	CRSingle (D1) [kcounts/s]	CRSingle (D2) [kcounts/s]	CRCoin [kcounts/s]	CRT [ps]
Reference	10.4±0.5	10.2±0.5	434.3±21.8	433.2±24.4	33.8	34.1	1.97	252
rf_pulse, FA=30°	10.3±0.5	10.1±0.5	433.6±21.8	433.3±24.2	33.8	34.2	1.95	252
rf_pulse, FA=90°	10.4±0.5	10.0±0.5	434.0±22.0	433.0±24.3	33.8	34.1	1.97	254
rf_pulse, FA=200°	10.4±0.5	10.1±0.5	434.1±21.8	433.5±24.3	33.8	34.1	1.96	252
rf_pulse, FA=700°	10.3±0.5	10.1±0.5	434.0±22.0	433.4±24.2	33.8	34.2	1.96	253

As such, the energy resolution for detector 1 resulted in 10.3±0.5 %, 10.4±0.5 %, 10.4±0.5 %, 10.3±0.5 %, and 10.4±0.5 % for the tests using *rf_pulse* sequences with flip angles of 30°, 90°, 200°, 700°, and the reference measurement, respectively. The energy resolution for detector 2 was 10.1±0.5 %, 10.0±0.5 %, 10.1±0.5 %, 10.1±0.5 %, and 10.2±0.5 % for the test using *rf_pulse* sequences with flip angles of 30°, 90°, 200°, 700°, and the reference measurement, respectively.

The photo peak position for detector 1 was 433.6±21.8 ns, 434.0±22.0 ns, 434.1±21.8 ns, 434.0±22.0 ns, and 434.3±21.8 ns for the test using *rf_pulse* sequences with flip angles of 30°, 90°, 200°, 700°, and the reference measurement, respectively. The photo peak position for detector 2 was 433.3±24.2 ns, 433.0±24.3 ns, 433.5±24.3 ns, 433.4±24.2 ns, and 433.2±24.4 ns for the test using *rf_pulse* sequences with flip angles of 30°, 90°, 200°, 700°, and the reference measurement, respectively.

Furthermore, whether the PET events remain distorted during the RF on phase was investigated. This test employed the previously described approach using the progression of the counts in the subgroups for different start points. However, for an applied *rf_pulse* sequence with FA=200°, the subgroups had a comparable number of 1.51×10^5±355.84 events for detector 1 and 1.52×10^5±346.77 events for detector 2 when the front-end filters were used (Figure 115).

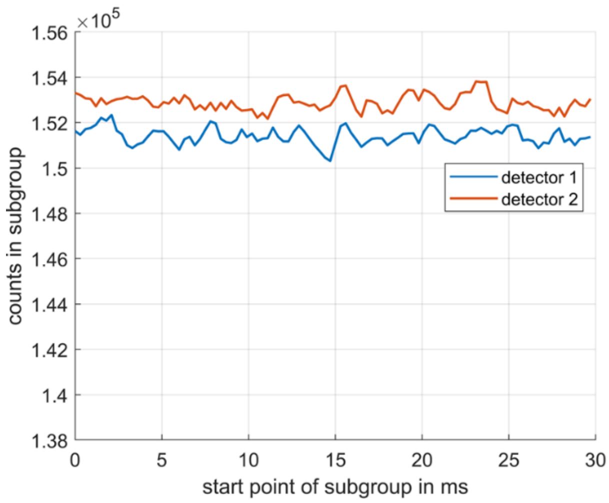

Figure 115: Progression of counts in the subgroups of the PET events acquired during an applied rf_pulse sequence with FA=200° and with front-end filters installed.

An identification of the RF on phase is not possible with this approach. Instead, the color-coded histogram, which represents multiple energy histograms, was used, as shown in Figure 116 (left).

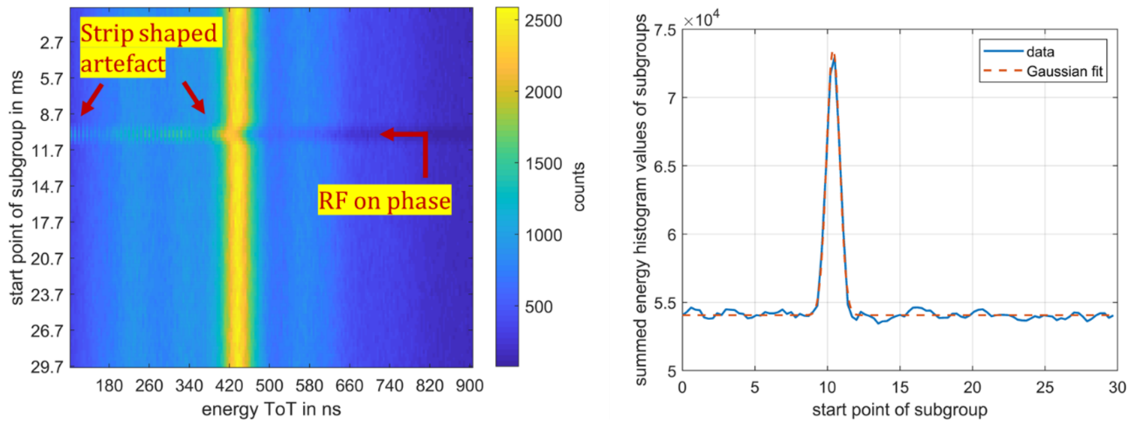

Figure 116: Left: Color-coded representation of energy histograms for the 100 event subgroups acquired during the application of the rf_pulse sequence with 200° FA and without front-end filter installed. Right: Summed energy histogram values between 100 ns and 380 ns for each subgroup.

The color-coded histogram is based on PET event data acquired during the application of the 200° FA *rf_pulse* sequence without the front-end filters installed. As such, it is possible to verify that the color-coded histogram identified distortions in the energy values. Strong distortions for the energies of the events acquired in the RF on phase were detected. The resulting alternating pattern and the photo peak's shift to the left of the energy spectrum (Figure 113 yellow) introduced distortions in the row at the start point of 10.5 ms of the RF on phase (Figure 116 left). The area left to the photo peak revealed alternating pixel colors and showed that the photo peak itself (Figure 116 left, yellow line) was distorted to the left. In addition, the height of the stripe-shaped artifact in Figure 116 was calculated by a Gaussian fit. The resulting FWHM of the Gaussian function, as shown in Figure 116 (right), was 1.06 ms, compared to the 1.00 ms PW of the *rf_pulse* sequence. Finally, when the front-end filters were installed, no energy values distortions were observed for *rf_pulse* sequences with FA=200° and FA=700°, respectively (Figure 117).

In order to investigate potential distortions to the time stamps, the coincidence timing histograms in the RF on phase and the RF off phase of the *rf_pulse* sequence with FA=200° were analyzed with no front-end filters.

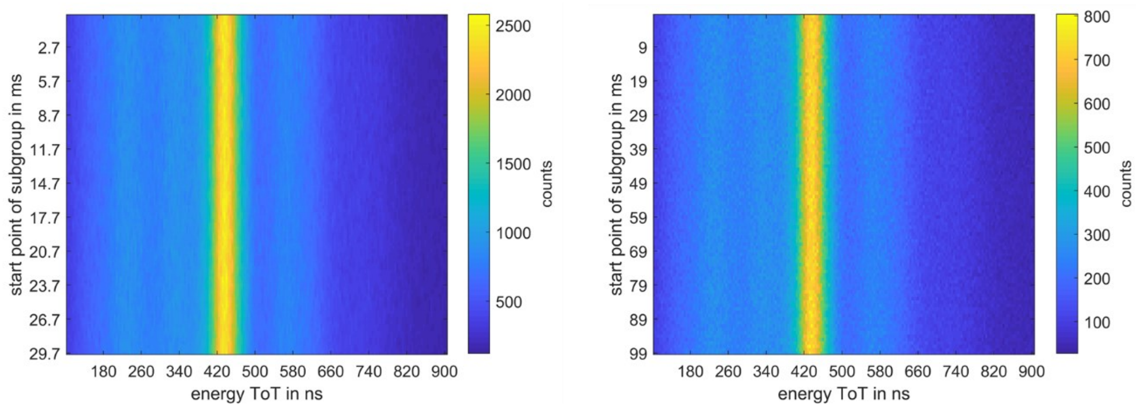

Figure 117: Color-coded representation of energy histograms for the 100 event subgroups acquired during the application of the rf_pulse sequence with front-end filter installed. Left: For rf_pulse sequence with 200° FA. Right: For rf_pulse sequence with 700° FA.

In Figure 118 (left), the probability of events inside the main Gaussian distribution of the coincidence timing histogram was reduced in the RF on phase by a factor of 4.3 in comparison to the reference measurement (events with a time stamp difference between -2 ns and 0 ns were used for this calculation).

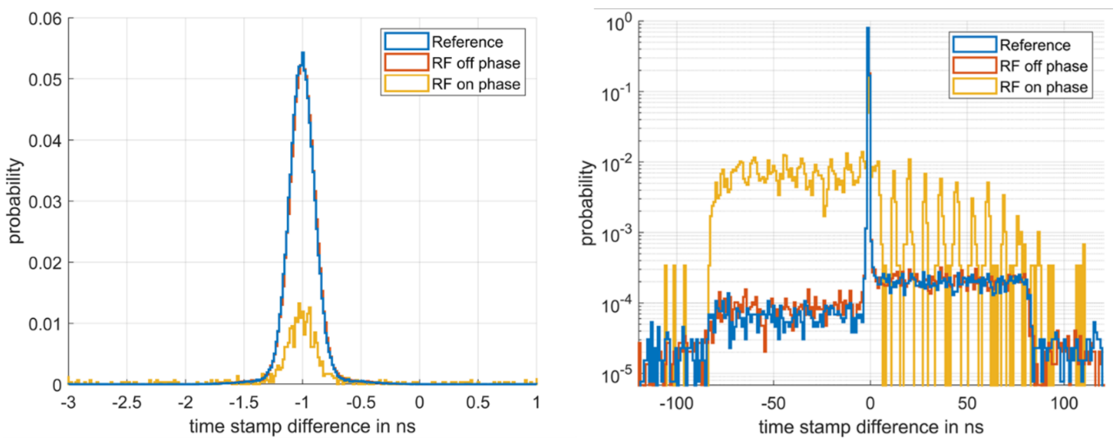

Figure 118: Coincidence timing histograms without front-end filters installed for an applied rf_pulse sequence with FA=200° (red and yellow) and with no RF pulses applied (blue). Left: Linear representation of the main Gaussian distribution (with 0.015 ns bin width). Right: Logarithmic representation between -120 ns and 120 ns (with 0.9 ns bin width).

In contrast, the probability of events with a distorted time stamp difference outside the main Gaussian distribution increased in the RF on phase by a factor of 48.1 in comparison to the reference (events with a time stamp difference smaller than -2 ns or higher than 0 ns were used for this calculation). The same measurement was repeated with the front-end filters installed and additional *rf_pulse* sequences. Figure 119 demonstrates that no changes to the coincidence timing spectrum were observed due to RF distortion.

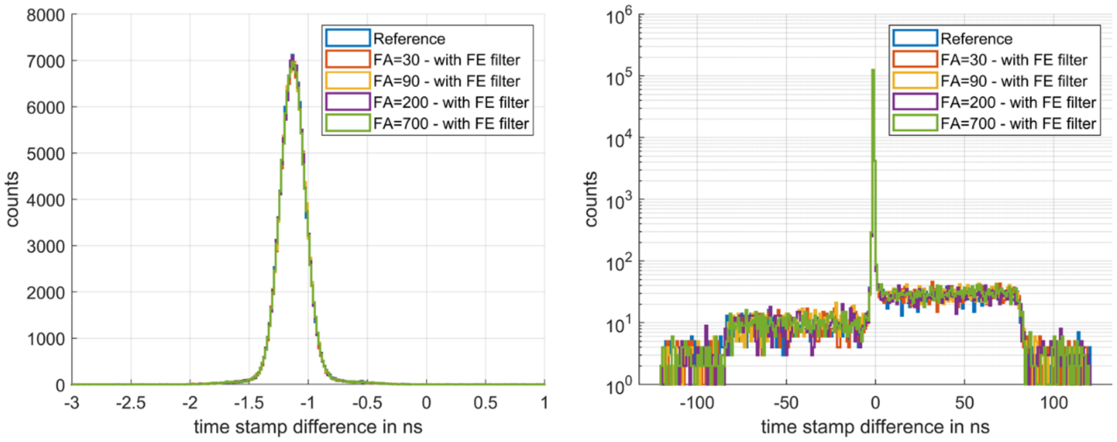

Figure 119: Coincidence timing histograms with installed front-end filters and the application of rf_pulse sequences with different flip angles. Left: Linear representation of the main Gaussian distribution (with 0.015 ns bin width). Right: Logarithmic representation between -120 ns and 120 ns (with 0.9 ns bin width).

This finding is in accordance with the stable CRT values of 252 ps, 254 ps, 252 ps, 253 ps, and 252 ps for the test using *rf_pulse* sequences with flip angles of 30°, 90°, 200°, 700°, and the reference measurement, respectively, as shown in Table 7.

Although the timing histograms and the CRT values of the test with the front-end filters did not show any distortion during the application of the *rf_pulse* sequences, it is possible that the time stamps of a small number of events were still affected, though not enough to cause an observable variation in the CRT values or timing histograms. This small number relates to the duty cycle of the applied *rf_pulse* sequence and thus is 3.3 % and 1.0 % for the *rf_pulse* sequences with flip angles of 200° and 700°, respectively.

As such, to ensure that the time stamps of the PET events were not distorted during the two low duty cycle *rf_pulse* sequences, the color-coded timing histograms were used (Figure 120 left). To validate the color-coded timing histograms, the timing histogram for the measurement without the front-end filters installed was compared to the corresponding timing histogram while the 200° FA *rf_pulse* sequence was applied. The distortions visible in the conventional timing histogram in Figure 118 (right, yellow) correspond to the color variations of the pixels in the area around a start point of 10.5 ms in Figure 120 (left).

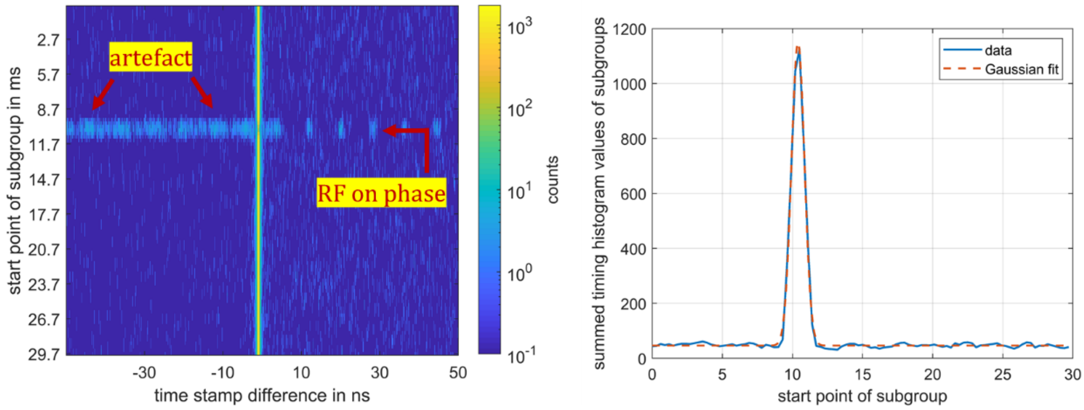

Figure 120: Left: Color-coded timing histogram for the 100 event subgroups acquired during the application of the rf_pulse sequence with 200° FA and without front-end filters installed. Right: Summed timing histogram values between -50 ns and -2 ns for each subgroup.

In addition, the height of the artifact in Figure 116 was calculated by a Gaussian fit. The resulting FWHM of the Gaussian function (Figure 120 right) was 1.09 ms, compared to the 1.00 ms PW of the *rf_pulse* sequence. Hence, it was possible to use the color-coded timing histograms for this analysis.

Finally, when the front-end filters were installed, no time stamp distortions were observed for *rf_pulse* sequences with FA=200° and FA=700°, respectively (Figure 121).

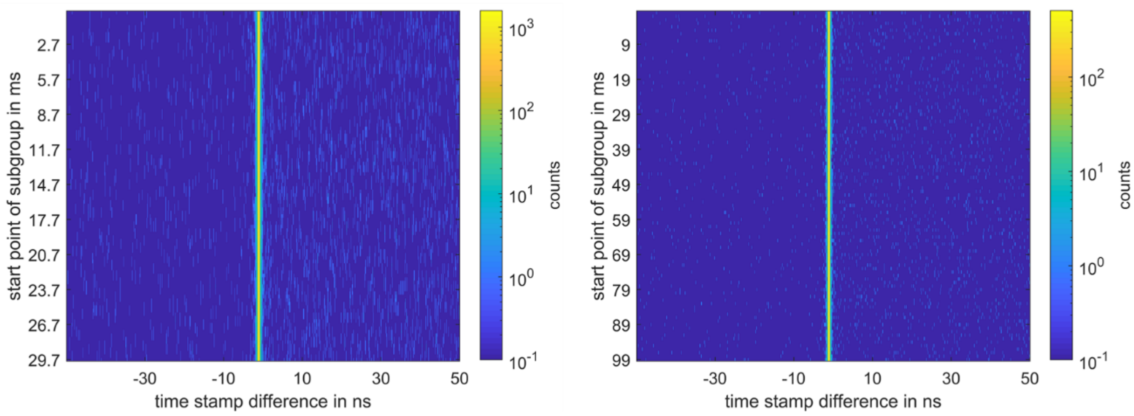

Figure 121: Color-coded timing histograms for the 100 event subgroups acquired during the application of the rf_pulse sequence with front-end filters installed. Left: For rf_pulse sequence with 200° FA. Right: For rf_pulse sequence with 700° FA.

In addition to preventing the RF pulses from distorting the PET event time stamps and energy values, the front-end filters also helped maintain an undistorted event rate. This finding is shown in Table 7 by the single event count rate for detector 1, with 33.8 kcounts/s for the measurements applying *rf_pulse* sequences with flip angles of 30°, 90°, 200°, 700°, and the reference measurement, respectively. Moreover, the single event count rate of detector 2 was 34.2 kcounts/s, 34.1 kcounts/s, 34.1 kcounts/s, 34.2 kcounts/s, and 34.1 kcounts/s for the measurement using *rf_pulse* sequences with flip angles of 30°, 90°, 200°, 700°, and the reference measurement, respectively. The coincidence count rate was 1.95 kcounts/s, 1.97 kcounts/s, 1.96 kcounts/s, 1.96 kcounts/s, and 1.97 kcounts/s for the measurement using *rf_pulse* sequences with flip angles of 30°, 90°, 200°, 700°, and the reference measurement, respectively, demonstrating that the operation of the PET modules was not affected.

Influence of the PET Modules on the Performance of the MRI Scanner

The RF noise spectrum acquired with the RF breast coil did not reveal any differences between the normal operation of the PET modules (Figure 122 left) and the reference measurement with the PET modules powered off (Figure 122 right).

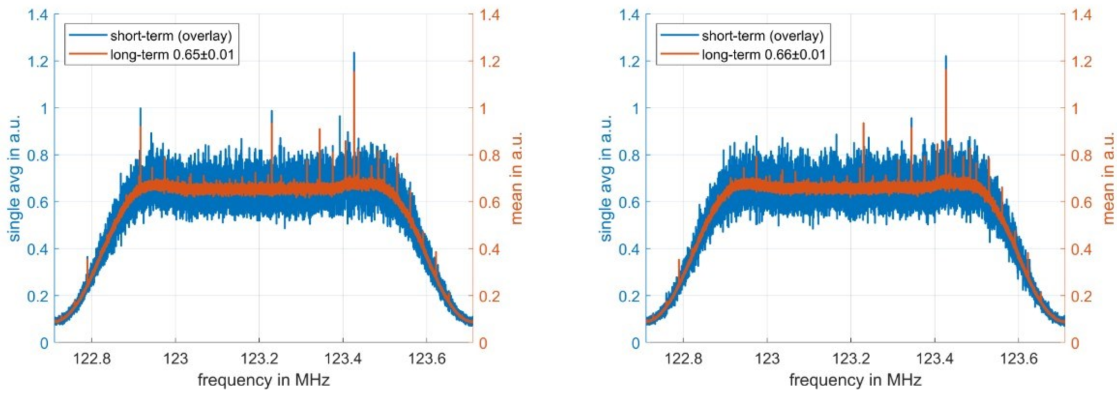

Figure 122: RF noise spectra acquired with the RF breast coil. Left: Normal operation of the PET modules encapsulated in the shielding boxes. Right: Reference with the PET modules powered off.

The mean value of the spectra when the PET modules were operating was stable at 0.66±0.01 in comparison to the reference measurement of 0.65±0.01. Furthermore, the spectrum acquired with the *rf_noise* sequence did not display any differences when the PET modules were powered on (Figure 123 top) compared to the reference measurement (Figure 123 bottom).

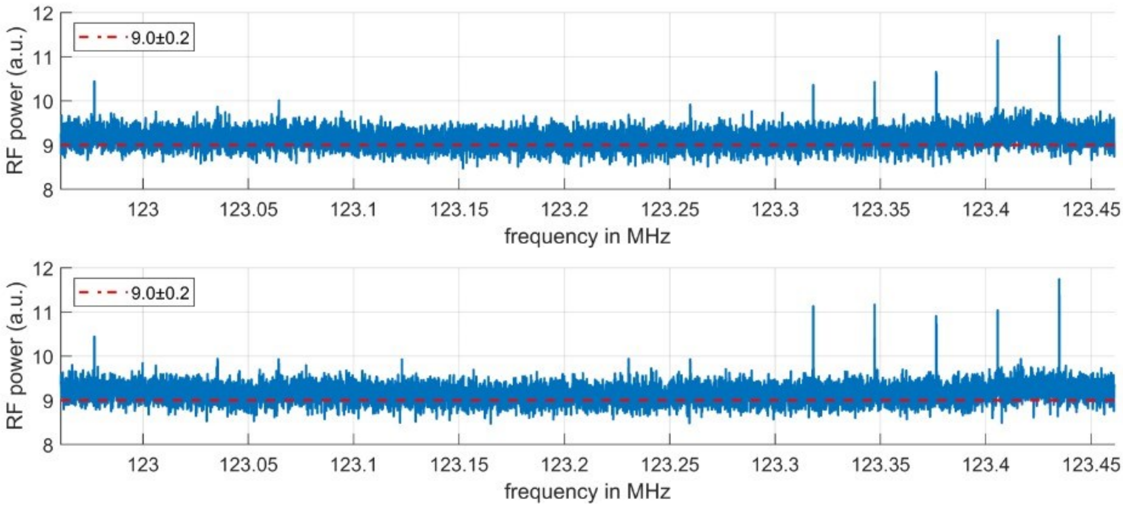

Figure 123: Spectra acquired with the rf_noise sequence and the RF breast coil. Top: Normal operation of the PET modules encapsulated in the shielding boxes. Bottom: Reference with the PET modules switched off

The mean value of the RF power values over the total spectrum remained stable at 9.0±0.2 for the measurement taken while the PET modules were operating and the reference measurement. The small spikes visible in the spectra in Figure 122 and Figure 123 are negligible, as they also occurred in the reference measurement and might be explained by the binning algorithm.

6.6.3 Discussion and Conclusion

All measurements for setup F were performed with a clock signal for the PET modules derived from the clock signal of the MRI scanner. Therefore, it was possible to synchronize the clocks between both modalities.

In addition, a comprehensive analysis was performed, which split the PET event data into multiple subgroups to identify the events acquired during the phase when the RF pulses were transmitted. In this RF on phase, the energy values of the PET values were distorted, resulting in an alternating pattern in the energy histogram for energy values left of the photo peak and a decrease in the photo peak position by 16.2 ns in comparison to the reference measurement. However, in the phase when no RF pulses were transmitted, the energy values were not affected. The same effect was observed for the PET event time stamps, where distortions were also only measured during the RF on phase. These distortions caused a decrease in the number of coincident events in the main Gaussian distribution, the region of events that are assumed to be real coincident events, by a factor of 4.3 compared to the reference measurement. Furthermore, the number of events with a time stamp difference outside the main Gaussian distribution increased by a factor of 48.1 in comparison to the reference measurement. These findings indicate that penetrating the PET modules with RF waves did result in distorted PET data, although this distortion is not permanent, rather is limited to the phase of application of the RF pulses.

As distortions were observed for the setup without front-end filters, an analysis was conducted to determine whether a distortion-free operation was possible with the use of filters. For this comprehensive analysis, three different approaches were used.

First, the energy and timing spectra were compared between the reference measurement and measurements applying *rf_pulse* sequences with flip angles of 30°, 90°, 200°, and 700°. Thereafter, all distortions that were visible in the energy and timing histograms when no filters were used were prevented by the use of front-end filters. This finding suggests that the distortion of the PET events was due to the coupling of RF waves on the power cables and that the new front-end filters can mitigate this distortion on the PET modules.

Second, typical PET detector performance parameters were compared between the measurements using the four *rf_pulse* sequences and the reference measurement. No significant difference was observed. As an example, the performance parameters are given for the 700° FA *rf_pulse* sequence in comparison to the reference measurement: the energy resolution for detectors 1 and 2, the photo peak position for detectors 1 and 2, the single event count rate for detectors 1 and 2, the coincident event count rate, and the CRT were 10.3±0.5 % and 10.1±0.5 %, 434.0±22.0 ns and 433.4±24.2 ns, 33.8 kcounts/s and 34.2 kcounts/s, 1.96 kcounts/s, and 253 ps for the 700° FA *rf_pulse* sequence, in comparison to 10.4±0.5 % and 10.2±0.5 %, 434.3±21.8 ns and 433.2±24.4 ns, 33.8 kcounts/s and 34.1 kcounts/s, 1.97 kcounts/s and 252 ps for the reference measurement, respectively.

Third, a method was developed to identify distortions in the energy values and time stamps if only a small fraction of 1.0 % of the events are potentially affected by RF distortion. This method's ability to identify these small distortions was validated, as the 1.0 ms pulse width of the *rf_pulse* sequence was calculated to 1.09 ms and 1.06 ms through analysis of the distorted time stamps and energy values, respectively. Despite this comprehensive analysis, no distortions to the energy values and PET event data time stamps were observed for *rf_pulse* sequences with flip angles of 200° and 700° when the front-end filters were installed. Therefore, using the front-end filters allows the PET modules to operate normally inside the MRI scanner.

Section 6.5.2 (setup E) demonstrated that the PET module shielding boxes helped the MRI scanner's RF receiver coil operate normally. The same results were confirmed for the RF breast coil with the PET modules placed in close proximity to the coil elements. As such, the spectra of the test sequences *rf_noise* and *rf_noise_spectrum* did not exhibit any significant differences compared with the reference measurements when the PET modules were operated in the shielding boxes. The accordance between the reference measurement and the measurement with the PET modules operating is also reinforced by the mean values of the spectra with 9.0±0.2 and 9.0±0.2 for the spectra acquired with the *rf_noise* sequence and 0.65±0.01 and 0.66±0.01 for the spectra acquired with the *rf_noise_spectrum* sequence, respectively.

Importantly, as the test setup with the RF breast coil is comparable to the PET modules' intended application in the breast PET/MRI insert, no RF distortions of the total breast PET/MRI insert are expected, and the PET modules can be fully operated within the MRI scanner.

7 Conclusive Discussion and Outlook

Multiple breast-specific PET systems have been developed, with the majority incorporating a dual-panel detector design [101]–[110]. With this design, two parallel planar detectors are typically positioned above and below the compressed breast. This analogy to classical X-ray-based mammography led to the term positron emission mammography (PEM).

However, these systems are only capable of acquiring limited-angle tomographic images, resulting in anisotropic spatial resolution. In order to cover a larger FOV, a rectangular design [111] was developed as well as designs that rotate two [112] or more planar detectors [113] or have a semi-ring coverage [114] to enhance angular sampling.

Finally, the ring-shaped designs, called dedicated breast PET (dbPET) systems [115], were developed by various groups [116]–[122], enabling full 3D tomographic imaging with a high sensitivity due to the increased solid angle coverage.

In contrast to these systems, this thesis presents the combination of a dedicated breast PET insert and a whole-body PET/MRI scanner. The assigned LORs between both PET systems allow the breast tissue and the lymph nodes in the axilla and mediastinum regions to be imaged with a high resolution. This approach, called a virtual pinhole PET insert [123], demonstrated improved spatial resolution and contrast recovery for tumors close to the breast PET insert. However, the original purpose of this prototype was for head-and-neck cancer imaging applications, and the reported half-ring geometry was not designed for the specific anatomy of the breast. Thus, the sensitivity of the prototype is inferior to the design proposed in this work, which features a high solid angle coverage. Finally, the virtual pinhole PET insert does not support the dual modality approach of a combined PET and MRI, which serves as this thesis's motivation for developing a dedicated breast PET insert incorporated into a whole-body PET/MRI system.

To date, two other groups have reported attempts to develop an MRI compatible breast PET insert. The Brookhaven National Laboratory breast scanner, which is based on the RatCAP system [124], was the first attempt at a dedicated breast PET insert for simultaneous PET/MRI. However, this project seems to be discontinued, as no further work has been reported other than phantom measurements with a single ring prototype. In addition, the reported results indicate that MRI compatibility problems, such as an increased PET singles count rate during RF pulsing, remained unsolved. [125]

The latest work on a breast PET/MRI insert comes from the Digital Hybrid Breast PET/MRI for Enhanced Diagnosis of Breast Cancer (HYPMED) [126] project, which is based on the Hyperion III PET detector platform [127], a continued development of the preclinical PET/MRI insert Hyperion II [128]. In contrast to the concept for the breast insert proposed in this work, the HYPMED insert is intended to operate inside a standalone clinical MRI scanner. This setup, however, does not allow for imaging distant lesions in the axilla and mediastinum regions, as it does not support simultaneous PET imaging of the whole body. Therefore, an additional PET scan needs to be performed in a whole-body PET scanner to obtain additional information beyond the primary tumors of the breast cancer. The second scan results in increased costs as well as in higher stress and higher radiation exposure for the patient. Finally, as the additional scan would be performed with a conventional clinical PET scanner, no increase in the spatial resolution would be achieved, which is necessary for the enhanced identification of a potential metastasis.

The combination of the breast PET insert and the whole-body PET proposed in this thesis, which is the basis for achieving superior spatial resolution in the thorax region, requires simultaneously processing the events acquired by both PET systems. This work showed that the clock signal of the HPK PET modules can be synchronized with the Biograph mMR. This step is the prerequisite for processing coincidence events between both systems. The feasibility of simultaneous coincidence processing has recently been demonstrated between a flat panel PET insert and the whole-body PET/CT scanner Biograph 40 (Siemens Healthineers, Erlangen, Germany) [129].

The work presented in this thesis consists of conceptional steps and design ideas as well as comprehensive tests of the HPK PET modules to evaluate their suitability for the breast PET/MRI insert.

First, the stable operation of the PET modules was demonstrated over a wide range of time and temperature conditions. As such, for an applied airflow cooling of 1.0 bar along with a time skew correction and HVPS temperature compensation, the following performance parameters were measured over 120 minutes and a temperature range of 23.56°C to 27.90°C: a photo peak position of 426±0.9 ns, an energy resolution of 10.4±0.1 %, a peak position of the timing histogram of -1.032±0.001 ns, and a CRT of 254±2 ps.

Furthermore, the HPK PET modules permit the flexible use of specialized PET detectors required for the breast insert.

The prototype detector developed in this work demonstrated that the HPK PET electronics could resolve small scintillation crystals together with an MPPC array of self-chosen dimensions via a light sharing approach. For this process, an LSO scintillation array with a crystal size of 1.51×1.51×10 mm^3 was precisely identified in combination with an MPPC array with a 3.0 mm×3.0 mm photosensitive area for each channel. The feasibility of this coupling was proven by a high PVR of 16.9±7.2 and 13.0±6.4 for a representative column and row of the scintillation crystal array, respectively. In order to use the light sharing readout method to identify small crystals, the gain of the ASIC had to be increased in comparison to the standard setting. This gain increase resulted in an increase of the measured PET event energy values, as shown by the photo peak position of 433.8± 34.1 ns and 942.3±96.8 ns for the standard and increased gain settings, respectively. The increased gain setting resulted in an energy resolution of 15.9±2.8 %, compared to the 16.2±3.7 % for the standard gain setting. In summary, this thesis demonstrated the feasibility of the readout of a customized prototype detector, which is a prerequisite for further developing the breast PET/MRI insert. Consequently, different scintillator block configurations can be tested, as can different approaches for acquiring depth of interaction information. Aside from considering the feasibility of the hardware, different detector designs will be further crosschecked with simulations of the breast insert. This involves further dimensioning the PET detectors and system electronics so that they have a sufficient count rate capability to account not only for the tracer uptake in the breast region but also for the unspecific uptake in nearby organs, such as the heart or liver.

The original intention for developing the breast PET/MRI insert was to exploit the daisy chain feature of the HPK PET modules, where multiple modules share one data communication line, thus reducing the number of cables and back-end electronics. The feasibility of connecting 16 HPK PET modules to form an entire ring of a PET scanner was recently demonstrated [130]. However, this daisy chain feature was not implemented in the version of the PET module that used optical fibers for signal transmission, which was used for the MRI compatibility measurements in this thesis. Instead, a new method for combining multiple PET modules with a single optical fiber transmission line is currently under development, which has the potential to compactly integrate the PET modules required for the breast PET/MRI insert.

To confirm the suitability of the HPK PET modules for the breast PET/MRI insert, this work includes a comprehensive evaluation of their capacity to operate inside a 3T MRI scanner. Conventionally, the components for an MRI compatible PET insert are specifically designed for this purpose at an early phase of development. However, the original version of the HPK PET modules was never intended to be used within an MRI scanner but rather for the implementation of a single modality PET scanner. Therefore, the work conducted in this thesis demonstrates the successive steps and modifications required to integrate the PET modules into an MRI compatible system.

The first modifications for MRI compatibility involved replacing the HVPS, which used an inductor prone to suffer from the static magnetic field, dismantling the heat sink to avoid heating by eddy currents, and removing the ferromagnetic structures for mechanical support. These modifications demonstrated that the PET modules' back-end electronics were affected by the static magnetic field, including exposure to the 200 mT fringe field that hindered their operation.

Consequently, the back-end electronics were placed outside of the MRI scanner room. In addition, switching the gradient fields with a slew rate of 50 T/ms^{-1} and transmitting RF pulses with a flip angle of 45° prevented the PET modules from operating; however, this effect was prevented by replacing the copper-based signal lines with optical fibers. This modification allowed for the MRI scanner and PET system to operate simultaneously, although performance degradation was evident on both sides. In regard to the MRI scanner, the RF sensitive receiver structure was distorted by noisy RF emissions originating from the PET modules. Placing the PET modules in an accurately sealed copper shielding box 18 µm in thickness attenuated the RF distortion to such a low level that it did not affect the performance of the MRI scanner. This was verified by two test sequences, *rf_noise* and *rf_noise* spectrum, which measured the receiving spectrum of the body coil. The results indicated consistency between the mean values of the spectra for the PET modules operating inside the 3T MRI scanner and a reference measurement with the PET modules switched off was 46.2±1.6 and 46.0±1.6, respectively, and 88.0±2.4 and 87.0±2.4 for the spectra acquired with the *rf_noise* and *rf_noise_spectrum* sequences, respectively.

In regard to the PET insert, the interference of the RF pulses transmitted by the MRI scanner's body coil caused severe distortions in the PET modules. This interference was demonstrated by changes to the energy, time stamps, and count rate of the PET events, which were correlated with the characteristics of the specific pulse sequences, such as the duty cycle and the amplitude. Examples of these changes include the CRT, which was degraded by 76 ps when applying an RF pulse with 80° FA, and the decrease of the photo peak position in the energy histogram by 16.2 ns during the phase of transmission of a 200° FA RF pulse compared to the reference measurement. Additionally, the count rate dropped by 8.35 % in the phase of transmission of a 200° FA RF pulse in comparison to the reference measurement.

Furthermore, these effects were shown to be temporary, only present during the time when the RF pulses were transmitted. This distortion originated from coupling of the RF waves on the power supply cable, which then propagated as noise to the PET detectors inside the shielding boxes. Finally, a low-pass filter located at the input of the shielding boxes (in addition to the power filter at the MRI scanner's wall) helped prevent these PET data distortions. This finding was confirmed for a variety of *rf_pulse* sequences, including sequences with high duty cycles up to 50 % (FA=90°) and sequences with a high RF power up to 700° FA (duty cycle of 1.0 %).

To confirm that RF distortions of the PET events were prevented, typical PET performance parameters are provided for the 700° FA *rf_pulse* sequence in comparison to the reference measurement with no RF pulses. The energy resolution for detectors 1 and 2, the photo peak position for detectors 1 and 2, the single event count rate for detectors 1 and 2, the coincident event count rate, and the CRT were 10.3±0.5 % and 10.1±0.5 %, 434.0±22.0 ns and 433.4±24.2 ns, 33.8 kcounts/s and 34.2 kcounts/s, 1.96 kcounts/s and 253 ps and 10.4±0.5 % and 10.2±0.5 %, 434.3±21.8 ns and 433.2±24.4 ns, 33.8 kcounts/s and 34.1 kcounts/s, 1.97 kcounts/s and 252 ps for the 700° FA *rf_pulse* sequence and the reference measurement, respectively.

Furthermore, switching the three gradient fields with a maximum gradient field strength of 20 mT/m at a slew rate of 100 T/ms^{-1} did not result in PET module performance degradation, as demonstrated by comparing the following performance parameters: the energy resolution for detectors 1 and 2 , the photo peak position for detectors 1 and 2, the single event count rate for detectors 1 and 2, the coincident event count rate and the CRT were 10.5±0.6 % and 10.1±0.5 %, 442.8±29.5 ns and 434.7±26.5 ns, 33.3 kcounts/s and 33.4 kcounts/s, 2.13 kcounts/s and 335 ps when the gradient field was switched, in comparison to 10.5±0.6 % and 10.1±0.5 %, 443.9±29.6 ns and 434.1±26.5 ns, 33.2 kcounts/s and 34.4 kcounts/s, 2.13 kcounts/s and 332 ps for the reference measurement. It should be noted that all tests on RF distortion and gradient switching robustness were performed beyond the settings used for a common clinical patient scan, instead of using settings that reflect the worst-case scenario at the limitations of the scanner.

As the PET modules will be operated in close proximity to the MRI breast coil for the intended application of the breast PET/MRI insert, the RF distortion tests were also conducted with the PET modules integrated into the four channel breast coil from NORAS. No degradations of the breast coil due to RF distortions from the receiver coil were observed. As such, there was consistency between the mean values of the spectra for the PET modules operating between the elements of the breast coil and a reference measurement with the PET modules powered off was 9.0±0.2 and 9.0±0.2, and 0.66±0.01 and 0.65±0.01 for the spectra acquired with the *rf_noise* and *rf_noise_spectrum* sequences, respectively.

In order to achieve full MRI compatibility, it needs to be ensured that the homogeneity of the B_0 and B_1 fields is not degraded. [131] Initial tests with the two detectors showed that the increase in the B_0 field inhomogeneity of 0.254 ppm is acceptable, as this is below the value of acceptance for MRI compatibility with the Biograph mMR for the B_0 inhomogeneity of 0.5 ppm.

In addition, the local changes to the B_1 field were not severe; for instance, the inhomogeneity of the B_1 field only increased by 12.5 % due to the PET modules. For this test scenario, a variation of up to 10.0 % is the threshold to meet the MRI compatibility specifications. At the current stage of development, this slight excess of the threshold is tolerable, as it does not severely degrade the MRI scanner's performance. Changes to the shielding and orientation of the final insert's PET detectors with respect to the B_1 field have the potential to decrease this inhomogeneity below the acceptance threshold.

High magnetic susceptibility materials such as nickel or iron should be avoided as much as possible to maintain the high uniformity of the static magnetic field, which is necessary for the MRI scanner to function properly. In the current prototype, the main sources of potential B_0 inhomogeneities are the connectors for the power cables; however, due to their size and the impossibility of integrating them into the final design, they will not be used for the final breast insert. Furthermore, shimming can account for local variations of the B_0 field.

The RF field homogeneity degrades because of the shielding boxes, which use layers of copper as a shielding material; hence, absorption is the primary shielding mechanism for this setup. The RF fields are expected to be absorbed at the surfaces of the shielding boxes, and secondary RF fields are generated, which attenuate the primary field distribution [132].

In general, the B_0 and B_1 fields are affected by the amount, type, and location of the materials that are placed inside the MRI scanner [133]. The same holds true for potential interferences caused by switching the gradient fields, such as eddy current loops that are induced by the rapidly switching magnetic fields. The resulting issues, such as heating, secondary field generation, and potential mechanical vibrations, must be considered [134].

The impact of these potential interferences on MRI compatibility will be further investigated using a full detector assembly for the final breast insert. In addition, the design of the shielding boxes with respect to geometry and material must be investigated. A comprehensive comparison between materials with different characteristics for shielding low and high frequency RF fields, such as copper, carbon fiber composite, and phosphor bronze mesh, will be made. [135]

Several other groups have also addressed the issue of MRI compatibility when using a PET insert inside a clinical MRI scanner. However, the incompatibility between both systems was observed with the first APD-based brain insert [25], as well as for more recently developed inserts based on SiPMs for dedicated brain imaging [136]–[139] or a small ring structure [140]. Despite their different designs, all groups share the same basic approaches to guarantee MRI compatibility, as this thesis has shown. First, the amount of the PET electronics exposed to the harsh conditions inside the MR bore is minimized as much as possible. Thus, the signals of the front-end are transmitted either via differential, coaxial, or optical transmission lines, which result in a potentially high insensitivity to RF interference. Second, the PET detector and front-end electronics are encapsulated in RF robust cassettes made of shielding materials, such as carbon fiber or thin layers of copper.

In summary, one of this thesis's main objectives was to demonstrate whether the HPK PET modules and the 3T MRI scanner could simultaneously operate without any performance degradation to either system. This research proves this possibility, paving the way for a breast PET/MRI insert based on the HPK PET modules. However, the application of this MRI compatible version of the HPK PET modules must not be restricted to a breast PET/MRI insert that operates inside a 3T MRI scanner. Other applications could include a combined whole-body PET/MRI scanner based on these PET modules or a PET insert dedicated for brain imaging. Recently, preliminary tests inside a high-field 7T MRI scanner showed positive results regarding MRI compatibility [141] by using the modified setup of the HPK PET modules developed during the course of this work, which serves as an example of the impact this thesis can have on future projects.

Appendix: MRI Test Sequences for Evaluating MRI Compatibility

For clinical routine, the MRI scanner's transmission and receiver components are concurrently used to acquire an image, as described in Chapter 2.2. In order to narrow down the effects of MRI incompatibility to one of these components, the sequences in this section were designed to observe effects to and from the individual components involved in the MR image generation process. The test sequences are available in the service menu of the Biograph mMR.

rf_pulse

A sequence of repetitive RF pulses with a frequency of 123.21 MHz is transmitted without RF signal detection. The duration of each RF pulse is set by the pulse width (PW). If not otherwise stated, the PW is set to 1 ms. After the repetition time (TR), the next RF pulse is transmitted. Furthermore, the flip angle (FA), which should be achieved with the application of a single RF pulse, can be adjusted. The correlation between the FA and the strength of the transmitted B_1 field B_{1trans} can be calculated with the following formula:

$$B_{1trans} = 11.7\mu T * \frac{FA}{180°} * \frac{1\,ms}{PW}.$$

The formula is based on the proportionality of B_{1trans} and FA and the indirect proportionality of B_{1trans} and PW. [142] In addition, the transmitted B_1 field for a reference pulse with PW =1ms and FA=180° was measured with the software of the Biograph mMR to 11.7 µT.

The duty cycle of an RF pulse sequence corresponds to the relative time when RF pulses are transmitted. It is defined as the ratio of the PW of the RF pulse to the TR.

grad_freepulse

A sequence of repetitive gradient pulses is transmitted without RF signal detection. Figure 124 shows the transient progression of the gradient field strength for the gradient pulses used in this thesis. The gradient field strength is ramped up to the peak gradient strength G_{peak} over the time t_{ramp}. This gradient field strength is constant over the time t_{pulse_max} and subsequently ramped up to

0 mT/m. During the second half of the gradient pulse, the first trapezoidal signal is repeated but with a negative polarity. After the TR, the next gradient pulse is transmitted. If not otherwise stated, the *grad_freepulse* sequences used in this work have a TR equal to the width of the gradient pulse (i.e., no delay between successive gradient pulses), as shown in Figure 124.

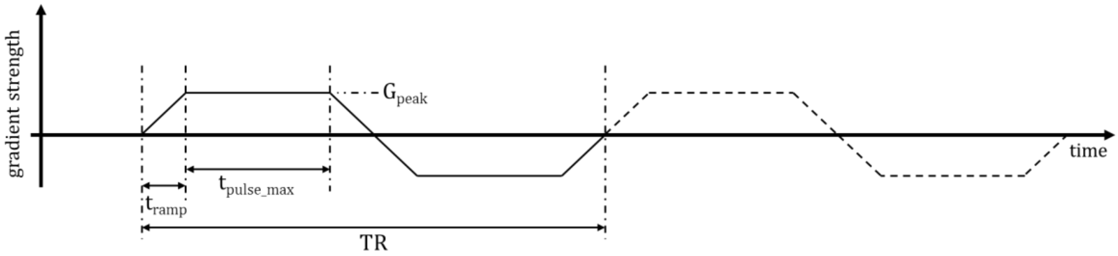

Figure 124: Gradient pulses over time for the grad_freepulse sequence with bipolar pulse-pairs.

Furthermore, the standard setting for t_{pulse_max} is 1 ms and 20 mT/m for G_{peak}, and if not otherwise stated, all three gradients were switched at the same time. The variations of t_{ramp} and G_{peak} lead to a change of the slew rate SR according to the formula:

$$SR = \frac{G_{peak}}{t_{ramp}}.$$

The maximum gradient performance of the Biograph mMR is 45 mT/m at a slew rate of 200 T/m/s.

rf_noise_spectrum

The *rf_noise_spectrum* is a proprietary sequence with repetitive data reception without RF signal generation (i.e., without gradient switching or RF pulse transmission). The MRI scanner's RF reception system can be checked for interfering RF signals. A fast Fourier transformation of the received RF signals with a step size of 61.035 Hz was used to display the RF power spectrum. In total, 30 short-term spectra were acquired, each consisting of 50 measurements. The mean of these short-term spectra was referred to as the long-term spectrum. A high receiving bandwidth of 1 MHz was used within a receiving band of 123.21 MHz±500 kHz. The receiving bandwidth was increased for this sequence in comparison to the MRI scanner's normal operation and is thus well suited for accurately identifying sources of RF distortion.

rf_noise

An analog to the *rf_noise_spectrum* sequence, the *rf_noise* sequence was used to evaluate RF distortions in the RF reception system. Hereby, a narrower bandwidth of ±250 kHz at 123.21 MHz was used. Furthermore, to cover the entire system receiving bandwidth, a variation of the center frequency from slice to slice was performed. In total, 50 slices, each covering 10 kHz, were acquired. These settings are comparable to the normal operation of an MRI scanner. If no distortions are visible in the spectrum of the *rf_noise* sequence, the MRI scanner's RF reception system can operate normally.

field

The *field* is a proprietary sequence that uses a 2D spin echo to represent the static field (B_0) homogeneity. Each interference stripe in the resulting image corresponds to a change of the B_0 field of 0.254 ppm.

rf_field

The *rf_field* is a proprietary sequence that uses a 2D spin echo to represent the RF field (B_1) homogeneity. Each interference stripe in the resulting image corresponds to a change of the B_1 field of 6.25 %.

Bibliography

[1] F. Bray, J. Ferlay, I. Soerjomataram, R. L. Siegel, L. A. Torre, and A. Jemal, "Global cancer statistics 2018: GLOBOCAN estimates of incidence and mortality worldwide for 36 cancers in 185 countries," *CA. Cancer J. Clin.*, vol. 68, no. 6, pp. 394–424, Nov. 2018.

[2] Robert Koch-Institut, "Krebs in Deutschland 2013/2014," *Gesundheitsberichterstattung des Bundes*, pp. 72–75, 2017.

[3] P. A. Ganz and P. J. Goodwin, "Breast Cancer Survivorship: Where Are We Today?," in *Advances in experimental medicine and biology*, vol. 862, P. A. Ganz, Ed. Cham: Springer International Publishing, 2015, pp. 1–8.

[4] A. Rembielak, M. Green, A. Saleem, and P. Price, "Diagnostic and therapeutic imaging in oncology," *Medicine (Baltimore).*, vol. 44, no. 1, pp. 6–9, Jan. 2016.

[5] B. J. Pichler, H. F. Wehrl, A. Kolb, and M. S. Judenhofer, "PET/MRI: The Next Generation of Multi-Modality Imaging?," *Semin. Nucl. Med.*, vol. 38, no. 3, pp. 199–208, May 2008.

[6] M. S. Judenhofer *et al.*, "Simultaneous PET-MRI: a new approach for functional and morphological imaging," *Nat. Med.*, vol. 14, no. 4, pp. 459–465, Apr. 2008.

[7] H. F. Wehrl, A. W. Sauter, M. R. Divine, and B. J. Pichler, "Combined PET/MR: A Technology Becomes Mature," *J. Nucl. Med.*, vol. 56, no. 2, pp. 165–168, Feb. 2015.

[8] M. S. Judenhofer and S. R. Cherry, "Applications for Preclinical PET/MRI," *Semin. Nucl. Med.*, vol. 43, no. 1, pp. 19–29, Jan. 2013.

[9] G. Delso *et al.*, "Performance Measurements of the Siemens mMR Integrated Whole-Body PET/MR Scanner," *J. Nucl. Med.*, vol. 52, no. 12, pp. 1914–1922, 2011.

[10] J. G. Mannheim *et al.*, "PET/MRI Hybrid Systems," *Semin. Nucl. Med.*, vol. 48, no. 4, pp. 332–347, Jul. 2018.

[11] L. Umutlu and K. Herrmann, *PET/MR Imaging: Current and Emerging Applications*. Cham: Springer International Publishing, 2018.

[12] D. Botsikas *et al.*, "Clinical utility of 18F-FDG-PET/MR for preoperative breast cancer staging," *Eur. Radiol.*, vol. 26, no. 7, pp. 2297–2307, Jul. 2016.

[13] T. A. Heusner *et al.*, "Diagnostic accuracy of fused positron emission tomography/magnetic resonance mammography: initial results," *Br. J. Radiol.*, vol. 84, no. 998, pp. 126–135, Feb. 2011.

[14] J. Grueneisen *et al.*, "Positron Emission Tomography/Magnetic Resonance Imaging for Local Tumor Staging in Patients With Primary Breast Cancer," *Invest. Radiol.*, vol. 50, no. 8, pp. 505–513, Aug. 2015.

[15] N. Ergul *et al.*, "Assessment of multifocality and axillary nodal involvement in early-stage breast cancer patients using 18F-FDG PET/CT compared to contrast-enhanced and diffusion-weighted magnetic resonance imaging and sentinel node biopsy," *Acta radiol.*, vol. 56, no. 8, pp. 917–923, Aug. 2015.

[16] A. C. Pujara, E. Kim, D. Axelrod, and A. N. Melsaether, "PET/MRI in Breast Cancer," *J. Magn. Reson. Imaging*, vol. 49, no. 2, pp. 328–342, 2019.

[17] K. Pinker *et al.*, "Improved differentiation of benign and malignant breast tumors with multiparametric 18fluorodeoxyglucose positron emission tomography magnetic resonance imaging: A feasibility study," *Clin. Cancer Res.*, vol. 20, no. 13, pp. 3540–3549, 2014.

[18] J. Schmitz *et al.*, "Decoding intratumoral heterogeneity of breast cancer by multiparametric in vivo imaging: A translational study," *Cancer Res.*, vol. 76, no. 18, pp. 5512–5522, 2016.

[19] B. Aklan *et al.*, "Toward simultaneous PET/MR breast imaging: Systematic evaluation and integration of a radiofrequency breast coil," *Med. Phys.*, vol. 40, no. 2, p. 024301, Feb. 2013.

[20] I. Dregely *et al.*, "A 16-channel MR coil for simultaneous PET/MR imaging in breast cancer," *Eur. Radiol.*, vol. 25, no. 4, pp. 1154–1161, Apr. 2015.

[21] C. Catana, "Principles of Simultaneous PET/MR Imaging," *Magn. Reson. Imaging Clin. N. Am.*, vol. 25, no. 2, pp. 231–243, May 2017.

[22] S. Vandenberghe and P. K. Marsden, "PET-MRI: a review of challenges and solutions in the development of integrated multimodality imaging," *Phys. Med. Biol.*, vol. 60, no. 4, pp. R115–R154, Feb. 2015.

[23] B. Pichler *et al.*, "Performance test of a LSO-APD PET module in a 9.4 Tesla magnet," *1997 IEEE Nucl. Sci. Symp. Conf. Rec.*, vol. 2, pp. 1237–1239, 1997.

[24] B. J. Pichler *et al.*, "Performance test of an LSO-APD detector in a 7-T MRI scanner for simultaneous PET/MRI.," *J. Nucl. Med.*, vol. 47, no. 4, pp. 639–47, Apr. 2006.

[25] H.-P. W. Schlemmer *et al.*, "Simultaneous MR/PET Imaging of the Human Brain: Feasibility Study," *Radiology*, vol. 248, no. 3, pp. 1028–1035, Sep. 2008.

[26] J. F. Schenck, "The role of magnetic susceptibility in magnetic resonance imaging: MRI magnetic compatibility of the first and second kinds," *Med. Phys.*, vol. 23, no. 6, pp. 815–850, Jun. 1996.

[27] H. F. Wehrl, M. S. Judenhofer, A. Thielscher, P. Martirosian, F. Schick, and B. J. Pichler, "Assessment of MR compatibility of a PET insert developed for simultaneous multiparametric PET/MR imaging on an animal system operating at 7 T," *Magn. Reson. Med.*, vol. 65, no. 1, pp. 269–279, Jan. 2011.

[28] J. A. Disselhorst, I. Bezrukov, A. Kolb, C. Parl, and B. J. Pichler, “Principles of PET/MR Imaging,” *J. Nucl. Med.*, vol. 55, no. Supplement_2, p. 2S–10S, Jun. 2014.

[29] G. B. Saha, *Physics and radiobiology of nuclear medicine*, 3rd ed. New York: Springer, 2006.

[30] T. Hosny, “Basic Radiation Physics,” in *Basic Science of PET Imaging*, Springer, 2017.

[31] S. N. Ahmed, *Physics & Engineering of Radiation Detection*. Academic Press, 2007.

[32] T. Brown and N. Yasillo, “Radiation safety considerations for PET centers,” *J. Nucl. Med. Technol.*, vol. 25, pp. 98–103, 1997.

[33] W. W. Moses, “Fundamental limits of spatial resolution in PET,” *Nucl. Instruments Methods Phys. Res. Sect. A Accel. Spectrometers, Detect. Assoc. Equip.*, vol. 648, pp. S236–S240, Aug. 2011.

[34] G. F. Knoll, *Radiation Detection and Measurement*, 4th ed. Hoboken, N.J.: John Wiley, 2010.

[35] C. M. Davisson, “Interaction of y-Radiation with Matter,” in *Alpha-, Beta- and Gamma-Ray Spectroscopy*, Elsevier, 1968, pp. 37–78.

[36] R. D. Evans, *The Atomic Nucleus*. New York: McGraw-Hill, 1957.

[37] C. L. Melcher, “Scintillation crystals for PET,” *J. Nucl. Med.*, vol. 41, no. 6, pp. 1051–1055, 2000.

[38] D. L. Bailey, D. W. Townsend, M. N. Maisey, D. W. Townsend, and P. E. Valk, *Positron Emission Tomography*. Springer, 2005.

[39] P. Lecoq and A. Chao, *Inorganic scintillators for detector systems : physical principles and crystal engineering*. New York, NY: Springer Berlin Heidelberg, 2016.

[40] “Photomultiplier Tubes (PMT).” https://www.sense-pro.org/lll-sensors/pmt (accessed Mar. 04, 2019).

[41] M. E. Phelps, *PET: Physics, Instrumentation, and Scanners*. New York, NY: Springer New York, 2006.

[42] B. J. Pichler *et al.*, “Performance test of an LSO-APD detector in a 7-T MRI scanner for simultaneous PET/MRI.,” *J. Nucl. Med.*, vol. 47, no. 4, pp. 639–47, Apr. 2006.

[43] M. Dahlbom, *Physics of PET and SPECT Imaging*. CRC Press, 2017.

[44] K. Sato, Y. Enomoto, and Y. Adachi, “A technical guide to silicon photomultipliers (MPPC),” 2018.

[45] D. Renker and E. Lorenz, “Advances in solid state photon detectors,” *J. Instrum.*, vol. 4, no. 04, p. P04004, 2009.

[46] SensL, "An Introduction to the Silicon Photomultiplier," pp. 1–16, 2011.

[47] S. Awadalla, *Solid-state radiation detectors: technology and applications*. CRC Press, 2015.

[48] Piatek Slawomir, "Physics and operation of the MPPC silicon photomultiplier," *Hamamatsu Corporation & New Jersey Institute of Technology*, 2014. http://www.hamamatsu.com/us/en/community/optical_sensors/articles/physics_and_operation_of_mppc/index.html.

[49] I. Britvitch, I. Johnson, D. Renker, A. Stoykov, and E. Lorenz, "Characterisation of Geiger-mode avalanche photodiodes for medical imaging applications," *Nucl. Instruments Methods Phys. Res. Sect. A Accel. Spectrometers, Detect. Assoc. Equip.*, vol. 571, no. 1–2, pp. 308–311, Feb. 2007.

[50] V. Andreev *et al.*, "A high-granularity scintillator calorimeter readout with silicon photomultipliers," *Nucl. Instruments Methods Phys. Res. Sect. A Accel. Spectrometers, Detect. Assoc. Equip.*, vol. 540, no. 2–3, pp. 368–380, Mar. 2005.

[51] N. Dinu *et al.*, "Temperature and bias voltage dependence of the MPPC detectors," *IEEE Nucl. Sci. Symp. Conf. Rec.*, no. 2, pp. 215–219, 2010.

[52] A. N. Otte, D. Garcia, T. Nguyen, and D. Purushotham, "Characterization of three high efficiency and blue sensitive silicon photomultipliers," *Nucl. Instruments Methods Phys. Res. Sect. A Accel. Spectrometers, Detect. Assoc. Equip.*, vol. 846, pp. 106–125, 2017.

[53] M. M. Khalil, *Basic Science of PET Imaging*, 1st ed. Springer, 2017.

[54] E. Warburg, O., Wind, F., Negelein, "The metabolism of tumors in the body," *J. Gen. Physiol.*, vol. 182, no. 1, pp. 519–530, 1926.

[55] Y. Yonekura *et al.*, "Increased accumulation of 2-deoxy-2-[18F]Fluoro-D-glucose in liver metastases from colon carcinoma.," *J. Nucl. Med.*, vol. 23, no. 12, pp. 1133–7, Dec. 1982.

[56] T. G. Turkington, "Introduction to PET instrumentation.," *J. Nucl. Med. Technol.*, vol. 29, no. 1, pp. 4–11, Mar. 2001.

[57] J. Langner, "Development of a Parallel Computing Optimized Head Movement Correction Method in Positron Emission Tomography," 2003. http://nbn-resolving.de/urn:nbn:de:bsz:14-qucosa-23396.

[58] S. R. Cherry, J. A. Sorenson, and M. E. Phelps, *Physics in Nuclear Medicine*, 4th ed. Philadelphia, PA: Elsevier, 2012.

[59] S. E. Derenzo, "Mathematical Removal of Positron Range Blurring in High Resolution Tomography," *IEEE Trans. Nucl. Sci.*, vol. 33, no. 1, pp. 565–569, 1986.

[60] A. M. Alessio, E. Butterworth, J. H. Caldwell, and J. B. Bassingthwaighte,

"Quantitative imaging of coronary blood flow," *Nano Rev.*, vol. 1, no. 1, p. 5110, 2010.

[61] M. Kapusta, M. Moszynski, and M. Balcerzyk, "Comparison of the scintillation properties of LSO: Ce manufactured by different laboratories and of LGSO: Ce," *Rec. 1999 IEEE*, vol. 47, no. 4, pp. 1–5, 1999.

[62] H. O. Anger, "Scintillation camera," *Rev. Sci. Instrum.*, vol. 29, no. 1, pp. 27–33, 1958.

[63] T. Orita *et al.*, "Dynamic Time Over Threshold Method," *IEEE Trans. Nucl. Sci.*, vol. 59, no. 6, pp. 3213–3217, 2012.

[64] A. Alessio and P. Kinahan, "PET Image Reconstruction," in *Nuclear Medicine*, vol. 2, Mosby, 2006.

[65] F. H. Fahey, "Data acquisition in PET imaging," *J. Nucl. Med. Technol.*, vol. 30, no. 2, pp. 39–49, 2002.

[66] S. Vandenberghe, E. Mikhaylova, E. D'Hoe, P. Mollet, and J. S. Karp, "Recent developments in time-of-flight PET," *EJNMMI Phys.*, vol. 3, no. 1, 2016.

[67] M. Conti, "State of the art and challenges of time-of-flight PET," *Phys. Medica*, vol. 25, no. 1, pp. 1–11, 2009.

[68] M. Conti, "Improving time resolution in time-of-flight PET," *Nucl. Instruments Methods Phys. Res. Sect. A Accel. Spectrometers, Detect. Assoc. Equip.*, vol. 648, no. SUPPL. 1, pp. S194–S198, 2011.

[69] W. W. Moses, "Recent advances and future advances in time-of-flight PET," *AIP Conf. Proc.*, vol. 1204, pp. 119–125, 2009.

[70] W. W. Moses and S. Member, "Time of Flight in PET - Revisited.pdf," *Ieeexplore.Ieee.Org*, vol. 50, no. 5, pp. 1325–1330, 2003.

[71] M. Conti, "Focus on time-of-flight PET: The benefits of improved time resolution," *Eur. J. Nucl. Med. Mol. Imaging*, vol. 38, no. 6, pp. 1147–1157, 2011.

[72] S. Surti and J. S. Karp, "Design considerations for a limited angle, dedicated breast, TOF PET scanner.," *Phys. Med. Biol.*, vol. 53, no. 11, pp. 2911–21, Jun. 2008.

[73] M. Ito, S. J. Hong, and J. S. Lee, "Positron emission tomography (PET) detectors with depth-of- interaction (DOI) capability," *Biomed. Eng. Lett.*, vol. 1, no. 2, pp. 70–81, May 2011.

[74] M. Schmand *et al.*, "Performance results of a new DOI detector block for a high resolution PET-LSO research tomograph HRRT," *IEEE Trans. Nucl. Sci.*, vol. 45, no. 6, pp. 3000–3006, 1998.

[75] H. Liu, T. Omura, M. Watanabe, and T. Yamashita, "Development of a depth of interaction detector for γ-rays," *Nucl. Instruments Methods Phys.*

Res. Sect. A Accel. Spectrometers, Detect. Assoc. Equip., vol. 459, no. 1–2, pp. 182–190, Feb. 2001.

[76] H. Du, Y. Yang, J. Glodo, Y. Wu, K. Shah, and S. R. Cherry, “Continuous depth-of-interaction encoding using phosphor-coated scintillators,” *Phys. Med. Biol.*, vol. 54, no. 6, pp. 1757–1771, Mar. 2009.

[77] Y. Shao *et al.*, “Design studies of a high resolution PET detector using APD arrays,” *IEEE Trans. Nucl. Sci.*, vol. 47, no. 3, pp. 1051–1057, Jun. 2000.

[78] F. P. Schmidt, A. Kolb, and B. J. Pichler, “Optimization, evaluation and calibration of a cross-strip DOI detector,” *Phys. Med. Biol.*, vol. 63, no. 4, p. 045022, Feb. 2018.

[79] R. W. Brown, Y.-C. N. Cheng, E. M. Haacke, M. R. Thompson, and R. Venkatesan, *Magnetic ressonance imaging: Physical Principles and Sequence Design*. Wiley Blackwell, 2014.

[80] Michael L. Lipton, *Totally Accessible MRI: A User’s Guide to Principles, Technology, and Applications*. Springer New York, 2008.

[81] M. A. Brown and R. C. Semelka, *MRI Basic Principles and Applications*, 3rd ed. Hoboken, NJ, USA: John Wiley & Sons, Inc., 2003.

[82] Siemens Healthcare, *Magnets, Spins, and Resonances - An introduction to the basics of Magnetic Resonance*. Erlangen, Germany, 2015.

[83] D. W. McRobbie, E. A. Moore, and M. J. Graves, *MRI from Picture to Proton*. Cambridge: Cambridge University Press, 2017.

[84] H. H. Quick, R. Ladebeck, and J.-C. Georgl, “Whole-Body MR/PET Hybrid Imaging: Technical Considerations, Clinical Workflow, and Inital Results,” *MAGNETOM Flash*, no. 46, pp. 88–100, 2011.

[85] V. S. Lee, *Cardiovascular MR Imaging: Physical Principles to Practical Protocols*, 1st ed. Lippincott Williams & Wilkins, 2005.

[86] “BI 320-PA-SI (for Siemens Tim® MRT).” http://www.noras.de/en/mri-products/breast-biopsy-solutions/bi-320-pa-si/ (accessed Apr. 05, 2019).

[87] S. S. D. Hamamatsu Photonics K.K., “MPPC module for PET KACC9009E03,” 2017.

[88] J. A. Merino Bonilla, M. Torres Tabanera, and L. H. Ros Mendoza, “Breast cancer in the 21st century: From early detection to new therapies,” *Radiol. (English Ed.*, vol. 59, no. 5, pp. 368–379, Sep. 2017.

[89] R. Branch, N. Cancer, C. Prevention, and S. Branch, “Relation of Tumor Size, Lymph Node Status, and Survival in 24,740 Breast Cancer Cases,” 1989.

[90] “Prototype Breast Cancer Imaging System May Improve Patient Care,” 2009. https://www.bnl.gov/newsroom/news.php?a=110975 (accessed Apr. 05, 2019).

[91] S. and A. Collins, “What is breast cancer?” https://www.cancer.org/cancer/breast-cancer/about/what-is-breast-cancer.html (accessed Apr. 05, 2019).

[92] G. Delso *et al.*, “Performance Measurements of the Siemens mMR Integrated Whole-Body PET/MR Scanner,” *J. Nucl. Med.*, vol. 52, no. 12, pp. 1914–1922, Dec. 2011.

[93] A. M. Karlberg, O. Sæther, L. Eikenes, and P. E. Goa, “Quantitative comparison of PET performance—Siemens Biograph mCT and mMR,” *EJNMMI Phys.*, vol. 3, no. 1, p. 5, Dec. 2016.

[94] Y.-C. Tai, H. Wu, D. Pal, and J. A. O’Sullivan, “Virtual-Pinhole PET,” *J. Nucl. Med.*, vol. 49, no. 3, pp. 471–479, Mar. 2008.

[95] J. R. Vaughan, J Thomas and Griffiths, *RF Coils for MRI*. John Wiley & Sons, 2012.

[96] S. S. D. Hamamatsu Photonics K.K., “MPPC module for PET KACC0011E02,” 2016.

[97] S. S. D. Hamamatsu Photonics K.K., “PET MODULE EVAKIT01 Instruction Manual K29-B62154,” 2017.

[98] S. S. D. Hamamatsu Photonics K.K., “MPPC for scintillation S14160 series,” 2017.

[99] S. S. D. Hamamatsu Photonics K.K., “TOF-PET module (LC, PET Module Generation 4.1) K29-B62052,” 2018.

[100] Siemens AG, “System Owner Manual: MAGNETOM Prisma,” 2015.

[101] T. G. Turkington *et al.*, “A large field of view positron emission mammography imager,” *2002 IEEE Nucl. Sci. Symp. Conf. Rec.*, vol. 3, pp. 1883–1886, 2002.

[102] N. K. Doshi, R. W. Silverman, Y. Shao, and S. R. Cherry, “maxPET, a dedicated mammary and axillary region PET imaging system for breast cancer,” *IEEE Trans. Nucl. Sci.*, vol. 48, no. 3, pp. 811–815, Jun. 2001.

[103] K. Murthy *et al.*, “Positron emission mammographic instrument: Initial results,” *Radiology*, vol. 215, no. 1, pp. 280–285, 2000.

[104] S. M. Srinivas *et al.*, “A Dedicated Breast Positron Emission Tomography Scanner: Proof of Concept,” *J. Med. Imaging Radiat. Sci.*, vol. 45, no. 4, pp. 435–439, Dec. 2014.

[105] D. L. Freese *et al.*, “Spatial resolution uniformity, isotropy, and the effect of depth of interaction information in a 1mm3 resolution, limited-angle PET system,” *2014 IEEE Nucl. Sci. Symp. Med. Imaging Conf.*, pp. 1–4, Nov. 2014.

[106] Y. Zhang *et al.*, “The System Design, Engineering Architecture, and Preliminary Results of a Lower-Cost High-Sensitivity High-Resolution

Positron Emission Mammography Camera," *IEEE Trans. Nucl. Sci.*, vol. 57, no. 1, pp. 104–110, Feb. 2010.

[107] L. MacDonald, J. Edwards, T. Lewellen, D. Haseley, J. Rogers, and P. Kinahan, "Clinical Imaging Characteristics of the Positron Emission Mammography Camera: PEM Flex Solo II," *J. Nucl. Med.*, vol. 50, no. 10, pp. 1666–1675, Oct. 2009.

[108] E. L. Rosen, T. G. Turkington, M. S. Soo, J. A. Baker, and R. E. Coleman, "Detection of Primary Breast Carcinoma with a Dedicated, Large-Field-of-View FDG PET Mammography Device: Initial Experience," *Radiology*, vol. 234, no. 2, pp. 527–534, Feb. 2005.

[109] M. C. Abreu *et al.*, "Clear-PEM: A dedicated pet camera for improved breast cancer detection," *Radiat. Prot. Dosimetry*, vol. 116, no. 1–4, pp. 208–210, 2005.

[110] M. F. Smith, R. R. Raylman, S. Majewski, and A. G. Weisenberger, "Positron emission mammography with tomographic acquisition using dual planar detectors: Initial evaluations," *Phys. Med. Biol.*, vol. 49, no. 11, pp. 2437–2452, 2004.

[111] G. C. Wang, J. S. Huber, W. W. Moses, J. Qi, and W. S. Choong, "Characterization of the LBNL PEM camera," *IEEE Trans. Nucl. Sci.*, vol. 53, no. 3, pp. 1129–1135, 2006.

[112] Y. Wu *et al.*, "PET characteristics of a dedicated breast PET/CT scanner prototype," *Phys. Med. Biol.*, vol. 54, no. 13, pp. 4273–4287, Jul. 2009.

[113] R. R. Raylman *et al.*, "The positron emission mammography/tomography breast imaging and biopsy system (PEM/PET): design, construction and phantom-based measurements," *Phys. Med. Biol.*, vol. 53, no. 3, pp. 637–653, Feb. 2008.

[114] A. Ferrero, Q. Peng, G. W. B. Jr, B. Sumanasena, W. W. Moses, and R. D. Badawi, "Preliminary performance characterization of DbPET2.1, a PET scanner dedicated to the imaging of the breast and extremities," *Biomed. Phys. Eng. Express*, vol. 1, no. 1, p. 015202, Jun. 2015.

[115] D. Narayanan and W. A. Berg, "Dedicated Breast Gamma Camera Imaging and Breast PET," *PET Clin.*, vol. 13, no. 3, pp. 363–381, Jul. 2018.

[116] A. Karimian *et al.*, "CYBPET: a cylindrical PET system for breast imaging," *Nucl. Instruments Methods Phys. Res. Sect. A Accel. Spectrometers, Detect. Assoc. Equip.*, vol. 545, no. 1–2, pp. 427–435, Jun. 2005.

[117] K. K. Miyake *et al.*, "Performance evaluation of a new dedicated breast PET scanner using NEMA NU4-2008 standards," *J. Nucl. Med.*, vol. 55, no. 7, pp. 1198–1203, 2014.

[118] K. Nishimatsu *et al.*, "Higher breast cancer conspicuity on dbPET compared to WB-PET/CT," *Eur. J. Radiol.*, vol. 90, pp. 138–145, May 2017.

[119] L. Li *et al.*, "Ability of the Positron Emission Mammography system, PEMi,

in detection of millimeter-sized lesions," *IEEE Nucl. Sci. Symp. Conf. Rec.*, pp. 1–7, 2013.

[120] H. Baghaei *et al.*, "A Breast Phantom Lesion Study With the High Resolution Transformable HOTPET Camera," *IEEE Trans. Nucl. Sci.*, vol. 57, no. 5, pp. 2504–2509, Oct. 2010.

[121] L. Moliner *et al.*, "Design and evaluation of the MAMMI dedicated breast PET," *Med. Phys.*, vol. 39, no. 9, pp. 5393–5404, Aug. 2012.

[122] M. Iima *et al.*, "Clinical performance of 2 dedicated PET scanners for breast imaging: initial evaluation.," *J. Nucl. Med.*, vol. 53, no. 10, pp. 1534–42, 2012.

[123] A. J. Mathews, S. Komarov, H. Wu, J. A. O'Sullivan, and Y.-C. Tai, "Improving PET imaging for breast cancer using virtual pinhole PET half-ring insert.," *Phys. Med. Biol.*, vol. 58, no. 18, pp. 6407–27, Sep. 2013.

[124] B. Ravindranath *et al.*, "A simultaneous PET/MRI breast scanner based on the RatCAP," *2008 IEEE Nucl. Sci. Symp. Conf. Rec.*, no. d, pp. 4650–4655, Oct. 2008.

[125] B. Ravindranath *et al.*, "Results from prototype II of the BNL simultaneous PET-MRI dedicated breast scanner," *IEEE Nucl. Sci. Symp. Conf. Rec.*, pp. 3315–3317, 2009.

[126] C. Kuhl *et al.*, "Novel PET / MRI technology for enhanced breast cancer diagnosis," *Diagnistic Imaging Eur.*, no. November, pp. 18–19, 2017.

[127] B. Weissler *et al.*, "Hyperion III – A flexible PET detector platform for simultaneous PET/MRI," *IEEE Nucl. Sci. Symp. Med. Imaging Conf. Rec.*, p. MIC-08-02, 2019.

[128] B. Weissler *et al.*, "A Digital Preclinical PET/MRI Insert and Initial Results," *IEEE Trans. Med. Imaging*, vol. 34, no. 11, pp. 2258–2270, Nov. 2015.

[129] J. Jiang *et al.*, "A second-generation virtual-pinhole PET device for enhancing contrast recovery and improving lesion detectability of a whole-body PET/CT scanner," *Med. Phys.*, vol. 46, no. 9, pp. 4165–4176, Sep. 2019.

[130] A. Stolin *et al.*, "Evaluation of Hamamatsu PET Imaging Modules for Dedicated TOF-Capable Scanners," *IEEE Trans. Radiat. Plasma Med. Sci.*, vol. 3, no. 6, pp. 634–639, Nov. 2019.

[131] J. Schenck, "the role of magnetic susceptibility in magnetic resonance imaging: MRI magnetic compatibility of the first and second kind," *Medical Physics-Lancaster Pa-*. 1996.

[132] M. S. H. Akram *et al.*, "MRI compatibility study of an integrated PET/RF-coil prototype system at 3 T," *J. Magn. Reson.*, vol. 283, pp. 62–70, 2017.

[133] C. R. Camacho, D. B. Plewes, and R. M. Henkelman, "Nonsusceptibility artifacts due to metallic objects in MR imaging," *J. Magn. Reson. Imaging*,

vol. 5, no. 1, pp. 75–88, Jan. 1995.

[134] C. Clinical, A. Iagaru, T. Hope, and P. Veit-haibach, *PET/MRI in Oncology*. Cham: Springer International Publishing, 2018.

[135] B. J. Lee, R. D. Watkins, C.-M. Chang, and C. S. Levin, “Low eddy current RF shielding enclosure designs for 3T MR applications,” *Magn. Reson. Med.*, vol. 00, pp. 1–8, Jun. 2017.

[136] A. J. González *et al.*, “The MINDView brain PET detector, feasibility study based on SiPM arrays,” *Nucl. Instruments Methods Phys. Res. Sect. A Accel. Spectrometers, Detect. Assoc. Equip.*, vol. 818, pp. 82–90, May 2016.

[137] F. Nishikido *et al.*, “Development of a full-ring ‘add-on PET’ prototype: A head coil with DOI-PET detectors for integrated PET/MRI,” *Nucl. Instruments Methods Phys. Res. Sect. A Accel. Spectrometers, Detect. Assoc. Equip.*, vol. 863, pp. 55–61, 2017.

[138] A. Del Guerra *et al.*, “TRIMAGE: A dedicated trimodality (PET/MR/EEG) imaging tool for schizophrenia,” *Eur. Psychiatry*, vol. 50, pp. 7–20, 2018.

[139] B. J. Lee, R. D. Watkins, K. S. Lee, C. Chang, and C. S. Levin, “Performance evaluation of RF coils integrated with an RF-penetrable PET insert for simultaneous PET/MRI,” *Magn. Reson. Med.*, vol. 81, no. 2, pp. 1434–1446, Feb. 2019.

[140] H. S. Yoon *et al.*, “Initial Results of Simultaneous PET/MRI Experiments with an MRI-Compatible Silicon Photomultiplier PET Scanner,” *J. Nucl. Med.*, vol. 53, no. 4, pp. 608–614, Apr. 2012.

[141] B. R. C. Catana, L. Byars, F. Schmidt, P. G. Lahoz, B. Guerin, M. Judenhofer, J. Herraiz, T. Witzel, M. Kapusta, J. Corbeil, L. Wald, J. M. Udias, B. Pichler, M. Schmand, “Update on the Development of the 7-T MR-compatible PET Detector and System Technology for the Human Dynamic Neurochemical Connectome Scanner,” in *PET/MRI workshop SNMMI/ISMRM*, Nov. 2019.

[142] J. Wang, W. Mao, M. Qiu, M. B. Smith, and R. T. Constable, “Factors influencing flip angle mapping in MRI: RF pulse shape, slice-select gradients, off-resonance excitation, andB0 inhomogeneities,” *Magn. Reson. Med.*, vol. 56, no. 2, pp. 463–468, Aug. 2006.

List of Figures

List of Tables

Abbreviations

APD	avalanche photo diode
ASIC	application specific integrated circuit
cFOV	center field of view
CRT	coincidence resolving time
CT	computed tomography
DFT	discrete Fourier transform
DOI	depth of interaction
ERES	energy resolution
FA	flip angle
FE	front-end
FBP	filtered back projection
FDG	^{18}F-fluordeoxyglucose
FFC	flexible flat cable
FID	free induction decay
FOV	field of view
FPGA	field programmable gate array
FWHM	full width at half maximum
G-APD	Geiger mode avalanche photodiode
GND	ground reference potential
HVPS	high voltage power supply
LFS	lutetium fine silicate
LOR	line of response
LSO	lutetium oxyorthosilicate
MRI	magnetic resonance imaging
NMR	nuclear magnetic resonance
OSEM	ordered subset expectation maximization
PCB	printed circuit board
PDE	photon detection efficiency
PET	positron emission tomography
PMT	photomultiplier tube
PVR	peak to valley ratio
PW	pulse width
RF	radio-frequency
RMS	root mean square
SiPM	silicon photon multiplier
SNR	signal to noise ratio
TDC	time to digital converter
TOF	time of flight
ToT	time over threshold

Declaration Statement

Hiermit erkläre ich die zur Promotion eingereichte Arbeit mit dem Titel „Towards the Development of a Breast PET/MRI Insert for a Clinical Whole-Body PET/MRI Scanner“ selbstständig verfasst, nur die angegebenen Quellen und Hilfsmittel benutzt und wörtlich oder inhaltlich übernommene Stellen als solche gekennzeichnet zu haben. Ich erkläre, dass die Richtlinien zur Sicherung guter wissenschaftlicher Praxis der Universität Tübingen (Beschluss des Senats vom 25.05.2000) beachtet wurden. Ich erkläre, dass ein professionelles Korrektorat der Firma Scribbr gegen Bezahlung erfolgt ist, welches sich auf Sprache, Konsistenz und akademischen Sprachgebrauch beschränkte. Ich versichere an Eides statt, dass diese Angaben wahr sind und dass ich nichts verschwiegen habe. Mir ist bekannt, dass die falsche Abgabe einer Versicherung an Eides mit einer Freiheitsstrafe bis zu drei Jahren oder mit Geldstrafe bestraft wird.

Die Dissertation wurde in der vorgelegten oder in ähnlicher Form noch bei keiner anderen Institution eingereicht. Ich habe bisher keine erfolglosen Promotionsversuche unternommen.

Tübingen, den 27.09.2021

____

(Fabian Schmidt)

Declaration of Contributions

The work conducted in this thesis was performed at the Department of Preclinical Imaging and Radiopharmacy under the supervision of Professor Dr. Bernd Pichler. I, Fabian Schmidt, herewith declare that this dissertation is my own original work, except where indicated through the proper use of citations and references. The following support was provided by other people:

The PET Insert System Design

The three geometric designs for the breast PET insert were elaborated together with Christian Pommranz, who performed the GATE simulations of the breast PET insert (which are not part of this thesis).

Customized PET Detector Based on the Hamamatsu PET Electronics

The process of determining the layout of the printed circuit board to adapt the photosensor to the signal processing board of the Hamamatsu PET modules was supported by Dr. Christoph Parl.

MRI Compatibility of the PET Modules

The MRI test sequences used with the Biograph mMR were programmed and adjusted during measurements by Ralf Ladebeck. Furthermore, Ralf Ladebeck, Dr. Johannes Breuer, and Dr. Dieter Ritter helped set up the measurement setups for the MRI compatibility tests on site. Discussions with the Siemens MI and MR group helped develop modifications for the setup and refine the tests.

I created the front-end filter board, which is based on a filter developed by the Siemens MI group. Dr. Martin Judenhofer contributed to the layout of the printed circuit board of the front-end filter board.

Publications and Presentations

Publications

F. P. Schmidt, A. Kolb, and B. J. Pichler, *“Optimization, evaluation and calibration of a cross-strip DOI detector,”* Phys. Med. Biol., vol. 63, no. 4, p. 45022, Feb. 2018.

Conference Contributions

F. P. Schmidt, C. M. Pommranz, J. C. Krämer, S. J. Diebold, J. G. Mannheim, C. la Fougère and B. J. Pichler, *“Development of a Breast PET Insert for the Biograph mMR,”* Deutsche Gesellschaft für Nuklearmedizin 59. Jahrestagung (NuklearMedizin 2021 – digital), Göttingen, Germany, 2021.

F. P. Schmidt, C. M. Pommranz, J. C. Krämer, S. J. Diebold, J. G. Mannheim and B. J. Pichler, *“Development of a Breast PET Insert for a Clinical Whole-Body PET/MRI Scanner,”* IEEE Nuclear Science Symposium and Medical Imaging Conference (NSS-MIC), Boston, Massachusetts, USA, 2020.

F. P. Schmidt, R. Ladebeck, L. Eberler, J. Breuer, N. Zhang, M. Judenhofer, L. Byars, M. Schmand and B. J. Pichler, *“Mutual Interference Study on MRI Compatibility of the Hamamatsu PET Modules inside a 3T MRI scanner,”* IEEE Nuclear Science Symposium and Medical Imaging Conference (NSS-MIC), Manchester, United Kingdom, 2019.

F. P. Schmidt, C. Parl, R. Ladebeck, J. Breuer, N. Zhang, M. Schmand and B. J. Pichler, *“MRI compatibility of a PET detector based on the HPK C13500 series PET module,”* IEEE Nuclear Science Symposium and Medical Imaging Conference (NSS-MIC), Sydney, Australia, 2018.

F. P. Schmidt, C. Parl and B J. Pichler*, “MR compatibility evaluation of the HPK C13500 series PET module for organ-specific RF/PET-detectors,”* IEEE Nuclear Science Symposium and Medical Imaging Conference (NSS-MIC), Atlanta, Georgia, USA, 2017.

F. P. Schmidt, A. Kolb and B. J. Pichler*, “Evaluation of a cross strip encoding DOI PET detector,”* IEEE Nuclear Science Symposium and Medical Imaging Conference (NSS-MIC), Strasbourg, France, 2016.

Acknowledgements

First, I want to express my gratitude to my doctoral advisor Professor Dr. Bernd Pichler. Without any doubt, he had the greatest scientific and personal impact on me among all of the people who accompanied me throughout my PhD. I want to thank him for the many opportunities he gave me, such as an excellent environment for scientific work, interdisciplinary insights into the preclinical and clinical fields, the chance to take on more responsibilities, and the freedom to choose the focus of my work. I highly appreciate the trust Bernd put in me; he always made me feel as though I was not only his PhD student but also a greatly appreciated colleague.

Furthermore, I want to thank Professor Dr. Josef Jochum for his willingness to take on the secondary supervision of this thesis.

My sincere gratitude goes to the Siemens molecular imaging detector R&D group for our close collaboration over the past years. I appreciate the warm welcome they greeted me with on each of my visits to Rockford. In particular, my gratitude goes to Dr. Matthias Schmand, Dr. Johannes Breuer, Dr. Nan Zhang, Dr. Martin Judenhofer, and Larry Byars for our profound scientific exchanges and for always having an open ear for me when questions came up throughout my thesis. I want to especially thank Matthias and Nan for attracting my interest to positron emission tomography during my master's thesis and their valuable recommendation to pursue a PhD in the field of molecular imaging.

I cannot thank the Siemens MR group enough, including Dr. Dieter Ritter, Ludwig Eberler, and especially Ralf Ladebeck, for their continuous support and discussion of MR-related questions. Special thanks go to Ralf and Johannes for their endurance, as they spent several nights with me by the Biograph mMR.

Furthermore, I appreciate the discussions with the Hamamatsu Photonics team and especially with Takuya Kato who never tired of providing me information about the use of the PET modules.

My acknowledgements would be incomplete without extending a gratifying note to my past and present colleagues at the Werner Siemens Imaging Center and in particular to the detector physics group, with special thanks to Dr. Armin Kolb, Dr. Christoph Parl, Christian Pommranz and Paul Soubiran, Dr. Julia Mannheim, and Dr. Andreas Schmid, who kindly helped with proofreading this thesis. Furthermore, I would like to thank Dr. Rebecca Rock for her administrative support.

Lastly, a heartfelt thanks to my family and especially to my beloved wife Eva. This work would never have been possible without her warm-hearted and continuous support, patience, and understanding over the past years.

Thank you!